DOCTORAL THESIS IN MEDICAL TECHNOLOGY AND MEDICAL SCIENCE
STOCKHOLM, SWEDEN 2019

Non-invasive imaging for improved cardiovascular diagnostics

Shear wave elastography, relative pressure estimation, and tomographic reconstruction

DAVID MARLEVI

Karolinska Institutet

NON-INVASIVE IMAGING FOR IMPROVED CARDIOVASCULAR DIAGNOSTICS

Shear wave elastography, relative pressure estimation, and tomographic reconstruction

DAVID MARLEVI

Doctoral Thesis

KTH Royal Institute of Technology
School of Engineering Sciences in Chemistry, Biotechnology and Health
Department of Biomedical Engineering and Health Systems
Division of Biomedical Imaging
SE-141 52 Huddinge

Karolinska Institutet
Department of Clinical Sciences
SE-171 77 Stockholm

Akademisk avhandling som med tillstånd av Kungliga Tekniska Högskolan och Karolinska Institutet framlägges till offentlig granskning för avläggande av teknologie och medicine doktorsexamen fredagen den 20 september 2019 klockan 09:00 i sal T2, Hälsovägen 11C, Kungliga Tekniska Högskolan.

Main supervisor

Assoc. Prof. Matilda Larsson
KTH Royal Institute of Technology
Stockholm, Sweden

Co-supervisors

Prof. Reidar Winter
Karolinska Institutet
Stockholm, Sweden

Assoc. Prof. Massimiliano Colarieti-Tosti
KTH Royal Institute of Technology
Stockholm, Sweden

Faculty opponent

Prof. Kathryn Nightingale
Duke University
Durham, NC, United States of America

Evaluation committee

Prof. Ulf Hedin
Karolinska Institutet
Stockholm, Sweden

Prof. Alistair Young
King's College London
London, United Kingdom

Assoc. Prof. Paola Nardinocchi
Sapienza University of Rome
Rome, Italy

TRITA-CBH-FOU-2019:38
ISBN 978-91-7873-251-7

Department of Biomedical Engineering
and Health Systems
KTH Royal Institute of Technology

Department of Clinical Sciences
Karolinska Institutet

Cover: Shear wave propagation through a carotid AHA type VI plaque

Print: Universitetsservice US-AB, Stockholm, 2019

till Linda

List of publications

This thesis is based on the following eight publications. At the end of this thesis, all publications are provided in their published or prepared manuscript form:

I. **Arterial stiffness estimation by shear wave elastography: validation in phantoms with mechanical testing**

E. Maksuti, E. Widman, **D. Larsson***, M.W. Urban, M. Larsson, A. Bjällmark
Ultrasound in Medicine & Biology, vol. 42, p. 309-321, 2016

II. **Plaque characterization using shear wave elastography – evaluation of differentiability and accuracy using a combined *ex-vivo* and *in-vitro* setup**

D. Marlevi, E. Maksuti, M.W. Urban, R. Winter, M. Larsson
Physics in Medicine & Biology, vol. 63, no. 23, 235008 (17pp), 2018

III. **An *ex-vivo* setup for characterization of atherosclerotic plaque using shear wave elastography and micro-computed tomography**

D. Larsson*, J. Roy, T.C. Gasser, M.W. Urban, M. Colarieti-Tosti, M. Larsson
2016 IEEE International Ultrasonics Symposium (IUS), Tours, France, 2016
DOI: 10.1109/ULTSYM.2016.7728810

IV. **Shear wave elastography enables detection of vulnerable carotid plaques – MRI-validation of combined spatiotemporal and frequency-dependent wave analysis**

D. Marlevi, S. Mulvagh, R. Huang, J.K. DeMarco, H. Ota, J. Huston, R. Winter, T.A. Macedo, S.S. Abdelmoneim, M. Larsson, P. Pellikka, M.W. Urban
Manuscript in review

*David Larsson is the pre-marital name of David Marlevi

V. Estimation of cardiovascular relative pressure using virtual work-energy

D. Marlevi, B. Ruijsink, M. Balmus, D. Dillon-Murphy, D. Fovargue, K. Pushparajah, C. Bertoglio, M. Colarieti-Tosti, M. Larsson, P. Lamata, C.A. Figueroa, R. Razavi, D.A. Nordsletten
Scientific Reports, vol. 9, article number 1375, 2019

VI. Non-invasive estimation of relative pressure in turbulent flow using virtual work-energy

D. Marlevi, H. Ha, D. Dillon-Murphy, J.F. Fernandes, D. Fovargue, M. Colarieti-Tosti, M. Larsson, P. Lamata, C.A. Figueroa, T. Ebbers, D.A. Nordsletten
Manuscript in review

VII. Altered aortic hemodynamics and relative pressure in patients with dilated cardiomyopathy

D. Marlevi, J. Mariscal-Harana, J. Sotelo, B. Ruijsink, M. Hadjicharalambous, L. Asner, E. Sammut, R. Chabiniok, S. Uribe, R. Winter, P. Lamata, J. Alastruey, D.A. Nordsletten
Manuscript in review

VIII. Multigrid reconstruction in tomographic imaging

D. Marlevi, H. Kohr, J.-W. Buurlage, B. Gao, K.J. Batenburg, M. Colarieti-Tosti
Manuscript accepted, IEEE Transactions on Radiation and Plasma Medical Sciences, 2019

Abstract

Throughout the last century, medical imaging has come to revolutionise the way we diagnose disease, and is today an indispensable part of virtually any clinical practice. In cardiovascular care imaging is extensively utilised, and the development of novel techniques promises refined diagnostic abilities: ultrasound elastography allows for constitutive tissue assessment, 4D flow magnetic resonance imaging (MRI) enables full-field flow mapping, and micro-Computed Tomography (CT) permits high-resolution imaging at pre-clinical level. However, following the complex nature of cardiovascular disease, refined methods are still very much needed to accurately utilise these techniques and to effectively isolate disease developments.

The aim of this thesis has been to develop such methods for refined cardiovascular image diagnostics. In total eight studies conducted over three separate focus areas have been included: four on vascular shear wave elastography (SWE), three on non-invasive cardiovascular relative pressure estimations, and one on tomographic reconstruction for pre-clinical imaging.

In Study I-IV, the accuracy and feasibility of vascular SWE was evaluated, with particular focus on refined carotid plaque characterisation. With confined arterial or plaque tissue restricting acoustic wave propagation, analysis of group and phase velocity was performed with SWE output validated against reference mechanical testing and imaging. The results indicate that geometrical confinement has a significant impact on SWE accuracy, however that a combined group and phase velocity approach can be utilised to identify vulnerable carotid plaque lesions *in-vivo*.

In Study V-VII, a non-invasive method for the interrogation of relative pressure from imaged cardiovascular flow was developed. Using the concept of virtual work-energy, the method was applied to accurately assess relative pressures throughout complex, turbulence-inducing, branching vasculatures. The method was also applied on a dilated cardiomyopathy cohort, indicating arterial hemodynamic changes in cardiac disease.

Lastly, in Study VIII a method for multigrid image reconstruction of tomographic data was developed, utilising domain splitting and operator masking to accurately reconstruct high-resolution regions-of-interests at a fraction of the computational cost of conventional full-resolution methods.

Together, the eight studies have incorporated a range of different imaging modalities, developed methods for both constitutive and hemodynamic cardiovascular assessment, and utilised refined pre-clinical imaging, all with the same purpose: to refine current state cardiovascular imaging and to improve our ability to non-invasively assess cardiovascular disease. With promising results reached, the studies lay the foundation for continued clinical investigations, advancing the presented methods and maturing their usage for an improved future cardiovascular care.

Keywords: *Medical imaging, Cardiovascular disease, Atherosclerosis, Hemodynamics, Ultrasound, Shear Wave Elastography (SWE), Magnetic Resonance Imaging (MRI), 4D flow MRI, Relative Pressure, Virtual Work-Energy, micro-Computed Tomography (micro-CT), Tomographic reconstruction, Pre-clinical imaging*

Populärvetenskaplig sammanfattning

Medicinsk avbildning utgör idag en central del av modern klinisk diagnostik, och bildgivande diagnostikverktyg har kommit att i grunden förändra sättet på vilket dagligt kliniskt arbete utförs. Medicinsk bildteknik används också i stor utsträckning inom hjärt-kärldiagnostik, och i takt med att nya tekniker utvecklas kan förfinad information inhämtas: ultraljudsbaserad elastografi möjliggör avbildning av vävnaders mekaniska egenskaper, fyrdimensionella blodflödesmönster kan kartläggas genom 4D flödes-magnetresonanstomografi (MRI), och mikro-Datortomografi (mikro-CT) möjliggör preklinisk avbildning i mikrometerupplösning. För att kunna dra nytta av dessa teknikers potential i ett kliniskt sammanhang behövs dock förfinade och validerade analysverktyg, särskilt med tanke på hjärt-kärlsjukdomars komplexa och multifaktoriella natur.

Syftet med följande avhandling har varit att utveckla sådana metoder för förbättrad hjärt-kärlavbildning. Avhandlingen innehåller totalt åtta delarbeten fördelat över tre fokusområden: fyra inom vaskulär skjuvvågselastografi (SWE), tre inom icke-invasiv tryckfallsmätning, och en inom pre-klinisk tomografisk bildrekonstruktion.

I studie I-IV utvärderades vaskulär SWE, med särskilt fokus på teknikens potential för förfinad karaktärisering av karotisplack. I alla studier undersöktes SWE grupp- och fashastighet, med estimerade hastigheter och styvheter validerade mot mekanisk referensmätning eller kompletterande avbildning. Resultaten visar hur spatialt avgränsade kärl eller plack har en tydlig inverkan på SWE:s noggrannhet, men indikerar även hur rupturbenägna plack kan identifieras genom en kombination av grupp- och fashastighetsanalys.

I studie V-VII utvecklades en ny metod för icke-invasiv tryckfallsmätning baserad uteslutande på uppmätt 4D-flödesdata. Genom en komplett flödesmekanisk beskrivning i kombination med ett virtuellt flödesfält kan exakta och robusta tryckfallsmätningar genomföras genom komplexa, turbulensinducerande, och kliniskt relevant kardiovaskulära strukturer. Metoden användes också för att analysera en klinisk kohort med dilaterad kardiomyopati, där tydliga förändringar i arteriellt blodtrycksbeteende detekterades.

I studie VIII utvecklades en metod för multidimensionell bildrekonstruktion av tomografisk mikro-CT-data. Genom domän- och operatorseparering visar resultaten hur högupplöst rekonstruktion av en subdomän kan uppnås till en bråkdel av den totala tids- eller minnesåtgången som annars fordras för en fullupplöst bildrekonstruktion.

Tillsammans har de åtta delstudierna använt ett antal olika avbildningsmodaliteter, applicerat både vävnadsbaserat och hemodynamisk utvärdering av hjärt-kärlsystemet, och slutligen inkluderat preklinisk avbildning, allt för att uppnå samma mål: att förbättra klinisk hjärt-kärlavbildning och ge en fördjupad förståelse av olika hjärt-kärlsjukdomars kliniska manifestation genom icke-invasiv avbildning. Avhandlingen utgör också grunden för fortsatta vetenskapliga studier, där de utvärderade metoderna kan komma att förfinas ytterligare som del av en mer omfattande klinisk implementering.

Nyckelord*: Medicinsk avbildning, Hjärt-kärlsjukdomar, Ateroskleros, Hemodynamik, Ultraljud, Skjuvvågselastografi (SWE), Magnetresonanstomografi (MRI), 4D flödes-MRI, Tryckfall, Virtuellt flöde, mikro-Datortomografi (mikro-CT), Tomografisk rekonstruktion, Preklinisk avbildning*

Acknowledgements

This thesis would not have been possible without the help and feedback from a lot people, supporting me both academically and privately during the last five years. Even though too many to list, I guarantee that I remember you all, and I am eternally grateful for all that you have done. However, there are a few people who stand out and deserve a special mention.

First and foremost, I would like to thank my main supervisor **Matilda Larsson** for steering me through my five years as a PhD student, and for providing endless support throughout. Thank you also to my co-supervisor **Massimiliano Colarieti-Tosti** for being similarly supportive, for always being open for discussions and feedback, and for spending hours discussing the ins and outs of fundamental imaging physics. In particular, thank you both for being so open and positive towards new collaborations and project ideas, and for allowing this thesis to grow in so many exciting and different directions.

Second, I would like to thank my clinical supervisor **Reidar Winter** for providing clinical input and for welcoming me into the clinical research environment. Thank you also for being genuinely interested in technical novelties, and for your enthusiasm in pushing technical developments into clinical practice.

Albeit not a supervisor on paper, a big part of this thesis would not have been possible without the guidance, support, and input provided by **David Nordsletten** at King's College London and the University of Michigan. Thank you for welcoming me in London, thank you for your enthusiasm for translational biomedical research, and thank you for tirelessly providing feedback and invaluable input on everything we have done together. You are a truly inspiring academic from whom I have learned so much, and it has been a real pleasure to work and collaborate with you.

Similarly, **Matthew Urban** at the Mayo Clinic in Rochester, Minnesota, has been a significant contributor to the conducted shear wave studies. Thank you for our numerous discussions on ultrasound imaging, and for unselfishly allowing me to take part in your exciting clinical research work.

Outside of academia, I would like to thank my parents, **Hanna** and **Jörgen**, as well as brother, **Adam**, for unconditional support throughout my entire academic journey, regardless of where in the world I have been.

Lastly, I would like to thank my wife **Linda**. Thank you for always being there for me, for inspiring me, for challenging me, and for making me want to become better every day. Without you none of this would have been possible, and I am truly grateful for each moment that I am allowed to spend together with you.

David Marlevi

Stockholm, 9 August 2019

Abbreviations

1D	One dimensional
2D	Two dimensional
2DFFT	Two dimensional fast Fourier transform
3D	Three dimensional
4D	Four dimensional
4D flow MRI	Three dimensional, time-resolved phase contrast magnetic resonance imaging
AAD	Acute aortic dissection
ACEI	Angiotensin-converting-enzyme inhibitor
AHA	American Heart Association
A-mode	Amplitude mode
ARFI	Acoustic radiation force impulse
AV-plane	Atrioventricular plane
BMI	Body mass index
B-mode	Brightness mode
CAC	Coronary artery calcification
CE-T1W	Contrast enhanced T1-weighted
CEUS	Contrast-enhanced ultrasound
CFD	Computational fluid dynamics
Cine SSFP MRI	Cine steady state free precession magnetic resonance imaging
CMOS	Complementary metal oxide semiconductor
CO	Cardiac output
CoA	Coarctation of the aorta
CRP	C-reactive protein
CT	Computed tomography
CTA	Computed tomography angiography
CW	Continuous wave
CVD	Cardiovascular disease
DBP	Diastolic blood pressure
DCM	Dilated cardiomyopathy
DSA	Digital subtraction angiography
Ea	Arterial elastance
ECG	Electrocardiogram
EDPVR	End-diastolic pressure-volume relation
EDV	End-diastolic volume
EF	Ejection fraction
EOA	Effective orifice area
ESPVR	End-systolic pressure-volume relation

ESV	End-systolic volume
FBP	Filtered back projection
FDG-PET	[^{18}F]-Fluorodeoxyglucose positron emission tomography
FDM	Finite difference method
FEM	Finite element method
FT-cycle	Freeze-thaw cycle
HCM	Hypertrophic cardiomyopathy
HDL	High-density lipoproteins
HR	Heart rate
ICOSA6	Six-directional icosahedral flow encoding
IMT	Intima-media thickness
IQ-data	In-phase and quadrature data
IVC	Isovolumetric contraction
IVR	Isovolumetric relaxation
IVUS	Intravascular ultrasound
LDL	Low-density lipoproteins
LV	Left ventricle
LVOT	Left ventricular outflow tract
MLU	Medial lamellar unit
M-mode	Motion mode
MPRAGE	Magnetisation-prepared rapid acquisition gradient echo
MRE	Magnetic resonance elastography
MRI	Magnetic resonance imaging
NMR	Nuclear magnetic resonance
NYHA	New York heart Association
OCT	Optical coherence tomography
ODL	Operator discretisation library
oxLDL	Oxidised low-density lipoproteins
PCI	Percutaneous coronary intervention
PC-MRI	Phase contrast magnetic resonance imaging
PET	Positron emission tomography
PPE	Poisson pressure equation
PW	Pulsed wave
PVA	Poly(vinyl alcohol)
PWI	Pulse wave imaging
PWV	Pulse wave velocity
RANSAC	Random sample consensus
RF	Radiofrequency
RLP	Residual lipoprotein
ROI	Region of interest
RV	Right ventricle
SBP	Systolic blood pressure
SD	Standard deviation
SMC	Smooth muscle cell
SNR	Signal-to-noise ratio

SPECT	Single-photon emission computed tomography
SSI	Supersonic shear imaging
SSIM	Structural similarity index
STE	Stokes estimator
SV	Stroke volume
SWE	Shear wave elastography
T1W	T1-weighted
T2W	T2-weighted
TCFA	Thin-cap fibroatheroma
TGC	Time gain compensation
TKE	Turbulent kinetic energy
TOF-MRA	Time-of-flight magnetic resonance angiography
TP	Turbulence production
TPR	Total peripheral resistance
TTP	Time-to-peak
VENC	Velocity encoding
WERP	Work-energy relative pressure
WERP-t	Work-energy relative pressure with turbulence
νWERP	virtual Work-energy relative pressure
νWERP-t	virtual Work-energy relative pressure with turbulence

Table of contents

Paper II: Plaque characterization using shear wave elastography – evaluation of differentiability and accuracy using a combined *ex-vivo* and *in-vitro* setup

Paper III: An *ex-vivo* setup for characterization of atherosclerotic plaque using shear wave elastography and micro-computed tomography

Paper IV: Shear wave elastography enables the detection of vulnerable carotid plaques – MRI-validation of combined spatiotemporal and frequency-dependent wave analysis

Paper V: Estimation of cardiovascular relative pressure using virtual work-energy

Paper VI: Non-invasive estimation of relative pressure in turbulent flow using virtual work-energy

Paper VII: Altered aortic hemodynamics and relative pressure in patients with dilated cardiomyopathy

Paper VIII: Multigrid reconstruction in tomographic imaging

Part I

Research context

Chapter 1

Introduction

Dear Sir or Madam, will you read my book?
It took me years to write, will you take a look?

Paperback writer (John Lennon & Paul McCartney), 1966

There are many ways in which a thesis in biomedical engineering might begin, but with medical imaging being the primary focus of this work, appreciating images as a visual form of communication seems like a fitting start.

Throughout the history of mankind, images have been used as an effective and direct way of conveying or transferring information. Prehistoric cave or rock paintings are today recognised as early forms of visual communication, and even though written communication has come to dominate following the invention of alphabetic languages, visual image-based data representation can be found throughout history. Hieroglyphic pictograms were used in ancient Egypt and Greece to communicate over cultural borders, breakthroughs in optical lens developments enabled planetary studies during the early Renaissance, and modern-day understanding of imaging physics has allowed for the non-invasive assessment of complex biological phenomena.

Studying scientific processes through image-based assessment, or using physical phenomena to generate image outputs have also been commonly employed throughout history. The Greek mathematician Euclid outlined fundamental optical physics in his work *Optics* around 300 BC [1], and in the early 1700s Isaac Newton expanded this knowledge with astounding scientific rigour in his work *Opticks* [2], in which he outlined the fundamentals of diffraction and polychromatic optical behaviour. Through the development of quantum mechanics in the early 1900s, and by understanding fundamental atomistic behaviour highly refined image-based tools are now available with electron microscopy providing sub-nm imaging [3], and with research-based image tools enabling real-time study of functional physiological processes [4].

The development of advanced imaging has also had a direct impact in the medical field, where imaging has come to revolutionise the way we diagnose, monitor, and

treat patients. For cardiovascular disease – being the number one cause of death in the world today [5] – imaging is an indispensable part of clinical practice. Ultrasound imaging is routinely used to assess cardiovascular anatomy as well as to map intravascular flows or tissue motion [6]. X-ray fluoroscopy or Computed Tomography (CT) is commonly used to guide interventional cardiovascular procedures [7], and Magnetic Resonance Imaging (MRI) provides excellent soft tissue contrast, utilised to identify ischemic tissue changes or visualise complex congenital conditions [8]. Recent developments even promises novel imaging abilities: ultrasound elastography enables constitutive tissue evaluation [9], 4D flow MRI permits comprehensive assessment of vascular flows [10], and pre-clinical imaging renders acquisitions at μm resolution [11].

Evidently, there is no lack of data that can be generated. However this abundance of data requires careful consideration of the clinical impact of derived measures. In fact, refined tools and metrics are still very much needed to accurately and effectively make use of these novel developed imaging techniques, and it is only through careful, scientific studies that defined correlations between fundamental image behaviour and disease manifestation can be clarified. In this way, accurate, effective, and specific tools can be introduced into clinical practice, refining current-state clinical diagnostics and improving future health care through advanced imaging.

This thesis entitled *Non-invasive imaging for improved cardiovascular diagnostics – shear wave elastography, relative pressure estimation, and tomographic reconstruction* aims at developing such technical tools for refined image-based clinical diagnostics. Studies on constitutive tissue behaviour, hemodynamic flow analysis, and pre-clinical imaging are combined to provide a comprehensive take on certain aspects of cardiovascular image diagnostics, advancing diagnostic measures in clinical areas where effective imaging tools are of particular importance: atherosclerotic plaque characterisation, hemodynamic flow assessment, and high-resolution pre-clinical tomographic reconstruction.

The thesis consists of two parts. First, the research context is outlined within which all scientific studies have been performed. The research context is also presented together with a review of major methodological aspects, key results, main discussion points, and conclusions from all performed studies. Second, the main scientific contributions are given as a collection of appended papers and manuscripts, together with an outline of specific author contributions.

Chapter 2

Aims

The general aim of this thesis has been to refine current state cardiovascular image diagnostics, and to improve our ability to non-invasively assess cardiovascular disease. In addressing this aim, eight scientific studies have been performed and compiled to form this thesis. The specific aim of each respective study was:

Study I To assess the accuracy of shear wave elastography (SWE) for vascular applications by evaluating the effect of confined geometry on shear modulus estimation in simplified geometries and arterial phantoms, comparing data to reference mechanical testing.

Study II To assess the ability of SWE to differentiate atherosclerotic phantom plaques of different mechanical stiffness, quantifying output as a function of varying plaque geometry, acoustic radiation force push location, and imaging plane.

Study III To evaluate the feasibility of using SWE on atherosclerotic plaque tissue by constructing an experimental *ex-vivo* setup with combined reference micro-CT.

Study IV To evaluate the *in-vivo* performance of SWE for atherosclerotic carotid plaque characterisation by comparing output to reference MRI data in a defined patient cohort.

Study V To develop, implement, and validate a non-invasive method for the estimation of relative pressure from acquired full-field velocity data, making specific use of the concept of virtual work-energy to enable arbitrary probing of relative pressures throughout any imaged vascular structure.

Study VI To extend and evaluate the virtual work-energy method in Study V for incoherent, turbulence-driven flow fields.

Study VII To evaluate aortic hemodynamics in a cardiomyopathy cohort, specifically using non-invasive phase-contrast imaging to quantify changes in aortic relative pressure in patients with dilated cardiomyopathy.

Study VIII To develop a method for multigrid tomographic reconstruction for pre-clinical micro-CT imaging, enabling reconstructions with multiple discretisation or regularisation domains at a fraction of the required full-resolution computational time or cost.

Chapter 3

Background

The following section outlines the basic concepts and scientific context in which this thesis has been performed. Following an initial review of fundamental cardiovascular physiology and disease development, details on cardiovascular image diagnostics are provided. Specifically, areas of particular relevance to the thesis (atherosclerotic plaque characterisation, refined image-based hemodynamic analysis, and pre-clinical imaging) are presented in detail.

3.1. Cardiovascular physiology

The cardiovascular system represents an integral part of the human body, being accountable for the circulation of blood. Through this circulation, the cardiovascular system is responsible for transporting oxygen, nutrients and hormones to, and waste products away from all cells of the body. The cardiovascular system also mediates the systemic transport of cells such as leukocytes or immune cells, recruited as a direct response to disease or injury. By so, the cardiovascular system plays a fundamental role in maintaining body homeostasis, controlling e.g. nutrient supply [12], temperature [13] and pH [14], and actively adapting and optimising response to different physiological and pathological states.

Anatomically, the cardiovascular system consists of the heart and a fully connected vascular network of arteries and veins, permeating through all tissues of the body. Even though seen as two entities, the heart and the vasculature is working very much in parallel, forming a complex interplay of adaption and re-modelling in response to faced physiological or pathological condition. With the heart and vasculature transporting blood through the body, their interplay is also intuitively understandable as disruptions in e.g. the ejection of blood from the heart will directly affect and trigger a response from the downstream vasculature. Similarly, any blockage of vascular flow will instantly result in disrupted flow returning to the heart, and hence initiate cardiovascular system response.

Despite this, to facilitate in the basic understanding of their fundamental physiology, the heart and the vasculature will here be presented in separate sections. However, connecting the two, subsequent sections on arterial-cardiac interaction and cardiovascular hemodynamics are also provided. Here basic

concepts on cardiovascular interaction, as well as the fundamental behaviour of blood, blood flow, and blood pressure are provided, depicting specifically how they cooperate in the cardiovascular system.

3.1.1. Cardiac physiology

a) Cardiac anatomy

The heart, depicted in Figure 3.1(a), is the main muscular organ of the cardiovascular system, situated inside the thoracic cavity of all humans. Specifically positioned posteriorly and slightly to the left of the sternum, the heart resides inside the so called pericardium or pericardial sac. In short, the pericardium is a fibrous double-layer structure, connecting the heart to the neighbouring mediastinum as well as protecting and limiting the heart from excessive free motion. In fact, contrary to popular belief the pericardium or outermost shape and volume of the heart does not change significantly during cardiac pumping, but blood is rather ejected through piston-like displacement of the internal atrioventricular plane (AV-plane) [15]. To assist in this motion, the pericardium therefore acts as a lubricating layer, where intrapericardial fluid allows for a smooth and energy-optimised gliding of these internal structures against the pericardial sac.

Inside the pericardium resides the myocardium or heart muscle, made up of four different compartments (two ventricles and two atria) typically sub-classified into two different sides (the right and the left heart). The right heart, consisting of the right atrium and right ventricle, is responsible for collecting deoxygenated blood entering from the inferior and superior vena cava, and subsequently ejecting this blood into the pulmonary circulation. Flowing through the pulmonary circulation, gas exchange of carbon dioxide (CO_2) and inhaled oxygen (O_2) is performed, re-oxygenising blood that is later being directed through the pulmonary veins into the left atrium. In the left heart, re-oxygenised blood in the left atrium is then fed forward into the left ventricle, which acts as the main pump for the systemic circulation, or the circulation of blood through the rest of the body.

With the right and left heart responsible for these two different circulation systems, the two sides also work against two different vascular resistances. In fact, under normal physiological conditions, the pulmonary circulation contains only around $1/10^{th}$ of the total blood volume, and shows a vascular resistance of around $1/5^{th}$ of that of the systemic circulation [16]. With flow Q and resistance R connected to the pressure gradient ΔP through

$$Q = \frac{\Delta P}{R}, \tag{3.1}$$

the left ventricle thus have to work against a pressure five times higher than that of the right ventricle in order to maintain equal flow over the two sides (a prerequisite

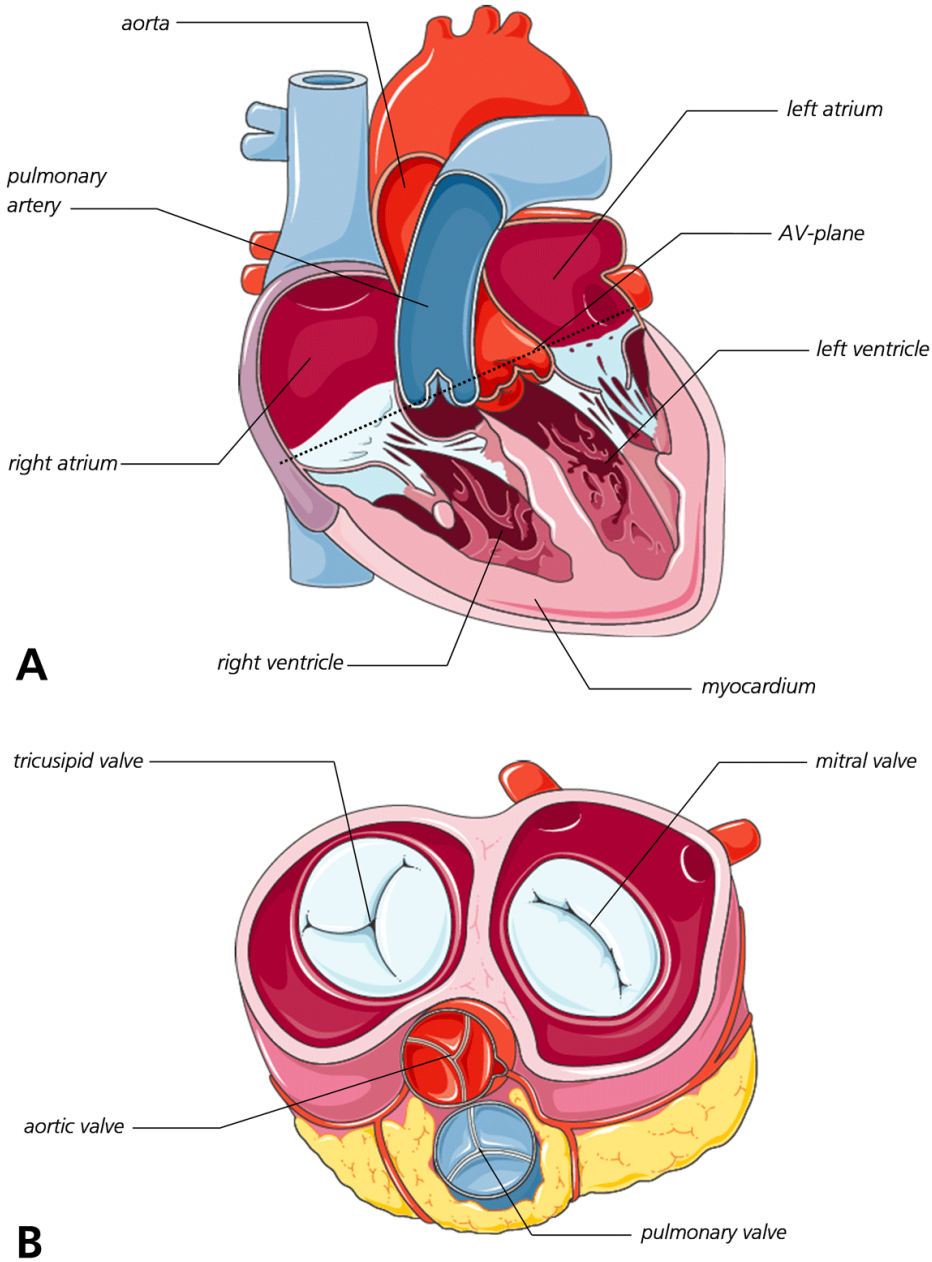

Figure 3.1: Illustration of the anatomy of the heart. (A) Depiction of all four heart chambers, as well as the major connecting arteries and veins. (B) Depiction of the intracardiac valves, visualised as an AV-plane cut through the heart. *Modified with permission from Smart Servier Medical Art.*

for maintained homeostasis). Consequently and following this increased mechanical load on the left side, the left ventricle is significantly thicker than the right one, and also requires more blood from the coronary arteries with two of the three main coronary arteries perfusing the left ventricle [12].

Keeping each heart chamber separated are the four intracardiac valves: the tricuspid valve, the pulmonary valve, the mitral valve, and the aortic valve, all depicted in Figure 3.1(b) cutting through the AV-plane of the heart. As seen, the tricuspid and mitral valve separates right and left atrium and ventricle, respectively, whereas the pulmonary and aortic valve is traversed after ejection from each respective ventricle. In principal, the opening and closing of each valve is a purely passive process, governed exclusively by the pressure differences between each cardiac chamber. Albeit passive, the valves do direct the flow in a unidirectional manner, optimising the efficiency of blood flow through the heart.

In addition to the passive valve cusps, the two atrioventricular valves are also attached to intraventricular papillary muscles, connecting the valves to the intraventricular endocardium, and making sure that the tricuspid and mitral valves stay shut during ventricular ejection. With such, the closed valves prevent blood to flow in a reverse back-flow direction.

Coupling to the basic anatomy of heart, it is important to underline that the heart is developed specifically to optimise the flow of blood, with the heart efficiently working against the physiological pressures of the pulmonary and thoracic aorta. In fact, the wrapping of the right heart around the larger left ventricle, or the half-ellipsoidal shape of the ventricles have been proposed to optimise blood flow, through so called cardiac looping [17] or asymmetric redirection of blood flow [18]. With the valve cusps protruding into the ventricles, shear-layer formation creating vortex-like structures in the ventricles have similarly been suggested to play a fundamental role in the energy-efficient direction of blood through the heart [19]. On the same lines, the varying orientation of muscle fibres in the myocardium (undergoing a 180-degree directional shift from endocardium to epicardium [20]), as well as the principle direction of intraventricular pressure gradients [21-23] have also been proposed to streamline the ejection of blood from the heart. All this highlights the fact that the anatomy of the heart is in direct connection to the hemodynamic flow of blood through it.

b) The cardiac cycle

The cardiac cycle describes the interchanging phases of filling and ejection of the different heart chambers over time. The cardiac cycle can in principle be divided into two main phases: systole and diastole. During systole, the ventricles contract and eject blood through the pulmonary and aortic valves out into the pulmonary and systemic circulation. Conversely, during diastole the ventricles relax and are instead filled with blood coming from the two atria.

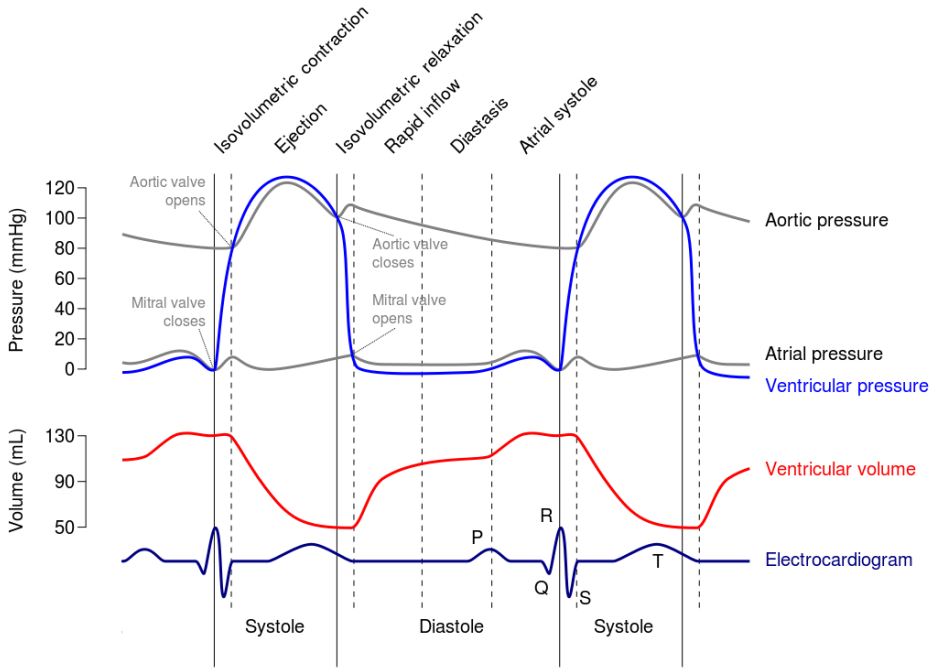

Figure 3.2: Wigger's diagram depicting pressures and left ventricular volume over approximately two cardiac cycles. Additionally, a corresponding ECG-recording with identified P, Q, R, S, and T-segments are marked. *Modified with permission from Wikimedia commons.*

To aid in the understanding of the cardiac cycle, a so called Wigger's diagram is depicted in Figure 3.2. Importantly, the diagram shows how the interchanging phases of contraction and relaxation (or ejection and filling) can be directly related to the intraatrial, intraventricular, and intraaortic pressures.

Even though strictly initiated by a period of atrial contraction, we choose to describe the cardiac cycle from the onset of systole. The systolic phase is initiated at the peak of the R-wave, which triggers ventricular contraction, pulling the atrioventricular plane towards the apex, and consequently generating a rapid increase in intraventricular pressure. As soon as the pressure in the ventricle exceeds that of the atrium, the atrioventricular valve closes. Before the intraventricular pressure reaches that of the ascending aorta, there is therefore a short phase in which all heart valves are closed. This phase is typically described as the isovolumetric contraction (IVC); a phase of increasing intraventricular pressure without any detectable change in intraventricular volume (the phase is however not strictly isometric as studies have shown interchangeable myocardial fibre shortening and lengthening during the IVC-phase [24, 25]).

With increasing contraction, the intraventricular pressure increases and at a certain point exceeds that of the aorta. As soon as this happens, the intraventricular blood will push open the aortic (or, in the right heart, pulmonary) valve, and initiate a

phase of so called rapid ejection. For a short period of time, the intraventricular pressure exceeds that of the aorta, whereas in the later reduced ejection phase, the opposite is true. At the late stages of systolic ejection, the aortic and pulmonary valves however still remain open following the forward-flowing momentum of the ejected blood [26].

With the ventricles now going from contraction to relaxation, the inertia of the ejected blood decreasing, and the intraventricular pressures similarly going down, the aortic and pulmonary valves close shut. Again, a phase of isovolumetric change is initiated, however this time in the form of isovolumetric relaxation (IVR). This represents the end of ventricular systole, and the start of diastole.

As soon as the intraventricular pressure goes below that in the atria, the mitral and tricuspid valves open, allowing blood to flow from the atria into the ventricles. With the intraventricular pressure below the atrial pressure during this early rapid filling phase, the induced pressure gradient causes a distinct suction of blood from atria into the ventricles [27, 28], sometimes depicted as the E-wave of the diastolic phase.

With the pressure gradient causing blood to flow from atria to ventricles, the pressure differences quickly evens out between the respective compartments, and a subsequent slow filling phase called diastasis starts [29].

Once the entire myocardium is relaxed, the onset of a new cardiac cycle is initiated through atrial contraction, during which a small increase in atrial pressure and subsequent ventricular volume can be detected. This late filling during diastole (caused by atrial systole) is sometimes depicted the A-wave of the diastolic phase.

The continuous contraction and relaxation of the myocardium is controlled by an electrical conduction system. Continuous polarisation and depolarisation of myocytes (governed by the continuous change of cell membrane permeability towards ionic substances) creates so called excitation-contraction coupling, where electrical excitation generates muscular contraction. Starting by a depolarising of the sinus node (situated at the top end of the right atrium), a cardiac cycle is initiated by this electrical pulse spreading to the atrioventricular node (inside the top part of the intraventricular septum), with a subsequent splitting of this pulse into both left and right bundle branches (depolarising both right and left ventricles). This sequence of depolarisation and returning repolarisation is typically depicted in an electrocardiogram, shown at the lower end of the Wigger's diagram in Figure 3.2. In short, the cardiac cycle in an electrocardiogram is initiated by the P-wave, representing the depolarisation of the atria starting at the sinus node, initiating atrial contraction. Following this, the QRS-complex completes the spread of ventricular depolarisation, the ST-segment represents the time during which the ventricles are depolarised, and the T-wave represents the final repolarisation of the ventricles; all happening during the systolic phase. With an electrocardiogram (ECG) easily measured non-invasively using the technique of electrocardiography,

analysis of electrocardiogram abnormalities is a very common first-line diagnostic procedure for incoming cardiac patients.

3.1.2. Vascular physiology

a) Vascular anatomy

The vasculature is the overall name of the complex network of arteries and veins, originating from the heart and distributing blood to capillary beds throughout the body. In general, the vasculature can be classified into an arterial and a venous side, with arteries transporting oxygenated blood away from the left ventricle and veins transporting deoxygenated blood back to the right atrium. Note that a slight exception to this classification is present in the pulmonary circulation where the pulmonary arteries transport deoxygenated blood away from the right ventricle (to be re-oxygenised in the pulmonary capillaries), and the pulmonary veins transport this re-oxygenised blood back to the left atrium.

On both the arterial and venous side the vasculature consists of a branched vessel systems, depicted in Figure 3.3. On the arterial side, all blood ejected from the left ventricle enters the ascending aorta, which then branches off into smaller arteries transporting blood throughout the body: the carotid arteries directing blood to the cerebral vasculature, the subclavian arteries carrying blood to both arms, the abdominal aorta directing blood caudally, itself branching off into renal arteries, femoral iliac arteries, etc. Importantly, at the very beginning of the ascending aorta and right behind the aortic valve cusps, two small coronary arteries (the left and right coronary artery) also branch off to perfuse the myocardium itself.

Once transported through the main arteries, the vasculature bifurcates further into smaller arterioles and finally capillaries, where the main exchange of nutrients and waste products are performed between the transported blood and the apparent cell tissue.

After exiting the capillaries, the blood now enters the venous side of the vasculature, which to some extent can be seen as the mirrored, collecting system, to the branching and distributing arterial side. On the venous side, the capillaries fuse into venules, which then collect further and form larger veins. As a final stage on the venous side, the large inferior and superior vena cava collects all returning deoxygenised blood, directing it back into the right atrium where yet another cardiac cycle can be initiated.

The fundamental layer structures of vascular tissue will be described in-detail in the upcoming section, but it is worth mentioning that the structural properties of the vasculature are optimised for an efficient transportation of blood. The role of the arteries is to transport and transfer the transiently pumped blood from the heart, into a continuously flowing stream of blood in the more peripheral capillaries.

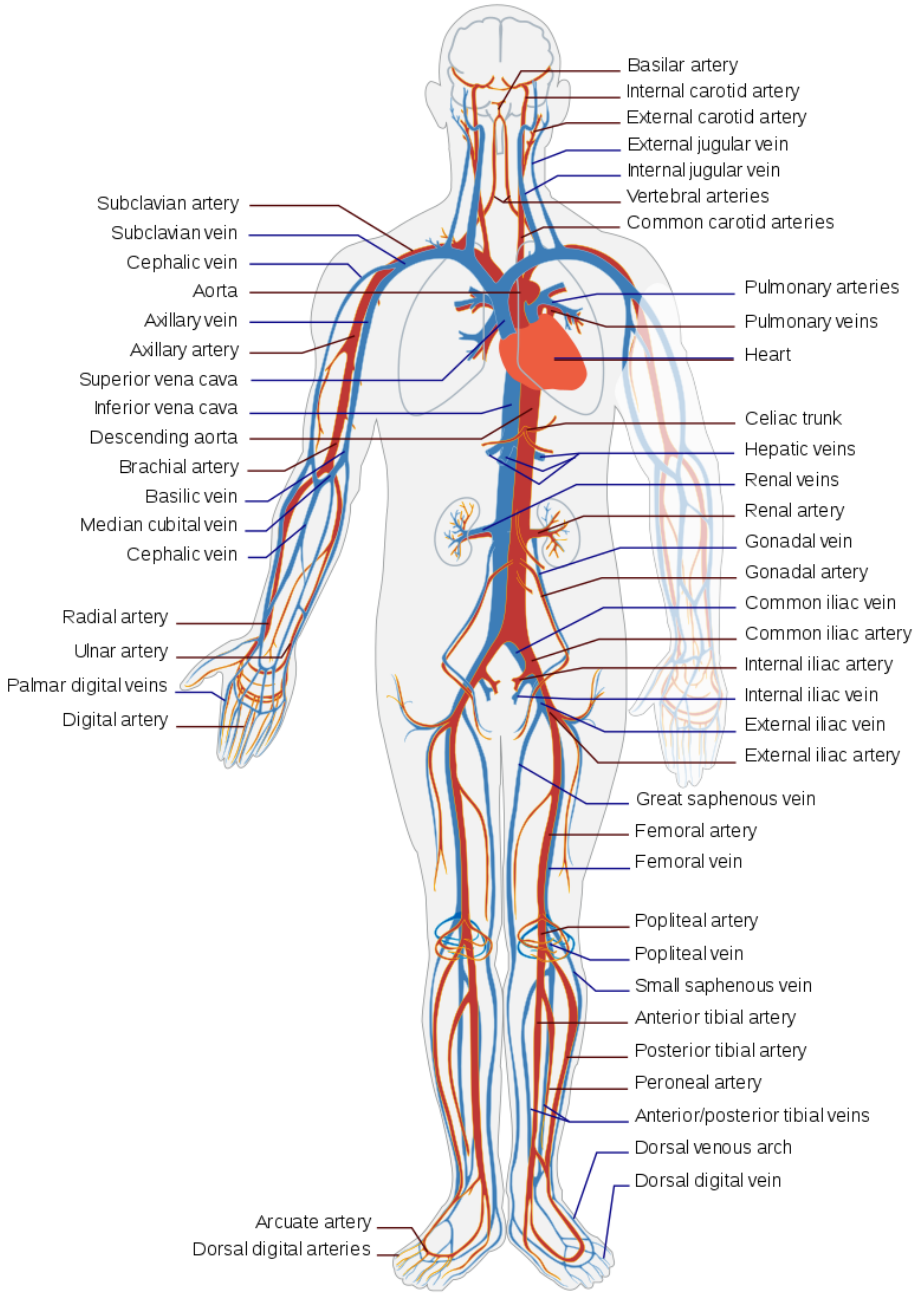

Figure 3.3: Illustration of the anatomy of the vasculature, including both the arterial (red) and venous (blue) side. *Modified with permission from Wikimedia commons.*

Specifically, this is achieved by the mainly elastic and distensible properties of the arteries, where part of the initial systolic pulse is stored as potential energy in the distended arteries. During diastole, the elastic recoil of the arteries revert this potential energy into kinetic energy, maintaining a forward-flowing blood stream, making sure that there is a continuous supply of blood flow in the peripheral capillaries.

Note that in addition to the elastic component described above, arteries do show a defined viscous constitutive component as well [30], albeit not as pronounced as its elastic counterpart [31, 32].

b) Vascular tissue structure

In principle, all vascular tissue in the body has the same structural layout. In short, three distinctive layers can be identified: the intima (tunica intima), the media (tunica media), and the adventitia (tunica adventitia or tunica externa), depicted in Figure 3.4.

The intima represents the lumen-facing innermost layer of the vessel, with its primary function related to cellular signalling and transport between blood stream and internal tissue [33]. The intima consists of a thin layer of endothelial cells, shown to have a significant influence on the initiation and development of vascular disease following its regulation of vascular tone and inflammatory response mechanisms [34]. However, the intima does not markedly influence the structural integrity of the vessel wall due to its limited thickness and lack of structural components [35].

The media is the middle layer of the vessel wall. In contrast to the intima, the media has a defined structural component, with the layer made up of a complex network of smooth muscle cells (SMCs), elastin and collagen fibres. In fact, sub-medial layers (so called medial lamellar units (MLU) [36]) have been identified, with the orientation of collagen fibres in each MLU directly affecting the distribution of mechanical stress in the vascular wall [37, 38]. By such, the medial layer is identified as the mechanically most significant layer of the vessel wall [35], at least during the strain levels typically faced under normal physiological conditions.

The outermost layer of the vessel wall is the adventitia, mainly made up of bundles of collagen fibres in larger so called fibrils (themselves intertwined in a helical arrangement [39]). With its high collagen content, the adventitia acts as an outer protective mechanical layer, attaching the vessel to surrounding tissue and giving mechanical support at high intraluminal load, preventing vascular overstretch [35].

As mentioned, these three layers are in principle present throughout the vasculature, however differing in distribution and size throughout the body. Specifically, the cellular content and structural components within each layer of the

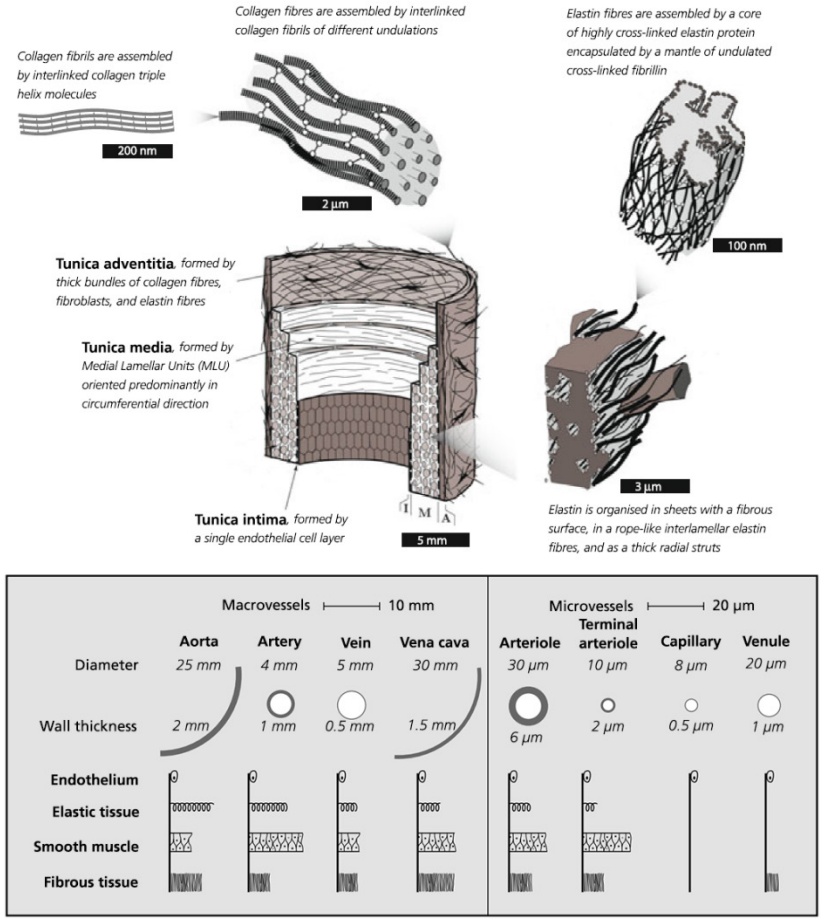

Figure 3.4: The structure of the vascular wall, showing its three main layers: tunica intima, tunica media, and tunica adventitia. Also, a diagram of tissue composition throughout the vasculature is given, illustrating differences in tissue structure. *Modified and reproduced with permission* [39, 40].

vessel wall vary distinctly based on the functional property of the given vasculature. As shown in Figure 3.4, the larger arteries and veins all have a relatively high degree of elastic tissue, together with reinforcing fibrous tissue and SMC content [40] in order to maintain the important distensible properties of the tissue, whilst still giving support for the forward-flowing blood. Notice also how the arterial side has a distinctly thicker vascular wall compared to the venous side, following the higher absolute blood pressures on the arterial side.

Conversely, in the more peripheral arterioles, capillaries, and venules, the elastic content of the vascular wall is significantly smaller, with the capillaries consisting almost exclusively of the thin intima endothelial layer [41]. This is all possible following the slow and continuous flow of blood in these peripheral parts of the vasculature.

3.1.3. Arterial-cardiac interaction

As described, the heart and the vasculature interact in a closed loop system, working in parallel to provide adequate blood flow throughout the pulmonary and systemic circulation. By so, cardiac alterations will result in vascular reactions, and vice versa – a concept often referred to as arterial-cardiac interaction or ventricular-vascular coupling [42, 43].

Two important concepts worth mentioning with regards to arterial-cardiac interaction are the pressure-volume diagram, and remodelling following vascular stiffening.

The pressure-volume diagram is a commonly deployed metric used to describe the relation between ventricular volume and pressure throughout the cardiac cycle, as depicted schematically in Figure 3.5. In principle, the pressure-volume loop connects the constitutive relation between pressure and volume at ventricular relaxation (the end-diastolic pressure-volume relation (EDPVR)) and the constitutive relation between pressure and volume at full ventricular contraction (the end-systolic pressure-volume relation (ESPVR)).

During diastole, the ventricles are filled and increase in volume from the end systolic volume (ESV) to the end diastolic volume (EDV), with the pressure-volume relation converging towards the EDPVR. At the point of EDV, the mitral valve closes, and the IVC is represented by the build-up in pressure without change in ventricular volume, as seen by the vertical rise in the pressure-volume diagram at EDV. Once the aortic valve opens, the curve loops back all the way to the ESPVR, reached just as the aortic valve closes. The cardiac cycle is then finalised and the pressure-volume diagram is closed once the IVR is completed.

Importantly, this type of diagram depicts the relation between cardiac pressure and volume, and how increasing ventricular volumes will be resisted by an increasing work-load or counter-acting pressure. The diagrams can also help in the intuitive understanding of how myocardial constitutive behaviour affects cardiac efficiency, where myocardial stiffening (increasing slopes of EDPVR and ESPVR) will result in increased filling resistance. Similarly, the pressure-volume diagrams entail information on arterial influence, where the so called effective arterial elastance (Ea, connecting ESPVR and EDVR in Figure 3.5) will shift the pressure-volume relation as a function of peripheral resistance, preload, afterload, and heartrate, to name only a few [44-46].

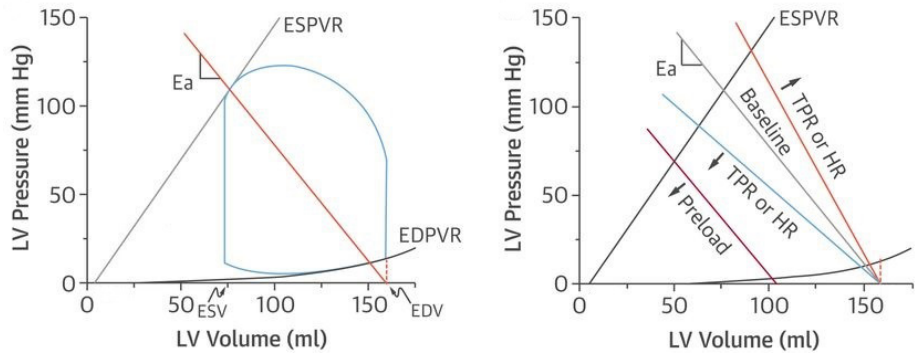

Figure 3.5: Example of a normal pressure-volume loop (left), showing the relation between left ventricular pressure and volume which connects the end-systolic pressure volume relation (ESPVR) with the end-diastolic volume relation (EDPVR). Note the rapid changes in volume at the end systolic volume (ESV) and end diastolic volume (EDV), respectively, as well as the effective arterial elastance (Ea). The slope of Ea will also be related to several factors (right) such as total peripheral resistance (TPR), heart rate (HR), or preload. *Modified and reproduced with permission* [47].

3.1.4. Cardiovascular hemodynamics

As described in the previous few sections, the central role of the cardiovascular system is to transport blood throughout the entire body, maintaining systemic homeostasis. For this reason, disruptions in the natural flow of blood are often directly related to the onset of cardiovascular disease [48-51]. Similarly, it is by the unifying flow of blood that the heart and vasculature can interact and adapt to different physiological states [52, 53]. For this reason, a short review of the basics of cardiovascular hemodynamics is essential when reviewing cardiovascular function, and is here provided as a final and unifying component of cardiovascular physiology.

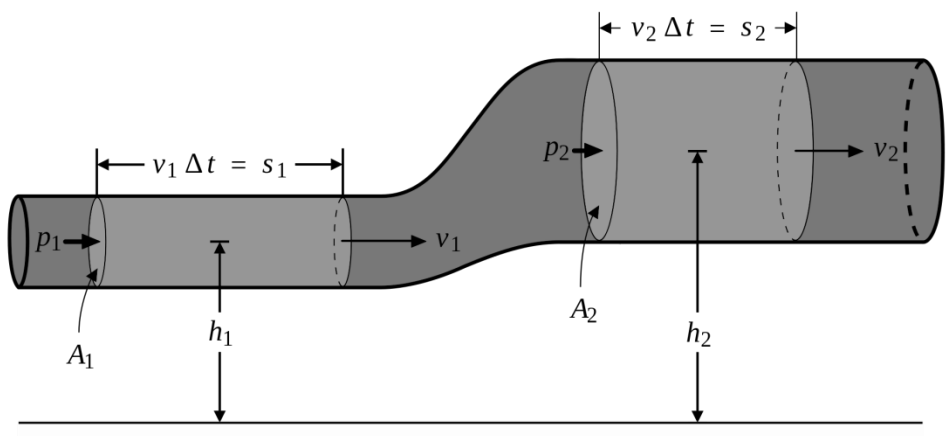

Figure 3.6: Schematic single pipe flow, used to describe Bernoulli's principle. *Modified with permission from Wikimedia commons.*

a) Governing physical principles

From a fluid mechanical perspective, blood can be described in identical fashion to that of any given viscous fluid. By so, blood also follows the fundamental laws of fluid mechanics, described briefly in this section. Importantly, these theoretical descriptions provide a direct coupling between blood flow and blood pressure, and describe how these two interact at any given spatial or temporal point.

Even though strictly governed by the complete Navier-Stokes equations (explained in subsequent paragraphs), it is worth starting from a simpler description of flow. The Bernoulli equation is such a simplified formulation, stating that for an inviscid non-conductive fluid the sum of kinetic and gravitational potential energy is constant [54, 55]. If assessing a system such as the one depicted in Figure 3.6, this states that

$$\frac{1}{2}v_1^2 + \frac{p_1}{\rho} + gh_1 = \frac{1}{2}v_2^2 + \frac{p_2}{\rho} + gh_2, \tag{3.2}$$

with v the velocity, p the pressure, ρ the density, g the gravitational acceleration, and h the height above a given reference plane. Index 1 and 2 refers to arbitrary positions along the vessel as shown in Figure 3.6. Assuming negligible gravitational effects (as commonly done in clinical practice [56, 57]), and re-ordering Equation 3.2, we reach a direct relation between velocity and pressure where

$$p_2 - p_1 = \frac{1}{2}\rho(v_1^2 - v_2^2). \tag{3.3}$$

In other words, a decrease in velocity will be reflected by an increase in pressure. Or: at any vascular narrowing where the cross-sectional decrease will lead to an increase in velocity (due to the conservation of mass), we will experience a decrease in pressure. Such changes in relative pressure is therefore a typical metric for assessing vascular coarctation narrowing [58, 59], valve stenosis [60, 61], etc.

The Bernoulli equation is however only strictly valid for an inviscid non-conductive fluid. Additionally, the Bernoulli equation originates from a steady-state system, meaning that any transient inertial effects will not be taken into account. In the greater vessels of the vasculature, where we have a continuous pulsatile flow of blood, this is clearly not the case.

Expanding into an inviscid, non-conductive case however allowing for transient changes, Euler's momentum equation states that

$$\frac{\partial \boldsymbol{v}}{\partial t} + \boldsymbol{v} \cdot \nabla \boldsymbol{v} = -\frac{1}{\rho}\nabla p + \boldsymbol{g}, \tag{3.4}$$

with $\boldsymbol{v}$ denoting the 3D velocity vector. Reformulating Equation 3.4 into a 1D problem and re-organising terms, we get an expression for the infinitesimal pressure difference as

$$\frac{\partial p}{\partial s} = -\rho \left(\frac{\partial v}{\partial t} + v \frac{\partial v}{\partial s} + g \frac{\partial h}{\partial s} \right). \tag{3.5}$$

Again h depicts the height above the reference plane in Figure 3.6, whereas s and ds is a streamline and infinitesimal streamline step from 1 to 2, respectively. Integrating along s and neglecting again all gravitational effects, we end up with the so called Unsteady Bernoulli equation [62], for which

$$p_2 - p_1 = \rho \left[\frac{1}{2}(v_1^2 - v_2^2) - \int_s \frac{\partial v}{\partial t} ds \right]. \tag{3.6}$$

As seen, Equation 3.6 is very similar to Equation 3.3, however now including the transient kinetic component of the velocity along s.

For a complete description of 3D blood flow we however resort to the Navier-Stokes equations, describing the conservation of mass and momentum for any incompressible fluid. Specifically, the Navier-Stokes equations state that for an isothermal, incompressible, Newtonian, viscous fluid the following holds

$$\rho \frac{\partial \boldsymbol{v}}{\partial t} + \rho \boldsymbol{v} \cdot \nabla \boldsymbol{v} - \mu \nabla^2 \boldsymbol{v} + \nabla p = 0 \tag{3.7}$$

$$\nabla \cdot \boldsymbol{v} = 0, \tag{3.8}$$

with μ depicting the dynamic viscosity of the fluid. Importantly, the different terms in Equation 3.7 represents different fluid mechanical components of the flow. Specifically, the first and second term represent the kinetic and advective (or convective) inertia terms, describing the temporal and spatial flow resistance. The third term involves the viscous resistance, originating from the viscosity of the fluid, and lastly, the fourth term involves the spatial gradient of the pressure field. In addition to this, Equation 3.8 states the conservation of mass or divergence-free requirement, valid for any incompressible fluid.

Again, the fluid mechanical description gives us a direct connection between pressure and velocity, this time at any given 3D spatiotemporal point. However, non-linear terms and second order derivatives complicates accurate computation, and these full-form description are therefore rarely used in clinical practice [60, 61]. However, their incorporation may improve the accuracy of prediction [63-65], which will be a main topic of discussion in this thesis.

b) Turbulence

In the healthy human cardiovascular system, blood flows in a relatively stable way and transition into so called turbulent flow regimes are seldom encountered [66]. However following pathological disturbances, increasing vascular constriction and flow complexity may result in the development of these turbulent flow regimes [67-69].

Just as for laminar flows, the kinetic and advective inertia, viscous resistance, and pressure distribution can be described by the Navier-Stokes equations. However, for turbulent flows, stochastic and chaotic flow fluctuations will disturb the analytical assessment of the given flow field, introducing turbulence-driven variations in the evaluated terms.

A fully analytical description of turbulence is still not reached, in part because of the stochastic nature of turbulence [70, 71]. In laminar blood flow, the movement of blood is roughly assumed to repeat itself over consecutive cardiac cycles. On the contrary, even though turbulent regimes can be identified in given vascular structures, the specific flow behaviour at a given spatial positon will not be analytically repetitive. Instead, we will experience chaotic, stochastic fluctuations within these turbulent regimes. For that reason, we may treat turbulence in a statistical rather than analytical way.

Instead of assessing blood flow at a specific time point, we instead choose to observe the velocity field $\boldsymbol{v}$ over n number of cardiac cycles with period T. By so we can define a linear expected value operator E (commonly used in probability theory [72]) collecting data over all cycles such that

$$E[v(t)] = \frac{1}{n}\sum_{k=1}^{n} v(t + kT). \tag{3.9}$$

Applying E to our Navier-Stokes equations in 3.7-3.8, we get

$$\rho\frac{\partial E[\boldsymbol{v}]}{\partial t} + \rho\nabla \cdot E[\boldsymbol{vv}] - \mu\nabla^2 E[\boldsymbol{v}] + \ \nabla E[p] = 0 \tag{3.10}$$

$$\nabla \cdot E[\boldsymbol{v}] = 0. \tag{3.11}$$

Further, by setting $\boldsymbol{V} = E[\boldsymbol{v}]$ and $P = E[p]$ to be the mean of our observed velocity and pressure field, we can expand Equations 3.10 and 3.11 into

$$\rho\frac{\partial \boldsymbol{V}}{\partial t} + \rho\nabla \cdot E[\boldsymbol{vv}] - \mu\nabla^2 \boldsymbol{V} + \ \nabla P = 0 \tag{3.12}$$

$$\nabla \cdot \boldsymbol{V} = 0. \tag{3.13}$$

Lastly, it can be shown that $E[\boldsymbol{vv}] = E[\boldsymbol{v}]E[\boldsymbol{v}] + \mathrm{Cov}[\boldsymbol{v},\boldsymbol{v}] = \boldsymbol{VV} + \mathrm{Cov}[\boldsymbol{v},\boldsymbol{v}]$. Here, $\mathrm{Cov}[\boldsymbol{v},\boldsymbol{v}]$ is the so called covariance matrix, describing the product of deviations in velocity from their expected mean value $\boldsymbol{V}$. Using this in Equations 3.12-3.13 renders a final modification to the Navier-Stokes equations

$$\rho\frac{\partial \boldsymbol{V}}{\partial t} + \rho\nabla\cdot(\boldsymbol{VV}) + \rho\nabla\cdot\mathrm{Cov}[\boldsymbol{v},\boldsymbol{v}] - \mu\nabla^2\boldsymbol{V} + \nabla P = 0 \tag{3.14}$$

$$\nabla\cdot\boldsymbol{V} = 0, \tag{3.15}$$

where specifically the term $\rho\nabla\cdot\mathrm{Cov}[\boldsymbol{v},\boldsymbol{v}]$ numerically handles flow deviations, typically arising from turbulent flows.

In summary, turbulence-driven stochastic flow fluctuations can thus be incorporated numerically into the analytical Navier-Stokes equations. From a practical point of view, this would be achieved by not only assessing the mean velocity and pressure field, but by including measures of covariance or deviation within an assessed flow field. As an example of how such incoherent velocity fluctuations might appear, Figure 3.7 depicts the flow in a stenotic flow phantom, where typical stochastic variations can be seen in velocity, together with an increase in flow deviations post-stenosis [73].

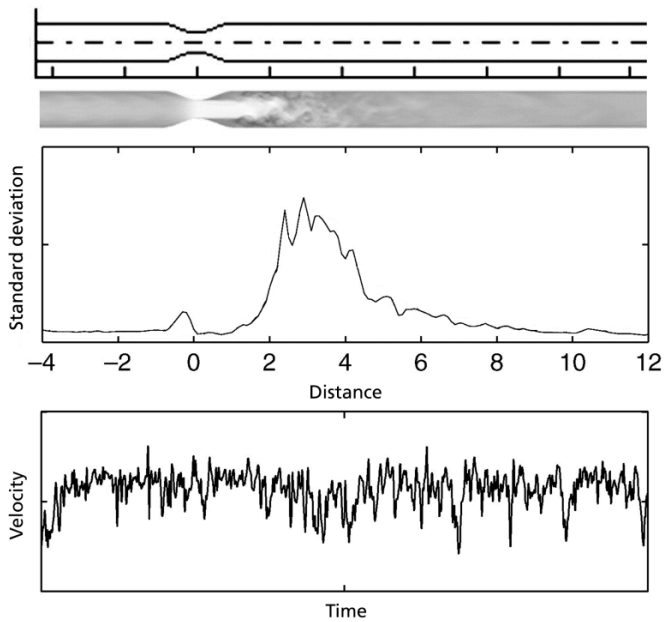

Figure 3.7: Illustration of incoherent flow fluctuations after a stenosis, presented for data from a stenotic flow phantoms: (top) phantom geometry and velocity field, with flow going from left to right, (middle) velocity standard deviations along the pipe length, and (bottom) velocity fluctuations over time post-stenosis. *Modified and reproduced with permission* [73].

c) Blood flow

Blood flow is a term typically used to refer to the motion of blood, or rather the velocity of blood in the cardiovascular system (a measure of distance travelled per unit time). With blood being continuously ejected from the heart, and with the anatomy of the vasculature changing throughout the body, blood flow will vary distinctly throughout the cardiovascular system. Inside the heart, peak velocities are typically encountered when blood is passed from atrium to ventricle during the early diastolic filling, with healthy peak intracardiac velocities of around 1.5 m/s [74]. The intracardiac movement of blood is itself a very complex process, where rotational spinning [18], vortex formation [75], and optimised redirection of blood towards ejection [76], seem to be common ventricular features.

Once ejected from the heart, slightly higher velocities can be seen across the pulmonary and aortic valves, however these quickly decrease as the blood travels towards more peripheral vessels. In fact, in the microcirculation significantly lower velocities of only a few mm/s are observed [77], before velocities are increased in the venous return.

The assessment of blood flow has become an instrumental part of routine clinical care. Blood flow over the intracardiac valves are part of echocardiography standard practice [6, 8] to evaluate valvular stenosis [61] or regurgitation [78], where guidelines are directly referring to velocity values in classifying disease stage [6, 61, 78]. Additionally, the development of full-field techniques such as 4D flow MRI, has opened up for expanded flow-based cardiovascular analysis, evaluating the 4D distribution of flow [10, 76, 79], vortices [19, 75], kinetic energy [80] and turbulence [81, 82], to mention only a few.

To quantify blood flow and describe cardiac function, a few standard metrics are commonly deployed. A few of these are:

i. *End Diastolic Volume (EDV)*: Total amount of ventricular blood at the end of diastole. Typically around 140 mL in the healthy left ventricle [83].
ii. *End Systolic Volume (ESV)*: Total amount of ventricular blood at the end of systole. Typically around 50 mL in the healthy left ventricle [83].
iii. *Ejection Fraction (EF)*: The ratio of ESV/EDV, representing the fraction of blood being ejected from the ventricle. Typically around 55-70% [83].
iv. *Stroke Volume (SV)*: The volume of blood being ejected in one heartbeat (EDV – ESV). Typically around 95 mL [83].
v. *Cardiac Output (CO)*: The volume of blood being ejected per unit time, generally given by SV times the patient heartrate. Typically around 4 L/min at rest [84].

All terms above by default refer to the left ventricle, but right ventricular values (given by an 'RV' prefix) can also be identically reported.

d) Blood pressure

Pressure is defined as force per unit area. For the cardiovascular system, this can be translated into that blood pressure is the pressure exerted by the blood onto the vascular wall.

A typical blood pressure curve recorded at two different points in the thoracic aorta is provided in Figure 3.8, showing the peak in systolic pressure, followed by a dropped diastolic pressure. The dicrotic notch typically appears following the closure of the aortic valve, hence representing the end of systole.

However, as described briefly in previous sections, blood pressure changes throughout the cardiovascular system partially follow the functional roles of the different parts of the vasculature. At the aortic outlet when the blood is ejected from the left ventricle, typical blood pressures values of 120/80 mmHg (systolic/diastolic) are reported [85]. However, following pathological changes, hypertensive or hypotensive states can significantly alter the range of both systolic and diastolic blood pressures seen in patients [86, 87].

With the ejected blood, a blood pressure pulse starts travelling through the cardiovascular system, changing its appearance and absolute values as showcased in Figure 3.8. The pressure wave gets distorted as it travels through the vasculature, and specifically, the systolic pressure peak increases and narrows in extension as we travel away from the heart. There are multiple reason to this change, but it originates in part from the narrowing of the arterioles, the changing velocity of the travelling pulse wave, the bifurcations and tortuous geometry of the vasculature, as well as from biomechanical properties of the vessel wall [40, 66, 88].

The increase in pressure pulse diminishes as the blood travels into the arterioles, where a distinct increase in vascular cross-section dampens both velocity and pressure. Again this is to enable nutrient exchange in the microcirculation [77].

As the pressure pulse changes throughout the vasculature, the assessment of relative pressure or pressure difference is common in clinical practice, reflecting this change in the travelling pressure pulse. Quite simply, the relative pressure denotes the difference in pressure between two given points. Figure 3.8 shows the absolute pressure recorded at the ascending and descending aorta, together with a subtraction of the two rendering the relative pressure between ascending and descending aorta.

With the pressure pulse varying with arterial properties, and similarly with pressure magnitude changing with changing cross-section (as described theoretically at the beginning of Section 3.1.4.), assessment of relative pressure can act as a valuable tool in assessing cardiovascular function. The metric is used as a recommended guideline metric for valvular stenosis and aortic coarctation [59, 61, 78], and have similarly shown value in assessing intracardiac pressure drops in patients with

hypertrophic cardiomyopathy [89, 90]. Similarly, the assessment of novel metrics such as so called hemodynamic forces [22, 91] have been related to evaluated pressure gradients, underlining the use of relative pressure.

A last note is that, confusingly, relative pressure nomenclature differs in literature, and different terms have interchangeably been used clinically. Typically we use the term pressure drop to denote the difference in pressure between two given positions. This is identical to the relative pressure. The pressure gradient is however the pressure drop over length between the same two positions.

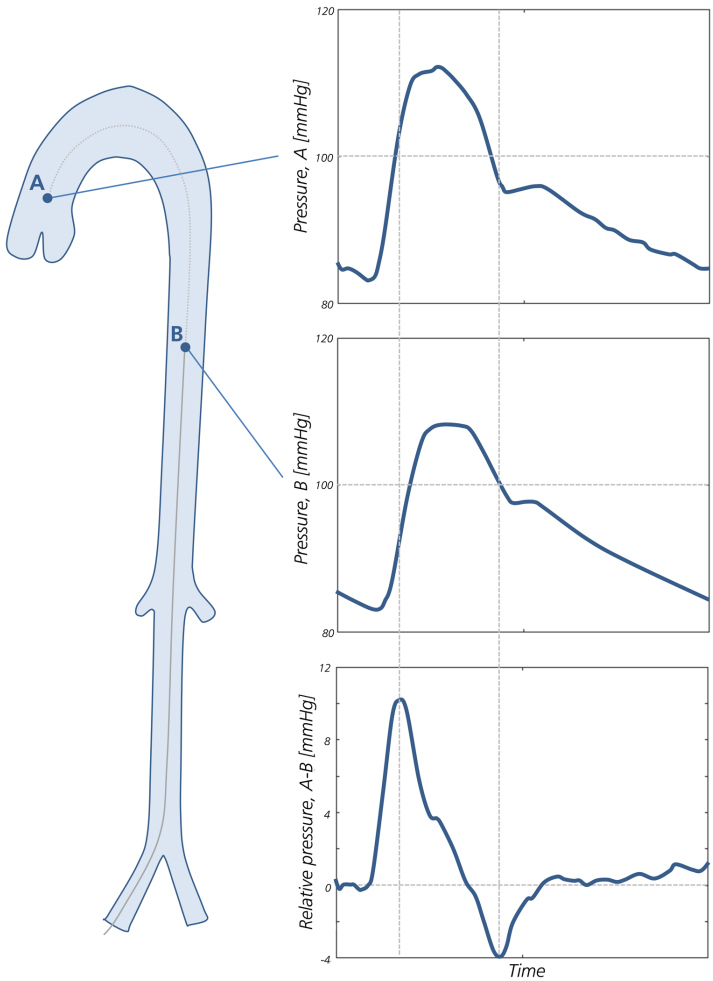

Figure 3.8: Example of catheterised pressure measurements in the ascending (A) and descending (B) aorta, showing absolute pressure traces, as well as a derived relative pressure (A-B).

e) Hemodynamic cardiovascular interaction

Summing up the basics of cardiovascular hemodynamics, it is important to remember that blood flow and blood pressure do not reside as separate entities. Instead, the two are tightly connected to one another, with velocity changes causing direct pressure response, and vice versa. However, as the relation between the two is non-linear, the derivation of one from the other is not a simple task, and external factors such as vessel geometry and time scale will influence both flow and pressure.

That flow and pressure interact in the cardiovascular system is however clear. The velocity increase over stenotic regions is directly connected to the pressure drop over the same stenosis [61]. Valvular regurgitation (backflow) will conversely affect the pressure build-up in the preceding heart chamber [78]. Along the same lines, hypertensive aortic pressures will increase cardiac afterload, requiring higher intraventricular systolic pressures and consequently a more forceful intraventricular flow [92]. If not, a decrease in EF will be present, initiating a complex chain of cardiac remodelling mechanisms, further altering hemodynamic behaviour [52]. To this, the hemodynamic interaction between flow and pressure will have a joint impact on the constitutive remodelling of vascular tissue, where e.g. vascular stiffening will have a direct influence on the travelling pressure wave. Further details on specific cardiovascular disease and its hemodynamic alteration are provided in Section 3.2.

3.2. Cardiovascular disease

Cardiovascular disease (CVD) is the leading cause of death in the world today, responsible for approximately 31% of all deaths worldwide [5], being a major health concern in all regions of the world [93]. Within the umbrella term of CVD, a majority of all deaths are accounted for by either ischemic heart disease (mainly myocardial infarction due to blockage of coronary arteries, ~38-46% of all CVD) or cerebrovascular disease (mainly cerebrovascular stroke, ~34-37% of all CVD) [5].

Following its immense societal impact, extensive research and development efforts have been invested in understanding the development, manifestation, diagnosis, and prevention of CVD. This includes the development of novel and refined pharmaceuticals, genetic identification of CVD-related risk alleles [94], refinement of non-invasive image-based diagnostic tools, as well as the identification of primary and secondary prevention techniques, where life-style related factors such as smoking, obesity, and diet all have shown to have a direct influence on CVD-development [95-97].

In the following, a condensed summary of the most common CVD types is presented. In particular, emphasis will be given on the development of atherosclerotic plaque (a key component in both myocardial and cerebrovascular

disease) as well as the relation between disrupted hemodynamics and CVD development in a few selected disease types. The following review is divided into a cardiac and a vascular subsection.

3.2.1. Cardiac disease

Cardiac disease or heart disease are disease types affecting the myocardium or other intracardiac structures. By so, heart disease is directly related to a disrupted ability to pump blood out into the vasculature, manifested either through systolic or diastolic dysfunction. Below follows a short review of some of the most common cardiac diseases, including definitions, primary diagnostics, as well as details on disease-specific hemodynamic alterations.

a) Ischemic heart disease

Ischemic heart disease is characterised by a restricted or impaired blood supply of the myocardium, caused by a complete or partial blockage of one or several sections of the coronary arteries (also referred to as coronary artery disease). This is itself typically caused by the build-up of intraluminal atherosclerotic plaque, where a complete coronary blockage from plaque rupture, plaque erosion, or complete plaque build-up lead to acute myocardial ischemia (for a detailed review on the process of atherosclerotic plaque development, see Section 3.2.2.).

Depending on the degree of coronary blockage, the ischemic event can be either transient or persistent, where in the latter case risk for permanent myocardial damage is imminent. If such myocardial necrosis occurs, the disease is referred to as a myocardial infarction [98] (or heart attack), where a regional section of the myocardium is permanently impaired.

Regarding diagnosis, ischemic heart disease is initially assessed through the manifestation of stable or unstable angina. With such, ECG monitoring is the recommended method of establishing the presence of myocardial infarction [99], where regional complete myocardial damage (i.e. including both subendocardial and subepicardial damage) is characterised by a typical ST-elevation. When more subtle myocardial damage is observed, there might be cases where no ST-elevation is observed, and instead further referring to coronary angiography or angiogram might be performed [100]. In both cases however, assessed coronary blockage might be treated by re-opening of the damaged vessel through so called coronary stenting, performed through a percutaneous coronary intervention (PCI).

With ischemic heart disease directly affecting the myocardium, it also has a direct impact on the pumping mechanisms and hemodynamic abilities of the heart. Specifically, a blockage in coronary flow will increase coronary resistance, and consequently require increased cardiac work-load following a potentially slightly increased afterload (which itself may lead to further remodelling through cardiac hypertrophy, hypertension, etc.) [101]. Additionally, an infarcted myocardial area

will similarly affect intracardiac hemodynamics. Image-based studies have shown that patients with myocardial infarction have altered intraventricular diastolic vortex formation [102] as well as valvular net flow [103], and that some of these flow metric might even differentiate patient groups from one another [104]. Similarly, alterations in the main direction of the intraventricular pressure gradient (referred to as the hemodynamic force) has shown to correlate to left ventricular dyssynchrony [22], potentially resulting from regional myocardial damage. Along the same lines, it has been shown how patients with an ST-elevated myocardial infarction manifest elevated right- and left-sided filling pressures [105], working as a compensatory mechanism to maintain cardiac output in patients with this impaired pumping mechanism.

Apart from the intracardiac hemodynamic changes described above, coronary stenosis or coronary blockage will also directly impair the hemodynamics inside the coronary arteries. As previously described, the narrowing of a stenotic coronary vessel will be characterised by a drop in intracoronary pressure where such can be clinically assessed by either indirect stenosis degree assessment [106, 107], or direct invasive pressure evaluation during PCI [108]. Note however that with the restricted dimensions of the coronaries, the observed pressure drops and related coronary blood velocities are typically fairly low, and related down-stream turbulence is consequently low or even negligible in such low-flow regimes.

b) Cardiomyopathies

Cardiomyopathies refer to diseases directly affecting the myocardium. Cardiomyopathies cover a heterogeneous group of diseases, with mixed definitions occurring in literature [109, 110]. Traditionally, a sub-classification into dilated, hypertrophic, and restrictive cardiomyopathies is however performed, and will for simplicity be used below.

i) Dilated cardiomyopathy

Dilated cardiomyopathy (DCM) is a cardiac disease characterised by dilation and impaired contraction of one or two of the ventricles, typically occurring in the absence of abnormal loading conditions (from e.g. valvular disease or hypertension) [109]. The degree of dilation varies, but in severe cases a doubling of the ventricular dimension has been clinically reported [111] (importantly however is that the degree of dilation is not a univocal predictor for patient outcome [112]). The underlying cause for the dilation is not clearly defined, but is rather a multifactorial combination of genetic, infectious, inflammatory, and metabolic factors [113].

In DCM, the dilation develops gradually, and with the increasing ventricular size DCM patients typically observe increasing systolic dysfunction (following from increasing ventricular volumes and decreasing EF), which at an advanced stage may induce heart failure [114].

Regarding diagnosis, DCM is manifested through fatigue and shortness of breath, and can non-invasively be assessed through standard echocardiography, where specifically longitudinal monitoring can uncover the degree of increasing dilation. For more refined measurements of ventricular geometry, cardiovascular MRI can be performed [115], as can endocardial biopsy reveal specific etiological factors [116]. With the dilation generally seen as an irreversible process, treatment is typically introduced to suppress underlying disease factors (through e.g. anti-inflammatory agents) or to reduce the loading of the heart by implantable assist devices [117].

The myocardial changes associated with DCM will directly affect cardiac function and cardiovascular hemodynamics. The increase in ventricular size alone will increase both EDV and ESV, and consequently intraventricular pressures will decrease unless the heart increases the exercised load. This decrease in intraventricular pressure typically decreases the heart's ability to eject blood into the vasculature [118]. To further compensate for this, an even more pronounced dilation may develop, progressing the patient into a more severe DCM state.

Apart from the intraventricular pressures, DCM ventricular dilation will also reduce intraventricular blood flow velocities, as well as increase the residence time and amount of blood residing inside the ventricles over several cardiac cycles [119]. With such, the dilation constitutes to an increasing risk for intraventricular thrombi formation and subsequent systemic embolisation [120].

ii) Hypertrophic cardiomyopathy

Hypertrophic cardiomyopathy (HCM) is a disease where a section of the heart (generally including the intraventricular septum) becomes abnormally enlarged. The thickening of the myocardium will cause a protrusion into the intraventricular cavity, and often decrease ventricular stroke volume unless a simultaneous dilation is induced (a combination of HCM and DCM is in fact not uncommon [109]). HCM is typically regarded as an inherited cardiomyopathy [109], even though myocardial thickening may also be induced by chronically increased pre- or afterload [121].

For diagnosis, HCM is as other cardiomyopathies typically assessed by non-invasive imaging; first-line through echocardiography but more advanced stages can be evaluated using cardiovascular MRI [90]. With its defined heredity, genetic testing is also part of recommended guidelines [122] even though such techniques are not routinely available in daily clinical practice. For treatment, common cardiac pharmacological agents (beta blockers, calcium channel blockers, etc.) are typically used, whereas any other invasive procedure such as surgical removal of part of the protruding myocardium is only done in more advanced or non-compliant cases [90, 122].

Hemodynamically, HCM is dominantly manifested through diastolic dysfunction [123]. In particular, HCM is associated with increased diastolic filling pressure following the reduced intraventricular cavity, as well as a reduced diastolic relaxation due to the decrease in ventricular compliance and the remaining systolic contraction load from the obstructed ventricular outflow tract [124]. Generally, HCM typically increases intraventricular pressures and the obstructing myocardial mass has even shown to induce the development of distinct systolic intraventricular pressure gradients [90]. In severe cases of HCM, the intraventricular septal thickening will even cause an obstruction of the left ventricular outflow tract, representing a major problem for the ejection of blood into the vasculature [125]. In such cases, changes in intraventricular and valvular pressure drops are observed, and the outflow tract obstruction is in guidelines even defined by the magnitude of this induced pressure drop [122]. Along the same lines, the stenotic narrowing of the outflow tract has been associated with increased post-stenotic turbulence production [126], however the exact clinical implications and impact of such is still to be determined.

iii) Restrictive cardiomyopathy

Restrictive cardiomyopathy is a more rare form of heart disease, where pathological myocardial stiffening is observed without any noticeable hypertrophy. This stiffening will cause an increase in EDPVR and hence complicate diastolic filling (decreasing EDV). Apart from that, ventricular size is generally preserved, however the stiffened myocardium typically renders an atrial dilation as a response to the noncompliant ventricles [127].

As with the other cardiomyopathies, ECG monitoring and echocardiographic imaging are first-line evaluation techniques, even though restrictive cardiomyopathy might be difficult to diagnose following the apparent normal ventricular shape. Tissue Doppler or cardiac MRI offers more refined tools for quantifying restrictive cardiomyopathy [90].

Hemodynamically, the increased myocardial stiffening typically manifests itself through diastolic dysfunction, even though varying degrees of systolic dysfunction has also been reported especially in more advanced staged of restrictive cardiomyopathy [128, 129]. The reduced diastolic filling of restrictive cardiomyopathy subjects typically leads to a pattern of increased early diastolic filling velocities, but a sharp decrease in late diastolic flow [128]. With progression, the disease may lead to compensatory dilation or hypertrophy, which at more advanced stages may result in acute heart failure [130].

c) Valvular disease

A very common form of heart disease is so called valvular disease, where abnormal changes of one or several of the intracardiac valves affect blood flow and cardiac

efficiency. In the following, a short description of the two most common types, valvular stenosis and valvular regurgitation, will be presented.

Valvular stenosis refers to an abnormal narrowing of a valve opening, typically caused by atherosclerotic formation on the valve leaflets [131], congenitally valve malformation [132], or as a result of rheumatic heart disease [133]. In all cases the narrowing of the valve causes an increase in inflow velocity, and consequently an increased pressure drop. For this reason, echocardiographic flow assessment or invasive pressure measurements are typically recommended in characterising the severity of a diagnosed stenosis [134]. In fact, in advanced stages of valvular stenosis such as severe aortic stenosis, aortic outflow velocities of above 3-4 m/s may lead to post-stenotic turbulence and irreversible pressure drops [81, 135], where the degree of such could correlate to disease staging.

In valvular regurgitation (or valvular insufficiency) the valve does not close shut after its open phase, resulting in abnormal back-flow or leakage through the valve. There are several causes initiating valvular regurgitation, where so called valvular prolapse (collapse of a valvular leaflet) [136] or myxomatous valve degeneration (deterioration of valve tissue) [137] are the most common identified ones. With the back-flowing valve leakage, regurgitation shifts the pressure differences between cardiac chambers and disrupts the isolvolumetric phases. For the left ventricle, this means that mitral regurgitation (leakage from left ventricle to left atrium) increases preload, whilst at the same time decreases afterload. Together this will result in a slight decrease in forward-flowing aortic ejection, as part of the SV is now used to push blood backwards through the mitral valve. Conversely, in aortic regurgitation (leakage from aortic outlet to left ventricle), an increased SV is ejected into the left ventricular outflow tract to compensate for the back-flow. By so, the ascending aorta will be abnormally extended, increasing systolic blood pressure, and subsequently decreasing diastolic blood pressure (likened to the effect introduced by arterial stiffening) [138].

As with valvular stenosis, valvular regurgitation is typically examined using echocardiography, but other imaging techniques such as computed tomography (CT) or cardiac MRI are mentioned in current guidelines [78].

In both valvular stenosis and valvular regurgitation, the impairment in flow through the heart impacts exerted pressure and resulting volumes. As a consequence pathological remodelling mechanisms of hypertrophy, dilation, or even hypertension may occur, transferring the patient into a long-term worse cardiac state with the risk for future acute heart failure [78, 130].

3.2.2. Vascular disease

Vascular disease are disease types affecting the vascular part of the cardiovascular system and, as with all CVD, directly affects and disrupts the systemic transport of

blood. Below follows a short review of some of the most common vascular diseases, with specific focus on the development of atherosclerotic plaque.

a) Atherosclerosis

Atherosclerosis is a systemic, inflammatory disease, characterised by the build-up of intraluminal plaques, protruding into the luminal cavity. As the plaque development progresses, increased regional stenosis and risk for subsequent plaque rupture poses a major health risk, where thrombus formation or complete vascular blockage as a result from a ruptured or eroded plaque often lead to life-threatening complications.

The development of atherosclerotic plaques is a complex and heterogeneous process, and several different plaque types have been identified [139, 140] with a range of different risk-factors deemed influential in the establishment of the disease [141, 142]. However, some general stages have been identified in the development of the disease, as outlined below. A summarising illustration is also provided in Figure 3.9.

i) Atherosclerosis typically initiates from systemic endothelial dysfunction [139]. Specifically, the intima endothelium loses its ability to properly regulate vascular tone and permeability [143], and instead triggers localised inflammation (a wide range of both modifiable and non-modifiable risk factors have been identified in triggering endothelial dysfunction, such as e.g. high blood cholesterol levels [144], hypertension [145], diabetes [146], diet [95], and smoking habits [96]).

ii) The endothelial dysfunction renders an upregulation of vascular permeability of lipoproteins, leading to the initiation of an atheroma beneath the endothelial layer. This is typically formed by neutrophils and monocytes, who in a subsequent step recruit circulating blood cholesterol (low-density lipoproteins, LDL) into the wall. Once inside the wall, oxidised LDL (oxLDL) crystals form so called fatty streaks in-between the intima and media layer – a typical hallmark of early-stage atherosclerosis.

iii) With oxLDL crystals trapped inside the vessel wall, macrophages start to encompass them forming larger so called foam cells, representing the core of the developed plaque [147].

iv) The process in iii) continues with the plaque increasingly protruding into the intraluminal space. At this stage, smooth muscle cells from the media migrate to the intima, producing extracellular matrix molecules and encapsulating the plaque core with a so called collagen-rich fibrous cap [148]. Inefficient clearance of dead cells inside the atheroma might form a lipid-rich necrotic core of the plaque [139],

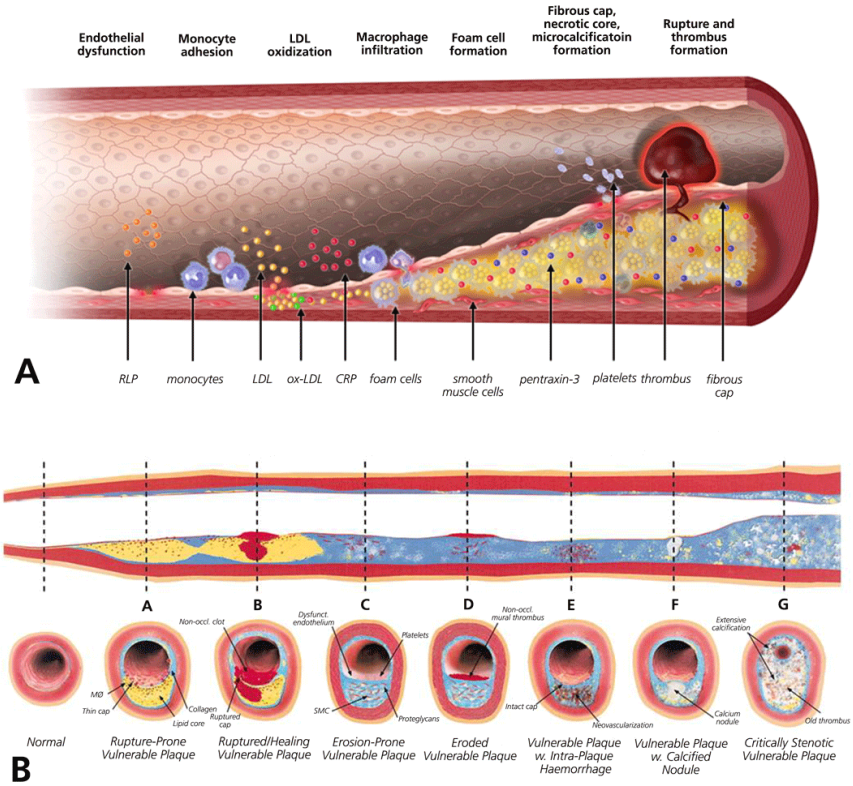

Figure 3.9: (A) Development stages of atherosclerosis from initiation to rupture, depicting important progression steps, as well as acting plaque constituents (residual lipoproteins (RLP), low-density lipoprotein (LDL), oxidised-LDL (ox-LDL) and C-reactive protein (CRP)). (B) A few identified vulnerable plaque types. *Reproduced with permission* [141, 149].

and atheroma macrophage activation might also promote calcium deposition within this necrotic core, forming so called microcalcifications [150].

v) At this stage, the atherosclerotic plaque might develop in many different ways, and the distribution and formation of fibrous cap, necrotic core, and calcifications in iv) varies greatly between different plaques. The further progression of the plaque is thus highly heterogeneous, but using very crude classification one might differentiate between a *stable* plaque, where an inactive core is covered by a relatively thick layer of fibrous tissue, and an *unstable* or *vulnerable* plaque, where a highly active and proliferating core is covered by a thin fibrous cap (so called thin-cap fibroatheroma, TCFA) [151, 152].

vi) Both stable and unstable plaques protrude into the intraluminal cavity, but whilst stable plaques do not develop much beyond v), the thin fibrous cap of the unstable vulnerable plaques are prone to rupture as a consequence of increasing internal load [152] or upon collagen

degeneration [153]. At plaque rupture, thrombogenic factors from the plaque interior attracts platelets in the blood stream, forming a thrombus coagulant that severely disrupts or even fully blocks the downstream blood flow.

Following the established development process, classifications have been proposed in staging atherosclerotic plaque development. A commonly deployed classification score comes from the America Heart Association (AHA), with a conventional (for histopathological analysis) and a modified classification (for image-based MRI analysis), both depicted in Table 3.1 [140].

Table 3.1: Conventional and modified AHA classification of atherosclerotic plaque

Conventional AHA Classification		Modified AHA Classification	
Type I:	Initial lesion with foam cells	Type I-II:	Near-normal wall thickness, no calcification
Type II:	Fatty streak with multiple foam cell layers		
Type III:	Preatheroma with extracellular lipid pools	Type III:	Diffuse intimal thickening or small eccentric plaque with no calcification
Type IV:	Atheroma with a confluent extracellular lipid core	Type IV-V:	Plaque with a lipid or necrotic core surrounded by fibrous tissue with possible calcification
Type V:	Fibroatheroma		
Type VI:	Complex plaque with possible surface defect, haemorrhage, or thrombus	Type VI:	Complex plaque with possible surface defect, haemorrhage, or thrombus
Type VII:	Calcified plaque	Type VII:	Calcified plaque
Type VIII:	Fibrotic plaque without lipid core	Type VIII:	Fibrotic plaque without lipid core and with possible small calcifications

Regarding clinical symptoms of atherosclerosis, the increasing protrusion of the plaque will obstruct the flow of blood, giving rise to e.g. angina pectoris, fatigue, or vascular claudication. If ruptured or eroded, more severe thrombotic events might lead to local ischemia or acute emboli formation such as myocardial infarction or stroke, each with its associated clinical indicators. However, a defined complication of atherosclerosis is that patients might be asymptomatic up until relatively

advanced development stages [141]. High-risk patients will be assigned preventive lipid-lowering, antiplatelet therapy [144], and non-invasive imaging has been proposed as a monitoring tool for the progression of atherosclerosis [8, 100]. Once symptomatic, guidelines still however very much rely on evaluating the degree of stenosis, where a stenotic protrusion of above 60-75% generally leads to invasive endarterectomy (surgical removal of the atherosclerotic plaque) [106]. Other invasive procedures also include vascular stenting or bypass surgery [154], to relieve the effect of the developed plaque.

As evident above, the key clinical question in atherosclerosis lies in so called plaque risk stratification – separating vulnerable rupture prone plaques from the more stable plaque formation. This will be discussed in-detail in Section 3.4.1., but in-short the multifactorial background of atherosclerosis makes such differentiation complicated. Whilst we can classify different plaque types morphologically, it is paradoxically not always the plaque with the highest stenosis that is the most rupture-prone [155, 156]. Also, even if morphology seems evidently important, a range of different types of vulnerable plaque types have been identified in literature (including a thin fibrous cap, large necrotic core, increased plaque inflammation, increased neovascularisation, intraplaque haemorrhage, and active plaque inflammation, as shown in Figure 3.9) [141], complicating the diagnosis. The *in-vivo* assessment of plaque morphology is also not univocal, and echogenicity [157], inflammation [158] and constitutive behaviour [151, 152] have all been proposed as substitute in deriving plaque vulnerability.

Lastly on specific hemodynamic considerations of atherosclerosis, it is clear how atherosclerotic development and local stenotic protrusions disrupt blood flow and increase local blood velocities and pressure drops. Hence, assessment of absolute velocity magnitudes or absolute pressure drops through invasive catheterisation has been used to analyse plaque development or evaluate the need for coronary stenting [159, 160]. Another interesting hemodynamic factor is evident in how *local* atheroma and lipid-retention is triggered from a generally *systemic* endothelial dysfunction. For such, increased wall shear stresses and non-laminar flow around vascular bifurcations have been identified as possible hemodynamic factors initiating plaque development [51]. Hypertension has also been identified as a risk factor for atherosclerosis [145], even though the isolated influence of elevated pressure on plaque formation are still under investigation.

b) Hypertension

Hypertension is a pathological state in which the arterial blood pressure is elevated above normal values, and where the cardiovascular system consequently has to work against a persistently higher work-load. Even though varying between individuals, guidelines cut-off values for diagnosed hypertension are set at systolic blood pressures $\geq$ 140 mmHg and diastolic blood pressures $\geq$ 90 mmHg (albeit isolated systolic hypertension is also identified) [161].

Elevated blood pressure is generally asymptomatic, but the connection between increased blood pressure and cardiovascular risk has been extensively investigated [162], with hypertension deemed an independent risk factor for stroke, myocardial infarction, heart failure, and sudden cardiac death [161], to name only a few. Hypertension is also a highly prevalent disease, with an estimated 25-45% of the entire adult population identified as hypertensive [161, 163], with numbers increasing with increasing age.

Hypertension is a multifactorial disease, and the underlying causes are difficult to isolate. For some specific pathology such as renal or endocrine disease, hypertension is identified as secondary following the onset of the primary pathology [164]. However, so called primary hypertension is more diffusely developing without any cofounding pathophysiological initiation, and only specific risk factors such as genetic variations, smoking, obesity, or age have been identified to increase the risk for the disease [161].

From a hemodynamic perspective hypertension greatly influence the behaviour of the cardiovascular system. The increased arterial blood pressure is equivalent to an increased afterload, which the heart needs to work against to maintain sufficient ejection of blood. By that, a hemodynamic reaction of increasing intraventricular velocities and increasing intraventricular blood acceleration [165] is observed, which may further trigger pathological remodelling through hypertrophy or dilation [166]. The hypertensive hemodynamics also leads to increased turbulent and erratic flow, through which hypertension is a risk factor for valvular stenosis [61]. Conversely, pulmonary hypertension (increased blood pressure in the pulmonary circulation) typically affects the diastolic abilities of the left heart, being a hypothesised component in diastolic heart failure [167], as well as being a risk factor for right ventricular failure [168].

The relation between hypertension and arterial stiffening is also worth mentioning. The increase in arterial stiffness with age is evident [169], so is the increasing prevalence of hypertension [163]. That the two coincide is not surprising: with increasing blood pressure the arteries have to withstand increased exerted load, triggering arterial remodelling and upregulation of collagen production. Conversely, stiffened aortas will decrease distensibility, and hence increased pressures are required to maintain systemic circulation. The order in which the two manifest themselves are still under evaluation, but it has been hypothesised that slight vascular stiffening might precede the onset of clinically evident hypertension [170, 171].

c) Other vascular disease

Even though atherosclerosis and hypertension are by far the most common vascular diseases, a few other vascular complications are worth mentioning within the scope of this thesis. Specifically, aortic coarctation and aortic dissection are mentioned in brief.

i) Aortic coarctation

Aortic coarctation is a generally congenital condition, represented by a local narrowing of the aorta typically in or around the initial aortic bend. The disease accounts for around 4-6% of all congenital heart defects, with an overall prevalence of around 4 per 10 000 births [172]. Hemodynamically, the narrowing can be treated as a local stenotic region, where the cardiovascular system needs to overcome an additionally imposed pressure gradient to successfully pump blood through the systemic circulation. Thus, assessing local pressure drops are part of guidelines for aortic coarctation monitoring [59], and systemic arterial hypertension is common among this specific patient cohort [173]. This increased afterload will render compensatory effects on the cardiac side, leading to potential cardiovascular remodelling.

ii) Aortic dissection

Aortic dissection is a pathological condition where an intraluminal injury allows blood to tear open and flow in-between the layers of the arterial wall. By so the condition represents a serious cardiovascular event, associated with high mortality and the need for acute surgical repair [174]. The disease is not congenitally present, but high incidence-rates are reported in patients with a congenital bicuspid aortic valve potentially following the disrupted outflow [175], as well as in patients with other more rare congenital heart conditions [176]. However, severe hypertension and aortic stiffening have also shown to correlate to aortic dissection, where the risk of initiating vascular damage seems elevated [176]. Hemodynamically the opening of a parallel false lumen severely complicates blood flow, induces regions of high turbulence and irregular flow [177].

3.3. Cardiovascular imaging

Medical imaging has become an indispensable part of modern-day clinical diagnostics, and even though used in virtually every diagnostic field, imaging has come to play a particularly central role in cardiovascular health care. Echocardiography has become a cornerstone of first-line cardiovascular diagnostics, providing direct assessment of cardiac structure as well as refined information on intracardiac flow and tissue constitutive behaviour. For alternative diagnostics, cardiac MRI and CT provide excellent spatial resolution and image contrast, with specific developments of 4D flow MRI enabling the 3D(+time) study of blood flow through the entire cardiovascular system. With other emission-based modalities such as Positron Emission Tomography (PET) and Single-Photon Emission Computed Tomography (SPECT) providing refined information on tissue metabolism and function, a comprehensive mapping of cardiovascular physiology is thus enabled through medical imaging.

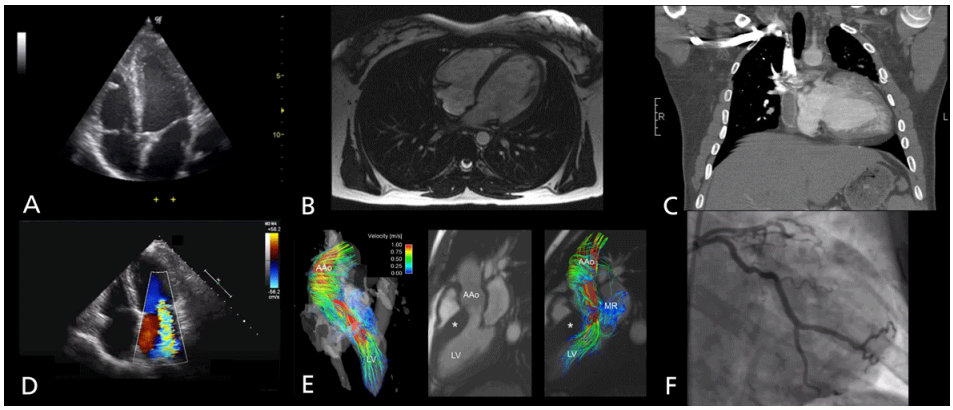

Figure 3.10: Examples of structural and functional cardiovascular imaging, provided by ultrasound ((A) B-mode and (D) Colour Doppler), MRI ((B) T1-weighted and (E) 4D flow) and CT ((C) spiral CT and (F) Coronary angiography). *Reproduced with permission from Wikimedia commons and* [79].

In the following section, a basic review of cardiovascular imaging is provided focussing primarily on ultrasound imaging, MRI, and CT, respectively. For the sake of the thesis, specific emphasis is given on the assessment of cardiovascular flow and ultrasound elastography. An example of some of the structural and functional imaging provided by ultrasound, MRI, and CT is given in Figure 3.10.

3.3.1. Ultrasound imaging

The use of ultrasound as a tool for clinical diagnostics dates back to 1942, when Dussik in a pioneering work showed how acoustic waves could be used to detect neuromas in brain tissue [178]. From this, Edler and Hertz showed its first application to cardiac assessment, correlating received pulse-echoes to the movement and position of the myocardial walls [179]. With clinical scanners introduced in the late 1960s, the diagnostic usage of ultrasound imaging has since increased exponentially, and today ultrasound imaging of the heart and the vasculature constitutes routine practice in modern-day clinical diagnostics.

Ultrasound is defined as acoustic pressure waves, propagating with frequencies above the audible limit of human hearing (20 kHz). As the propagation of these acoustic waves depends on the density and compressibility of the traversed tissue, any change in such imposed by material boundaries or inhomogeneities will give rise to changes in propagating wave form and reflection. Internal structures can thus be reconstructed by recording the amplitude and travel-time of echoes originating from an emitted ultrasound wave.

a) Fundamental imaging physics

From a theoretical point of view, the propagation of an acoustic wave can be related to the internal stresses imposed on the traversed material. This can be

described by the homogeneous equation of motion for a seismic wave (Euler's equation of motion), which with neglected body forces states that

$$\rho \frac{\partial^2 \boldsymbol{u}}{\partial t^2} - \nabla \cdot \sigma = 0, \tag{3.16}$$

where ρ is the medium density, $\boldsymbol{u}$ the wave displacement tensor, and σ the stress tensor.

Through constitutive relations, σ is related to the imposed strains ε by

$$\sigma = C\varepsilon, \tag{3.17}$$

where C is the elasticity tensor of a given material, describing its specific constitutive behaviour. For an isotropic, homogeneous, and linear elastic material, C can be represented exclusively by the two Lamé constants

$$\lambda = \frac{2\nu G}{1 - 2v} \tag{3.18}$$

$$\mu = G, \tag{3.19}$$

where G is the elastic shear modulus (describing the material resistance to shear deformation), and v is the Poisson's ratio (describing the relation between transverse and axial strain upon imposed deformation).

Inserting Equations 3.17-3.19 into 3.16, this renders Navier's equation of motion for isotropic elastic medium

$$\rho \frac{\partial^2 \boldsymbol{u}}{\partial t^2} - \mu \nabla^2 \boldsymbol{u} - (\lambda + \mu) \nabla (\nabla \cdot \boldsymbol{u}) = 0. \tag{3.20}$$

A common way of solving Equation 3.20 is by a so called Helmholtz decomposition, where the wave propagation $\boldsymbol{u}$ is split into a rotational component $\nabla \times \boldsymbol{H}$ and a non-rotational component $\nabla \phi$. Combined with Equation 3.20 this renders an equation system on the form

$$\nabla^2 \phi - \frac{1}{c_L} \frac{\partial^2 \phi}{\partial t^2} = 0 \tag{3.21}$$

$$\nabla^2 \boldsymbol{H} - \frac{1}{c_s} \frac{\partial^2 \boldsymbol{H}}{\partial t^2} = 0. \tag{3.22}$$

Importantly, this shows how an acoustic wave propagates in *two separate modes*: one *compressional pressure wave*, and one *shear wave*, with compressional and shear wave speeds c_L and c_s given by

$$c_L = \sqrt{\frac{\lambda + 2\mu}{\rho}} \tag{3.23}$$

$$c_s = \sqrt{\frac{\mu}{\rho}}. \tag{3.24}$$

However, the two wave modes not only differ in apparent wave speed, but also in their respective mode of propagation. The compressional wave travels through alternating compression and rarefaction of the traversed medium (with displacements parallel to the direction of propagation), whereas the shear wave travels by local shearing of the material (with displacements perpendicular to the direction of propagation), see Figure 3.11.

It can be shown that inside an infinite homogeneous medium, the two wave modes travel without any virtual interaction [180]. However, in the presence of geometrical boundaries, interactions between compressional and shear wave modes complicate the theoretical description, and more refined analytical solutions are needed. For the sake of cardiovascular imaging, this becomes a pressing issue when imaging thin vascular tissue or geometrically confined plaques.

When referring to clinical ultrasound imaging, we are typically referring to compressional pressure waves travelling through the imaged tissue. The wave propagation is then described using the non-rotational part in Equation 3.20, with

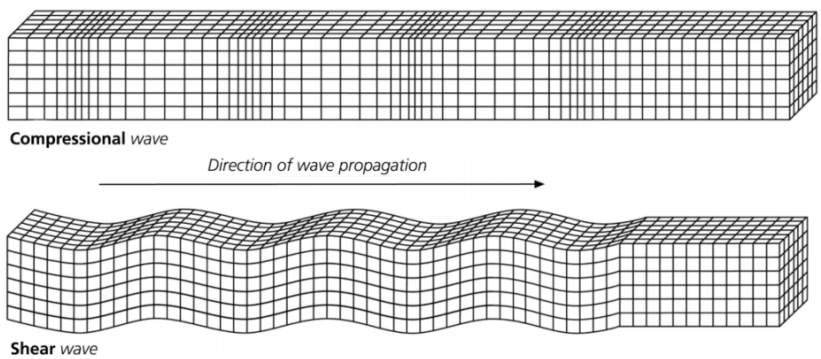

Figure 3.11: The two different modes of acoustic wave propagation: Compressional wave propagation (alternating compressions and rarefactions in the direction of the wave propagation), and Shear wave propagation (localised isovolumetric shearing transverse to the direction of the wave propagation). *Modified and reproduced with permission* [181].

the wave propagation governed by the compressional wave speed c_L. Importantly, the compressional speed of acoustic waves varies very little between different biological tissue [182], and is usually assumed to be 1540 m/s. In fact, this assumption of constant wave speed is essential in clinical ultrasound imaging, where elapsed pulse-echo time can be directly converted to travelled distance.

Conversely, shear wave propagation is less utilised in routine clinical ultrasound imaging. However, within ultrasound elastography imaging, externally imposed shear waves are utilised to provide information on the distribution of shear properties within an imaged object. As the shear wave speed of acoustic waves varies markedly between biological tissue (~10^3 Pa for glandular soft tissue, ~10^8 Pa for epidermis cartilage) [182], a differentiation of different tissue structures could be achieved by analysing their constitutive properties.

b) Pulse-echo imaging

The main principle of clinical ultrasound is the pulse-echo technique, in which a brief ultrasound wave is transmitted into an imaged object before being subsequently registered through its returning echoes. As the wave propagation changes as a function of traversed material, and as the amplitude and intensity of the reflected echo is related to the material interfaces encountered, a reconstruction of the imaged interface boundaries can be achieved, as depicted in Figure 3.12. Importantly, reflections will not only occur at defined tissue boundaries, but also from small scatters within a tissue section. Such scatters give rise to typical speckle-patterns, detectable by conventional ultrasound imaging.

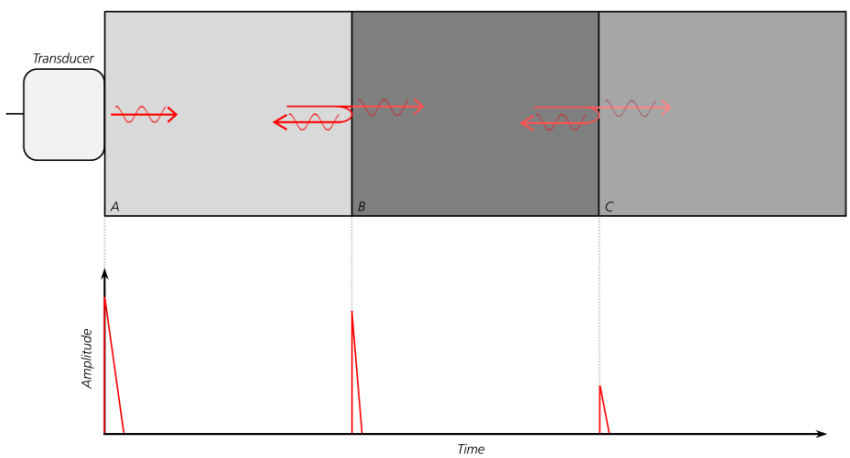

Figure 3.12: Schematic overview of the principle of ultrasound pulse-echo imaging with a transmitted wave reflected back to the transducer at tissue boundaries. The magnitude of the reflected amplitude corresponds to the difference in acoustic impedance between materials A, B, and C, respectively.

The above depicted simple pulse-echo sequence is sufficient for single-element imaging, however, in clinical practice imaging is typically performed using a range of elements inside an imaging transducer. By exciting elements in different sequence, varying element-weighting over the transducer (apodisation), steering the ultrasound beam during the imaged session, or shifting focus-depth (again by shifting element excitation), acquisitions can be optimised for specific application tasks.

To this, post-processing of the retrieved echo signal (the so called radio frequency (RF) data) can be altered to enhance certain regions of the imaged object, dampen the effect of certain high- or low-frequency artefacts (through band-pass filtering), or compensate for increased attenuation at increasing depth (time gain compensation (TGC)).

c) Structural imaging

Using the general principles of pulse-echo imaging, the basic structure of biological tissue can be directly reconstructed. If staying with a one-element setup (the basic pulse-echo technique) so called amplitude (A)-mode imaging can be generated. Here, the amplitude of the retrieved echo-signal is directly displayed. Albeit directly showing the interactions of the retrieved echo signal (identical to the data displayed by Edler and Hertz in the 1950s [179]) its clinical usage is today very limited

Brightness (B)-mode imaging is the most commonly used display mode, created by showing amplitude data from sequentially aligned transducer elements. With that, a grey-scale depiction of the amplitude represents a 2D slice of the imaged object. B-mode imaging is typically used in imaging the myocardium in echocardiography, or to evaluate arterial dimensions and the presence of plaques by vascular ultrasound [6].

Motion (M)-mode imaging is an alternative amplitude display mode, where a single line transducer output is displayed as a function of time. This is typically used in assessing intracardiac valve behaviour [61], or when assessing potential myocardial dyssynchrony [6].

d) Functional imaging

Medical ultrasound can also be used to assess functional properties. In particular, imaging of intracorporeal blood flow through Doppler imaging has become a standardised tool in routine medical ultrasound. Additionally, assessment of constitutive behaviour through ultrasound elastography has gained increasing attention over the last few decades.

i) Doppler imaging

When imaging static tissue, the principles described in previous sections hold where the reflected echo-signal can be interpreted as defined interfaces inside the imaged object. However, when imaging a moving object (such as the flow of blood), the reflected wave will experience a shift in frequency. This phenomenon has been well known for a long time, and is called the Doppler effect after its discoverer. Consequently, in Doppler imaging, the frequency shift between emitted and received echo-signal is related to the velocity of the imaged object.

It can be shown that the relation between the frequency shift f_d and emitted frequency f_0 is related by

$$f_d = 2f_0 \frac{v \cos\theta}{c}, \tag{3.25}$$

where v is the velocity of the moving object and c the propagation speed of the ultrasound. Importantly, θ is the insonation angle between the ultrasound beam and the velocity of the moving object, indicating clearly the angle dependency of Doppler ultrasound [183]. In other words: in ultrasound Doppler we are assessing the velocity component *in the direction of the ultrasound beam*. Following directly from the trigonometric cosine-function, an insonation angle of 10° corresponds to an error of 1.5% in maximum velocity, whereas an insonation angle of 30° corresponds to an error of 23.5%. Clinical guidelines typically recommend an insonation angle of no more than 60° [61], but even assessment errors of up to 50% might occur. Specifically, even though angle compensation algorithms are typically incorporated into current clinical imaging systems, the accuracy of Doppler ultrasound will decrease if assessing tortuous vasculature or turbulent flow (refined ultrasound-based Doppler flow assessment is however under current development [184-186]).

Clinically, two sets of Doppler modes are typically utilised: Continuous-wave (CW)-Doppler and Pulsed-wave (PW)-Doppler. In CW-Doppler, continuous transmission of a single-frequency wave is performed together with a continuous receiving of the reflected, Doppler-shifted signal. This provides direct assessment of the Doppler shift, but does not enable any spatial positioning of the retrieved signal. Instead, PW-Doppler assesses the frequency shift at a specific depth-of-interest.

Both CW- and PW-Doppler are commonly used in echocardiography, primarily to assess intraventricular flow velocities and stage degrees of both stenosis and regurgitation [61, 78]. Doppler assessment of the moving myocardium (tissue Doppler) is also used to assess both systolic and diastolic dysfunction [183], and qualitative classification of intraventricular flow can be achieved using so called colour Doppler (2D visualisation of Doppler shift frequencies).

ii) Elastography

Elastography refers to a set of medical imaging techniques used to map the constitutive properties of investigated tissue. In part the technique originated from the fact that tissue constitutive behaviour will affect acoustic wave propagation, but also from the observation that pathological changes often relate to a change in tissue elasticity [187-190]. Age-induced arterial stiffening has been well-known for a long time [169], and similar stiffening of the myocardium seem evident in restrictive cardiomyopathies [127] and in patients with heart failure with preserved ejection fraction [191]. Additionally, plaque constitutive behaviour has been related to plaque stability [192], and consequently elastographic techniques have been gaining increasing attention in the field of cardiovascular diagnostics.

In short, elastography is based on inducing a local tissue displacement, and then subsequently imaging the tissue reaction to this displacement. The local tissue displacement can be either induced by external (static or transient) excitation [187], by direct excitation through a focussed ultrasound-generated acoustic radiation force [182, 193], or induced naturally by physiological processes [194]. Following this, the imaging of tissue reaction can either be performed by directly assessing the induced displacement or strain field, or by tracking the acoustic waves propagating from the initial point of excitation. Once assessed, the displacement, strain, or induced wave propagation can further be related to apparent elastic properties, providing an imaged-based mapping of tissue elasticity.

With such, the field of ultrasound elastography contains a range of different sub-techniques, all with its defined image specifications and setup. Excellent reviews of different techniques can be found in in [193, 195], but to mention a few of the most prominent ones intravascular strain imaging uses an intravascular probe to directly assess the imposed strain-field from intravascular pressure [194], acoustic radiation force impulse (ARFI) imaging assesses direct strain fields using an imposed acoustic radiation force induced displacement [196], and shear wave elastography (SWE, sometimes also supersonic shear imaging, SSI) tracks the induced shear wave following an initiated acoustic-radiation force displacement, and maps tissue elasticity as a function of the assessed shear wave speed [182].

Among the sub-techniques of ultrasound elastography, SWE is one of the more prominent techniques having been explored and applied for both cardiac [197] and vascular [198] stiffness estimation. In short, SWE consists of three main steps:

1. Local, transient tissue excitation, giving rise to the propagation of shear waves through the investigated tissue
2. Image-based tracking of the shear waves by ultrafast plane wave imaging
3. Reconstruction of constitutive properties from the estimated shear wave motion

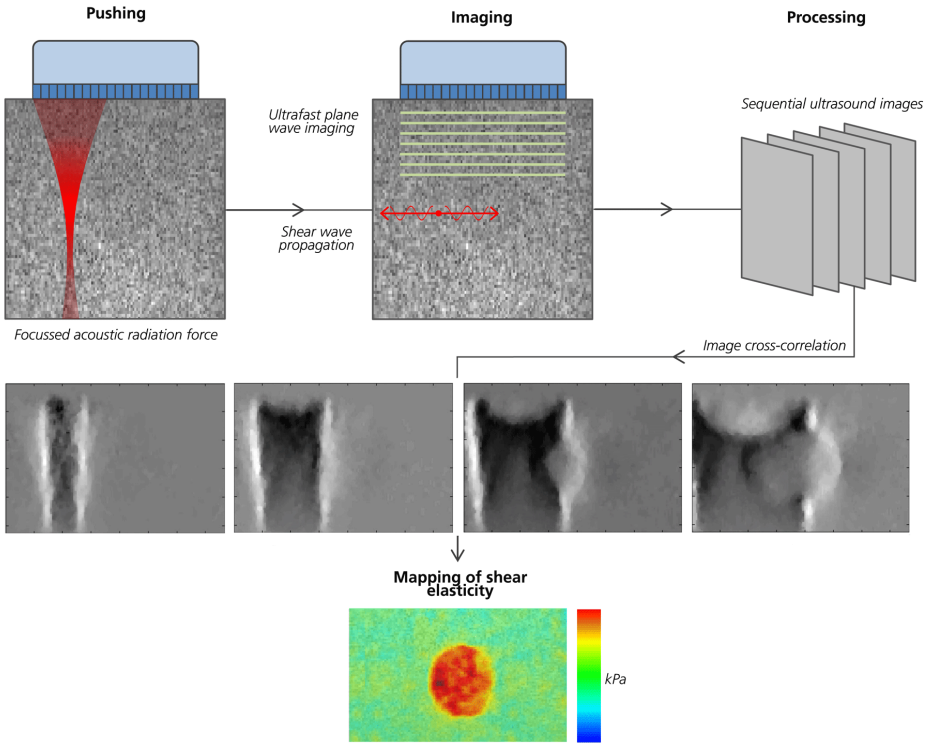

Figure 3.13: Schematic overview of the principle of shear wave elastography. A local tissue deformation is induced by a focussed acoustic radiation force (pushing) which initiates shear wave propagation. By fast switching to ultrafast plane wave imaging (imaging) the motion of the travelling wave can be captured in a series of sequential ultrasound images. By cross-correlation (processing) the deformation and wave front can be visualised as a function of time. With shear wave speed correlated to tissue elasticity, the wave front will distort in the presence of, in this case, a stiffer nodule. By correlating wave speed to constitutive behaviour a quantitative image of shear elasticity can be generated (mapping of shear elasticity). Note how elasticity variations can be present even in the case of homogeneous echogenicity.

Step 1. is achieved by focussing an ultrasonic beam in one (SWE) or several (SSI) locations, where this focussed acoustic radiation force push gives rise to a sudden and local tissue displacement. As a constitutive response to this local displacement, acoustic waves will start to propagate from the epicentre of the push, out through the imaged tissue. Importantly, both compressional and shear waves will be induced in the tissue, however, following the difference in bulk and shear modulus in biological soft tissue the two will propagate with significantly different wave speeds (as given in Equations 3.23 and 3.24).

In fact, shear waves will propagate at a wave speed of a few m/s in soft biological tissue. The motion of such a wave cannot be captured using conventional B-mode frame rates, however using the concept of ultrafast plane wave imaging (where an unfocussed ultrasound beam is transmitted by simultaneous excitation of all transducer elements) [199] frame rates of >1 kHz can be achieved. By so, the

propagation of the travelling shear wave can be captured by quickly switching from the focussed acoustic radiation push (step 1. in the list above), to ultrafast plane wave imaging (step 2. in the list above).

The wave propagation can then be recovered by image cross-correlation [200], where subsequent images of the displacement and non-displaced state are combined to amplify displaced tissue regions. With such, the wave propagation can be visualised and apparent wave speeds quantified (step 3. in the list above). As outlined in Equation 3.24, shear modulus can be directly derived from shear wave speed, *under the assumption of infinite media wave propagation*. This is commonly deployed in conventional elastography assessments, but is violated in thin vascular or constricted plaque tissue. In such cases, wave guide theory would have to be utilised to relate shear wave speed to apparent thickness [201-203].

An illustrative overview of the basic principles of SWE is provided in Figure 3.13. As depicted, the shear wave front is altered when entering a stiffer nodule. Importantly, such variations in shear elasticity may even be present in regions with homogeneous B-mode echogenicity.

3.3.2. Magnetic resonance imaging

MRI is a medical imaging modality utilising the distribution of net magnetic polarisation in an object in the presence of an externally applied magnetic field. Originally discovered in the form of nuclear magnetic resonance (NMR) [204], refinement by Lauterbur, Bloch, and Purcell [205-207] made the technique viable for clinical purposes. Today, MRI is used as a powerful tool for non-invasive structural and functional analysis, and is used for a number of purposes in cardiovascular diagnostics: accurately assessing intracardiac dimensions [208], differentiating myocardial scar tissue from myocardial injury [209], estimating 3D flow features throughout the cardiovascular system [10], and even assessing intracardiac fibre orientation using diffusion tensor MRI [210].

a) Fundamental imaging physics

The fundamental concept of MRI lies in the magnetic momentum or *spin* of sub-atomic particles. The magnetic momentum can be likened by a magnet, where the particle has a positive and a counter-acting negative magnetic pole. For clinical imaging purposes the proton has such a defining spin, meaning that it also possesses certain magnetic properties.

Under normal circumstances, the spins of the protons in the human body is randomly oriented. However, if subjected to an externally applied magnetic field B_0, the net spins will align and start to precess around the axis of B_0. Specifically, the precession or Larmor frequency ω will be related to the field strength of B_0 by

$$\omega = \gamma B_0, \tag{3.26}$$

where γ is the gyromagnetic ratio.

However, all spins will not orientate themselves identically, but rather there will exist a slight favouring of parallel orientation over anti-parallel orientation. Consequently, in the presence of B_0, there will be a net magnetisation M in the investigated tissue (being parallel to the applied B_0).

Now by invoking a pulsed external field B_1 (often called an RF-pulse) orthogonal to B_0, M will be tipped away from B_0 (see Figure 3.14). Specifically M will flip down towards the transverse plane orthogonal to B_0, with the flip angle (deviation of M from B_0) governed by the strength and duration of the RF-pulse.

Once the RF-pulse is removed, an opposite motion will occur and the spins will start to relax back into their original B_0-governed equilibrium state. The relaxation is what forms the actual MRI-image, and is in principle governed by two processes:

i) *T1-relaxation* or spin-lattice relaxation, describing the time required for the *recovery of magnetisation in the direction of* B_0

ii) *T2-relaxation* or spin-spin relaxation, describing the time required for the *decay of magnetisation in the direction of* B_1

As the spin orientation and net magnetisation returns into the orientation of B_0, these relaxation times or net movement of magnetic momentum will be proportional to the Larmor frequency of the tissue, enabling mapping of tissue morphology using dedicated receiver coils.

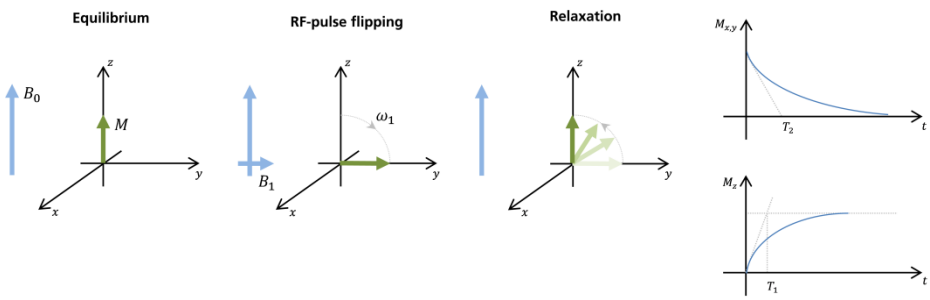

Figure 3.14: Fundamental principles of MRI signal generation. With the imposed magnetic field B_0 a net magnetisation M will be present. With an induced orthogonal RF-pulse, the net magnetisation will flip an angle ω_1 (maximum 90°). Once terminated, the net magnetisation will relax back from the flipped to the non-flipped configuration, with the change in magnetisation measured either as a function of magnetisation recovery in z-direction (T1) or as magnetisation decrease in the transverse xy-plane (T2).

b) Image formation

As described above, following an exciting RF-pulse different tissue structures can be identified based on their proton density and relaxation time. However, simple observation of the induced signal is not enough to spatially position the acquired data. For this, a specific pulse sequence needs to be applied to spatially encode the induced signal.

The gradient echo sequence is a typical MRI sequence used for such 3D positioning. In principle, a gradient echo sequence consists of three different sequential steps:

i) *Slice selection,* or selective RF excitation is represented by a spatial magnetisation gradient G_z applied in the direction of the main field B_0, and simultaneous with the RF-pulse. Since the spins will now be excited to a gradient in the z-direction, the RF pulse can be tuned to only excite spins within a specific frequency range; only spins in resonance with the RF-pulse will be excited. Thus, positioning of the retrieved signal in z-direction can be achieved.

ii) *Frequency encoding* is represented by yet another spatial magnetisation gradient, but this time by G_x. Using G_x, the Larmor frequency of the excited spins will vary as a function of x-position, and can be analysed separately through Fourier decomposition of the retrieved output signal. Thus, positioning of the retrieved signal in x-direction can be achieved.

iii) *Phase encoding* represents the final spatial encoding, achieved by yet another gradient G_y. Here the phase of the signal (rather than frequency) is analysed, where progressively increasing or decreasing G_y is applied to accumulate different phase changes along the y-axis. By analysing the final phase shift as a function of location, positioning of the retrieved signal in y-direction can be achieved.

In addition to the above, when imaging cardiovascular structures, data might also vary as a function of time (due to e.g. the AV-plane motion of the heart, or the respiratory displacements inside the intrathoracic cavity). For such, *image gating* is typically utilised, where data is sampled over a number of consecutive cycles and either prospectively or retrospectively assigned to a specific temporal gate. For cardiovascular imaging, simultaneous ECG recording provides excellent correlation to specific cardiac phases, where acquisitions are typically triggered at the detection of a new R-tag (systolic onset). This however also means that data is acquired as a mean average over a number of cycles, and highly transient events might be difficult to capture.

c) Structural imaging

Using the principles in the previous section, the structure of biological tissue can be reconstructed based on their respective relaxation time. As described both T1 and T2-relaxation occur, wherefore structural MRI images are either described as T1-weighted or T2-weighted. For cardiovascular purposes, T1-weighted images are the most commonly used, with these images enhancing soft tissue contrast [211], as well as providing excellent contrast between blood pool and vascular tissue. T2-weighted images are less common for cardiac assessment, but has been employed to identify reperfusion injury [212], myocardial iron overload [213], and even global myocardial inflammation [214].

d) Functional imaging

MRI does not only enable the study of morphology, but also offers the ability to study functional physiological processes. To exemplify, functional MRI (fMRI, evaluating changes in oxygen-saturated haemoglobin) has been utilised to study brain activity [215], and time-of-flight MR angiography (evaluating the temporal process of magnetic saturation) has successfully been employed to identify aneurysmal developments [216]. For cardiovascular purposes, the use of phase contrast MRI (PC-MRI) to assess cardiovascular blood flow has become a fundamental part of cardiac MRI assessment [217]. In the following section, fundamental basics of PC-MRI are provided.

i) Phase-Contrast MRI

The imaging basics of PC-MRI is in part identical to the spatial position imaging described above; by applying varying gradients and utilising spin relaxation times, an image can be formed. In PC-MRI however, the application of a bipolar gradient is utilised: first a de-phasing is introduced by a positive gradient, which is then reversed by an identical but negative gradient. Any static particle will thus return to its original un-phased state, however any particle that has moved inside the object during the application of the bipolar field will have a net phase shift ϕ. The concept is depicted graphically in Figure 3.15, showing that particles moving at identical velocity will after the bipolar gradient have identical phase shift.

Since velocities are assessed by an induced phase shift, a pre-defined velocity window or *velocity encoding* (VENC) will exist corresponding to $\phi = \pm 180°$. Any larger velocities inducing larger phase shifts will induce aliasing (wrapping), typically encountered in high-velocity PC-MRI flows. In such cases, an increased VENC (by modifying the magnitude of the bipolar gradient *prior* to acquisition) or unwrapping algorithms (during post-processing) has to be applied. Importantly, the VENC will affect the resolution in acquired velocities, and is also directly related to image quality. In fact, it can be shown that VENC is related to signal-to-noise-ratio (SNR) as

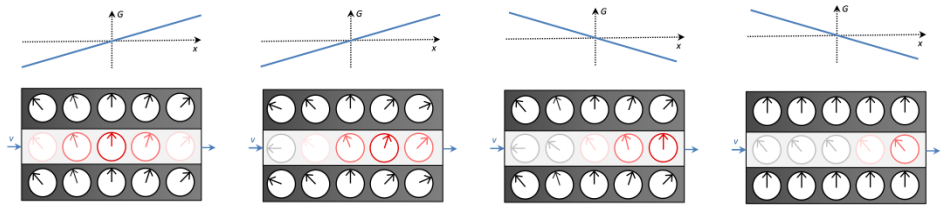

Figure 3.15: Fundamental principles of phase-contrast MRI. Using a bipolar gradient ($+G/-G$) spins with increasing phase shift ω will be induced by the initial positive gradient, before being reverted by the subsequent negative gradient. Static tissue (upper and lower row) will thus have a resulting net $\omega = 0$. However, for moving tissue (middle row, moving to the right with velocity $\boldsymbol{v}$), the movement through the spatial gradient will cause $\omega \neq 0$. Specifically, after the bipolar gradient, a given ω will be related to a given $\boldsymbol{v}$ (with constant $\boldsymbol{v}$ in the figure, the entire mid-row ends up with identical ω).

$$SNR = \frac{\sqrt{2}}{\pi}\frac{VENC}{\sigma}, \tag{3.27}$$

where σ is the standard deviation in the acquired velocity field.

Using slice selection, phase encoding, and frequency encoding, blood flow can also be mapped in 3D. Most commonly though is the selection of a single-plane PC-MRI, where so called 2D time-resolved (CINE) PC-MRI images are acquired, providing information on one-directional velocity through a given image plane.

ii) 4D flow MRI

If applying bipolar gradients in all spatial dimensions, a comprehensive mapping of 3D flow can be achieved. Adding image gating, so called 4D flow MRI (3D flow over time) can be assessed [10, 76, 79]. With such, complete mapping of cardiovascular flow is in principle enabled, and the technique has been extensively applied to study intracardiac flow, derive refined 3D flow parameters for cardiovascular assessment, as well as investigate flow in vascular disease [19, 22, 76, 91, 218-221]. Importantly however is to recall that with bipolar gradients applied in all three dimensions, 4D flow MRI typically requires relatively long scan times (to date around 5-10 minutes). Improvements have been made using accelerated pulse sequences or readout techniques [222, 223], but the acquired flow field will still represent a mean average of the cardiovascular flow over the entire scan time.

3.3.3. Computed Tomography

Computed Tomography (CT) is an imaging modality using the attenuation of photons to reconstruct internal tissue structures. X-rays were discovered by Roentgen in 1895 [224], and the reconstruction of 3D structures through sequential X-ray acquisitions around an object was exploited for medical purposes by Hounsfield, Cormack, and Oldendorf in the 1960s [225-227]. Since then the clinical field of CT has expanded significantly, being utilised for a range of

different diagnostic purposes. For cardiovascular analysis, CT is commonly used to assess coronary artery blockage [228], intracranial bleeding [229], or to examine the degree of plaque intrusions within the vasculature [106]. Angiogram imaging (2D X-ray imaging) is also used to guide clinicians during coronary reperfusion [7], atrial fibrillation ablation [230], aneurysm coiling [229], or other invasive catheter procedures [7].

a) Fundamental imaging physics

The fundamental physical process of CT imaging lies in the interactions of photons with matter. When travelling through any given media, photons interact in four principle ways

i) *Photoelectric absorption*, where the *entire* energy of the photon is transferred into the interacted media by excitation or ejection of a photoelectron.

ii) *Compton scattering*, where *part* of the photon energy is inelastically transferred to the excitation of a bound electron, resulting in a deviation in the photon's travelling direction.

iii) *Rayleigh scattering*, where photon energy is elastically transferred by excitation of the complete interacting atom, again resulting in a deviation in the photon's travelling direction.

iv) *Pair production* where a photon of sufficiently high energy (>1.022 MeV) transfers all of its energy into creating an electron-positron pair near an interacting nucleus.

The probability of the above four varies as a function of photon energy and interacting media, and photon-matter interaction is typically described by the attenuation coefficient μ given as the cross section per unit volume for a given interaction type.

At photon energies used for medical imaging purposes (spectrum <120 keV) Compton scattering is the dominant interaction mode in soft biological tissue, and it is only at fairly low energies (<30 keV) that photoelectric absorption becomes the dominating interaction mode. The exact threshold value however directly depends on the matter element or compound, and scales with atomic number.

If allowing N_0 photons to travel into an investigated object, the number of photons, N, transmitted without interaction through the entire object can be described by the Beer-Lambert law as

$$N = N_0 \exp\left[-\int_l \mu(x,E)dl\right], \tag{3.28}$$

where l is the total length that the photons need to traverse in unit direction x.

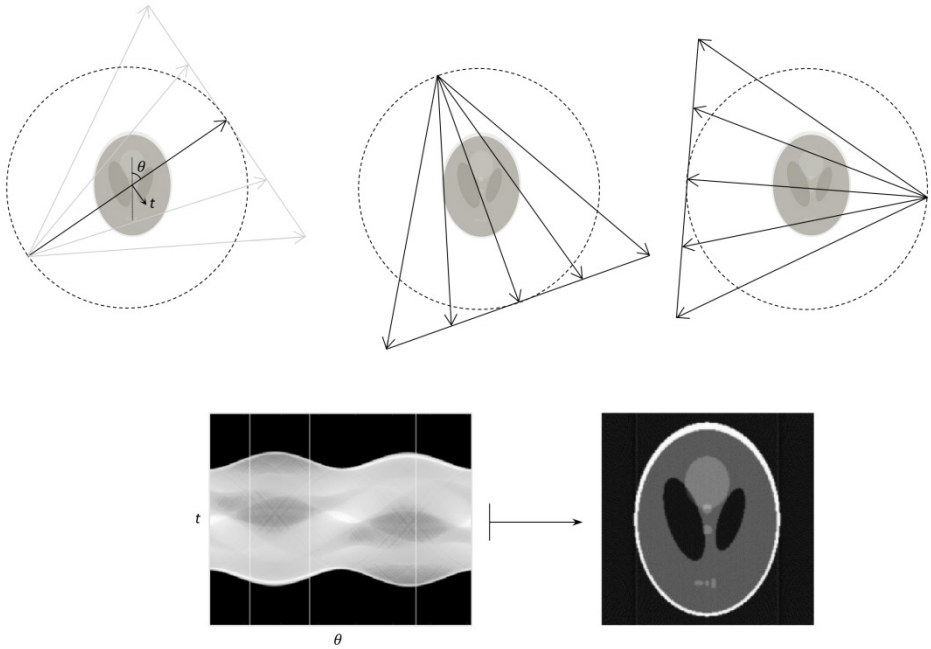

Figure 3.16: Fundamental principles of X-ray CT using a fan-beam geometry. Projection data is acquired by rotating the source-detector pair around the imaged object, with each projection collected as a function of t and θ. Assembling these over the entire image session generates the so called image sinogram (bottom left, white vertical lines highlighting the three acquisition positions in the upper row). The sinogram can then be used to reconstruct the imaged object (bottom right).

Clearly, the number of transmitted photons will be strongly dependent on μ. Solving for μ, Equation 3.28 can be converted into

$$p = -\ln\left[\frac{N}{N_0}\right] = -\int_l \mu(x,E)dl, \tag{3.29}$$

where p is the projection value, typically measured in an energy-integrated form.

The above forms the basis of CT, acquired by a source and detector system rotating around the imaged object, as shown in Figure 3.16. Using a mathematical description of the acquisition system, the interior structure of the imaged object can subsequently be reconstructed.

To describe the sequential rotation and collection of p in a CT, we utilise the Radon transform, R, defining that

$$R[f(x,y)](t,\theta) = \int_{l(t,\theta)} f(x,y)dxdy \tag{3.30}$$

where θ is the angular position of a given acquisition point, t is the position orthogonal to the source-detector direction, and f is the function of interest (in our case μ).

Sampling $R[f(x,y)](t,\theta)$ over a given number of projection angles renders an image sinogram (see Figure 3.16), where the energy-integrated projection value in each detector pixel is displayed as a function of angular position. Depending on the object attenuation traversed, different projection values will be collected at different detector positions and angles, respectively.

b) Image formation

In principle, CT is about sampling $R[f(x,y)](t,\theta)$ as described above. In its most simplistic form, this is achieved by a source and detector setup, where the two are positioned facing one another. By fixing the two onto a rotating gantry, their respective position around the object can be altered, and data can be collected over a range of angular positions.

Even though simple in theoretical terms, some complicating circumstances exist. Firstly, the X-ray source is seldom monochromatic but rather emits a polychromatic spectrum of photons from an X-ray source filament. This means that photons of different initial energy will impinge into the field-of-view, interacting differently as they traverse the object (as $\mu = \mu(E)$). The effect of such is in standard image reconstruction typically neglected, but *beam hardening* artefacts commonly occur where the probability of interaction will depend on photon path and photon energy, respectively. Post-processing techniques exist to calibrate for such typically by acquiring an additional image of a water-equivalent phantom [231], but refined reconstructions have also been proposed incorporating the polychromatic behaviour of the photon spectrum into the mathematical formulation [232].

Secondly, the fan, or in 3D cone, -beam distribution of photons from the source to the detector differs slightly from the parallel beam distribution assumed if using direct Radon transform reconstruction. Instead the photon path has to be incorporated into the description of the system, giving rise to the need for reformulated reconstruction approaches [233, 234].

c) Image reconstruction

Once data is sampled for all projection angles, what is left is to reconstruct the sought after $f(x,y)$ from this data. The reconstruction of an object from such *indirect* observations is mathematically described as an *inverse problem*. Following conventional variable representations, inverse problems deal with the reconstruction of a function f given observed data g, knowing that

$$g = A(f) + \delta g, \tag{3.31}$$

where A is the so called *forward operator*, modelling how the data is generated from the given object f. A can incorporate information on scanner geometry, angular sampling, and even spectrum distribution, in its attempt to accurately model the measurements f. To this δg represents additional noise appearing in all imaging systems.

A problem in medical tomographic imaging is however that the inverse problems we are facing are *ill-posed*, meaning that we cannot easily identify A^{-1}, that solutions are non-unique, and that small variations in g will give rise to significant changes in reconstructed f.

In addition to directly inverting the Radon transform in Equation 3.30 (typically by so called *filtered back projection* (FBP) [235]), we resort to optimisation schemes in trying to minimise the error or *data discrepancy* between $A(f)$ and g in a given setup. One example is the Moore-Penrose or generalised solution $f^{\dagger}$, given such that

$$f^{\dagger} \quad \text{minimises} \quad \|A(f) - g\|_2^2, \tag{3.32}$$

with the data discrepancy minimised by assessing the L^2-norm. The first-order optimality condition for this problem can be expressed as the normal equation

$$A^*(A(f) - g) = 0, \tag{3.33}$$

where A^* is the *adjoint operator* to A. Hence if identifying A and A^*, and given g, numerical reconstruction schemes can be employed to either directly or iteratively minimise the above and generate a sufficient $f^{\dagger}$ to approximate the true f.

Another option in solving $A(f) = g$ is using so called *regularisation* techniques. In contrast to Equation 3.31, a regularisation-based reconstruction introduces a regularisation function, S, acting on f, such that our solution $f^{\dagger}$ now satisfies

$$f^{\dagger} \quad \text{minimises} \quad \|A(f) - g\|_2^2 + \lambda S(f)\,. \tag{3.34}$$

Again the L^2-norm is chosen for the data discrepancy, but in addition S regularises $f^{\dagger}$ by penalising unwanted or unrealistic solutions, scaled specifically by the regularisation parameter λ. Importantly, by selectively choosing S and λ, certain features in the imaged object can be emphasised, such as enhanced tissue boundary contrast or enforced image smoothness.

With the above in mind, a rich spectrum of available numerical techniques exists to solve a tomographic inverse problem, extending far beyond the scope of this thesis. Excellent reviews with extensive mathematical detail are provided in [235],

but for clinical purposes the most commonly deployed reconstruction technique is the aforementioned FBP, utilising the inverse of R with filtering in the frequency domain, with similar solution schemes existing for fan- or cone beam setups [233, 234]. Common in research are the families of algebraic or iterative reconstruction techniques [236, 237], together with the aforementioned (variational) regularisation techniques [238]. For all these cases, task-specific reconstruction has proven successful in enhancing image contrast or diagnostic value, particularly for thoracic or cardiovascular purposes [239-241].

3.4. Cardiovascular image diagnostics

In the following section, a review of a couple of selected areas of cardiovascular image diagnostics is provided. Specifically, image-based atherosclerotic plaque characterisation, hemodynamic pressure assessment, and pre-clinical imaging will be reviewed, being in direct connection to the research work carried out in this thesis.

3.4.1. Carotid atherosclerotic plaque characterisation

The prevalence and associated risks of atherosclerosis are wide-ranging, and extensive work has been put into understanding and staging the disease. In particular, the rupture or erosion of plaques is strongly correlated to embolic cardiovascular events, and thus so called *atherosclerotic risk assessment* or *plaque risk stratification* is central. How can it be clinically determined whether a plaque is a dangerous rupture-prone one, or whether it is a safe, stable one? Albeit simple to formulate, the question has occupied scientists for decades, and even though the mechanisms of plaque development seem evident, the multifactorial complexity and range of plaque types complicates risk stratification. Cardiovascular imaging and image diagnostics has however provided clinicians with a powerful tool to assess atherosclerotic development *in-vivo*, and several methods have shown promise in early-stage clinical implementations [242-247].

a) Clinical routine assessment

Typically, clinical assessment of atherosclerosis is initiated on the basis of occurring cardiovascular symptoms (angina, exercise difficulties, fatigue, etc.). In fact, current guidelines advice against routine screening of asymptomatic patients, following the lack of evidence of any cardiovascular risk reduction [228, 248].

Once admitted, the first-line of evaluation is to assess the *degree of luminal plaque protrusion* or *vascular stenosis*. This is done by B-mode ultrasound imaging, as well as through Duplex imaging where B-mode and colour Doppler is overlaid. Using such, the degree of stenosis can be quantified both using geometrical dimensions as well as through hemodynamic flow assessment. Alternative complements to Duplex evaluations are CT angiography (CTA) or MRI, where again the degree of stenosis can be assessed through visual inspection. However, simple stenosis

assessment does not reveal any information on plaque morphology, and counter-intuitively, plaque vulnerability is not always correlated to a higher degree of stenosis [155, 156, 249]. This is partly due to positive arterial remodelling [250, 251], where a compensatory arterial enlargement is initiated during plaque progression, but stenosis-based assessment is also problematic since severe intraluminal protrusion only occurs at fairly late stages of plaque development [141, 252].

Instead, methods assessing plaque composition and morphology have been developed. Below follows a short review of such techniques, organised by imaging modality. Specific focus is given on ultrasound and ultrasound elastography, partially following the methods' clinical availability and cost-effectiveness, but primarily following the promising results such techniques have shown in quantifying plaques of different morphology and composition [242, 243, 246, 253-255]. An illustrative overview of some of the described techniques is given in Figure 3.17.

b) Ultrasound imaging for the assessment of carotid atherosclerosis

A wide range of ultrasound-based techniques exist to assess plaque morphology or vulnerability. In short, we might classify these as evaluating plaque morphology either by *structural assessment*, *elastographic assessment*, or by *indirect assessment*.

Structural assessment: In this thesis, structural assessment refers to methods directly evaluating the morphological appearance of a plaque in ultrasound B-mode imaging. This direct measurement of *plaque echogenicity* has in early studies showed to differentiate lipid-rich plaques from more fibrotic and calcified ones [256], and a number of studies have since indicated a correlation between echogenicity and plaque vulnerability [157, 257]. With echogenicity initially graded on a qualitative scale (the Gray-Weale scale [256]), a refined metric of plaque echogenicity has been proposed in the so called grayscale median (GSM), where the median average of all plaque pixel intensities is derived to determine plaque vulnerability. An inherent drawback of using plaque echogenicity however lies in the methods wide-ranging sensitivity [258], potentially following from the overlap in echogenicity between several different plaque features. As indicated in [258], both a lipid core and a fibrous plaque appear as echolucent homogenic, and both a calcified plaque and a plaque with intraplaque haemorrhage appear as echogenic heterogenic.

An alternative way of evaluating structural plaque features is by using contrast-enhanced ultrasound (CEUS), where studies have shown that intraplaque haemorrhage and intraplaque vasa vasorum can be visualised, showing correlation to an active, vulnerable, plaque centre [259, 260]. Similarly, CEUS might aid in differentiating soft echolucent plaque features from the intraluminal blood flow, even though the overlap in echogenicity within the plaque remains. The technique is however limited by the use of an external contrast agent, and has so far only been applied in a few clinical cases.

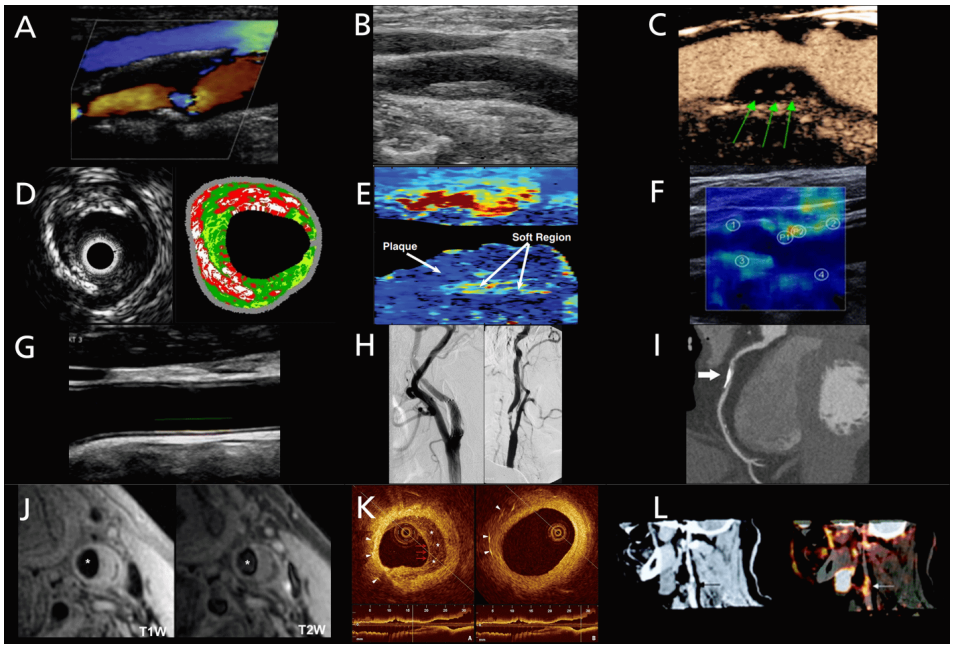

Figure 3.17: Overview of a few image techniques for plaque characterisation or plaque risk assessment. (A) Duplex ultrasound. (B) Echogenicity assessment through B-mode imaging. (C) Contrast-Enhanced Ultrasound, here used to identify intraplaque neovascularisation. (D) Intravascular ultrasound virtual histology. (E) Acoustic Radiation Force Impulse (ARFI) Imaging. (F) Shear Wave Elastography (SWE). (G) B-mode imaging for intima-media thickness (IMT) estimation. (H) CT Angiography of the coronary arteries. (I) Coronary artery calcification (CAC) scoring by CT. (J) Intraplaque soft tissue differentiation by MRI. (K) Optical coherence tomography. (L) PET/CT to evaluate plaque inflammation. *Assembled and reproduced with permission* [255, 261-266].

A method that refines traditional B-mode plaque assessment is the so called virtual histology [244]. Here, Fourier-based analysis of the RF-data is performed where different plaque features are identified based on statistical classification of each composites frequency distribution. Implemented for intravascular ultrasound (IVUS), the method has been applied in a number of clinical trials [267-269], however is limited by its invasiveness.

Elastographic assessment: Elastographic assessment refers to methods evaluating plaque vulnerability based on its constitutive properties. With plaque composition related to its stability, mapping of plaque elasticity could be similarly related to vulnerability. As shown in [192], calcified, fibrous, non-fibrous, and lipid-rich plaque constituents differ significantly in radial elastic modulus, indicating the potential of elastography plaque differentiation.

In its most direct form, strain imaging by speckle-tracking utilises formed speckle patterns to derive strain maps of investigated tissue [270, 271]. The strains are here induced by the intraluminal pressure pulses, and several studies have employed the technique to assess plaque composition, significantly distinguishing lipid-rich

plaques in a study by Naim et al. [192]. Similarly, non-invasive strain imaging has been applied to detect lipid compartments and calcified nodules in carotid plaques [242], to differentiate asymptomatic from symptomatic plaques [254], as well as to detect fibro-atheromatous plaques by refined beam compounding [253].

Strain imaging can also be utilised in IVUS, forming the field of IVUS elastography. As with non-invasive strain imaging, strains induced by intraluminal pressures are used to retrieve tissue strain distribution maps [194]. The technique has most prominently been employed in coronary arteries [272], successfully identifying lipid-rich and macrophage-prevalent areas *in-vivo* as well as demonstrating both high sensitivity and specificity [273]. As with the case of virtual histology however, IVUS elastography is clinically limited by the need for invasive catheterisation.

In contrast, acoustic radiation force-based methods uses externally induced displacements, having shown similar promise for refined plaque characterisation. ARFI imaging has been applied in several studies [243, 274, 275], specifically correlating areas of low displacement to collagen-rich components *in-vivo* [276]. However, soft-plaque components (lipid core, intraplaque haemorrhage) seem to show similar peak displacement values in ARFI [277], impairing its clinical application.

SWE similarly uses an externally imposed regional displacement, however tracks induced shear waves through the investigated tissue. The technique has been employed for plaque characterisation *in-vivo* [255, 278], but a complication exists in the geometrical constriction of arterial and plaque tissue. In such cases, the propagation of the induced shear waves will exhibit guided dispersion behaviour, where the assumptions of Equation 3.24 no longer holds.

To recapitulate, in the case of isotropic, homogeneous, infinite wave propagation, Equation 3.24 holds, giving a direct relation between estimated shear wave velocity and shear modulus. However, for non-infinite wave propagation, geometrical boundaries will interfere with the propagating wave. Analytical solutions have been derived for wave propagation through plates (using so called Lamb wave theory [201]), as well as for hollow cylinders [202], however in the case of more complicated geometries, numerical approximations have to be utilised to describe the propagating wave. For the specific case of arterial SWE, Bernal et al. [203] derived a practical analytical expression for the so called zero-order antisymmetric mode in a solid plate submerged in an inviscid incompressible fluid, which has since been successfully used to describe shear wave propagation in arterial and atherosclerotic phantoms *in-vitro* [198, 279]. Specifically, the expression states that under such circumstances, the relation between compressional and shear wave velocity, c_L and c_s, is given by

$$4\left(\frac{\omega}{c_L}\right)^3 \beta \cosh\left(\frac{\omega}{c_L}\cdot\frac{h}{2}\right)\sinh\left(\beta\frac{h}{2}\right) - \left(\left(\frac{\omega}{c_s}\right)^2 - 2\left(\frac{\omega}{c_L}\right)^2\right)^2 \sinh\left(\frac{\omega}{c_L}h\right)\cosh(\beta h) = \left(\frac{\omega}{c_s}\right)^4 \cosh\left(\frac{\omega}{c_L}h\right)\cosh(\beta h), \tag{3.35}$$

where β is defined as

$$\beta = \sqrt{\left(\frac{\omega}{c_L}\right)^2 - \left(\frac{\omega}{c_s}\right)^2}, \tag{3.36}$$

with ω the angular frequency, and h the estimated vessel wall thickness. With β and the embedded c_s proportional to shear elasticity, experimental arterial SWE results can be fitted to Equation 3.35 by varying resulting media elasticity. Note that this involves analysing the acquired shear wave's frequency-dependent velocity behaviour, or *phase velocity*, in contrast to the wave package *group velocity*, typically assessed using Equation 3.24.

Wave model-based elasticity measures have been performed both *in-vitro* [279] and *in-vivo* [280] for cardiovascular purposes. The techniques' accuracy and applicability is however still under investigation.

Finally on elastographic assessment techniques, a less explored technique is the so called thermal strain imaging (TSI) technique, where the fact that lipid-rich tissue exhibits a temperature dependent acoustic wave speed (compared to water-rich tissue) is utilised to classify tissue components [281]. Even though applied successfully in animals, the technique's applicability in humans remains to be investigated.

Indirect assessment: In this thesis, indirect assessment refers to methods indirectly evaluating plaque vulnerability by imaging of adjacent or related tissue structures. A common metric is the intima-media thickness (IMT), a quantity distinguishable by the difference in echogenicity between blood pool, intima-media, and adventitia, respectively. IMT measurements have even been applied for earlier-stage plaque assessment [282] showing relation to increased cardiovascular risk [283]. However, the method does naturally not differentiate between plaque types, and even though the method is part of clinical guidelines for assessing high-risk patients [8], a systematic review study found no support for the use of IMT in low to intermediate risk cohorts [284].

Lastly, another indirect assessment of the manifestation of atherosclerosis is by assessing arterial stiffness. Even though the causal direction is unclear [285] several studies have correlated increased arterial stiffness with atherosclerosis [286, 287].

Clinical guidelines recommend the estimation of pulse wave velocity (PWV) to estimate arterial stiffness [288], where the velocity of the arterial pressure pulse is related to arterial stiffness through the Moens-Korteweg equation [289]. The estimate is however often based on crude assessment of the arterial pulse, and inherent assumptions in the Moens-Korteweg equation limits accuracy. Instead, refined arterial stiffness estimations can be achieved either by elastography imaging or by pulse wave imaging (PWI), where regional stiffness is assessed by ultrafast tracking of intraarterial displacements, induced by the passing pressure wave [290]. The technique has mostly been employed for aneurysm developments [291] but a few examples exist of its application towards atherosclerotic evaluations [292].

c) CT for the assessment of carotid atherosclerosis

Transmission-based imaging can also be used to assess atherosclerotic lesions, and is as mentioned part of guidelines for stenosis grading. Both 2D digital subtraction angiography (DSA) [293] and 3D CTA can be used, however without revealing information about plaque composition.

Attenuation-based plaque characterisation can however be attempted with standard CT. With the attenuation of calcium far exceeding the attenuation of surrounding lipid-rich soft tissue, dense calcification can be detected at very high specificity and sensitivity levels using CT. This had led to the development of the coronary artery calcification (CAC) score [294] being one of few image-based plaque characterisation scores used in clinics. Being semi-quantitative, the scores weigh the attenuation of a given plaque with identified risk factors such as hypertension, obesity, and age, to determine the risk for future cardiovascular events. Studies have been performed indicating correlation between CAC score and event rate [295, 296], however plaque calcification is still not regarded as one of the hallmarks of a vulnerable plaque. Instead, calcification is typically seen as an advanced-stage stabilising force [297], and it remains to be seen whether CAC is comparable to more recently proposed soft-component plaque differentiation (using e.g. aforementioned ultrasound based techniques) in larger clinical studies.

Developments in the field of dual-energy or spectral CT (using energy-differentiating detectors) have also shown promise for plaque characterisation, where differentiation of lipid, calcium, and atheroma-included iron has been achieved both *ex-vivo* [298] and in pre-clinical *in-vivo* trials [299]. The techniques are though still in early-stage development, and their clinical usage remains to be evaluated.

Summarising the above, CT is a viable modality for plaque assessment, and is particularly advantageous for coronary artery assessment following its high spatial resolution. Its radiation-based nature however limits applicability, particularly as a screening-based imaging modality.

d) MRI for the assessment of carotid atherosclerosis

With the excellent soft tissue contrast of MRI, the modality has potential for accurate plaque characterisation. In fact, differentiation of soft tissue plaque components such as lipid-rich necrotic core, intraplaque haemorrhage, or fibrous tissue have been successfully achieved using MRI in a number of studies [140, 245, 300, 301], with high sensitivity and specificity reported specifically when combining T1- and T2-weighted images [302].

Alternative measures of plaque initiation have also been proposed by flow-based MRI. Regional wall-shear stresses and turbulence production, metrics proposed to correlate to plaque initiation [300, 301, 303, 304], can both be measured using 4D flow MRI [81, 305]. Additionally, as in the case of ultrasound imaging, MR elastography (MRE) has the theoretical potential for refined plaque analysis. However, to date no larger application of MRE for atherosclerotic analysis exists, primarily due to the restricted spatial resolution.

MRI is hence another interesting option for refined plaque characterisation, not least in acting as a non-invasive validation technique. However, clinical MRI is still limited by relatively poor spatial resolution, long acquisition times, and expensive equipment.

e) Other imaging techniques for the assessment of carotid atherosclerosis

In addition to the more conventionally used stenosis grading or plaque characterisation modalities above, a few other techniques for plaque analysis are worth mentioning.

A first class are the optical techniques, where an intravascular probe emitting near-infrared light is used to analyse plaque constituents. Specifically, Optical Coherence Tomography (OCT) has been successfully used in a number of coronary plaque studies [306-308], where differentiation of several soft tissue plaque components has been achieved at very high spatial resolution. The method has also been proposed as a viable technique for the assessment of plaque erosion [309]. This is a potentially important implication, since plaque erosion has been found to cause up to 30% of all sudden cardiac death events (compared to ~60% counted for by plaque rupture) [310], and is in general much less understood than plaque rupture.

Secondly, emission-based imaging such as PET or SPECT could be useful in their ability to identify regions of local inflammation. [^{18}F]-Fluorodeoxyglucose (FDG) PET has been used to image plaque inflammation [266] and has shown the potential of differentiating unstable plaques from smaller asymptomatic lesions [310]. However, apart from inflammatory identification, no differentiation between soft-tissue components can be achieved, and the technique is still hampered by its use of radiation and high cost.

3.4.2. Hemodynamic pressure assessment

The following section will focus on the hemodynamic assessment of blood pressure, or changes in blood pressure as the pressure wave travels through the cardiovascular system. As already mentioned, this is a clinically important metric describing the driving force of blood in the cardiovascular system, and is part of several clinical guidelines [59, 61, 90].

Despite its clinical value, pressure measurements are still largely restricted to invasive procedures, or to crude simplifications of the assessed hemodynamic environment. In part, this originates from the fact that pressure cannot be directly assessed using currently available imaging techniques, but is rather a metric that has to be derived from direct measurements of flow. With such, the accuracy of the assessment will depend both on the accuracy of the flow measurement, as well as on the accuracy of the fluid mechanical flow description. However, with refined imaging techniques now enabling full-field assessment of cardiovascular flow, refined pressure assessment methods have been proposed. In the following, a few of the most promising ones are reviewed and presented.

a) Clinical routine assessment

In clinical practice, the use of catheterised pressure sensors is regarded as gold-standard for the assessment of regional blood pressure [78]. Using such catheters, 1D real-time pressure data can be obtained, with a clinician guiding the position of the catheter tip by simultaneous angiographic imaging. The method enables the direct measurement of absolute pressure, but is also commonly used to assess relative pressure by either using a so called pullback procedure (where the catheter tip is pulled from one position to another), or by using a double-sensor probe. In cardiovascular diagnostics pressure assessment by catheterisation is a common procedure, however, the technique is still limited by its inherent invasiveness and the risks associated with such [311]. In fact, a recent study did show a significant increase in cerebral embolism in patients undergoing AV catheterisation [312], underlining the technique's limitation as a general-purpose method.

An alternative but even more common way of assessing absolute blood pressure is by sphygmomanometer cuffing, where an inflatable cuff and mechanical manometer are used to assess peripheral systolic and diastolic blood pressure. Even though accurate in assessing these two metrics, sphygmomanometer cuffing does not provide any information about central blood pressure, and is limited to peripheral limbs.

Medical imaging is also used in clinical routine to assess cardiovascular pressure. Specifically, relative pressure or pressure drops are typically measured by Doppler echocardiography, where acquired velocities are correlated to pressure changes by the Bernoulli principle. In its most basic form, and as used in clinical guidelines [313], the Bernoulli equation given in Equation 3.2 is simplified into

$$\Delta p = p_2 - p_1 = -4v_{max}^2, \tag{3.37}$$

where Δp is the pressure drop between pressure p_2 and p_1, and v_{max} is the maximum velocity at the most narrow part of an assessed stenosis or valve. The coefficient 4 comes from assumptions on blood density values (ρ = 1060 kg/m^3), as well as on the conversion required from Pa to mmHg (1 mmHg = 133 Pa).

Even though effective under certain conditions, it is important to remember that Equation 3.37 originates from a simplified description of cardiovascular flow, where any influence from kinetic or viscous behaviour is neglected. Similarly, the above assumes complete pressure recovery, meaning that any laminar or turbulent pressure loss is similarly neglected.

Consequently, apparent differences have been observed when comparing Doppler-based pressure assessment to invasive gold-standard catheterisation [314-316]. Specifically, it has been shown that a Doppler-based simplified Bernoulli approach typically overestimates true pressure drops, and that this overestimation increases with increasing stenosis degree [64]. This overestimation not only originates from the neglected viscous and kinetic flow components, but also from the fact that Doppler-measurements only evaluate flow in the direction of the interrogating ultrasound beam (as described in Section 3.3.1.). That is, in Doppler-based pressure assessment, the blood flow is considered as a single streamline; an assumption typically violated in stenotic flow. Additionally, energy dissipation due to turbulence production is also neglected in the simplified Bernoulli approach, having shown to similarly skew relative pressure assessment [317].

b) Alternative image-based techniques

Several methods have been proposed to extend on the simplified Bernoulli approach. Staying with the Doppler-based assessment, a modification by incorporating energy loss as a function of effective valve orifice area (EOA) was proposed by Garcia et al. [318], stating that

$$\Delta p = p_2 - p_1 = -4v_{max}^2 \left(1 - \frac{EOA}{A_A}\right)^2, \tag{3.38}$$

where A_A is the vessel cross-sectional area. With this extended Bernoulli effectively measuring *pressure recovery* (following the evaluated energy loss), the method has been shown to correlate to invasive catheterisation in simple geometries [318], and has similarly been proposed as a refined metric for grading valvular stenosis [316]. However, the extended Bernoulli approach still assumes negligible viscous effects (potentially deteriorating accuracy in low-flow regimes), and it has been hypothesised to perform less well in regions of mild-diffuse or multiple orifice stenosis [317]. Similarly, using Doppler assessment still assumes the

aforementioned single streamline setup, where an increased systematic bias may be observed with increasing stenosis degree.

Extending on the above, the development of full-field imaging techniques (4D flow MRI, ultrasound vector velocity imaging) has permitted a more accurate and complete description of cardiovascular flow. If assessing the transient velocity field along a given flow path or streamline, the unsteady Bernoulli formulation in Equation 3.6 can be utilised to derive relative pressures [62]. With such, the effect of inertial accelerations is added to the approach of the simplified Bernoulli equation. However, by only evaluating the velocity over a centre streamline of the velocity field, a large portion of the entire flow is still neglected, and applications into low-flow or complex vasculatures becomes restricted.

Instead, incorporating data from the full 3D(+time) velocity field, the complete Navier-Stokes equations (Equations 3.7-3.8) can be utilised to derive relative pressure, as was early suggested on acquired MRI data [319]. In a relatively recent approach, the re-formulation of the problem into a so called Poisson Pressure Equation (PPE) has been exploited to derive relative pressure from acquired clinical data [220, 320]. Specifically, the spatial pressure gradient ∇p is redefined as a volume source term b, stating that

$$b = \nabla p, \tag{3.39}$$

or, utilising Equation 3.7, reading

$$b = \nabla p = \mu \nabla^2 \boldsymbol{v} - \rho \frac{\partial \boldsymbol{v}}{\partial t} - \rho \boldsymbol{v} \cdot \nabla \boldsymbol{v}. \tag{3.40}$$

By applying the divergence operator on both sides, we reach what is typically denoted as a Poisson's equation, namely

$$\nabla \cdot b = \nabla \cdot \nabla p. \tag{3.41}$$

Using numerical solution schemes (typically the Finite Element Method (FEM)) the above can be solved at relatively high accuracy, with results provided as a 3D pressure field over the entire evaluated domain.

The PPE is advantageous in that it incorporates all components of the Navier-Stokes equations. However, by the application of an additional divergence operator in Equation 3.41 the pressure field will be assessed using higher order derivatives. By such, the method has shown to be very sensitive to the definition of the flow domain [64, 321], and in fact, even under simplified conditions, the PPE-approach has shown to have a strong underestimation bias [322]. Additionally, the complete FEM-solution of a 3D pressure field can be fairly computationally demanding, wherefore a PPE-approach might be limited in its clinical use.

As a variation on the PPE approach, Švihlová et al. [323] presented the Stokes estimator (STE), where an auxiliary flow field $\boldsymbol{w}$ is solved for as a Stokes problem with right-hand side defined by the pressure gradient ∇p. Specifically this means solving

$$\nabla^2 \boldsymbol{w} + \nabla p_{STE} = f(\boldsymbol{v}), \tag{3.42}$$

$$\nabla \cdot \boldsymbol{w} = 0, \tag{3.43}$$

with

$$f(\boldsymbol{v}) = \mu \nabla^2 \boldsymbol{v} - \rho \frac{\partial \boldsymbol{v}}{\partial t} - \rho \boldsymbol{v} \cdot \nabla \boldsymbol{v}. \tag{3.44}$$

In Švihlová et al. Equations 3.42-3.43 are computed using an FEM-solver, rendering a relative pressure field ∇p_{STE} associated to the auxiliary flow field $\boldsymbol{w}$. However, as this is constrained by Equation 3.44, given by the acquired real flow field $\boldsymbol{v}$, it will be directly correlated to the real relative pressure field ∇p.

The STE approach has shown increased accuracy compared to the PPE-approach [322], however has so far only been implemented in simplified *in-silico* geometries [323]. As with PPE, STE also potentially requires a computationally demanding solver, and the method's sensitivity to the defined flow domain remains to be investigated (even though the higher order derivatives of Equation 3.41 are avoided in the Stokes approach of Equations 42-43).

In an attempt to overcome the need for higher order derivatives, and to avoid the complete solution of a pressure field through an FEM-solver, a direct energy-based approach can instead be used. In particular, the so called Work-Energy Relative Pressure (WERP) method was proposed by Donati et al. [324], where the work-energy relation of the acquired flow field is evaluated. Specifically, to obtain the work-energy equation of the acquired flow, the Navier-Stokes equations in Equation 3.7-3.8 is multiplied by the velocity field $\boldsymbol{v}$, and integrated over the domain Ω, yielding

$$\begin{aligned} &\frac{\rho}{2}\frac{\partial}{\partial t}\int_\Omega (\boldsymbol{v}\cdot\boldsymbol{v})d\Omega + \rho\int_\Omega (\nabla\cdot\boldsymbol{v}\boldsymbol{v})\cdot\boldsymbol{v}d\Omega - \\ &\mu\int_\Omega \nabla^2\boldsymbol{v}\cdot\boldsymbol{v}d\Omega + \int_\Omega \nabla p\cdot\boldsymbol{v}d\Omega = 0. \end{aligned} \tag{3.45}$$

Again, Equation 3.45 now describes the work-energy within the acquired flow field $\boldsymbol{v}$, in the direction of the same field $\boldsymbol{v}$. Through integration by parts (converting

volume integrals over Ω to surface integrals over the domain boundary Γ with normal $\boldsymbol{n}$) the above can be expressed as a function of separate energy entities as

$$\frac{\partial K}{\partial t} + A - S + V + H(p) = 0 \tag{3.46}$$

where

$$\frac{\partial K}{\partial t} = \frac{\rho}{2} \int_{\Omega} (\boldsymbol{v} \cdot \boldsymbol{v})\, d\Omega, \tag{3.47}$$

$$A = \rho \int_{\Omega} (\boldsymbol{v} \cdot \nabla \boldsymbol{v}) \cdot \boldsymbol{v}\ d\Omega, \tag{3.48}$$

$$S = \int_{\Gamma} (\mu \nabla \boldsymbol{v} \cdot \boldsymbol{n}) \cdot \boldsymbol{v} d\Gamma, \tag{3.49}$$

$$V = \int_{\Omega} \mu \nabla \boldsymbol{v} : \nabla \boldsymbol{v}\, d\Omega, \tag{3.50}$$

$$H(p) = \int_{\Gamma} p\ \boldsymbol{v} \cdot \boldsymbol{n} d\Gamma. \tag{3.51}$$

Specifically, K denotes the kinetic energy of $\boldsymbol{v}$ within Ω, A the advective energy transfer of $\boldsymbol{v}$ in and out of Ω, and V the viscous energy dissipation. H and S denotes the energy input to the system, represented by the hydraulic power and shear energy rate, respectively.

By splitting the domain boundary Γ into an inlet, outlet, and vessel wall domain respectively ($\Gamma = \Gamma_i \cup \Gamma_o \cup \Gamma_w$), and assuming nearly constant pressure over inlet and outlet planes, we can expand the hydraulic power as

$$H(p) = p_i \int_{\Gamma_i} \boldsymbol{v} \cdot \boldsymbol{n} d\Gamma + p_o \int_{\Gamma_o} \boldsymbol{v} \cdot \boldsymbol{n} d\Gamma + p_w \int_{\Gamma_w} \boldsymbol{v} \cdot \boldsymbol{n} d\Gamma, \tag{3.52}$$

which, when negligible vessel compliance is assumed (i.e. $|\boldsymbol{v} \cdot \boldsymbol{n}| \ll 1$) simplifies into

$$H(p) = p_i \int_{\Gamma_i} \boldsymbol{v} \cdot \boldsymbol{n} d\Gamma + p_o \int_{\Gamma_o} \boldsymbol{v} \cdot \boldsymbol{n} d\Gamma = \Delta p \cdot Q. \tag{3.53}$$

In the above, the relative pressure $\Delta p = p_o - p_i$ is thus related to H by the *surface flux* Q, defined as

$$Q = \int_{\Gamma_o} \boldsymbol{v} \cdot \boldsymbol{n} d\Gamma = -\int_{\Gamma_i} \boldsymbol{v} \cdot \boldsymbol{n} d\Gamma. \tag{3.54}$$

where Q is the flux (or blood flow rate) through Γ_i or Γ_o, respectively. Note that Equation 3.54 is valid when the flow in and out of the domain Ω is equal, i.e. under strict mass conservation. This holds when assessing a single-vessel geometry (such as a stenosis or valve) but becomes violated if assessing bifurcating vasculatures.

With the shear energy rate S virtually zero when no major gradient exist in the direction of the boundary normal $\boldsymbol{n}$, we can thus rewrite Equation 3.46 as

$$\Delta p = -\frac{1}{Q}\left(\frac{\partial K}{\partial t} + A + V\right). \tag{3.55}$$

Thus, by assessment of kinetic, advective, and viscous energy components (directly computable from the velocity field as per Equations 3.47, 3.48 and 3.50) an estimation of relative pressure between a given inlet and outlet surface can be obtained (for detail of the mathematical derivation, see [324]).

Since presented, WERP has shown promise in assessing transvalvular relative pressure, specifically in situations where simplified Bernoulli estimates fail [64]. Also, WERP has shown to perform favourably to PPE-estimates in simplified geometries [322]. However, as mentioned Equation 3.55 only holds in the absence of bifurcating flow, and similarly the division with Q in Equation 3.55 also limits the method to systolic high-flow pressure events.

c) Alternative image-based techniques incorporating turbulence

In addition to the above mentioned methods, a separate sub-class of techniques exists, where the effect of turbulent flow features is incorporated in the fluid mechanical description (for the importance of turbulent flow structures, see Section 3.1.4.).

Some earlier work correlating the production of turbulent kinetic energy (TKE) to irreversible pressure drop exist in literature [81, 325], but for a direct derivation of relative pressure, two explicit methods are worth mentioning.

First, Gülan et al. [326] proposed computing turbulence production by a shear-scaling method, where the turbulence-driven relative pressure can then be computed by

$$\Delta p = -\frac{1}{Q}\int_{\Omega} 2\mu \boldsymbol{S}\boldsymbol{S} + c_E \rho \|\boldsymbol{S}\| \operatorname{diag}(\operatorname{Cov}[\boldsymbol{v},\boldsymbol{v}])\, d\Omega, \tag{3.56}$$

where $\boldsymbol{S}$ is the strain rate tensor of the mean velocity field (more specifically the symmetric component of the spatial gradient, i.e. $\boldsymbol{S} = \frac{1}{2}[\nabla \boldsymbol{v} + \nabla \boldsymbol{v}^T]$). The method has proven accurate *in-silico*, but *in-vitro* evaluations have shown a significant dependence on the empirical scaling coefficient c_E [317].

Second, Ha et al. [82] presented a method similarly using turbulence production, however expressing the pressure drop in terms of analysing work-energy in the acquired field (similar to the aforementioned WERP approach). With such the method is similar to the WERP formulation of Equation 3.55, and in case of a purely turbulence-driven relative pressure takes the form

$$\Delta p = -\frac{\rho}{Q}\int_{\Omega} \operatorname{Cov}[\boldsymbol{v},\boldsymbol{v}]\ \boldsymbol{S} d\Omega, \tag{3.57}$$

again utilising the strain rate tensor of the mean velocity field together with the covariance to derive relative pressure. As with the shear-scaling method, the turbulence production-based method in Equation 3.57 has rendered promising results *in-vitro* [317], however with *in-vivo* results still to be presented. Importantly, it should also be noted that the above has only been evaluated in steady-state static flow scenarios, and the expansion into transient kinetic flows is not directly permitted by the expression given in Equation 3.57.

3.4.3. Pre-clinical cardiovascular imaging

Pre-clinical imaging typically refers to imaging of living animals or *ex-vivo* tissue, carried out in a controlled laboratory environment. As such, pre-clinical imaging is an important research tool for in-depth studies of biological processes, where fundamental concepts or protocols can be developed prior to any implementation in humans (a pre-clinical phase, often including imaging session, are a fundamental first part of any clinical trial [327]). Importantly, following its non-invasive nature pre-clinical imaging also allows for longitudinal observations, where the complete natural progression of a disease or interventional effects can be studied.

Pre-clinical imaging and animal models are extensively used in cardiovascular research. In particular, with the development of gene knockout and transgenic murine breeds, animal models have become extremely effective in isolating causal factors for specific cardiovascular disease. The apolipoprotein-E knockout mice (ApoE-/-) is specifically designed for developing complex atherosclerotic lesions [328], and similar Leiomodin 2 knockout (Lmod2-/-) has shown to initiate pathologic cardiac dilation in mice [329]. Interventional procedures can also effectively induce certain pathological conditions, where coronary artery balloon occlusion is a typical procedure for initiating myocardial infarction [330] and

similarly pacemaker-induced chronic tachycardia can be used to initiate heart failure [331].

With specific disease initiated or pathways identified, imaging of these animal models is also common. As clinically, pre-clinical MRI can be performed to assess cardiac dimensions or plaque constituents [332], and emission-based tomographic imaging (SPECT or PET) can effectively reveal the degree of myocardial infarction [333] or image general metabolic function [334] in mice. Pre-clinical systems also allow for high-resolution imaging beyond what is possible using conventional clinical imaging. Micro-CT has been used to image rat myocardial infarction at sub-mm resolution [335], contrast-enhanced ultrafast ultrasound has recently been shown to effectively image the mouse cerebrovasculature at super-resolution (~μm) [336], and pinhole apertures have enabled pre-clinical sub-mm SPECT imaging [337]. Even though yet to be applied in the field of cardiovascular research, rapid detector and acquisition developments promise pre-clinical imaging at even higher spatial (nm [338]) or temporal (ps [339]) scale.

Similarly, *ex-vivo* imaging of tissue samples is an effective tool for non-invasive, detailed investigation in cardiovascular research. Again, micro-CT has been used in a number of studies to image endarterectomy or autopsy plaque specimens, revealing details of the vasa vasorum [340], comparing equivalent to histomorphometric analysis [341], and even used to correlate pre-clinical to clinical CT findings [247]. Similarly, pre-clinical MRI of myocardial tissue has been used to evaluate cardiac fibre orientation [247] or laminar structure [342]. Lastly, pre-clinical *ex-vivo* tissue imaging can also serve as an important bench-mark or validation for continued *in-vivo* analysis, such as shown in a number of arterial elastography studies [280, 343].

The technical details of pre-clinical imaging systems however differ from human-size clinical ones. In particular, translating clinical technologies to miniaturised pre-clinical scale requires improvement in system resolution and performance (comparative specifications for clinical versus pre-clinical imaging systems are provided in Table 3.2).

To achieve high-resolution CT-imaging (as in pre-clinical micro-CT) both X-ray source and detector have to be modified. For the X-ray source, so called micro-focus tubes are typically utilised where a μm focal spot size can be achieved, however at the cost of limited output power. Further, detector elements in the μm-range have to be employed. Technically, decreasing pixel size is not a manufacturing problem, however affects the detected photon flux and corresponding relative SNR in each pixel. To exemplify: changing from a 1 mm^2 pixel in a clinical system to a 10 μm^2 pixel in a pre-clinical one means that the photon flux of one clinical pixel is now divided onto 10000 pre-clinical pixels. Consequently, significantly increased X-ray flux or acquisition time is required to gain similar contrast in the pre-clinical system (as seen in the differences in typical scan time in Table 3.2). For static *ex-vivo* imaging this is not a major obstacle, but

for dynamic or longitudinal animal studies, this reduced spatial resolution or required increase in dose might influence output results.

For pre-clinical MRI, again the modification of required spatial resolution poses high demands on improved hardware. In practice, this means using stronger magnetic fields and applied gradients, dedicated receiver coils, and refined acquisition sequences. Specifically, field strengths of up to 21T have been used for pre-clinical MRI [344], differing significantly from clinical standard fields (~1.5T). To this, small and dedicated RF-coils [345] typically using phased-array setups with coil frequencies ~500Hz have to be utilised to induce and capture tissue electromagnetic relaxation. Additionally, as in micro-CT imaging, pre-clinical MRI SNR scales with acquisition time [346] wherefore pre-clinical MRI requires significantly longer scan times compared to clinical MRI acquisitions (see Table 3.2).

In its technical setup, pre-clinical ultrasound imaging does not necessarily differ from clinical imaging. Instead, an increase in transducer frequency allows for increased axial resolution, although at the expense of limited penetration depth. For pre-clinical imaging this is however not a major problem, as the imaged animal or tissue are typically fairly small.

For micro-ultrasound imaging, dedicated high-frequency transducers of up to 70 MHz can be used [347] to push acquired resolutions into the μm range. To this, developments of plane wave acquisitions schemes have in a pre-clinical setup been shown to enable single-digit μm resolution [336]. Importantly, both these setups do not compromise scan-time, wherefore pre-clinical ultrasound imaging can be virtually performed real-time, being of significant advantage to other pre-clinical modalities when studying dynamic phenomena.

Pre-clinical emission-based imaging (PET and SPECT) is also actively employed in small-animal and *ex-vivo* studies. Naturally, pre-clinical PET and SPECT systems require smaller image pixels, but the primary difference in SPECT-imaging is the collimation. By using pinhole instead of clinical standard parallel-hole collimation [337], a magnification of the imaged object is achieved, pushing image resolution into the sub-mm range. For PET, the reduction in ring diameter brings with it an improved spatial resolution, however the apparent fundamental physical resolution limit in PET (acollinearity of the annihilation photons, tissue positron range, etc. [348]) confines the possible resolution range of pre-clinical PET.

Table 3.2: Comparative specifications for typical clinical and pre-clinical imaging. Modified with permission from [349].

Modality	Spatial resolution		Study time		Pre-clinical design requirements
	Clinical	Pre-clinical	Clinical	Pre-clinical	
Ultrasound	~1 mm	~10 μm - 1 mm	Real-time	Real-time	Increased transducer frequency
CT	~0.1-1 mm	~10-100 μm	~5 s	≥15 min	Increased X-ray flux, reduced focal spot size, increased magnification
MRI	~1-10 mm	~200 μm	≥10 min	≥60 min	Increased field-strength, dedicated receiver coils
PET	~5 mm	1-2 mm	5-60 min	5-60 min	Reduced detector-element size, faster read-out electronics
SPECT	~1 cm	0.5-2 mm	30-90 min	30-90 min	Pinhole collimation

Chapter 4

Methodology

The following section presents a review of the material and methods used in the eight studies of this thesis. The section is divided into three main parts, reflecting the three focus areas of the thesis: ***Vascular shear wave elastography***, ***Non-invasive cardiovascular relative pressure estimation***, and ***Tomographic reconstruction for pre-clinical imaging***.

4.1. Vascular shear wave elastography

Four studies have been completed within ***Vascular shear wave elastography***, utilising ultrasound SWE to evaluate vascular function with a particular focus on atherosclerotic plaque assessment.

4.1.1. Study overview

With the four SWE-studies completed in serial sequence over a period of five years, they all build upon each other, utilising particular findings of one study to develop and optimise the setup of another. In particular, refined shear wave analysis has been implemented and tested from *in-vitro* validation to a final clinical *in-vivo* feasibility test with the general aim of progressing conventional SWE into cardiovascular diagnostics. As an illustrative overview, Table 4.1 summarises the basic methodological features of the four studies.

4.1.2. Experimental setup

With the four different SWE-studies ranging from *in-vitro* to *in-vivo*, a few different sets of experimental SWE setups were used.

a) In-vitro design

For Study I and II, phantom material samples were used as a substitute for real biological tissue. Poly(vinyl alcohol) (PVA) cryogel was used as phantom material.

PVA was initially deployed as a phantom material for arterial vessels [350], and has been extensively used in imaging research. Primarily, PVA is a useful phantom

Table 4.1: Methodological overview of the four SWE-based studies.

		Study			
		I	II	III	IV
Application area	Vascular	+			
	Atherosclerotic	+	+	+	+
Study design	*In-vitro*	+	+		
	Ex-vivo		+	+	
	In-vivo				+
Data analysis	SWE Group velocity	+	+	+	+
	SWE Phase velocity	+	+	+	+
Reference or validation method		Mechanical tensile testing	Geometrically unconfined SWE	Micro-CT	MRI

material following the excellent correspondence in acoustic and elastic tissue properties between PVA and soft biological tissue [351, 352]. Secondly, PVA is also a versatile phantom material due to the fact that its mechanical elasticity can be altered during manufacturing. By changing the number of freeze-thaw (FT)-cycles (the number of times the material is frozen and thawed during production) the material stiffness can be adjusted, with increasing stiffness following with an increasing number of FT-cycles.

In short, three groups of PVA phantoms were created:

i) For Study I, a set of fundamental geometrical shapes were manufactured to study the effect of geometrical constriction on wave propagation and SWE accuracy. Specifically, a thin plate (160x130x12 mm), a solid cylinder (diameter: 12 mm, height: 100 mm), and a hollow cylinder (same dimensions as the solid cylinder, but with an inner hollow opening of diameter: 6 mm) were created. For all three, 3 FT-cycles of 12 hours at approximately 22/-22°C was utilised.

ii) For Study I, a second set of arterial phantoms were manufactured to study SWE accuracy as a function of phantom stiffness. The hollow cylinder geometry from the geometrical analysis in i) was used, however with nine phantoms created: 3 at 3 FT-cycles, 3 at 4 FT-cycles, and 3 and 5 FT-cycles, respectively.

iii) For Study II, a set of phantom plaques were manufactured to study SWE accuracy on plaque stiffness differentiability. The phantom plaques were all 20 mm long, had an outer diameter of 14 mm, and varying tapered intraluminal openings. Specifically, intraluminal openings of 3.5, 5, and 7 mm were used, with a centred and off-centred (1:3 shift off-axis) lumen setup utilised. With each setup created at 2, 3, 4, and 5 FT-cycles, respectively, this created a total of 24 phantom plaques (4 stiffness levels, 3 intraluminal diameter openings, and 2 lumen positions, respectively).

To produce the above, custom made phantom moulds were created. For Study I, an acrylic block mould was created, with internal opening equal to the dimensions of the arterial phantoms. Grip fixations were added at each end grip to allow for easier fixation during imaging and reference mechanical testing. For Study II, 3D printed plaque moulds were created, where complementary plastic mould parts were enclosed by a surrounding poly(methyl methacrylate) cylinder, again to create an internal hollow compartment equalling the desired phantom plaque shape. For a summary, both moulds and generated phantoms are showcased in Figure 4.1.

In all *in-vitro* cases, the PVA phantoms were created from a solution in mass percentage of 87% deionised water, 10% fully hydrolysed PVA (molecular weight: 56.14 g/mol, density: 1.27 g/cm^3, Sigma-Aldrich, St. Louis, MO) and 3% graphite powder (molecular weight: 12.01 g/mol, density: 5 g/cm^3, particle size < 50 μm, Merck KGaA, Darmstadt, Germany). The solution was heated to approximately 65°C during continuous stirring before being poured into the phantom moulds.

Once created, the above arterial phantoms were mounted into specific experimental setups.

For Study I, again two sets of experiments were performed: one for the fundamental geometries, and one for the arterial phantoms.

For the plate geometry, the phantom was submerged in water and held up on each end by supporting acrylic blocks, allowing for a direct image assessment of the mid-part of the submerged plate.

For the solid and hollow cylinder, as well as for the nine arterial phantoms, a customised cylindrical fixation enclosure was created. Using the end fixtures of the arterial phantoms, the phantoms could be positioned in the middle of the enclosure, whilst being pressurised by connected inlet and outlet openings. Specifically, for the arterial phantoms, the cylindrical fixation box was connected to a vertical water column, pressurising the mounted phantoms at static pressures of 60, 80, 100, and 120 mmHg, respectively. Note that using a toric joint fixture, the outlet end of the fixation enclosure could be adjusted in axial direction, allowing for a slight pre-stretching of the phantoms to avoid any out-of-plane bulging following the intraluminal pressurisation.

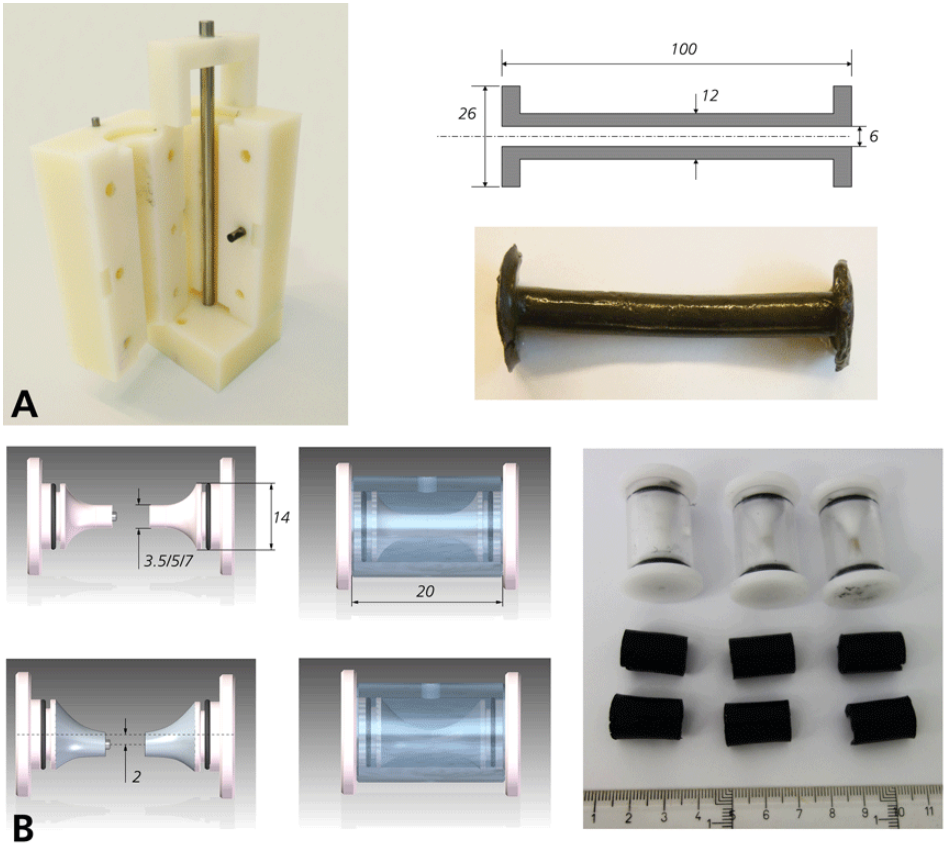

Figure 4.1: Phantoms and moulds used for Study I and II, showing (A) arterial phantoms, and (B) plaque phantoms. All dimensions are given in mm.

Once mounted, an upper opening in the fixation enclosure allowed for a mounted ultrasound transducer to image the arterial phantom. An overview of the experimental setup including fixation enclosure, pressure column, and mounted image transducer, is given in Figure 4.2.

For Study II, the plaque phantoms were used in a combined *ex-vivo* setup, with details provided in the subsequent section.

b) Ex-vivo design

For Study II, the manufactured phantom plaques were mounted into a customised *ex-vivo* setup. For this setup, a porcine aorta (female Swedish Yorkshire pig, weight: 32 kg, collected during medical training) was used to simulate the human carotid artery (length: 100 mm, diameter: 14 mm), with surrounding fascia removed and intercostal arterioles glued shut.

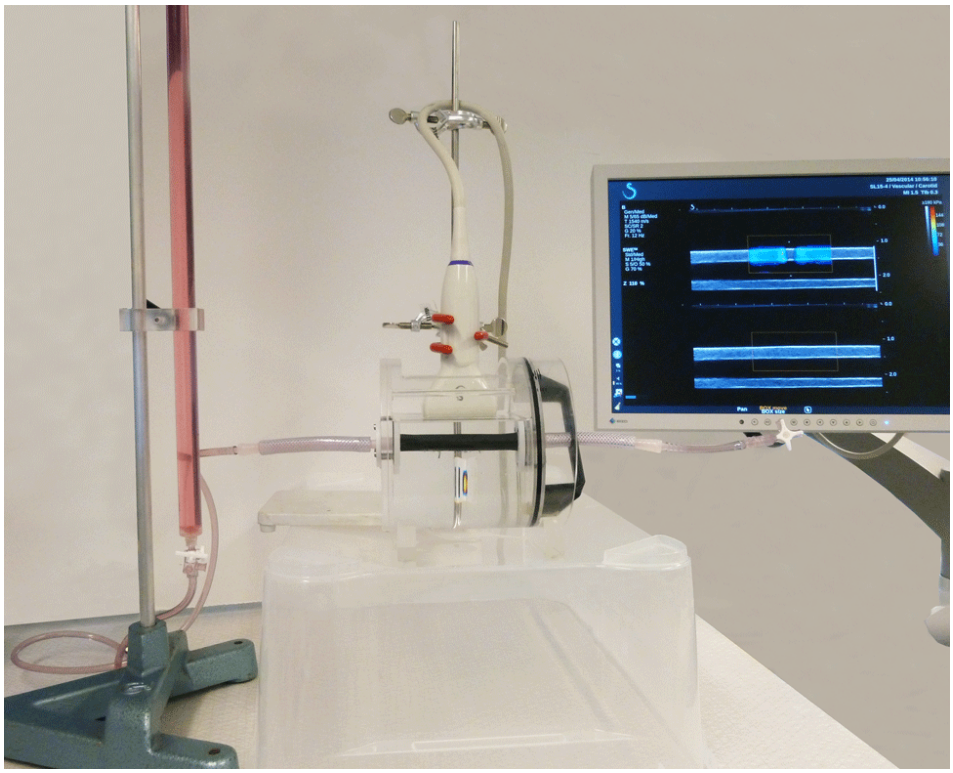

Figure 4.2: Experimental SWE setup used in Study I, showing fixation chamber, mounted image transducer, and connected pressurisation column.

A phantom plaque was inserted into the middle of the artery, and the artery was mounted onto customised end fixture, positioned to avoid excessive artery sagging. The artery was then rinsed and filled with deionised water, with the end fixtures closed shut to keep a constant intraluminal hydrostatic pressure of approximately 0 mmHg.

The end fixtures were subsequently mounted inside an enclosing rectangular box, in which agar material (1% agar (Merck, KGaA, Darmstadt, Germany), 3% graphite powder (molecular weight: 12.01 g/mol, density: 5 g/cm^3, particle size < 50 µm, Merck KGaA, Darmstadt, Germany), 96% deionised water) was moulded to mimic surrounding connective tissue. Specifically, agar was chosen as a surrounding media instead of PVA, following its relatively quick set time (approximately 1-2 hours from manufacturing to set material). Once set, an ultrasound transducer was mounted on top of the moulded block, having the porcine artery and inserted phantom plaque centred in the middle of the field-of-view, as shown in Figure 4.3. Following completion of a single imaging session, the surrounding agar tissue was removed, the artery cleaned, and the experiment repeated with another phantom plaque.

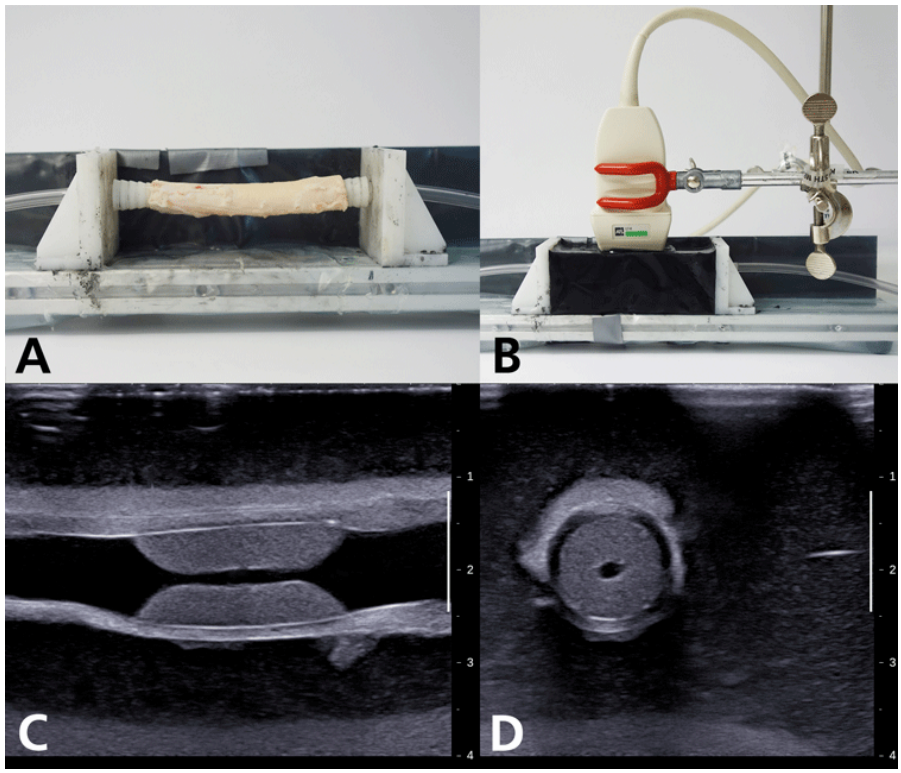

Figure 4.3: Experimental SWE setup used in Study II, showing (A) customised *ex-vivo* setup, (B) mounted image scenario, (C-D) longitudinal and transverse B-mode images.

Advancing from the phantom specimens used in Study I and II, Study III made use of a purely *ex-vivo* tissue sample. Specifically, one human atherosclerotic plaque sample was acquired from performed endarterectomy, with the plaque belonging to the Biobank of Karolinska Endarterectomies (BiKE) project.

Once extracted, the plaque sample was kept for 24 hours in formalin (to avoid biological degradation) and subsequently stored in ethanol prior to further testing. For the SWE imaging, the plaque was submerged in deionised water, resting statically on a stack of a large PVA plate and an absorbing rubber block, respectively. An ultrasound image transducer was then positioned above the plaque, tilted to image the plaque as straight as possible.

c) In-vivo design

For Study IV, 22 subjects with visually apparent carotid plaque lesions were enrolled and included (inclusion criteria: ≥18 years, suspected coronary artery disease, referred to the Mayo Clinic stress echocardiography laboratory, exclusion criteria: previous invasive cardiovascular surgery, contraindication to contrast

agents, pregnancy, or renal dysfunction). Subject characteristics are given in Table 4.2. All subjects participated under informed, written consent (Mayo Clinic Institutional Review Board Protocol 14-000555).

Table 4.2: Subject characteristics for the patient cohort of Study IV.

Demographics and risk factor	Mean ± SD or n	Range (if applicable)
Age, yrs	67.8 ± 8.4	45 – 84
Male, n	16 (80%)	
BMI, kg/m^2	30.6 ± 4.5	22.1 – 38.3
Hypertension, n	12 (60%)	
SBP, mmHg	127.6 ± 20.2	74 – 153
DBP, mmHg	75.3 ± 15.3	42 – 102
History of cardiovascular disease, n	12 (60%)	
Coronary artery disease, n	8 (40%)	
Stroke, n	4 (20%)	
Transient ischemic attack, n	1 (5%)	
Smoking status		
Active, n	4 (20%)	
Quite, n	5 (25%)	
Never smoked, n	11 (55%)	
Hyperlipidaemia, n	17 (85%)	
Total cholesterol, mg/dL	170.1 ± 41.3	120 – 263
Triglycerides, mg/dL	175.3 ± 107.7	50 – 420
HDL cholesterol, mg/dL	46.9 ± 14.3	23 – 80
LDL cholesterol, mg/dL	89.1 ± 37.3	48 – 170
Medication		
Aspirin, n	15 (75%)	
Statins, n	18 (90%)	
Nitrates, n	8 (40%)	
Beta blockers, n	12 (60%)	
Calcium channel blockers, n	5 (25%)	
ACEI, n	8 (40%)	

Carotid stenosis	
Severe (>70%), n	1 (5%)
Moderate (50-69%), n	3 (18%)
Not present (<50%), n	16 (80%)

From the 22 subjects, a total of 29 carotid plaques were identified. For each plaque and subject, SWE imaging was carried out, together with reference carotid MRI, all within the same episode of care (±4 weeks).

4.1.3. Image acquisition

Due to available laboratory equipment at the time of each study, and following the suitability of equipment during *in-vivo* scanning, a few different ultrasound setups were used in the four different studies.

In Study I and III, an Aixplorer (Supersonic Imaging, Aix-en-Provence, France) ultrasound machine with a custom, in-house shear wave research package (allowing for raw export of generated In-phase and Quadrature (IQ)-data) was used. An SL15-4 linear array transducer was utilised, generating an acoustic radiation force push sequence at 6 MHz at a push duration of 150 μs. Ultrafast plane wave imaging was automatically triggered following the push sequence, with imaging at 7.5 MHz and a pulse repetition frequency of 8 kHz. With the Aixplorer system generating a supersonic push line consisting of three consecutive focussed pushes at increasing depth, in both Study I and III an ROI was positioned such that the second of the three pushes was centred inside the phantom or plaque, respectively.

For the arterial phantoms in Study I, three consecutive acquisitions were acquired with pushing performed in longitudinal view, in the middle of both the posterior and the anterior phantom wall, respectively. For the geometry phantoms, pushes were positioned at the centre of each phantom.

For the plaque specimen in Study III, again three consecutive acquisitions were made, however with acquisitions collected in both longitudinal and transverse view, respectively. For the plaque phantom specimen, the push was positioned at the edge of the plaque, to enable wave propagation through the entire specimen.

For the combined plaque phantoms in Study II, a programmable Verasonics V1 system (Verasonics, Kirkland, WA, USA) was used, also allowing for direct readout of generated IQ-data. An L7-4 linear array transducer (Philips Healthcare, Andover, MA) was utilised, with a push frequency of 4.09 MHz, and push duration of 196 μs. Ultrafast plane wave imaging was performed at 6.43 MHz, at a pulse repetition frequency of approximately 11.8 kHz.

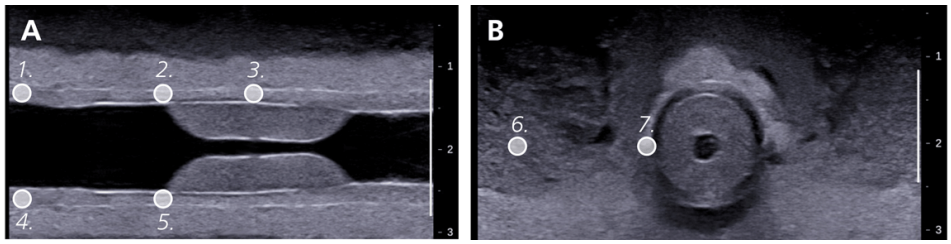

Figure 4.4: SWE push locations used in Study II.

To evaluate output accuracy as a function of push location, seven different acquisitions were performed in each phantom plaque. Specifically, pushing was performed:

1) In longitudinal view, approximately 20 mm away from the phantom plaque boundary in the anterior aortic wall
2) In the longitudinal view, just at the boundary of the phantom plaque at the anterior side
3) In the longitudinal view in the middle of the anterior part of the phantom plaque
4) In the longitudinal view, approximately 20 mm away from the phantom plaque boundary in the posterior aortic wall
5) In the longitudinal view, just at the boundary of the phantom plaque at the posterior side
6) In the transverse view, approximately 20 mm to the side of the porcine aorta
7) In the transverse view, at the edge of the porcine aorta

For clarity, the push locations are highlighted in Figure 4.4.

For Study IV, a clinical General Electrics (GE) Logiq E9 (General Electric Healthcare, Milwaukee, WI, USA) system, allowing for SWE acquisition through double-sided edge pushing was used. A 9L linear array transducer was utilised, pushing at 4.1 or 5 MHz with push duration of approximately 400 μs. Ultrafast plane wave imaging was performed at 5 MHz, tracking the shear wave throughout the imaged field-of-view. For each patient and plaque, imaging was performed in both longitudinal and transverse view, with an ROI selected to cover the entire plaque. Pushing was manually triggered by the sonographer, with in-house conversion enabling for IQ-data retrieval from each acquisition.

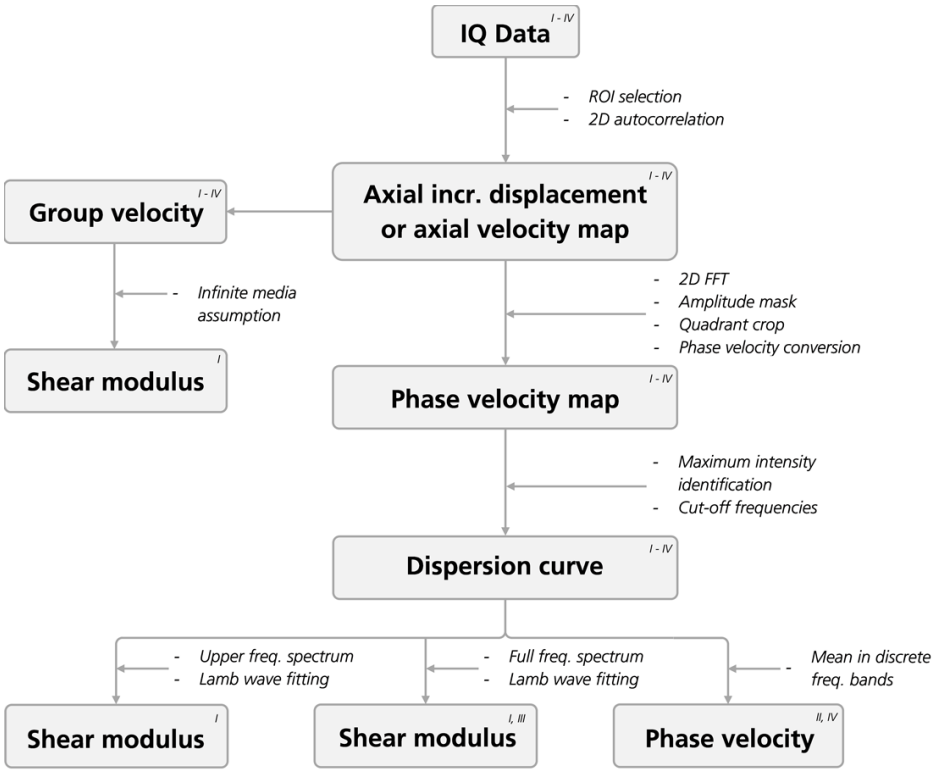

Figure 4.5: Methodological overview of the SWE data post-processing used throughout Study I-IV. Superscript indicates in which study which analysis was performed.

4.1.4. Image analysis and data post-processing

With IQ-data retrieved in all four studies, a set of post-processing image analysis steps were conducted in order to calculate either shear wave *group* or *phase velocity*, or to further estimate *elastic shear modulus* or *signal quality* of the evaluated sample. An overview of the performed analysis is given in Figure 4.5, with superscripts indicating which analysis was included in which Study.

a) 2D autocorrelation and axial incremental displacement and velocity maps

As a first step, tissue displacement and the temporal motion of the propagating wave was estimated by applying a 2D autocorrelator [200] on the IQ data, commonly used for ultrasound elastography.

Specifically, incremental axial particle displacement $\bar{u}$ was derived from the IQ data by

$$\bar{u} = \frac{c}{4\pi f_c} \frac{\tan^{-1}\left(\frac{\sum_{m=0}^{M-1}[\sum_{n=0}^{N-2}(Q(m,n)I(m,n+1) - I(m,n)Q(m,n+1))]}{\sum_{m=0}^{M-1}[\sum_{n=0}^{N-2}(I(m,n)I(m,n+1) + Q(m,n)Q(m,n+1))]}\right)}{2\pi + \tan^{-1}\left(\frac{\sum_{m=0}^{M-1}[\sum_{n=0}^{N-2}(Q(m,n)I(m+1,n) - I(m,n)Q(m+1,n))]}{\sum_{m=0}^{M-1}[\sum_{n=0}^{N-2}(I(m,n)I(m+1,n) + Q(m,n)Q(m+1,n))]}\right)}, \quad (4.1)$$

where I and Q denotes the in-phase and quadrature part of the IQ-data, respectively, acquired at N frames and M depth lines. f_c is the centre frequency of the acquisition, and c is the speed of sound in the imaged tissue, set to 1540 m/s. With the above, axial particle velocity can also be derived by dividing $\bar{u}$ by the frame time t.

With incremental axial particle displacement estimated in each pixel of the acquired image, the global wave front of the propagating wave can be represented by a so called *incremental axial displacement map*, or similarly by an *axial velocity map*. In short, such a displacement or velocity map is a 3D representation of the propagating wave over a selected number of depth lines in the acquired image. As seen in Figure 4.6, upon initiation from a focussed acoustic radiation force push, a shear wave will start to propagate from the push epicentre, changing its shape and position over time. By collecting incremental particle displacements or velocities at a given depth as a function of time, the propagation can hence be visualised in a 2D manner, with a depth-time map showing the intensity of the wave as it propagates through the tissue, as in Figure 4.6.

In Study I and III, incremental axial displacement maps were generated over five manually selected depth lines, positioned inside the phantom or plaque specimen, respectively. In Study II, a manually selected rectangular ROI was positioned inside the phantom plaques, within which axial velocity maps were estimated. For the *in-vivo* plaques in Study IV, the outlines of the plaque in each image view were manually delineated, within which axial velocity maps were estimated.

b) Group velocity estimation

Using the axial incremental displacement or velocity maps, the global envelope of the propagating shear wave can be visualised. With the wave represented in a space-time domain, the velocity of this wave can thus be assessed by evaluating the positional slope within the given map. This velocity is denoted the wave *group velocity*, c_g, since it again represents the envelope speed of the propagating wave.

In Study I and III, c_g was retrieved from the axial incremental displacement maps by applying a Radon transform [353], summing the wave peak signal as a function of angle in the displacement map, and estimating c_g based on the angle of maximum intensity. In Study I the entire map was utilised, whereas in Study III, visually identified sections of c_g was cropped, each generating a specific output.

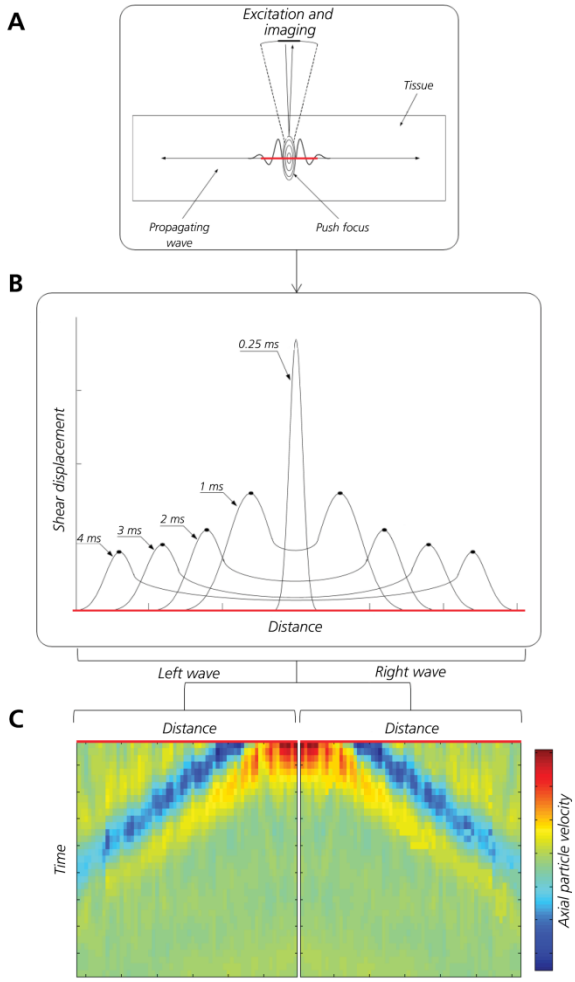

Figure 4.6: Schematic overview of the generation of an axial velocity map, showing (A) SWE setup, (B) correlated shear wave displacement as a function of time, and (C) coupled axial velocity map.

In Study II and IV, a time-to-peak (TTP) method [354] with an additional random sample consensus (RANSAC) filter [355] was employed to identify the peak intensity in the axial velocity maps. Using such, a linear fit with a corresponding c_g-slope could be automatically identified. In Study II, the TTP estimate was generated over the entire axial velocity maps, whereas in Study IV, the domain was cropped in half in both time and space, and if necessary, manually identification of the main wave was employed.

c) Phase velocity estimation

To retrieve the dispersion of the acquired signal, the axial incremental displacement or velocity maps were used as data input. The frequency content of

this wave envelope was retrieved by applying a 2D Fast Fourier Transform (FFT), transforming the data from space-time domain into a wave-number-frequency domain (hence sometimes denoted k-space). Specifically, the 2DFFT acts on the retrieved $\bar{u}$ as

$$FFT[\bar{u}(x,t)] = \sum_{m=-\infty}^{\infty} \left[\sum_{n=-\infty}^{\infty} e^{-i2\pi(kmx+fnt)} \right], \tag{4.2}$$

with k and f being the specific wave number and frequency, respectively.

Within Fourier space, the data were cleaned by an amplitude mask (set in all studies at 12 dB) to remove low-amplitude background signal. Following the symmetric nature of the 2DFFT the upper right quadrant were cropped and used for further analysis.

With Fourier space masked and cropped, a so called phase velocity map was generated, simply by converting the wave number dimension to phase velocity, c_p, using

$$c_p = \frac{2\pi f}{k}. \tag{4.3}$$

At a given frequency, c_p was then identified as the wave velocity for which maximum intensity is given in the phase velocity map. By connecting discrete wave velocities over the entire given frequency spectrum, a so called *dispersion curve* could then be obtained. An overview of the above processing sequence is given in Figure 4.7.

Important to note is that the dispersion curve is not the result of one propagating wave mode, but is rather the sum of all wave modes occurring within a given confined media. Both symmetric and antisymmetric wave modes appear in confined media [201, 202], and higher order modes will be excited at higher frequencies. Especially, in thin hollow media higher order modes will interfere at lower frequencies, causing characteristic bumps or dispersion curve deviations to appear [202, 203, 280]. However, for the sake of the analysis in all SWE studies of this thesis, and in-line with the expression derived in Equation 3.35, focus will here be on the so called zero-order antisymmetric mode, present throughout the entire frequency spectrum.

Another important aspect of the dispersion curve and the analysed Fourier domain data is that the frequency content will be dependent on defined acquisition and processing settings. Widman et al. [198] showed how shorter push duration generates increased frequency content, and similarly, harmonic wave tracking [356, 357] has also shown to affect frequency-based elastography wave speed estimates.

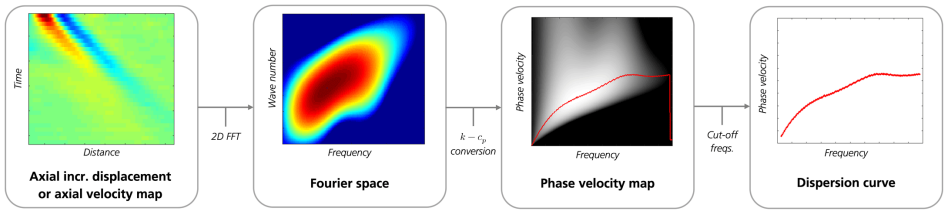

Figure 4.7: Phase velocity generation, starting from a cropped axial velocity map, and creating a k-space dispersion curve from which discrete phase velocities can be retrieved.

In Study I and III, the obtained dispersion curve was cropped at the lower end when the relative change between neighbouring c_p-values was >50%, and at the higher end when the intensity in the phase velocity map had decreased to <30% of the maximum intensity. With such, the dispersion curve was used as input for estimation of shear modulus.

For Study II and IV the retrieved phase velocity was analysed in discrete frequency band, where the mean phase velocity was estimated in each band. Specifically, mean phase velocities were in Study II estimated in bands of 450-550 Hz, 700-800 Hz, and 950-1050 Hz, and for Study IV in bands of 200-300 Hz, 300-400 Hz, and 400-500 Hz, respectively.

d) Shear modulus estimation

With group and phase velocity estimates retrieved, quantification of tissue shear elasticity is possible using appropriate constitutive description of the imaged medium, as well as a description of the acoustic wave propagation.

The most common way of estimating shear elasticity or shear modulus, μ, is by evoking Equation 3.24, where a simple and direct relation exist between wave speed, shear modulus, and density. This relation has been employed in numerous elastography studies [255, 278, 358, 359], and also forms the basis for direct elasticity reconstruction for clinical liver or breast elastography applications [360-362]. However, as pointed out several times, this relation only holds under the strict assumption that the wave propagates without geometrical constriction (so called infinite media assumption), and will be violated if assessing cardiac or vascular structures.

Regardless, to evaluate the accuracy of this direct estimate, in Study I group velocity-based estimates of shear modulus were derived using Equation 3.24.

For phase velocity analysis, in both Study I and III the leaky Lamb-wave-based estimate from Equation 3.35 (derived initially by Bernal et al. [203]) was fitted to the acquired dispersion curve. Specifically, by varying tissue shear modulus and keeping all other variables fixed (material thickness, density, speed of sound) a

Lamb-wave-based estimate of tissue shear modulus could be retrieved for the imaged material.

In Study I and Study III, Lamb wave fitting and dispersion-based shear modulus estimation was performed over the entire frequency spectrum. In Study I, an additional estimate was also obtained by only analysing data above a given frequency limit of 500 Hz (corresponding to approximately half of the acquired band width). This lower frequency cut-off was introduced following reasoning by Couade et al. [280], indicating that dispersion behaviour in a hollow cylinder converges to that of a plate-based Lamb model with increasing frequency.

e) Signal quality estimation

In Study II, signal quality was evaluated by two metrics: Signal-to-noise ratio (SNR) and maximum particle velocity.

The SNR was retrieved by identifying axial particle velocity signal from identified TTP-estimates, and conversely noise was quantified from the lower left corner of the same map with pixels being the farthest away from the propagating shear wave. With such, SNR was calculated by

$$SNR = \frac{m}{\sigma}, \tag{4.4}$$

where m was the mean of the signal, and σ the standard deviation of the noise.

Maximum particle velocity was identified as the single maximum particle velocity at any given time point within the identified ROI.

4.1.5. Reference imaging and validation setup

In all four SWE studies, reference imaging or complementary validation were performed in order to quantify and evaluate SWE output.

a) Study I – Mechanical tensile testing

In Study I, reference mechanical tensile testing was performed to assess phantom material shear modulus.

Importantly, mechanical testing of constitutive shear properties typically involves imposing direct shear loads [363] or, in the case of tubular structures, assessing the relationship between applied torque and resulting angular twist [364]. For the relatively soft PVA phantoms in Study I however, such testing would be complicated by material buckling and non-conforming geometries. For this reason, and under the assumption that the generated phantoms were homogeneous and isotropic, material shear modulus μ was derived from the tensile Young's or elastic modulus E by

$$\mu = \frac{E}{2(1+\nu)}, \tag{4.5}$$

with the Poisson's ratio ν = 0.5 for incompressible cryogel or soft tissue materials.

For the geometrical phantoms, tensile compression tests (quasi-static loading up to 10% strain) were performed on a large PVA cylinder, created from the same PVA batch as the tested phantoms. E was then estimated as the optimal linear slope of the generated stress-strain data.

For the pressurised arterial phantoms, customised end fixtures were mounted into the tensile testing machine, allowing for the phantoms to be tested in axial tension under the same stress conditions as during SWE measurements. Specifically, the arterial phantoms were pressurised at 60, 80, 100, and 120 mmHg, respectively (using the same water column system as in the SWE experiments), and an axial pre-stretch was applied identical to that in the SWE experiments. Quasi-static loading up to 10% strain was applied, and E was again estimated as the optimal linear slope of the measured stress-strain data.

All mechanical tests were performed using an MTS Insight 100 kN mechanical testing system (MTS Systems Corp., Eden Prairie, MN, USA) with an Instron M8500+ electric controller (Instron Worldwide, Norwood, MA, USA) and a VETEK 10 kg load-cell (capacity 100 N, accuracy limit <0.03%).

b) Study II – Geometrically unconfined SWE

In Study II, no quantification of shear elasticity was performed, but rather shear wave group and phase velocity were evaluated. For this reason, reference wave velocity values were obtained from large cylindrical PVA phantoms, created from the same batch as the phantom plaques, at 2-5 FT-cycles, respectively.

Importantly, the dimensions of these large cylindrical phantoms were such that the generated SWE propagation was unconstrained during acquisition. Hence, phantom plaque velocity values (where clear geometrical confinement was present) could be compared to velocities of an identical, but geometrically unconstrained wave.

c) Study III – Micro-CT

In Study III, *ex-vivo* plaque SWE imaging was complemented by micro-CT imaging. The imaging was performed using a built in-house micro-CT system, using a microfocus X-ray source (Hamamatsu MX-L10951-04, focal spot size: 15-80 μm), with a complementary metal oxide semiconductor (CMOS) flat panel (Hamamatsu C7942CA-22, total area: 12 cm^2, pixel size: 50 μm^2), frame grabber (EPIX PIXCI D2X-C7942), and steering gantry.

Pre-calibration of acquisition settings was performed on embedded *ex-vivo* plaques from the Karolinska BiKE-project, choosing a tube voltage: 36 kV, tube current: 800 mA, and frame time: 1500 ms, for optimal image contrast. 360 projections were collected in a tomographic acquisition, with projections calibrated for detector lag, dark current, faulty detector pixels, and geometrical misalignment. 3D image reconstruction was then performed using a simultaneous iterative reconstruction algorithm (SIRT), stopped at 400 iterations.

Reconstructed micro-CT images were visually compared to acquired B-mode and SWE images, correlating potential SWE changes to morphological micro-CT changes.

d) Study IV – MRI

In Study IV, the *in-vivo* SWE imaging was complemented with reference carotid MRI acquisitions carried out in connection to the ultrasound session. The imaging was performed using a 3T scanner with custom-made carotid phase-array surface 6-channel coils (Necocoil LLC) utilised together with a multi-contrast protocol [365]. Specifically, 3D time-of-flight MR angiography (TOF-MRA), magnetisation-prepared rapid acquisition gradient echo (MPRAGE), 2D pre-contrast black-blood T1 weighting (T1W), 2D T2 weighting (T2W), and post-contrast 2D black-blood T1W (CE-T1W) were performed, each providing information on different plaque components. All sequences had an in-pane resolution of 0.625 mm^2, with slice thickness of 1 or 2 mm in 3D or 2D sequences, respectively.

Plaque components were classified in the multi-contrast MR images using dedicated analysis tools (MRI-PlaqueView, VP Diagnostics, Seattle, WA, USA) [301, 366]. Particularly, plaque lipid-rich necrotic core, fibrous cap, intraplaque haemorrhage, loose matrix, and calcification were identified, with absolute and relative volumes quantified. Also, fibrous cap dimensions were measured, including maximum, mean, and minimum thickness. In general, the identification was based on pre-defined criteria where: a) lipid-rich necrotic core without haemorrhage appears as hypointense on T2W and CE-T1W, and isointense on T1W and MPRAGE, b) intraplaque haemorrhage appears as hyperintense on TOF, T1W, and MPRAGE, c) calcifications appear as hypointense on all sequences, d) loose matrix appear as hyperintense on T2W and CE-T1W, and e) fibrous cap was identified as the dark band separating lumen and the necrotic core in TOF and CE-T1W.

Lastly, each plaque was given a global type classification score following the modified American Heart Association (AHA) classification of atherosclerotic plaques [140].

4.1.6. Data evaluation

With slightly different data analysis for each study, data evaluation also varied accordingly.

a) Study I

For the geometrical phantoms, reference shear modulus from mechanical testing was compared to shear modulus calculated by group velocity, shear modulus calculated by the full band width phase velocity, and shear modulus calculated by phase velocities above 500 Hz, respectively, using a one-sample t-test (significant deviations inferred at $p < 0.05$).

For the arterial phantoms comparison was made with the mechanical testing of the pressurised, pre-stretch phantoms, again using a one-sample t-test to infer potential statistical differences ($p < 0.05$). For the arterial phantoms, results were also grouped as a function of pressure, FT-cycles, and wall position.

b) Study II

The ability to differentiate phantom plaques of different stiffness was evaluated using a two-sided Wilcoxon rank sum test (significance inferred at $p < 0.05$). This was performed in each image view, and for each derived velocity metric, respectively.

Signal quality as a function of push location was evaluated using a one-way analysis of variance (ANOVA) test, with a Tukey's range test serving as a post-hoc assessment to quantify significant differences.

c) Study III

The group velocity derived from the axial incremental displacement maps were visually correlated to 2D slices of the micro-CT reconstruction. Lamb wave-fitted phase velocity-based shear modulus estimate was generated as a proof-of-concept, and no quantification of accuracy was performed.

d) Study IV

The group and phase velocity data was evaluated as a function of AHA type, with differences statistically evaluated using a two-sided Wilcoxon rank sum test (significance inferred at $p < 0.05$).

Correlations between SWE metrics and MRI-identified plaque components were assessed by the Pearson and Spearman correlation coefficient (correlation defined at $|R| > 0.5$ and $p < 0.05$). If a plaque component could not be identified in a given plaque, it was excluded from that particular correlation analysis.

4.2. Non-invasive cardiovascular relative pressure estimation

Three studies have been completed in the field of non-invasive cardiovascular relative pressure estimation.

4.2.1. Study overview

The work on non-invasive relative pressure estimations build upon each other, extending and using a method developed in Study V. As an overview, Table 4.3 summarises the basic methodological features of the three studies.

Table 4.3: Methodological overview of the three studies on non-invasive relative pressure estimation

		Study		
		V	VI	VII
Application area	Cardiac	(+)	(+)	+
	Vascular	+	+	+
Study design	*In-silico*	+	+	+
	In-vitro		+	
	In-vivo	+		+
Concept		Method development	Method extension	Clinical study

4.2.2. Theory and method derivation

The developed method, termed the *virtual Work-Energy Relative Pressure (vWERP)* method, originates from an earlier direct work-energy method (WERP) derived by Donati et al. in 2015 [324], summarised briefly in Section 3.4.2. However, for completeness, a recapitulation of the method background is provided, although here outlined for the νWERP method variation.

For a complete description of 3D blood flow we resort to the Navier-Stokes equations, which for an isothermal, incompressible, Newtonian, viscous fluid $\boldsymbol{v}$ states that

$$\rho\frac{\partial \boldsymbol{v}}{\partial t}+\rho\boldsymbol{v}\cdot\nabla\boldsymbol{v}-\mu\nabla^2\boldsymbol{v}+\ \nabla p=0 \tag{4.6}$$

$$\nabla\cdot\boldsymbol{v}=0, \tag{4.7}$$

identical to the expression given in Equations 3.7-3.8. For the relative pressure analysis, we choose to evaluate a fluid domain Ω with boundaries Γ.

To obtain a work-energy formulation, Equations 4.6-4.7 can be multiplied with an arbitrary velocity field – or virtual field – $\boldsymbol{w}$, and integrated over the entire domain Ω, yielding

$$\int_{\Omega} \rho \frac{\partial \boldsymbol{v}}{\partial t} \cdot \boldsymbol{w} d\Omega + \int_{\Omega} \rho(\boldsymbol{v} \cdot \nabla \boldsymbol{v}) \cdot \boldsymbol{w} d\Omega - \int_{\Omega} \mu \nabla^2 \boldsymbol{v} \cdot \boldsymbol{w} d\Omega + \int_{\Omega} \nabla p \cdot \boldsymbol{w} d\Omega = 0. \tag{4.8}$$

If choosing $\boldsymbol{w} = \boldsymbol{v}$, this simplifies to the traditional WERP formulation [324], representing an expression of the actual work and energy within Ω. However, when $\boldsymbol{w} \neq \boldsymbol{v}$, Equation 4.8 instead describes the work-energy within $\boldsymbol{v}$ in the direction of the virtual field $\boldsymbol{w}$. Importantly though, the sought pressure field expressed within ∇p is still originating from $\boldsymbol{v}$, independent of $\boldsymbol{w}$; a key point in the usage of νWERP for clinical analysis.

Using integration by parts* to convert volume to surface integrals on the viscous third term, and identifying separate virtual energy terms, Equation 4.8 can be reformulated into

$$\frac{\partial K_e}{\partial t} + A_e - S_e + V_e + H(p) = 0, \tag{4.9}$$

where

$$\frac{\partial K_e}{\partial t} = \int_{\Omega} \rho \frac{\partial \boldsymbol{v}}{\partial t} \cdot \boldsymbol{w} d\Omega \tag{4.10}$$

$$A_e = \int_{\Omega} \rho(\boldsymbol{v} \cdot \nabla \boldsymbol{v}) \cdot \boldsymbol{w} \tag{4.11}$$

$$S_e = \int_{\Gamma} (\mu \nabla \boldsymbol{v} \cdot \boldsymbol{n}) \cdot \boldsymbol{w} d\Gamma \tag{4.12}$$

*Recall that integration by parts in higher dimensions states that $\int_{\Omega} \nabla \boldsymbol{v} \cdot \boldsymbol{w}\, d\Omega = \int_{\Gamma} \boldsymbol{v} \cdot \boldsymbol{w} \cdot \boldsymbol{n}\, d\Gamma - \int_{\Omega} \boldsymbol{v} \cdot \nabla \boldsymbol{w}\, d\Omega$, for any higher dimensional vector-valued function $\boldsymbol{v}$ and $\boldsymbol{w}$, over the domain Ω with boundary Γ and boundary normal vector $\boldsymbol{n}$.

$$V_e = \int_\Omega \mu \nabla \boldsymbol{v} : \nabla \boldsymbol{w} \, d\Omega \tag{4.13}$$

$$H(p) = \int_\Gamma p \, \boldsymbol{w} \cdot \boldsymbol{n} d\Gamma - \int_\Omega p \nabla \cdot \boldsymbol{w} \, d\Omega. \tag{4.14}$$

As in Equations 3.47-3.51 in Section 3.4.2., the above terms denote the kinetic energy (K_e), advective energy transfer (A_e), viscous energy dissipation (V_e), hydraulic power input (H) and shear energy rate (S_e) of $\boldsymbol{v}$, however this time in the direction of the virtual field $\boldsymbol{w}$.

With the goal of isolating the relative pressure between two boundaries, we can choose to assign certain attributes to $\boldsymbol{w}$. Specifically, by setting $\boldsymbol{w}$ to be a solenoidal field ($\nabla \cdot \boldsymbol{w} = 0$), and splitting the domain boundary into an inlet, outlet, and wall domain, respectively ($\Gamma = \Gamma_i \cup \Gamma_o \cup \Gamma_w$), the hydraulic power formulation in Equation 4.14 can be expressed as

$$H(p) = p_i \int_{\Gamma_i} \boldsymbol{w} \cdot \boldsymbol{n} d\Gamma + p_o \int_{\Gamma_o} \boldsymbol{w} \cdot \boldsymbol{n} d\Gamma + p_w \int_{\Gamma_w} \boldsymbol{w} \cdot \boldsymbol{n} d\Gamma, \tag{4.15}$$

which, in the case that $\boldsymbol{w} = 0$ on Γ_w (again something that can be user-assigned to $\boldsymbol{w}$), reduces into

$$H(p) = p_i \int_{\Gamma_i} \boldsymbol{w} \cdot \boldsymbol{n} d\Gamma + p_o \int_{\Gamma_o} \boldsymbol{w} \cdot \boldsymbol{n} d\Gamma. \tag{4.16}$$

Importantly, Γ_w does not necessarily need to represent a physical vessel wall, but can just as well represent the sum of the vessel wall and all other vascular outlets not considered in the specific relative pressure computation. As an example: if assessing a domain with N inlets and M outlets, Equation 4.16 still holds for any arbitrary inlet Γ_i and outlet Γ_o as long as $\boldsymbol{w} = 0$ on all remaining boundary domains (i.e. on Γ_w, $\sum_{n=0,n\neq i}^{N} \Gamma_n$, and $\sum_{m=0,m\neq o}^{M} \Gamma_m$, respectively).

With the above, applying the divergence theorem we observe that the total inflow Q given by $\boldsymbol{w}$ is identical to its outflow, i.e.

$$0 = \int_\Omega \nabla \cdot \boldsymbol{w} d\Omega = \int_\Gamma \boldsymbol{w} \cdot \boldsymbol{n} d\Gamma = \int_{\Gamma_i \cup \Gamma_o} \boldsymbol{w} \cdot \boldsymbol{n} d\Gamma, \tag{4.17}$$

which, for Equation 4.16 means that

$$H(p) = (p_i - p_o) \int_{\Gamma_i} \boldsymbol{w} \cdot \boldsymbol{n} d\Gamma = \Delta p Q. \tag{4.18}$$

Lastly, by ensuring that $\boldsymbol{w}$ acts in the surface normal direction, and knowing that the gradients of $\boldsymbol{v}$ are negligibly small at the vicinity of the vessel boundaries, the shear energy rate of Equation 4.12 can be effectively set to zero. Thus, Equation 4.9 can be reformulated into

$$\Delta p = -\frac{1}{Q}\left(\frac{\partial}{\partial t} K_e + A_e + V_e\right), \tag{4.19}$$

being identical to the WERP formulation in Section 3.4.2., however with each term now referring to the virtual work of $\boldsymbol{w}$.

All that remains for computing Δp is then to find a virtual field $\boldsymbol{w}$ in line with the assumptions outlined above. In theory, any such virtual field can be selected, but for simplicity, we choose to solve $\boldsymbol{w}$ as a Stokes problem, ensuring the existence of a unique solution and satisfying all the above outlined physical constraints. Specifically, $\boldsymbol{w}$ is solved as

$$\nabla^2 \boldsymbol{w} + \nabla \lambda = 0 \tag{4.20}$$

$$\nabla \cdot \boldsymbol{w} = 0 \tag{4.21}$$

$$\boldsymbol{w} = \begin{cases} -n, & \Gamma_i \\ 0, & \Gamma_w \end{cases} \tag{4.22}$$

where λ is the virtual pressure field corresponding to the virtual field $\boldsymbol{w}$**.** Note that no constraint is set at the outflow plane Γ_o.

4.2.3. Expansion for turbulent flow

In principle, the derivation in Section 4.2.2. holds for any velocity field governed by the Navier-Stokes equations. However, as discussed in Section 3.1.4., incoherent turbulent flows (i.e. stochastic flow fluctuations) may occur in certain pathological states where we can no longer describe the flow as quasi-periodic (i.e. that $\boldsymbol{v}(t) \sim \boldsymbol{v}(t + iT)$ for a given period T and $i \in \mathbb{N}$).

Instead we need to resort to a statistical description of the observed flow, all along the lines of the theory described in Section 3.1.4. In very brief summary, it was shown that if expressing the flow using a linear expected value operator E, the Navier-Stokes equations can be reformulated into

$$\rho\frac{\partial \boldsymbol{V}}{\partial t}+\rho\nabla\cdot(\boldsymbol{V}\boldsymbol{V})+\rho\nabla\cdot\mathrm{Cov}[\boldsymbol{v},\boldsymbol{v}]-\mu\nabla^2\boldsymbol{V}+\ \nabla P=0 \tag{4.23}$$

$$\nabla\cdot\boldsymbol{V}=0, \tag{4.24}$$

where an additional covariance term appears ($\mathrm{Cov}[\boldsymbol{v},\boldsymbol{v}]$), numerically handling the stochastic fluctuations due to turbulent flow regimes.

Thus, if assessing turbulent flows using the same virtual work-energy approach as before, all that is needed is to multiple Equations 4.23-4.24 with $\boldsymbol{w}$, and integrate the expression over Ω. Doing so, we end up with separated energy terms, specifically expressed as

$$\frac{\partial K_e}{\partial t}+A_e-S_e+V_e+H(p)+T_e=0, \tag{4.25}$$

where

$$\frac{\partial K_e}{\partial t}=\int_\Omega \rho\frac{\partial \boldsymbol{V}}{\partial t}\cdot\boldsymbol{w}d\Omega \tag{4.26}$$

$$A_e=\int_\Omega \rho(\boldsymbol{V}\cdot\nabla\boldsymbol{V})\cdot\boldsymbol{w} \tag{4.27}$$

$$S_e=\int_\Gamma (\mu\nabla\boldsymbol{V}\cdot\boldsymbol{n})\cdot\boldsymbol{w}d\Gamma \tag{4.28}$$

$$V_e=\int_\Omega \mu\nabla\boldsymbol{V}:\nabla\boldsymbol{w}\,d\Omega \tag{4.29}$$

$$H(p)=\int_\Gamma p\ \boldsymbol{w}\cdot\boldsymbol{n}d\Gamma-\int_\Omega p\nabla\cdot\boldsymbol{w}\ d\Omega, \tag{4.30}$$

together with the additional turbulent dissipation term

$$T_e=\int_\Omega \rho\ (\nabla\cdot\mathrm{Cov}[\boldsymbol{v},\boldsymbol{v}])\cdot\boldsymbol{w}\ d\Omega, \tag{4.31}$$

being the only additional change to the original νWERP formulation. With this addition for turbulent flows, the expansion is coined νWERP-t.

As before, using integration by parts we can convert Equation 4.31 as

$$T_e = \int_{\Gamma} \rho\ (\mathrm{Cov}[\boldsymbol{v},\boldsymbol{v}]\boldsymbol{n}) \cdot \boldsymbol{w}\ d\Gamma - \int_{\Omega} \rho\ (\mathrm{Cov}[\boldsymbol{v},\boldsymbol{v}]\colon \boldsymbol{w})\ d\Omega, \tag{4.32}$$

which under the assumption that $\boldsymbol{v}$ is negligibly small at the vessel boundary, and that the turbulence is similarly negligible at inlet and outlet regions (Γ_i and Γ_o), can be simplified into

$$T_e = -\int_{\Omega} \rho\ (\mathrm{Cov}[\boldsymbol{v},\boldsymbol{v}]\colon \boldsymbol{w})\ d\Omega. \tag{4.33}$$

With this, and using the same assumptions on $\boldsymbol{w}$ as in the original νWERP formulation, we can again isolate the relative pressure in Equation 4.25 as

$$\Delta p = -\tfrac{1}{Q}\left(\tfrac{\partial}{\partial t} K_e + A_e + V_e + T_e\right), \tag{4.34}$$

representing the extended νWERP-t method, applicable for flow regimes including turbulent energy dissipation.

4.2.4. Numerical implementation

Below follows a brief outline of the numerical realisation of νWERP and νWERP-t, as well as the general implementation on acquired clinical flow data. The entire processing chain was implemented and evaluated using MATLAB R2016a (MathWorks, Natick, MA, USA). A simplified overview of the required processing steps is given in Figure 4.8 (νWERP) and Figure 4.9 (νWERP-t).

a) Pre-processing and data segmentation

In principle, νWERP is not bound to any specific imaging modality, but is rather a method based on any full-field acquisition of 3D flow. However, in all three νWERP-based studies of this thesis, 4D flow MRI has been utilised.

Using 4D flow MRI, a vital pre-processing step lies in the calibration and correction of potentially erroneous data, following the presence of e.g. eddy currents, field inhomogeneities, or regions of signal aliasing.

Once corrected, segmentation of the vascular domain of interest (Ω in the theoretical derivation) has to be performed, isolating the fluid domain from surrounding tissue structures by the creation of a binary image mask. In all three studies, fluid domain segmentation was performed by semi-automated data thresholding on generated velocity magnitude images. Within the same segmentation, user-defined inlet and outlet planes also have to be selected, defining the region over which relative pressures are to be computed.

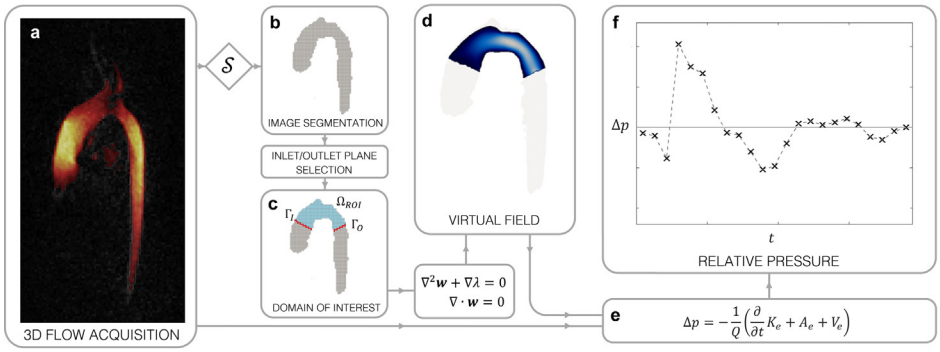

Figure 4.8: Processing step of **ν**WERP going from (a) acquired flow data, (b) segmented flow domain, (c) selection of inlet and outlet planes, (d) computation of virtual field, (e) assessment of virtual work-energy components, and (f) generated relative pressure trace.

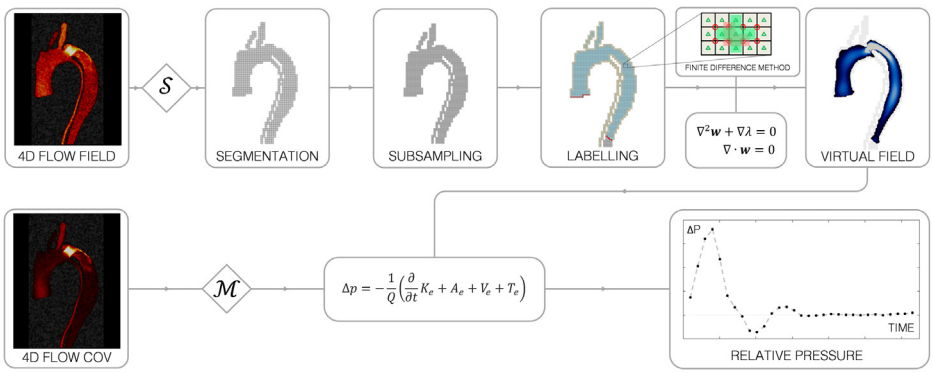

Figure 4.9: Processing step of **ν**WERP-t, similar to **ν**WERP in Figure 4.8 however with inclusion of acquired covariance data, which after diagonal masking is included in the energy balance to generate a relative pressure trace.

b) Noise filtering

With flow domain segmented, spatial noise filtering is incorporated into the νWERP method. Specifically, a *k*-order 3D polynomial fitting is used to approximate the signal within a defined voxel neighbourhood, with optimal filter settings (interpolation order and kernel size) defined by translating the estimated data noise level to a simplified 1D sinusoidal signal.

For νWERP-t, additional covariance filtering is applied. Specifically, negative diagonal entries of the Covariance matrix were removed in order to avoid non-physical entries (i.e. keeping strictly positive fluctuations of Cov[v_i, v_i] for i = 1,2,3).

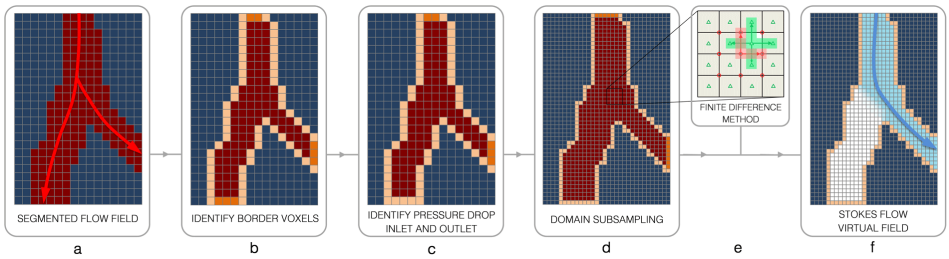

Figure 4.10: Computation of virtual field, $\boldsymbol{w}$, from segmented flow data. (a) Segmented flow domain, (b) Labelling of domain voxels, (c) Identification of inlet and outlet planes of interest, (d) Domain subsampling, (e) Virtual field computation by a FDM approach, (f) Output virtual field.

c) Virtual field computation

A fundamental component of vWERP is the computation of $\boldsymbol{w}$, outlined in Figure 4.10. The process is initiated by a labelling of the fluid domain, where all voxels within the field-of-view is marked as being either interior (entirely within the fluid domain), exterior (voxels being entirely outside the fluid domain), inlet/outlet (voxels being within the inlet/outlet planes), or wall voxels (separating interior and exterior domain, but not belonging to inlet or outlet), respectively. Using this labelling, appropriate boundary conditions can be set in the computation of $\boldsymbol{w}$.

Prior to the computation of $\boldsymbol{w}$ a domain subsampling is then performed. Specifically, the input data base-discretisation is subdivided by a chosen integer value, converting a single image voxel into several uniformly distributed nodal points. This operation is added to improve the accuracy of $\boldsymbol{w}$, and is complemented by an additional subsampling of $\boldsymbol{v}$.

With domain, labelling, and sub-sampling introduced, boundary conditions from Equation 4.22 are transferred onto appropriate nodal points, and $\boldsymbol{w}$ is solved numerically using a Finite Difference Method (FDM) with a staggered grid approach [367]. For efficient computation, an iterative solver based on the BFBT-preconditioning method [368] is additionally deployed (for specific details, please see [63]).

d) vWERP discretisation and operator estimation

For a numerical realisation, discretisation of the energy terms of Equation 4.19 has to be introduced. Since we are dealing with a voxelised version of Ω (denoted as Ω_{ROI} with corresponding inlet plane, outlet plane, and normal vectors $\Gamma_{I,ROI}$, $\Gamma_{O,ROI}$, and $\boldsymbol{N}$, respectively), we compute separate energy terms by evaluating $\boldsymbol{v}$ and $\boldsymbol{w}$ at each voxel (i, j, k) as

$$K_e(\boldsymbol{v},\boldsymbol{w}) = \rho dV \sum_{(i,j,k)\ \epsilon\ \Omega_{ROI}} \big(\boldsymbol{v}(i,j,k)\cdot\boldsymbol{w}(i,j,k)\big) \tag{4.35}$$

$$A_e(\boldsymbol{v},\boldsymbol{w}) = \rho dV \sum_{(i,j,k)\ \epsilon\ \Omega_{ROI}} \Big(\big(\boldsymbol{v}(i,j,k)\cdot G(\boldsymbol{v})(i,j,k)\big)\cdot\boldsymbol{w}(i,j,k)\Big) \tag{4.36}$$

$$V_e(\boldsymbol{v},\boldsymbol{w}) = \mu dV \sum_{(i,j,k)\ \epsilon\ \Omega_{ROI}} \big(G(\boldsymbol{v})(i,j,k) : G(\boldsymbol{w})(i,j,k)\big) \tag{4.37}$$

$$Q(\boldsymbol{w}) = dS \sum_{(i,j)\ \epsilon\ \Gamma_{O,ROI}} \big(\boldsymbol{w}(i,j)\cdot\boldsymbol{N}(i,j)\big), \tag{4.38}$$

where $dS = \prod_{i=1}^{2}\Delta x_i$ and $dV = \prod_{i=1}^{3}\Delta x_i$ are the pixel surface and voxel volume, respectively, based on the voxel length Δx in each spatial dimension. $G(\cdot)$ is the spatial gradient, operating on either $\boldsymbol{w}$ or the smoothed version of $\boldsymbol{v}$, respectively.

For νWERP-t, the incorporated turbulent energy dissipation term can be similarly discretised as

$$T_e(\boldsymbol{v},\boldsymbol{w}) = -\rho dV \sum_{(i,j,k)\ \epsilon\ \Omega_{ROI}} \big(\mathrm{Cov}[\boldsymbol{v},\boldsymbol{v}](i,j,k) : G(\boldsymbol{w})(i,j,k)\big) \tag{4.39}$$

using the same indexing as before.

With the above, the relative pressure can be estimated as for νWERP as

$$\Delta p_{t+\frac{1}{2}} = -\frac{1}{Q(\boldsymbol{w})}\left(\frac{\partial}{\partial t}K_e\big(\boldsymbol{v}_{t+\frac{1}{2}},\boldsymbol{w}\big) + A_e\big(\boldsymbol{v}_{t+\frac{1}{2}},\boldsymbol{w}\big) + V_e\big(\boldsymbol{v}_{t+\frac{1}{2}},\boldsymbol{w}\big)\right), \tag{4.40}$$

or for νWERP-t as

$$\Delta p_{t+\frac{1}{2}} = -\frac{1}{Q(\boldsymbol{w})}\left(\frac{\partial}{\partial t}K_e\big(\boldsymbol{v}_{t+\frac{1}{2}},\boldsymbol{w}\big) + A_e\big(\boldsymbol{v}_{t+\frac{1}{2}},\boldsymbol{w}\big) + V_e\big(\boldsymbol{v}_{t+\frac{1}{2}},\boldsymbol{w}\big) + T_e\big(\mathrm{Cov}_{t+\frac{1}{2}},\boldsymbol{w}\big)\right), \tag{4.41}$$

where central difference estimates of both $\boldsymbol{v}$, $\mathrm{Cov}[\boldsymbol{v},\boldsymbol{v}]$, and all spatial and temporal gradients are utilised to improve temporal accuracy.

4.2.5. Method evaluation and validation

In this thesis, νWERP was implemented and studied in a few different setups:

i) First, νWERP was tested *in-silico* to evaluate method performance in a set of challenging patient-specific cases, as well as to map spatiotemporal convergence behaviour as a function of image noise. This was performed as a first part of Study V.

ii) Second, νWERP was tested *in-vivo* to evaluate the methods clinical performance, as well as to validate it against invasive catheter measurements. This was performed as a second part of Study V.

iii) Lastly, the extension of νWERP-t into turbulent flows was evaluated *in-silico* as well as *in-vitro* in a controlled flow phantom setup, again validating method output against simulated or invasive measurements. This was performed in Study VI.

Below follows a brief overview of the different test-beds.

a) In-silico evaluation of νWERP

To evaluate νWERP performance, two different cardiovascular pathological conditions were studied *in-silico*: one model of a coarctation of the aorta (CoA) [369], and one model of an acute type B aortic dissection (AAD) [177]. In both cases, the models originated from image-based patient-specific computational fluid dynamics (CFD) analysis, where simulation output was used as input for the νWERP analysis. Importantly, with complete 4D pressure fields generated as an output from the CFD analysis, a defined ground-truth existed for the performed νWERP evaluation.

To mimic realistic imaging sampling, both models were spatiotemporally projected to resolutions of common 4D flow MRI acquisitions (voxel size: 2 mm^3, with 22 and 32 temporal phases over one cardiac cycle for CoA and AAD, respectively).

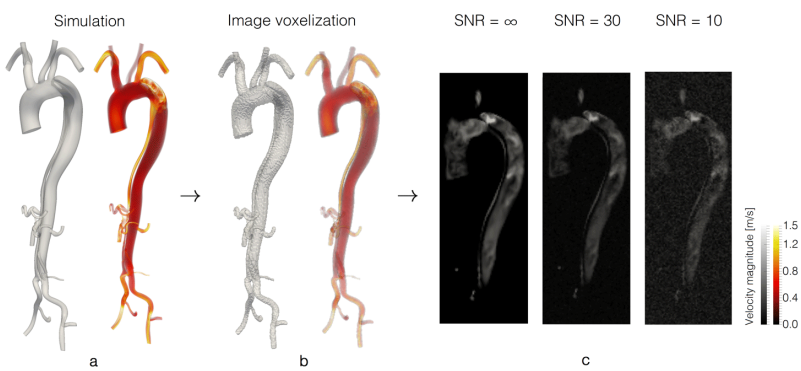

Figure 4.11: Generation of synthetic image data, based on simulated CFD output. (a) Simulation output. (b) Voxelised equivalent. (c) Cut-through images at three different noise levels.

Image noise was added at two different noise levels (SNR = 10 and 30, respectively), generating a set of 100 different flow fields at each noise level, with each model subsequently fed into the νWERP analysis pipeline. An overview of this process is given in Figure 4.11.

In each model, relative pressure was computed from aortic inlet to six different, arbitrarily chosen outlets. Importantly, outlets were chosen at several different bifurcating positions, specifically to extend beyond the application field of previously proposed method for non-invasive relative pressure estimations.

For the AAD model, effects of varying spatiotemporal sampling was also evaluated. This was done by generating models with varying spatial resolution (1-3 mm^3) and temporal resolution (8-64 phases), and evaluating relative pressure over a set of defined inlet and outlet planes. Again, each set was evaluated without noise, as well as at noise levels of SNR = 10 and 30, respectively.

For all cases, mean error between νWERP and the ground-truth CFD pressure field was quantified as

$$\varepsilon_{\Delta p} = \left(\frac{\sqrt{\sum_{n=1}^{N} (\Delta p_W|_n - \Delta p|_n)^2}}{\sqrt{\sum_{n=1}^{N} \Delta p|_n^{\,2}}} \right) \cdot 100, \tag{4.42}$$

where $\Delta p_W|_n$ is the νWERP estimate at a discrete time step t_n and $\Delta p|_n$ is the corresponding true data closest to the νWERP estimate within $t_{n-1} < t < t_{n+1}$.

In both *in-silico* models, νWERP output was also compared against alternative relative pressure methods, being Bernoulli (Equation 3.3), unsteady Bernoulli (Equation 3.6), and WERP (Equation 3.55), respectively. For a review of these methods, please see Section 3.1.4.

b) In-vivo validation of νWERP

To validate its clinical applicability, νWERP was also compared against gold-standard catheter-based invasive pressure measurements in a defined clinical cohort. Specifically, 4D flow MRI (Philips Achieva 1.5T, voxel size: 2 mm^3, 22 temporal phases) was acquired on a cohort of five anaesthetised adolescent patients with complex congenital heart disease. Absolute invasive pressures were recorded at ascending, mid-descending, and diaphragm level of the aorta, in each patient, respectively. From the pressure traces, relative pressures were computed by ECG-correlation, and subsequently compared to νWERP output. As previously, mean errors were computed by Equation 4.42, with root mean square error, ε_{rms}, and error at peak pressure, $\varepsilon_{\Delta p_{max}}$, additionally calculated as

$$\varepsilon_{rms} = \sqrt{\frac{\sum_{n=1}^{N} (\Delta p_{vWERP}(t_n) - \Delta p(t_n))^2}{N}} \cdot 100 \tag{4.43}$$

$$\varepsilon_{\Delta p_{max}} = \left| \frac{\Delta p_{W,max} - \Delta p_{max}}{\Delta p_{max}} \right| \cdot 100. \tag{4.44}$$

c) In-vitro evaluation of vWERP-t

To evaluate the accuracy of the νWERP-t, a series of steady-state turbulent flow cases were assessed. Specifically, a previously published dataset consisting of seven 3D-printed aortic valve phantoms was utilised, where turbulent flow fields had been imaged using 4D flow MRI with six-directional icosahedral flow encoding (ICOSA6) [317]. By so, both mean field flow quantities and incoherent, turbulence-driven flow fluctuations had been mapped. For each phantom, datasets were available at four different flow rates, with invasive pressure measurements obtained from installed pressure ports within the custom-made flow circuit. A visualisation of flow field, covariance, and virtual field is provided in Figure 4.12.

For each valve and flow rate, relative pressures were computed using νWERP-t and νWERP. For comparison, an extended WERP-t method was employed (using $\boldsymbol{w} = \boldsymbol{v}$ in νWERP-t), as well as the original WERP formulation (Equation 3.55). Additionally, the turbulence production method formulated in Equation 3.57, TP, was also employed as this had been specifically tested on the same phantom dataset in [317]. Important however, is that in [317], the TP method had been employed together with an additional covariance filtering where

$$-\mathrm{Cov}[\boldsymbol{v}, \boldsymbol{v}] : \nabla \boldsymbol{V} = \sum_{\alpha=1}^{3} \sum_{\beta=1}^{3} \max \left(-\mathrm{Cov}[\boldsymbol{v}_\alpha, \boldsymbol{v}_\beta] \frac{\partial \boldsymbol{V}_\alpha}{\partial X_\beta}, 0 \right), \tag{4.45}$$

at each voxel (i, j, k), effectively removing all negative integral arguments in Equation 3.57 from the relative pressure computations. Consequently, this masking was incorporated into the TP method when used in Study VI.

For all methods, accuracy was assessed for all methods using linear regression analysis between predicted and true relative pressure. Additionally, Bland-Altman plots were derived to evaluate potential bias in the relative pressure predictions.

d) In-silico evaluation of vWERP-t

To expand on the steady-state *in-vitro* phantoms, vWERP-t was also applied on a transient flow case. Specifically, the patient-specific *in-silico* AAD from the *in-silico* validation of vWERP was utilised, however with output generated over 10 consecutive cycles to initiate potential turbulent flow fluctuations.

From the simulated data, mean field and covariance data were generated in two sets: one derived from the first 3 cycles, representing an initiation phase with enhanced flow covariance, and one derived from the last 7 cycles, representing a more quasi-periodic flow with less pronounced flow covariance. For both sets, relative pressures were derived from the aortic outlet to an approximate 180° bend of the descending false lumen of the thoracic aorta. A visualisation of the flow field, covariance, and corresponding virtual field is provided in Figure 4.13.

As with the *in-vitro* cohort, relative pressure estimations were performed using vWERP-t, vWERP, WERP-t, WERP, and TP, respectively.

Accuracy was assessed using linear regression analysis between predicted and true relative pressure together with corresponding Bland-Altman plots. Mean errors over the entire simulated cardiac cycle were also derived using Equation 4.42.

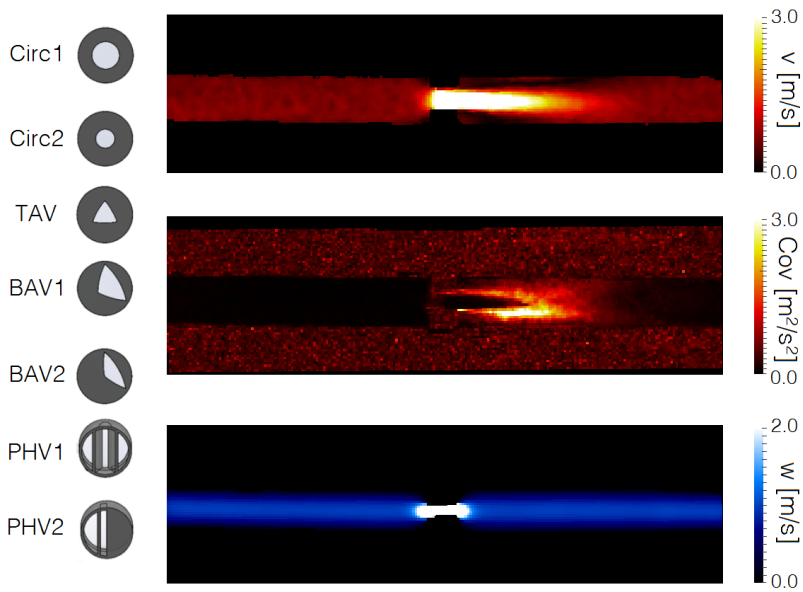

Figure 4.12: Different valve configurations (left) and example of mean field (upper), covariance (middle), and virtual field (lower) for the stenotic flow phantoms in Study VI.

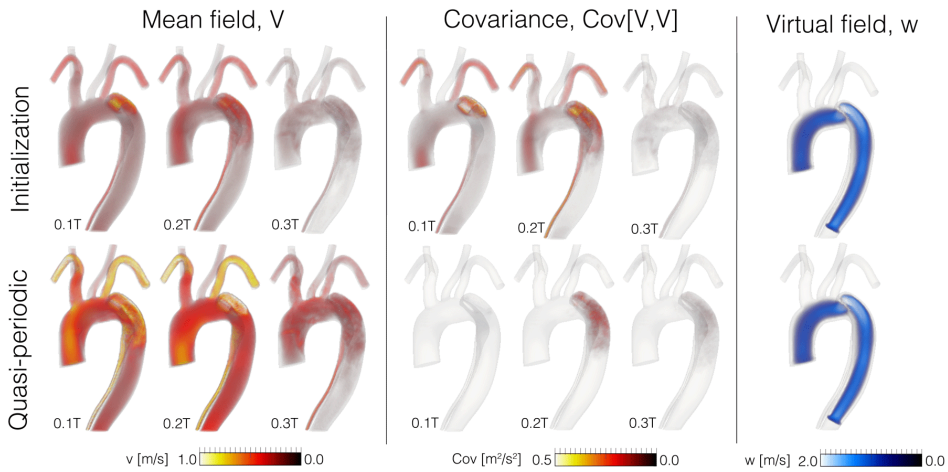

Figure 4.13: Mean field (left), covariance (middle), and virtual field (right) for the initialisation (upper row) and quasi-periodic phase (lower row) of the AAD *in-silico* data used in Study VI.

4.2.6. Clinical *in-vivo* analysis

Building on the findings from the method evaluation, νWERP was applied in a final clinical study. In Study VII, aortic hemodynamics was evaluated in a DCM cohort, evaluating potential aortic changes in cardiac disease.

a) Study population

14 patients treated for moderate DCM-related heart failure, and 16 healthy subjects were enrolled for the study, all participating under informed consent as approved by the Regional Ethics Committee, South East London, United Kingdom (REC, 12/LO/1456). The inclusion criteria were ≥18 years, suspected or known non-ischemic DCM-related heart failure (NYHA class III, using beta blockers), and the exclusion criteria were airway disease (asthma, chronic obstructive pulmonary disease, bronchitis), pregnancy, renal or hepatic impairment, previous history of angina or cardiac arrhythmias for which beta blockers were necessary, and known contraindications to MRI. Subject demographics are provided in Table 4.4.

Note that prior to imaging and data collection, the DCM subjects had their beta blocker treatment discontinued for 48 hours (this to study the response to esmolol administration as part of an independent side study).

Table 4.4: Subject characteristics for the patient cohort of Study VII. P-values were derived using a Mann-Whitney test or, in the case of nominal data, a χ^2 test.

Demographics	Volunteers (n = 16), mean ± SD or n (%)	DCM patients (n = 14), mean ± SD or n (%)	p-value
Age, yrs	42.4 ± 12.4	47.8 ± 10.7	0.23
Weight, kg	72.3 ± 14.9	82.3 ± 19.7	0.07
Height, cm	173.0 ± 8.7	167.9 ± 8.1	0.14
Body surface area, m^2	1.85 ± 0.23	1.96 ± 0.28	0.15
Male/Female, n/n	9 / 7	7 / 6	0.73

b) Imaging, data collection, and data processing

For each subject, a range of image-based and non-invasive data was collected:

i) Cardiac functional imaging.

To assess cardiac efficiency and anatomy, cine steady-state free precession (SSFP) MRI (retrospective ECG triggering, spatial resolution ~2x2x8 mm^3, temporal resolution ~20 ms) and 3D tagged MRI (prospective ECG triggering, spatial resolution ~3.4x7.7x7.7 mm^3, temporal resolution ~30 ms) was acquired on all subjects (ACHIEVA 1.5 Tesla, Philips Healthcare Best, The Netherlands). Left and right ventricular volumes and functional output metrics (EF, SV, CO, cardiac index (CI)) were calculated by manually delineating the ventricles at end systole and diastole in short-axis stacks (CVI software, Circle Cardiovascular Imaging Inc, Alberta, Canada).

ii) Vascular flow imaging and aortic relative pressure

In direct sequence to the cardiac imaging, 4D flow MRI was acquired (prospective ECG triggering, spatial resolution ~2.5 mm^3, temporal resolution ~30 ms, velocity encoding ~120 - 190 cm/s). With the thoracic aorta segmented using available in-house software, aortic relative pressures were derived using νWERP from the left ventricular outflow tract (LVOT) down to the diaphragm-level of the descending aorta. To quantify the output traces, three relative pressure metrics were derived: maximum relative pressure over the entire cardiac cycle, minimum relative pressure over the entire cardiac cycle, and time-to-peak relative pressure (TTP), respectively (an illustration of the three metrics is given in Figure 4.14).

Aortic PWV was derived by assessing the transit time between through-plane flow traces at LVOT and the diaphragm descending aorta [370], and, using these values, aortic stiffness estimates were calculated by the Moens-Korteweg equation [289].

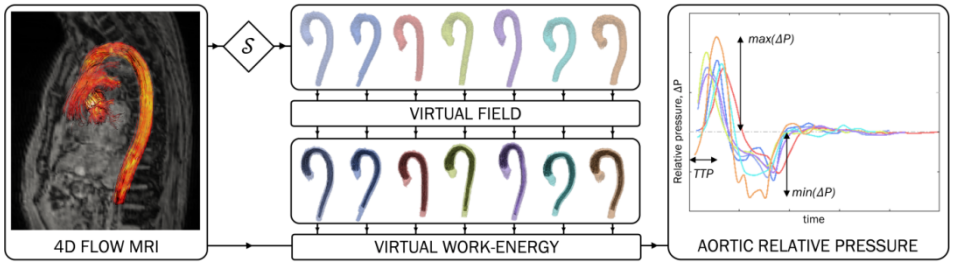

Figure 4.14: **v**WERP overview for Study VII. From each subject, maximum relative pressure, minimum relative pressure, and time-to-peak relative pressure (TTP) was quantified, as illustrated on the right.

iii) Central blood pressure estimation

Non-invasive central blood pressure was derived from brachial sphygmomanometer cuffing using dedicated clinical equipment (Centron cBP30, SunTech Medical Inc., Morrisville, NC, USA), where cuff-based measured are converted into central blood pressure estimates by means of optimised transfer functions [371].

c) Reference virtual cohort analysis

As a reference complement to the *in-vivo* analysis, and in order to isolate the independent influence of certain cardiovascular properties on aortic relative pressure, 1D simulations of aortic relative pressure were performed on a customised virtual cohort. The cohort was created by solving a system of 1D blood flow equations through a validated systemic circulatory model [372, 373], with cardiac and aortic anatomy and function adapted to patient-specific values derived from the imaging study.

Using the virtual cohort, aortic relative pressures were derived as a function of varying cardiac or aortic properties, respectively. Specifically, the independent influence of SV, heart rate, arterial peripheral resistance, aortic stiffness, and aortic area was evaluated by varying these entities independently around the virtual cohort mean. By so, the isolated influence from these five entities could be defined for each clinical subgroup, respectively.

d) Data analysis

Statistical differences in subject characteristics were evaluated using a Mann-Whitney U-test (continuous data) or χ^2 test (nominal data), both with significance inferred at $p < 0.05$. Differences in cardiac and arterial output metrics were also evaluated using a Mann-Whitney U-test, with significance inferred at $p < 0.05$. For all cases, potential outliers were assessed by the Tukey's fences method [374].

To this, correlation analysis between subject characteristics and derived aortic relative pressure metrics were performed by assessing the Pearson correlation coefficient (correlation defined at $|R| > 0.5$ and $p < 0.05$).

4.3. Tomographic reconstruction for pre-clinical imaging

As a final part of the thesis, a research paper has been written within pre-clinical imaging and X-ray tomographic reconstruction.

4.3.1. Study overview

In contrast to the other parts of the thesis, the work on tomographic reconstruction is represented by a single paper. The work is not aimed at any particular application area, however specific examples for cardiovascular evaluations are provided.

In general, a majority of the evaluations are performed on numerical *in-silico* phantoms, with some experimental *in-vitro* and *ex-vivo* tests added to complement the aforementioned evaluations.

4.3.2. Theory and method derivation

In this work a method for tomographic *multigrid* reconstruction is developed, where data from a single acquisition is reconstructed in multiple domains, using either different levels of spatial discretisation, numerical regularisation, or a combination of the two.

As outlined in Section 3.3.3., in X-ray tomographic image reconstruction we are dealing with recovering a function f based on observed data g and a descriptive forward operator A (generically connected by Equation 3.31). For medical purposes we typically seek to find f on a reconstruction domain $\Omega \subset \mathbb{R}^d$ where $d \in \{2,3\}$.

For the sake of multigrid reconstruction, consider an ROI $\Omega_1 \subset \Omega$ and a complement $\Omega_0 = \Omega \backslash \Omega_1$. With the two mapping the entire reconstruction domain, this means that

$$\begin{cases} \Omega_0 \cap \Omega_1 = \emptyset \\ \Omega_0 \cup \Omega_1 = \Omega \end{cases}. \tag{4.46}$$

An identical domain splitting can also be extended onto the sought after f by introducing *masked* functions

$$f_i(x) = \begin{cases} f(x), & \text{if } x \in \Omega_i \\ 0, & \text{otherwise} \end{cases}, \qquad i = 0,1. \tag{4.47}$$

We can then re-express our inverse problem from Equation 3.31 (neglecting noise) in the form of masked functions such that

$$g = Af = A(f_0 + f_1) = Af_0 + Af_1, \tag{4.48}$$

noting that this holds for any linear operator, or alternatively for any pointwise nonlinear operators A. Figure 4.15 shows a visualisation of this domain partitioning.

Similar splitting can be performed on the adjoint A^*. However, as Ω is part of the range of A^*, the splitting is performed post-hoc such that

$$A^*g = (A^*g)_0 + (A^*g)_1. \tag{4.49}$$

If applying this onto the normal equation (Equation 3.33), we see that

$$A^*Af = A^*g \qquad \Longleftrightarrow$$

$$A^*(Af_0 + Af_1) = A^*g \qquad \Longleftrightarrow$$

$$\begin{aligned} &(A^*Af_0)_0 + (A^*Af_0)_1 + (A^*Af_1)_0 + (A^*Af_1)_1 \\ &\quad = (A^*g)_0 + (A^*g)_1. \end{aligned} \tag{4.50}$$

If we in the above separate terms acting on different domains, we can rewrite the above as an equation system such that

$$\begin{matrix} (A^*Af_0)_0 + (A^*Af_1)_0 \\ (A^*Af_0)_1 + (A^*Af_1)_1 \end{matrix} = \begin{matrix} (A^*g)_0 \\ (A^*g)_1 \end{matrix}. \tag{4.51}$$

As seen and following the off-diagonal terms there will be a defined cross-talk between the different domains, where errors in f_0 will influence f_1 and vice versa.

It can also be shown that the expression in Equation 4.51 can be extended into regularised approaches, such as the general variational method given in Equation 3.34. For such, the split equation system is given by

$$\begin{matrix} (A^*Af_0)_0 + (A^*Af_1)_0 + \lambda_0 S(f_0) \\ (A^*Af_0)_1 + (A^*Af_1)_1 + \lambda_1 S(f_1) \end{matrix} = \begin{matrix} (A^*g)_0 \\ (A^*g)_1 \end{matrix}, \tag{4.52}$$

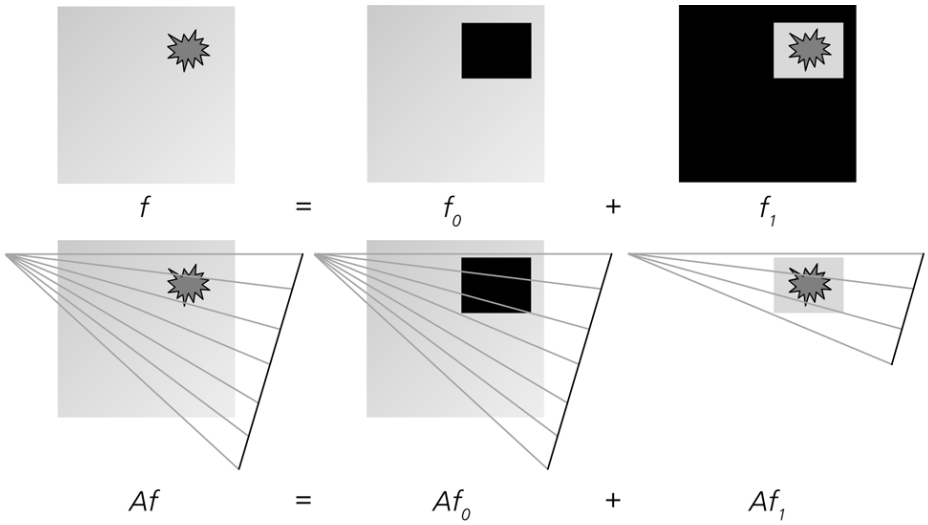

Figure 4.15: Simplified illustration of multigrid domain partitioning, showing how the disjoint Ω_0 and Ω_1 can be represented by masked functions f_0 and f_1. For linear, or pointwise non-linear operators, the partitioning can be similarly translated onto the forward problem.

where $S(f_i)$ represents the split subgradient of the variational approach. By so, Equation 4.52 also opens up for multigrid regularisation, where separated regularisation is achieved when $\lambda_0 \neq \lambda_1$.

4.3.3. Numerical implementation

With theory provided in Section 4.3.2., the domain splitting approach for multigrid reconstruction is implemented as a Python sub-library to the Operator Discretisation Library (ODL, https://github.com/odlgroup/odl). Implementation specifics can be found under the github repository https://github.com/kohr-h/odl-multigrid/. To exemplify the simplicity of use, below follows a pseudo-code comparison between conventional and multigrid discretisation reconstruction, both using typical implementation logic of ODL

Conventional reconstruction	Multigrid reconstruction

`# Define discretisation`
`reco_space = ...`
	`# Define discretisations`
	`coarse reco space = ...`
	`fine reco space = ...`
	`insert reco space =`
	`  insert_discr(coarse_reco_space,`
	`  fine_reco_space,`
	`  ...)`

`# Define geometry`
`angle partition = ...`
`detector_partition = ...`
`geometry =`
`  FanFlatGeom(angle part,`
`  detector part,`
`  ...)`
	`# Define geometry`
	`angle partition = ...`
	`detector_partition = ...`
	`geometry =`
	`  FanFlatGeom(angle part,`
	`  detector part,`
	`  ...)`

`# Define forward operator`
`ray trafo =`
`  RayTrafo(geometry,`
`  reco_space,`
`  ...)`
	`# Define forward operators`
	`coarse ray trafo =`
	`  RayTrafo(geometry,`
	`  coarse_reco_space,`
	`  ...)`
	
	`insert ray trafo =`
	`  RayTrafo(geometry,`
	`  insert_reco_space,`
	`  ...)`

	`# Define masking operator`
	`masking_operator =`
	`  MaskingOp(coarse_reco_space,`
	`  insert reco space,`
	`  ...)`
	
	`masked_coarse_ray_trafo =`
	`  coarse_ray_trafo * masking_operator`

	`# Create reduction operator`
	`sum ray trafo =`
	`  ReducOp(masked_coarse_ray_trafo,`
	`  insert_ray_trafo,`
	`  ...)`

`# Define reconstruction`
`# operator`
`reco_op = RecoOp(ray_trafo,`
`  ...)`
	`# Define reconstruction`
	`# operator`
	`reco_op = RecoOp(sum_ray_trafo, ...)`

`# Reconstruction` `reco = reco_op(data)`	`# Reconstruction` `reco = reco_op(data)`

As seen, domain splitting is achieved either by operator masking (`MaskingOp`) or by limiting the acting operator domain (`insert_ray_trafo` is limited to the domain defined by the `insert_discr`). Further, by invoking a reduction operator (`ReducOp`, identical to Equation 4.51), the multigrid approach is brought back into the general framework of ODL, where any reconstruction operator or optimisation scheme can be invoked.

4.3.4. Method evaluation

To evaluate the performance of the proposed multigrid reconstruction approach, a series of numerical and experimental tests were performed.

a) In-silico evaluation

For the *in-silico* evaluation, tomographic image data was simulated from a Shepp-Logan phantom using line-integral forward projection with a pixel discretisation of 400^2 and Gaussian noise with a standard deviation of 10%.

Three scenarios were evaluated

i) *Piecewise discretisation*, reconstructing at different levels of spatial discretisation, evaluating discretisation ratios of 1:1, 1:2, 1:4, 1:8, and 1:16 between the two different domains.

ii) *Piecewise regularisation,* reconstruction at different levels image regularisation, evaluating regularisation ratios of 10:1, 1:1, 0.1:1, 0.01:1, and 0.001:1 between the two different domains (baseline $\lambda = 8 \cdot 10^{-3}$).

iii) *Piecewise discretisation and regularisation*, combining i) and ii), evaluating ranging discretisation (1:1 to 1:16) at a regularisation ratio of 0.1:1.

In all cases, ROI was empirically set around the three dorsal inserts of the Shepp-Logan phantom.

For all cases, reconstruction quality was assessed by the Euclidean distance k between reoncstruction f and ground truth f_{true}, defined as

$$k = \int_{\Omega} \|f - f_{true}\|_2^2 dx, \tag{4.53}$$

as well as the structural similarity index (SSIM), given by

$$SSIM(f, f_{true}) = \frac{\left(2\mu_f \mu_{f_{true}} + c_1\right)\left(2\sigma_{f f_{true}} + c_2\right)}{\left(\mu_f^2 + \mu_{f_{true}}^2 + c_1\right)\left(\sigma_f^2 + \sigma_{f_{true}}^2 + c_2\right)}, \tag{4.54}$$

with μ and σ being the mean and variance of f and f_{true}, and c_1 and c_2 are conventionally used stabilising coefficients [375]. Additionally, an assessment of computation time on a single NVIDIA TITAN X GPU was also performed in all three cases, with the number of pixels increased from 400^2 to 12800^2.

b) Experimental evaluation

In addition to the numerical examples, multigrid reconstruction was also attempted on experimentally acquired micro-CT data.

As in Study III of the SWE-analysis, an in-house micro-CT system with a microfocus X-ray source (Hamamatsu MX-L10951-04, focal spot size: 15-80 μm),

a CMOS flat panel (Hamamatsu C7942CA-22, total area: 12 cm^2, pixel size: 50 μm^2, frame grabber (EPIX PIXCI D2X-C7942), and a steering gantry was utilised. From each acquisition, data was converted into standardised openCT format [376], with calibrations introduced for detector misalignment, detector lag effect, and defective detector pixels.

Three objects were imaged in the micro-CT setup:

i) *Low contrast calibration phantom*, used to identify low-contrast inserts of varying image contrast (4% and 8% contrast, respectively).
ii) *Ex-vivo atherosclerotic plaque*, used to exemplify the clinical usage of the proposed multigrid reconstruction approach.
iii) *3D-printed CT angiography of the thoracic cavity*, used as a second example of the usability of the approach, evaluating arbitrarily chosen ROIs within the field-of-view.

In all cases, image quality was assessed either on a basis of retrieved contrast (low contrast calibration phantom), or by mere qualitative visual inspection.

Chapter 5

Results

5.1. Vascular shear wave elastography

Study I: *Vascular shear wave elastography – method accuracy and stiffness reconstruction*

a) Fundamental geometries

For the geometrical phantoms of Study I, shear modulus estimation using three different estimation approaches is presented in Figure 5.1. Specifically, estimation using direct group velocity reconstruction, leaky Lamb-wave-based estimation using full bandwidth phase velocity, and leaky Lamb-wave-based estimation using high-pass filtered phase velocity (allowing $f > 500$ Hz) are all presented.

Results show that utilising group velocity to directly estimate shear modulus leads to significant underestimation of shear modulus in the evaluated confined phantoms (mean average of 15.1 ± 0.2, 8.1 ± 0.1, and 6.7 ± 0.1 kPa for the three different geometries, respectively).

For the plate phantom, the full bandwidth phase velocity-based leaky Lamb-wave estimation rendered optimal results, with no statistical deviation inferred from the reference mechanical testing (30.1 ± 2.6 kPa versus reference 30.5 ± 0.4 kPa).

For the solid cylinder, none of the methods could accurately match the reference value, even if smallest deviation was observed against full bandwidth phase velocity estimates. However, for the hollow cylinder the high-pass filtered phase velocity approach rendered accurate results, with no significant difference in estimated shear modulus observed against the reference mechanical testing (30.6 ± 3.2 kPa versus reference 30.5 ± 0.4 kPa).

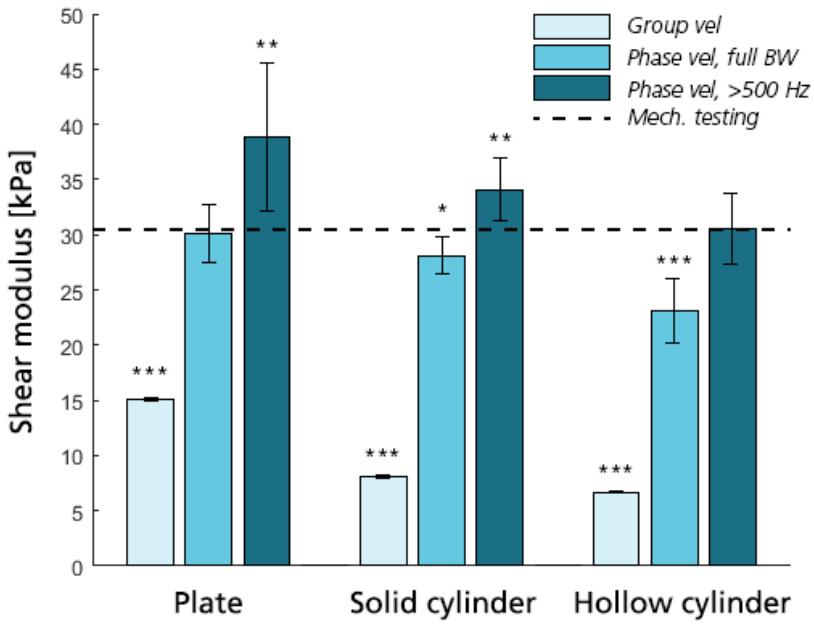

Figure 5.1: Elastic shear modulus estimation for the three different geometrical phantoms of Study I, calculated using three different estimation approaches (group velocity (light blue), full bandwidth (BW) phase velocity (medium blue), and phase velocities >500 Hz (dark blue)). Statistical difference from the mechanical testing reference (black dashed line) indicated as * ($p < 0.05$), ** ($p < 0.01$), or *** ($p < 0.001$).

b) Arterial phantoms

To validate the aforementioned findings, results from the pressurised arterial phantoms are provided in Figure 5.2. For the SWE-derived shear modulus, all values are calculated using the leaky Lamb-wave-based estimation with high-pass filtered phase velocity (allowing $f > 500$ Hz).

As seen, phantom shear modulus increased with increasing number of FT-cycles and intraluminal pressure, respectively. In general, good agreement was observed between SWE-derived measures and reference mechanical testing at all evaluated FT- and pressure levels, with a mean absolute error of 5.6 ± 4.1 kPa, corresponding to a relative error of 8.8 ± 6.0%.

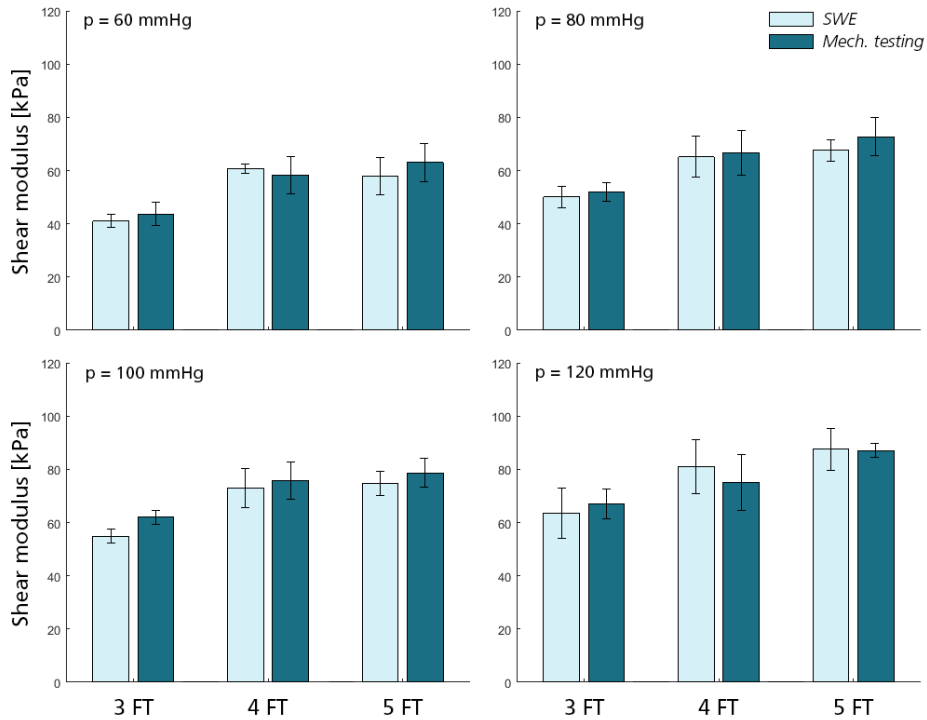

Figure 5.2: Elastic shear modulus estimation for the arterial phantoms (light blue), presented as a function of freeze-thaw (FT) cycles and intraluminal pressure (60, 80, 100, 120 mmHg), respectively. Reference mechanical testing values are also provided at each level (dark blue).

Study II: *Plaque characterisation by SWE – differentiability and accuracy*

a) Push location

Figure 5.3 shows SWE velocities as a function of push location, comparing values against reference velocities from a large cylindrical phantom. In this case, accuracy did not seem to improve as the push location was moved closer to the imaged phantom plaque. Instead, the most dominant difference is observed between longitudinal (push location 1-5) and transverse (push location 6-7) imaging plane, where a slightly higher underestimation seemed indicated in transverse view.

Group velocity was consistently underestimated regardless of push location. For the phase velocity, similar underestimation is apparent at lower frequencies (450-550 Hz), however with a distinct improvement apparent with increasing frequency. In particular, at the highest frequency band (950-1050 Hz) estimations are centred at an underestimation of -2%, compared to -18% and -4% at 450-500 Hz and 700-800 Hz, respectively.

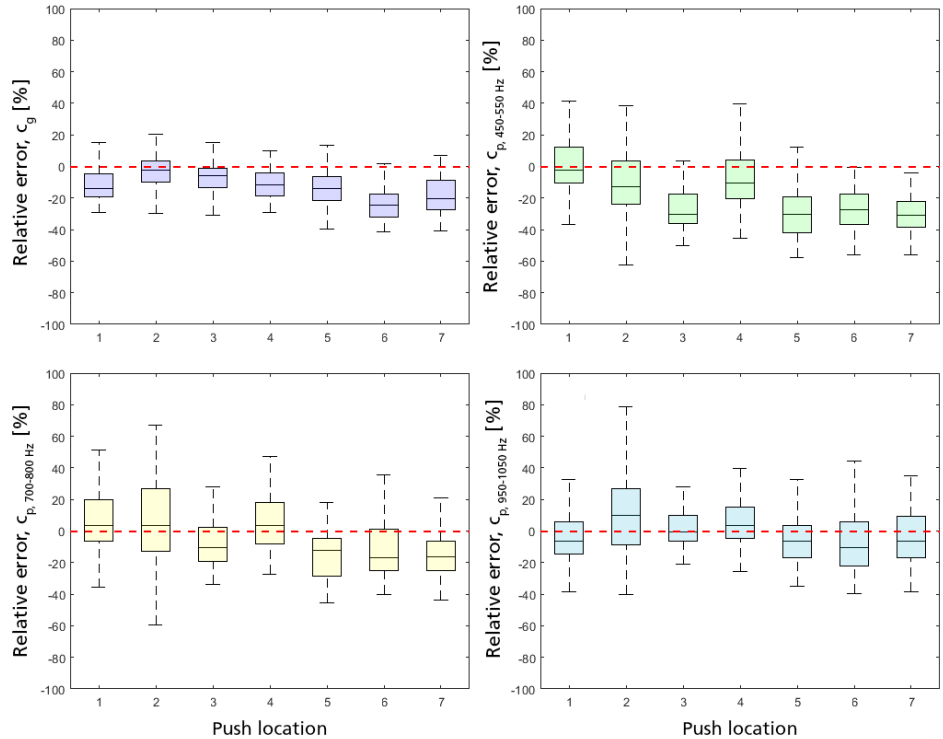

Figure 5.3: Accuracy of estimated SWE velocity as a function of push location, calculated as the relative error against reference unconfined SWE group velocity. Results are presented for group velocity (upper left), phase velocity at 450-550 Hz (upper right), phase velocity at 700-800 Hz (lower left) and phase velocity at 950-1050 Hz (lower right), respectively). Based on an ANOVA test with a Tukey post-hoc test for significance, all push locations differed significantly from each other apart from group velocity (1-3/4/5, 2-3, 3-4, 4-5, 5-7, 6-7), phase velocity 450-550 Hz (1-4, 2-4, 3-5/6/7, 5-6/7, 6-7), 700-800 Hz (1-2/4, 2-4, 3-5/6/7, 5-6/7, 6-7), and 950 – 1050 Hz (1-3/4/5/6/7, 2-3/4, 3-4/5/6/7, 4/7, 5-6/7, 6-7), respectively.

Albeit the underestimation, the group velocity estimates showed the lowest deviation out of the four evaluated metrics, with a standard deviation of approximately 11%, compared to 19, 21, and 20% for phase velocities at 450-550, 700-800, and 950-1050 Hz, respectively.

Regarding image quality, both SNR and maximum particle velocity increased as the push location was moved closer to the plaque. In particular, push location 3 (inside the anterior part of the plaque) rendered maximum SNR.

b) Differentiation of phantom plaques of varying stiffness

Figure 5.4 shows the summarised results for the assessed phantom plaques, with results separated as a function of plaque stiffness, as well as lumen size, lumen position, and plaque wall, respectively. For all plaque sizes, the results from the push location analysis are confirmed, where an underestimation of group velocity

seem apparent, with increasing accuracy seen with increase phase velocity frequency (comparing box plot output against the horizontal, red reference lines). Noteworthy, this underestimation seemed to increase with increasing phantom plaque stiffness, with an average group velocity underestimation of 0.4 m/s or 12% at 2FT-cycles, compared to 1.0 m/s or 18% at 5FT-cycles.

Despite the systematic underestimation, the ability to differentiate phantom plaques of different stiffness was strongest using group velocity analysis: out of the 18 evaluated group differences at different lumen sizes, 16 could be statistically inferred using group velocity. As a comparison, 7, 11, and 13 out of 18 could be differentiated using phase velocity at 450-500, 700-800, and 950-1050 Hz, respectively. Similar behaviour was also observed with varying lumen position and plaque wall, respectively, where group velocity again showed the highest ability to differentiate phantom plaques of different stiffness.

As a last result from Study II, Figure 5.5 shows SWE velocity estimates at different phantom plaque stiffness levels, given as a function of varying imaging plane. Again an underestimation is observed for group velocity and low-frequency phase velocity measures, with increasing accuracy seen at the highest frequency band (950-1050 Hz). Noteworthy, transverse imaging plane showed a more pronounced underestimation, with e.g. group velocity metrics showing a relative error of –9% versus -20% for longitudinal and transverse imaging, respectively.

With respect to differentiability, longitudinal imaging seemed superior to transverse imaging, where only 3 and 4FT-cycle phantom plaques could not be separated. Conversely, in transverse imaging, only group velocity estimation rendered comparable differentiation, with none of the stiffer plaques being distinguishable using phase velocity analysis.

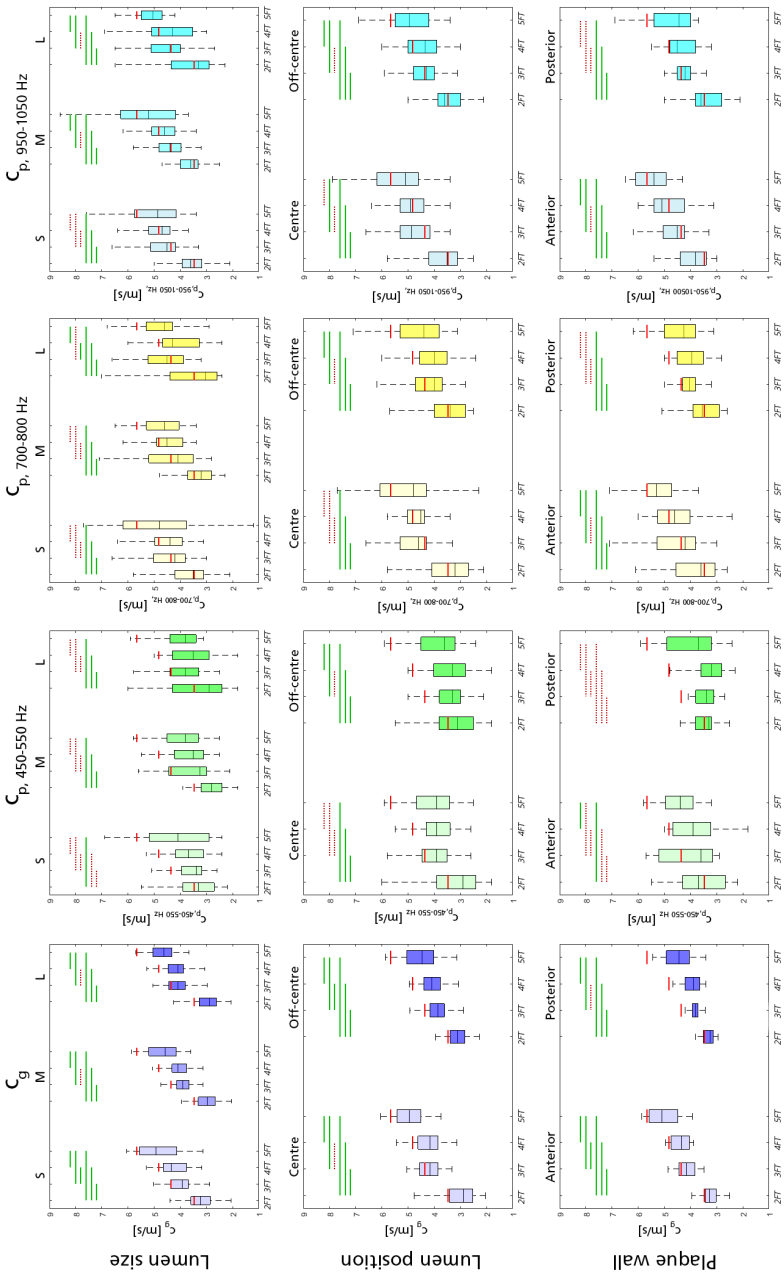

Figure 5.4: SWE results for different phantom plaque lumen size, position, and wall, respectively. Wave speeds given for group velocity, phase velocity at 450-550 Hz, phase velocity at 700-800 Hz and phase velocity at 950-1050 Hz, respectively. In each subfigure, results are given as a function of plaque stiffness (2-5 FT-cycles), with reference values in red. Statistical differences are inferred by the green horizontal bars, alternatively by the red dashed line if no difference could be inferred.

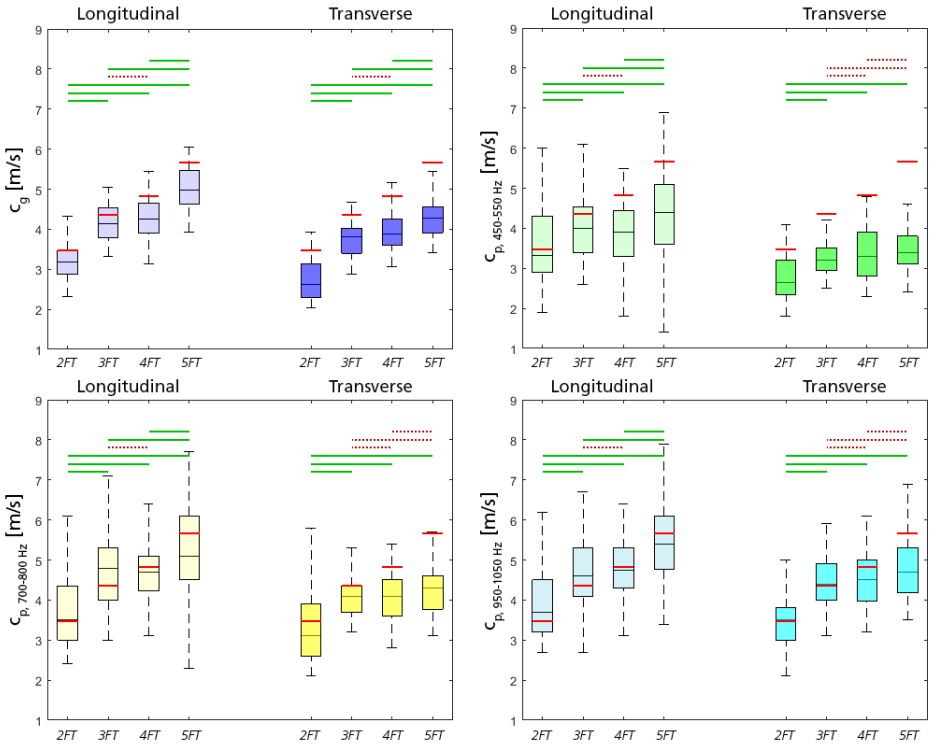

Figure 5.5: SWE results for different phantom plaques as a function of imaging plane. Results are presented in similar fashion to Figure 5.4.

Study III: *Experimental ex-vivo setup for SWE plaque assessment*

Figure 5.6 shows a reconstructed micro-CT image of the analysed endarterectomy specimen of Study III. As visually apparent, the specimen had a fairly irregular shape, covering almost the entire circumference of the intraluminal opening. At the anterior end, an approximately 2 mm calcified nodule could be identified. Soft tissue attenuation variations could also be seen in the vicinity of the nodule, however apart from that the micro-CT images seemed to indicate a fairly homogeneous plaque tissue specimen. Figure 5.6 also shows a B-mode image of the same plaque (delineated in orange), with acoustic push line (blue) and selected tracking depth (red) indicated. The reconstructed incremental displacement map is provided, with manually selected TTP-regions overlaid showing variations in the spatiotemporal wave front.

Starting from the push location, the wave seem to be travelling with a group velocity of 3.7 m/s, before increasing to 5.7 m/s after around 6 mm – a distance qualitatively corresponding to the calcified nodule visible in both B-mode and

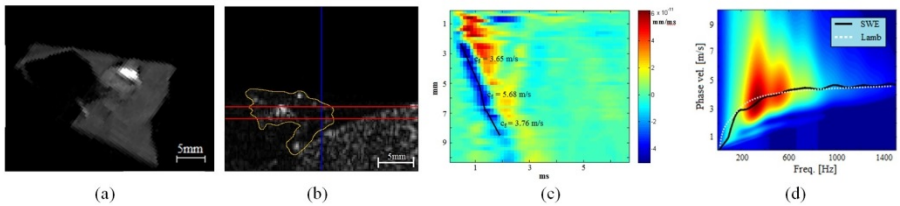

Figure 5.6: (a) longitudinal micro-CT reconstruction, (b) B-mode imaging with indicate push (blue) and tracking lines (red), (c) axial incremental displacement map, and (d) corresponding k-space and dispersion curve.

micro-CT image, respectively. Once having passed through the nodule, the group velocity retreats to its initial value of around 3.8 m/s.

With regards to phase velocity, the retrieved dispersion curve seemed to follow the dominant zero-order antisymmetric mode (A_0). As an example, the dispersion curve could be fairly well estimated by a full bandwidth leaky Lamb wave (white dashed line in Figure 5.6), with optimal fit given at a shear modulus of 36 kPa.

No valid data could be obtained in the transverse imaging plane.

Study IV: *In-vivo plaque characterisation by SWE – validation with MRI*

a) AHA type classification

In-vivo SWE and MRI were successfully performed in all but 2 subjects, rendering a total of 27 plaques for the final analysis. Out of these, AHA type III (n = 7), type V (n = 8), type VI (n = 8) and type VII (n = 4) plaques were identified. For these, group and phase velocities are provided in Figure 5.7.

AHA type VI plaques showed significantly higher group velocity in both longitudinal and transverse view, with a mean average of 5.8 m/s (longitudinal) and 7.3 m/s (transverse) compared to 4.0-4.2 m/s and 3.1-3.6 m/s for all other AHA types. This separation deteriorated when switching to phase velocity, even though a statistically significant differentiation could be observed at the highest frequency band (400-500 Hz) in longitudinal view (7.0 m/s versus 4.1-4.8 m/s).

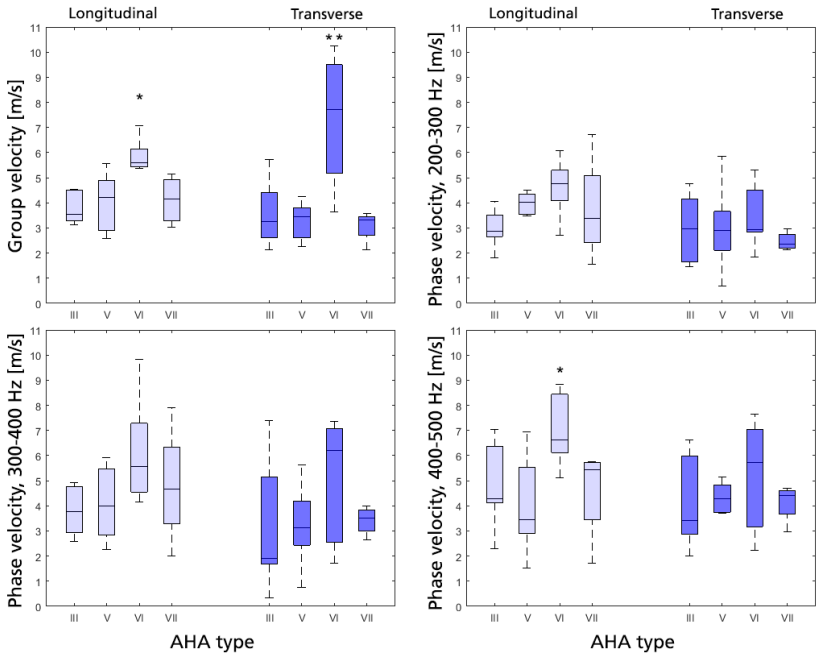

Figure 5.7: SWE group and phase velocity for the studied *in-vivo* cohort, classified according to plaque AHA type. Data is separated for longitudinal (light blue) and transverse (dark blue) imaging, respectively. Significance against all other groups is given as * ($p<0.05$) or ** ($p<0.01$).

b) Correlation analysis

Correlations for a few MRI-identified plaque parameters are provided in Figure 5.8. Specifically, the correlations are based on their apparent strength ($|R| > 0.5$, $p < 0.05$) as well as their relation to plaque stability.

For group velocity, positive correlation was observed against the amount of lipid-rich necrotic core in both imaging planes (Pearson $R = 0.57/0.58$, $p = 0.02/0.02$ for longitudinal/transverse imaging). Positive correlations were also observed with necrotic core volume (Pearson $R = = 0.60/0.62$, $p = 0.01/0.01$ for longitudinal/transverse imaging) as well as plaque cap volume; however in this case only seen in the longitudinal view (Pearson $R = 0.6$, $p = 0.02$).

For the phase velocity analysis, the number of correlated parameters increased with increasing frequency band, with a maximum of 4 correlations identified at 400-500 Hz. Specifically at 400-500 Hz, transverse imaging indicated negative nonlinear rank correlation to the ratio between fibrous cap and necrotic core volume (Spearman $R = -0.61$, $p = 0.02$), positive linear correlation against plaque calcification volume (Pearson $R = 0.64$, $p = 0.04$) and negative linear correlation against plaque loose matrix (Pearson $R = -0.64$, $p = 0.03$). Furthermore, at 300-

400 Hz longitudinal imaging indicated strong negative nonlinear rank correlation against plaque haemorrhage volume (Spearman R = -0.94, p = 0.02).

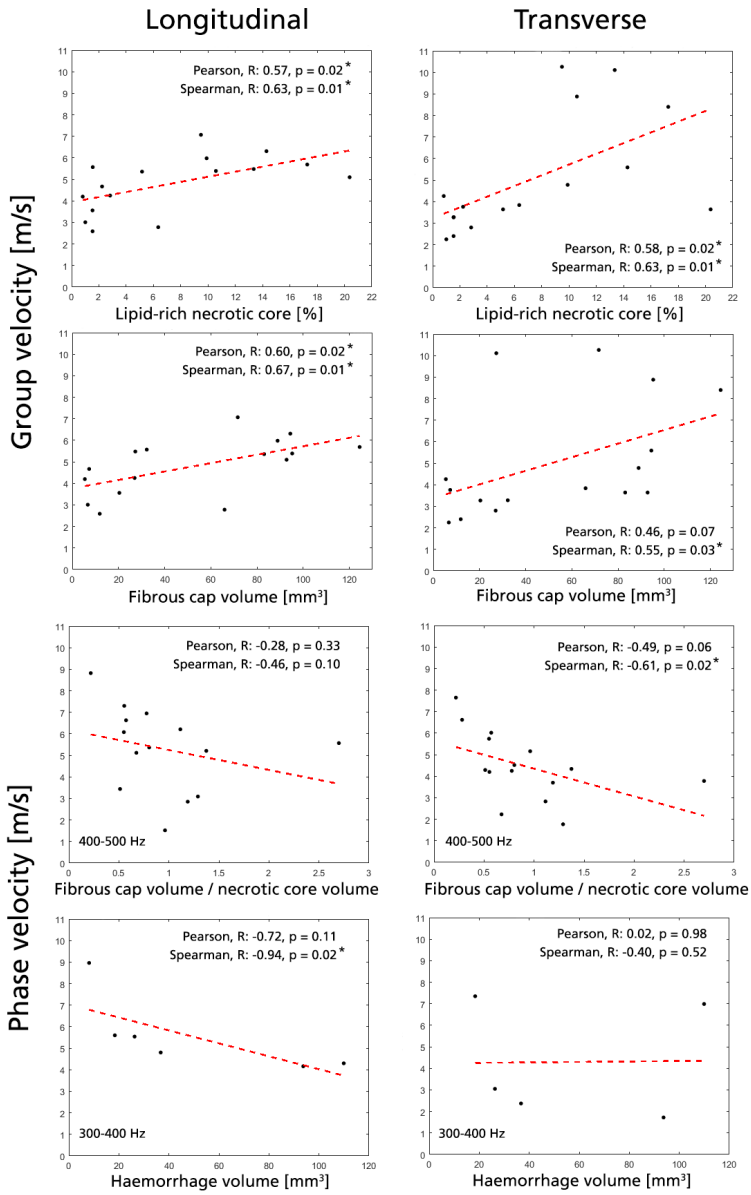

Figure 5.8: Correlations with group (uppermost rows) and phase velocity (lowermost rows) for a few selected plaque parameters, presented for longitudinal (left column) and transverse (right column) imaging, respectively.

5.2. Non-invasive cardiovascular relative pressure estimation

Study V: *Non-invasive cardiovascular relative pressure estimation using virtual work-energy*

a) vWERP in-silico evaluation

Results from the νWERP assessment of relative pressure in the patient-specific *in-silico* AAD is presented in Figure 5.9. For similar data on the *in-silico* CoA, see [63]. In the AAD, accurate estimates are generated throughout the vasculature, with output seemingly unaffected by the complex flow through the false lumen opening in the aortic arch. For all evaluated planes, a mean error of below 14/16/21% was reported at SNR = ∞/30/10.

A particularly challenging flow scenario is given for plane F, where a renal artery is connected first to the true lumen, and then into the false lumen through intraseptal tears. Despite this, accurate results could still be generated (mean error of 12%), given sufficient spatial sampling (1 mm^3).

The table within Figure 5.9 also shows spatiotemporal behaviour of νWERP when estimating relative pressure into true (A-E) and false (A-D) lumen, respectively. As expected, accuracy increases with increasing spatiotemporal sampling. However, at clinical sampling (2 mm^3 and 32 time frames), accurate estimates are given into both outlets and for all noise levels, respectively (mean error if 16/20/32% into true lumen, and 10/10/12% into the false lumen, at SNR = ∞/30/10).

At the noise-free state, slightly higher dependence against temporal sampling seems apparent. Specifically: with a twofold increase in temporal sampling a decrease in mean error of 32% is given, compared to a decrease in mean error of 19% in the case of a twofold increase in spatial sampling. The effect however diminishes with introduced image noise, where spatial and temporal refinements seem to generate similar accuracy improvements.

In the *in-silico* data, alternative relative pressure methods perform poorly, specifically since the evaluated models expand beyond the intended use of these specific methods. Bernoulli-based metrics neglects a large portion of the flow field, and have difficulties defining appropriate centre-line metrics when going through turbulent regimes as the one presented in the AAD lumen tear. Similarly, conventional WERP will diverge in late diastolic low-flow regimes, and as a result, all three renders inaccurate outputs. To exemplify, estimates into the true lumen of the AAD (A – E in Figure 5.9) renders mean errors of 100%, 88%, and >200% if applying the simplified Bernoulli, unsteady Bernoulli, or direct WERP method.

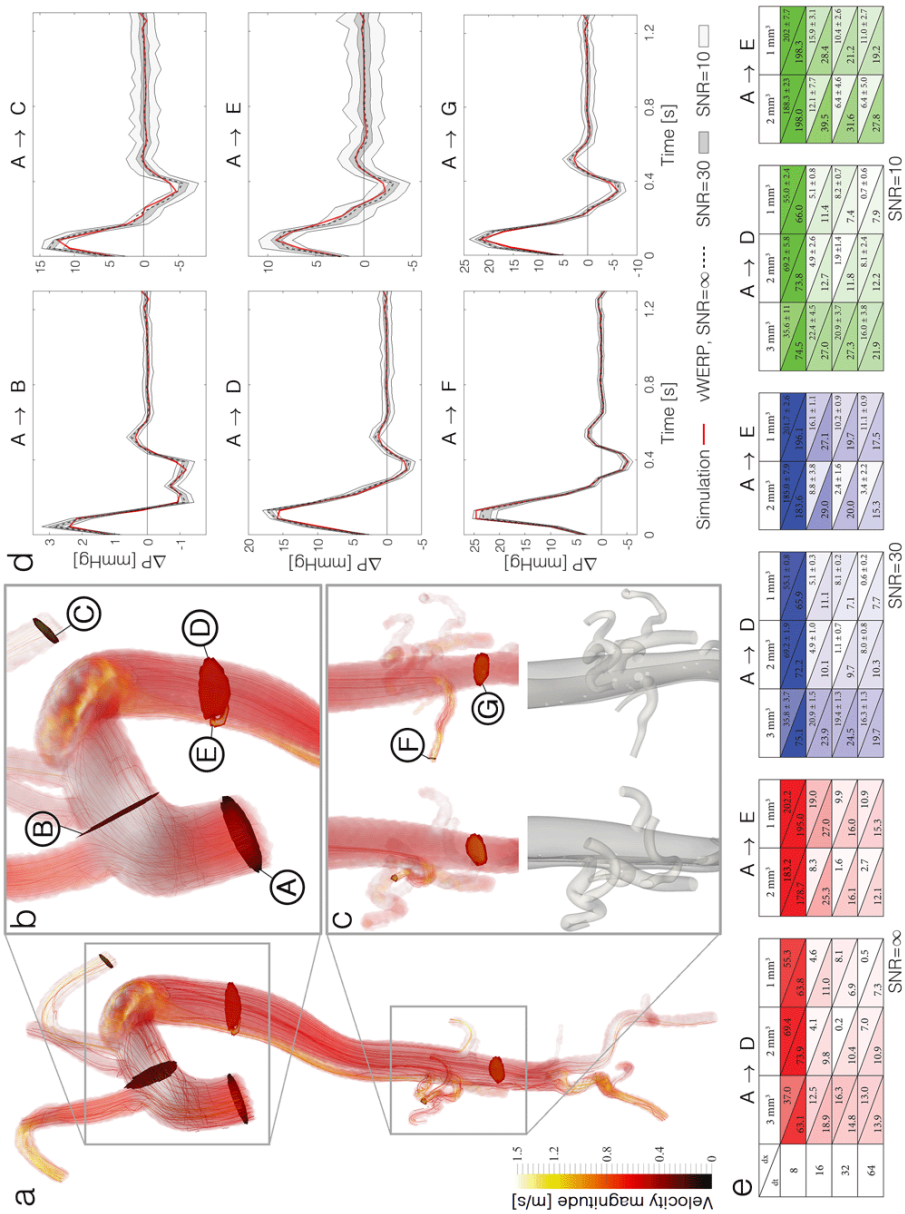

Figure 5.9: **v**WERP relative pressure estimations through a patient-specific AAD. (a) Visualised velocity field with (b-c) inlet (A) and outlet planes (B-G) shown in highlighted zoom boxes. (d) Relative pressure traces as a function of time, with data ground truth simulations given in red, and **v**WERP output given for SNR = ∞/30/10 in dashed black, dark grey, and light grey, respectively. (e) Spatiotemporal behaviour of the relative pressure estimation from A to D and E, respectively, with data shown for SNR = ∞/30/10 in red/blue/green. The tables present the mean error (lower left) and the error at peak relative pressure with standard deviation (upper right).

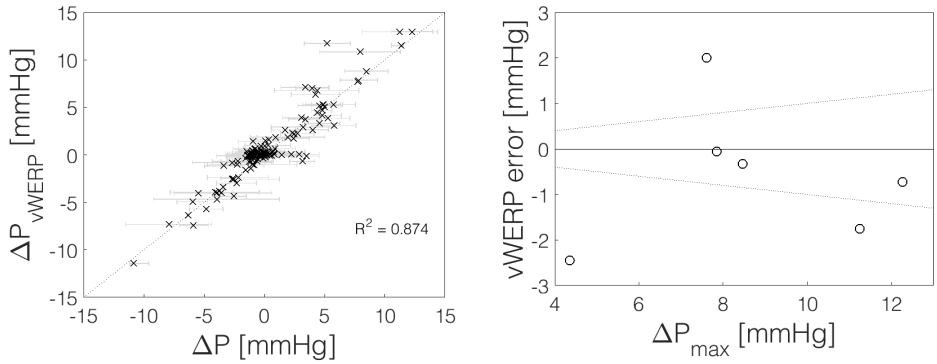

Figure 5.10: Cumulative results from the *in-vivo* evaluations showing (left) **ν**WERP estimates against invasive catheterisation in the *in-vivo* cohort, and (right) absolute error of **ν**WERP at peak relative pressure in the *in-vivo* cohort. Relative errors of ±10% are given by the dashed black lines.

b) νWERP in-vivo validation

For the *in-vivo* evaluation a mean error of 16 ± 13% was observed over all subjects, corresponding to an absolute error of <1.0 mmHg. Even though the error varied slightly over time, the initial systolic peak in maximum relative pressure seems accurately captured in all subjects, with a mean error of <18% or 1.2 mmHg (complete relative pressure traces are provided in [63]). As a cumulative summary of the validation, Figure 5.10 shows how a strong linear correlation between νWERP and catheter measurements is seen (k = 0.87), indicating only a slight underestimation of -0.6 ± 1.5 mmHg or -8 ± 26% over all evaluated subjects.

Study VI: *Extension of νWERP into turbulent flow regimes*

a) In-vitro validation

For the *in-vitro* stenotic flow phantoms, cumulative linear regression and Bland-Altman plots are provided in Figure 5.11. Additionally, tabulated numerical data is presented in full in the appended manuscript in Part II. As seen, νWERP-t showed high accuracy throughout all valves, with a 1:1 correlation observed from regression analysis and a mean error of 1.0 ± 4.1 mmHg. In comparison, the non-extended νWERP showed a systematic underestimation of -6.5 ± 6.7 mmHg and a linear regression slope of k = 0.78. For the real work-energy approaches, WERP-t and WERP showed distinctly larger errors (mean error of -10.9 ± 12.8 mmHg and -23.2 ± 29.2 mmHg, respectively), whereas TP rendered relatively accurate results (1.0 ± 4.1 mmHg, k = 0.89).

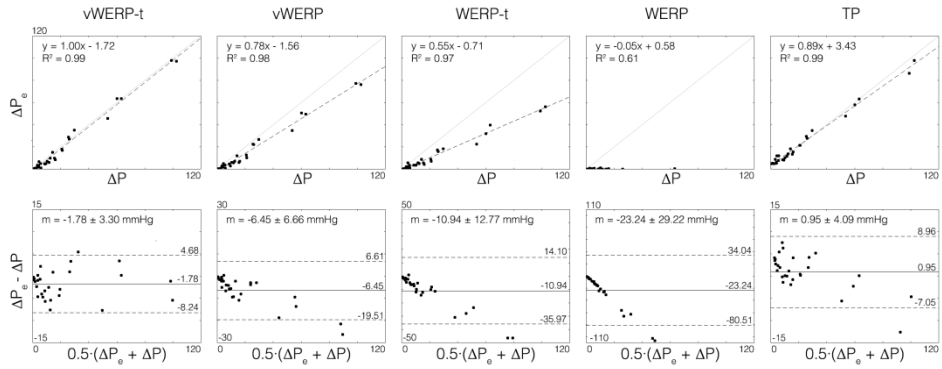

Figure 5.11: Cumulative results from the *in-vitro* stenotic flow phantoms, presented as linear regression plots (upper row, estimated relative pressure, ΔP_e, versus reference relative pressure, ΔP) and Bland-Altman plots (bottom row), respectively. Data shown for νWERP-t, νWERP, WERP-t, WERP, and TP, respectively.

With respect to energy components, the virtual νWERP-t approach was dominated by advective A_e, representing in average 76% of the total relative pressure, with only 21% added by T_e. In comparison, the real work-energy approaches were governed by turbulent T_e, contributing to in average 93% of the total relative pressure, with a comparably negligible advective A_e (approximately 2%).

b) In-silico verification

Relative pressure estimations through the transient *in-silico* data is provided in Figure 5.12-5.13. Relative pressure traces are shown for each evaluated estimation approach, together with separate plots showing how different energy components fluctuate over the cardiac cycle.

νWERP-t shows good agreement with reference *in-silico* relative pressures, having a mean error of 6.8% and 6.2% during the initiation and quasi-periodic phase, respectively. For the non-extended νWERP, estimations deteriorate around the systolic peak during the initiation phase following the lack of included T_e, and a mean error of 47.8% is reported. However, during the quasi-periodic phase, significantly lower T_e is seen, with the mean error decreasing to 6.9% is seen.

For the real work-energy approaches, significant output deterioration is observed, with mean errors exceeding 100% in all but one case (WERP-t having a mean error of 89.0% during the initiation phase). Cumulative visualisations of Figure 5.12-5.13 are provided in the appended manuscript in Part II.

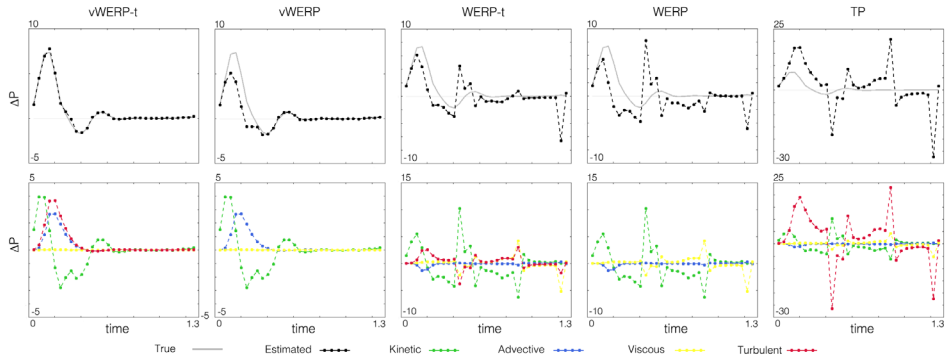

Figure 5.12: Relative pressure traces (upper row) through the *in-silico* AAD model during initialisation phase as predicted by νWERP-t, νWERP, WERP-t, WERP, and TP, respectively. Additionally, separated energy components (lower row) are presented for each estimation approach, shown as $\frac{\partial}{\partial t}K_e$ in green, A_e in blue, V_e in yellow, and T_e in red.

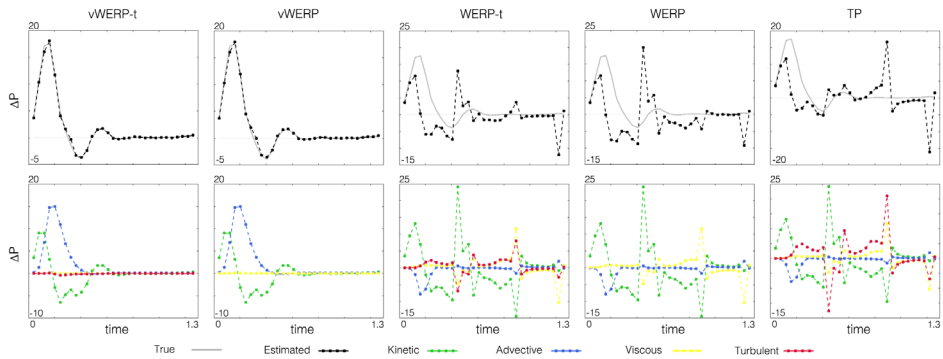

Figure 5.13: Relative pressure traces (upper row) through the *in-silico* AAD model during the quasi-periodic phase as predicted by νWERP-t, νWERP, WERP-t, WERP, and TP, respectively. Additionally, separated energy components (lower row) are presented for each estimation approach, shown as $\frac{\partial}{\partial t}K_e$ in green, A_e in blue, V_e in yellow, and T_e in red.

Study VII: *Aortic relative pressure in DCM*

Measurements and imaging was performed on all recruited subjects. Upon evaluation, the DCM cohort was split into two subgroups: one with reduced LV function (DCM_{red}, EF $<$ 50%, n = 9) and one with moderate LV function (DCM_{mod}, EF $\geq$ 50%, n = 5). Furthermore, one subject was excluded following a severely stenotic aortic valve (mean aortic outflow velocity = 1.8 m/s versus a group mean of 0.8 ± 0.3 m/s) and altered aortic geometry (aortic radius = 0.5 cm versus a group mean of 0.8 ± 0.1 cm, LVOT area = 1.5 cm^2 versus a group mean of 5.9 ± 2.9 cm^2). Complete characteristics are provided in the appended manuscript in Part II.

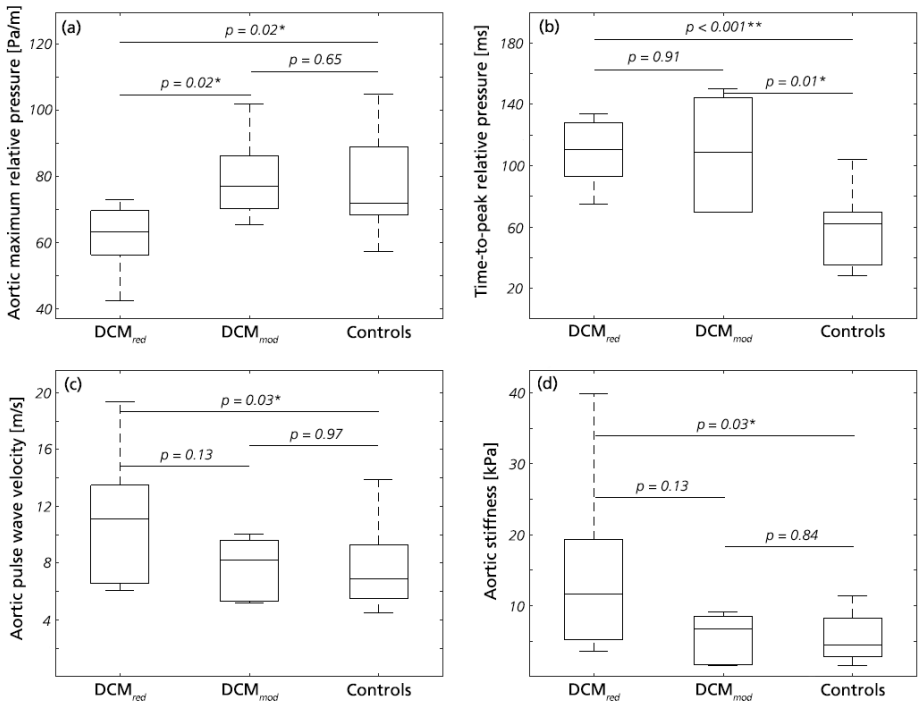

Figure 5.14: Maximum relative pressure, normalised time-to-peak, pulse wave velocity, and derived aortic stiffness shown for DCMs with reduced and moderate LV function, and the volunteer control group, respectively. P-values are reported for all intragroup comparisons, with significances indicated by *($p < 0.05$) or ** ($p < 0.01$).

a) Aortic hemodynamics in DCM

Aortic relative pressure, TTP, aortic pulse wave velocity, and aortic stiffness are shown for all subjects in Figure 5.14.

The DCM_{red} group had a significantly lower maximum aortic relative pressure compared to both the control and DCM_{mod} group, respectively. Similarly, a prolonged TTP was seen for all DCM patients, regardless of LV status. The DCM_{red} group also showed a significantly higher aortic PWV compared to the other two groups, with similar data derived for aortic stiffness.

b) Correlation to aortic relative pressure

Pearson correlation coefficients are presented in complete in the appended manuscript in Part II. In summary, no correlation was observed with maximum relative pressure in any of the DCM groups. For minimum relative pressure, correlation was only observed with weight in the DCM_{red} group.

For TTP, RVEF showed positive correlation in the DCM_{red} group, however, this trend was not reflected in the DCM_{mod} group. Generally weak correlation strengths were also reported with regards to PWV, and aortic stiffness, respectively.

Noteworthy is that the retrieved central blood pressure measurements did not correlate strongly to any of the assessed relative pressure parameters.

c) Influence of cardiovascular properties on aortic relative pressure

Aortic relative pressures for virtual along with clinical cohort groups are given in Figure 5.15 showing variations as a function of isolated cardiovascular parameters.

In the virtual cohort, aortic maximum relative pressure varied within a range of 23.9 - 56.5, 28.3 - 62.5, and 30.4 - 72.1, and Pa/m, compared to 61.2 ± 10.0, 79.6 ± 14.2, and 78.9 ± 18.0 Pa/m in the clinical cohort, with data presented for the DCM_{red}, DCM_{mod}, and control group, respectively.

In the virtual cohort, aortic stiffness and aortic area were the two dominating factors influencing relative pressure. For the DCM_{red} group, variations in aortic stiffness accounted for 47% of the possible variations in maximum relative pressure, 63% of the possible variations in the DCM_{mod} group, and 100% of the possible variations in the control group. On the other hand, variations in aortic area accounted for 87% of the possible variations in maximum relative pressure in the DCM_{red} group, 91% of the possible variations in the DCM_{mod} group, and 73% of the possible variations in the control group. Cardiac parameters had a comparably smaller influence, with only SV showing any noticeable visual impact. Here, variations in SV accounted for 66%, 46%, and 46% of the possible variations in maximum relative pressure in the DCM_{red}, DCM_{mod}, and control group, respectively.

For minimum relative pressure, aortic stiffness and aortic area were again deemed the primary determinants. Specifically, aortic stiffness equalled variations of 70, 63, and 94% of all possible variations in minimum relative pressure, compared to aortic area with 95, 100, and 72% (percentages given for the DCM_{red}, DCM_{mod}, and control group, respectively).

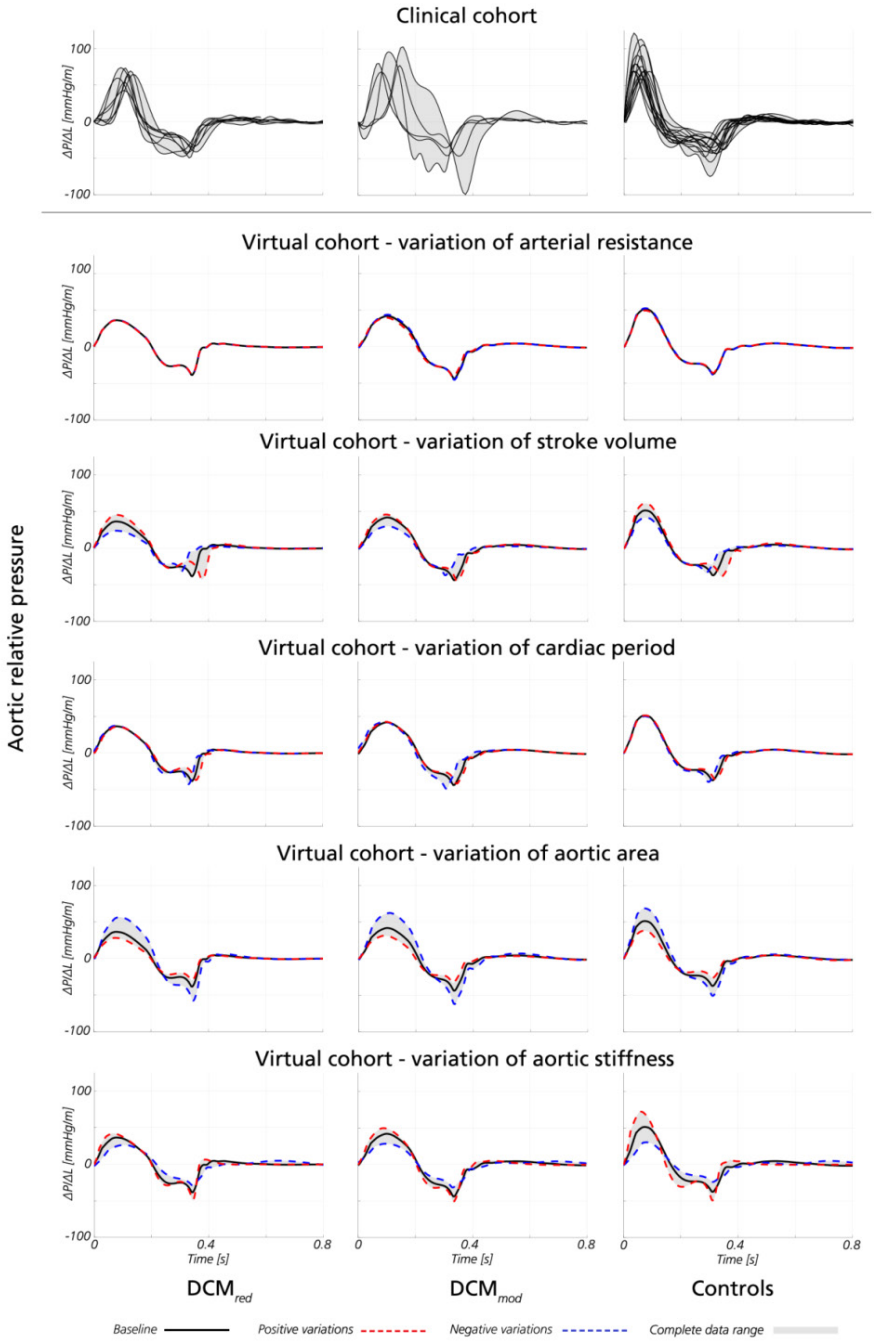

Figure 5.15: Aortic relative pressure from clinical (top row) and virtual (remaining rows) cohort. Data is presented for DCMs with reduced and normal EF, as well as for the volunteer control group. For the virtual cohort data, isolated variations are presented for arterial resistance, SV, cardiac period, aortic area, and PWV, respectively.

5.3. Tomographic reconstruction for pre-clinical imaging

***Study VIII*:** *Multigrid tomographic reconstruction for pre-clinical micro-CT imaging*

a) Numerical verification

Figure 5.16 shows a Shepp-Logan phantom, reconstructed using multiple discretisation domains. Numerical error quantification is provided in Table 5.1. As visually apparent, the three dorsal inserts can be recovered at all discretisation ratios. However, image quality deterioration becomes increasingly apparent towards the edges of the high-discretisation ROI.

Despite this, Euclidean distance and SSIM are fairly high even at the coarsest background discretisation (Euclidean distance = 2.56, SSIM = 0.87), indicating a fairly robust reconstruction of the ROI with varying background discretisation.

Similar results for variation in regularisation are provided in Figure 5.16, with numerical quantifications again given in Table 5.1. Compared to the multigrid discretisation without regularisation, the multigrid regularised reconstruction show more accurate SSIM and Euclidean distance, potentially following the noise-smoothing behaviour.

Results for the combination of multigrid discretisation and regularisation are provided in Figure 5.16. As previously, variations in discretisation ratio do not seem to impact the ability to recover the dorsal inserts, albeit image quality deteriorations towards the ROI edges seem apparent. With respect to SSIM and Euclidean distance, the combined approach seem to generate slightly more accurate values compared to the non-regularised case (e.g. at discretisation ratio 1:4, SSIM = 0.99 versus 0.88 when using added regularisation).

Regarding computational cost, a significant decrease in computation time is seen with decreasing background discretisation (at problem size $N = 12800^2$, a 1:16 reconstruction can be performed in less than 10% of the time required to complete a 1:1 reconstruction). These results are underlined in the combined discretisation and regularisation approach, where a speed-up of a factor of >35 is seen at the largest evaluated problem size (for $N = 12800^2$, 1:16/0.01:1 discretisation/regularisation requires 207 s, compared to 7385 s for conventional reconstruction). Noteworthy is also that for purely multigrid regularisation (i.e. identical discretisation in the two separated domains) no difference in computation was observed.

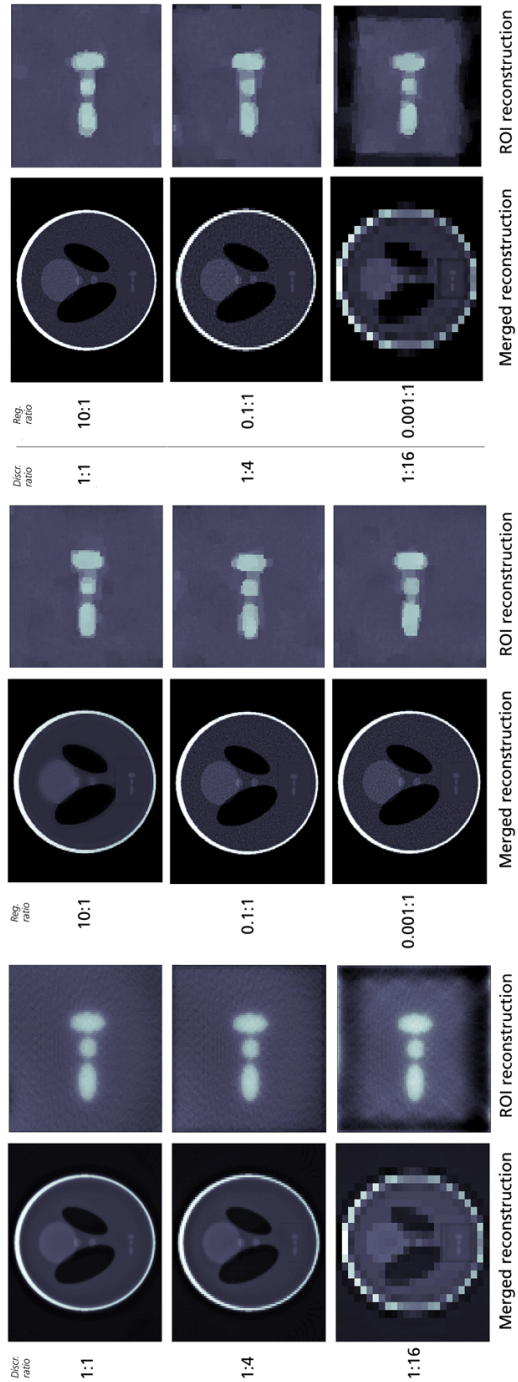

Figure 5.16: Multigrid reconstruction using piecewise discretisation (left), piecewise regularisation (middle), and combined piecewise discretisation and regularisation (right).

Table 5.1: SSIM and Euclidean distance for variations of multigrid discretisation and regularisation for the Shepp-Logan phantom in Study VIII.

	Discretisation	Regularisation	SSIM		Euclidean distance	
Multigrid discretisation	1:16	-	0.98	0.86	1.80	2.56
	1:8	-	0.99	0.87	0.95	2.14
	1:4	-	1.00	0.88	0.39	1.87
	1:2	-	1.00	0.89	0.12	1.73
	1:1	-	1.00	1.00	0.00	0.00
Multigrid regularisation	-	10:1	0.99	0.99	0.40	0.67
	-	1:1	1.00	1.00	0.00	0.00
	-	0.1:1	0.99	0.99	0.05	0.54
	-	0.01:1	0.99	0.99	0.06	0.52
	-	0.001:1	0.99	0.99	0.06	0.57
Multigrid discr. and regularisation	1:16	0.1:1	0.97	0.96	2.75	2.78
	1:8	0.1:1	0.99	0.99	0.82	1.01
	1:4	0.1:1	1.00	0.99	0.24	0.57
	1:2	0.1:1	1.00	0.99	0.07	0.46
	1:1	0.1:1	1.00	1.00	0.00	0.00

b) Experimental evaluation

For the experimental evaluation of the multigrid regularisation approach, three acquisitions sessions were performed, all shown in Figure 5.17. Apart from the visual, qualitative results, the low-contrast phantom insert (reference contrast 8%) were evaluated at different discretisation ratio. At all ratios, an approximate insert contrast of 9% was recovered, indicating reasonably accurate reconstruction even in the real-life experimental setting. Moreover, numerical data in Table 5.2 indicates robust behaviour even when using a fairly coarse background discretisation.

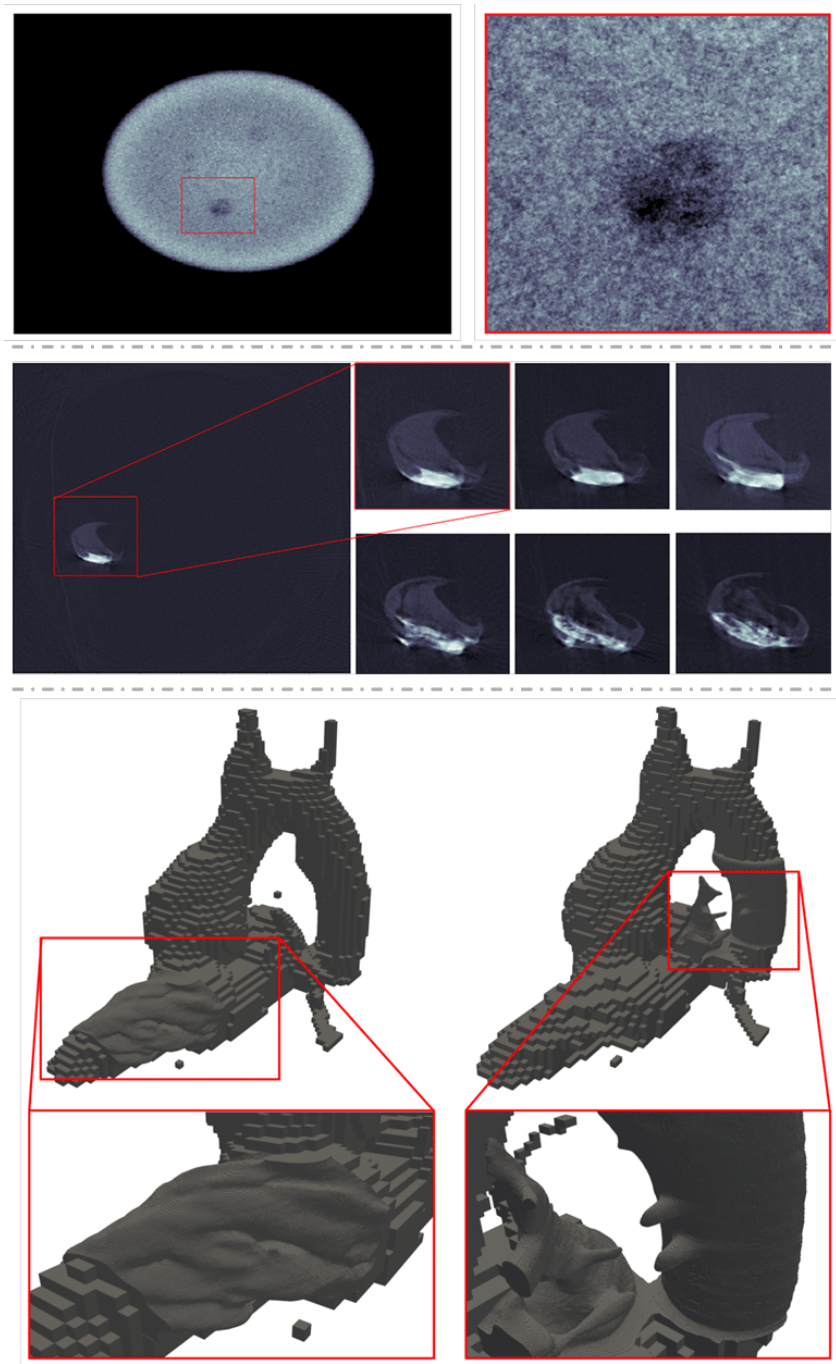

Figure 5.17: Experimental micro-CT acquisitions and multigrid discretisation reconstructions. Upper row: low-contrast phantom (insert reconstructed at 1:8 discretisation), middle row: endarterectomy plaque specimen, positioned entirely inside the high-resolution ROI, lower row: 3D-printed CTA, with two regions (epicardium and pulmonary veins) reconstructed at detector resolution.

Table 5.2: SSIM, Euclidean distance, and insert contrast for variations of multigrid discretisation and regularisation for the low contrast phantom in Study VIII.

Discretisation	SSIM	Euclidean distance	Insert contrast
1:64	0.86	974.49	0.09
1:32	0.93	222.35	0.09
1:16	0.98	217.49	0.09
1:8	1.00	47.20	0.09
1:4	1.00	16.02	0.09
1:2	1.00	4.42	0.09
1:1	1.00	0.00	0.09

Chapter 6

Discussion

Over the last century, truly remarkable advancements have been made in the field of medical science where interdisciplinary, translational research has led to a much more comprehensive understanding of human physiology and disease development. Today, scientific research is the foundation on which all clinical decisions are made, and it is through such efforts that we progress towards improved health care – developing and validating effective assessment tools, isolating and identifying accurate diagnostic biomarkers, and introducing novel evaluation techniques with improved clinical abilities.

Within this endeavour, medical imaging has played a particularly important role, and in cardiovascular health care imaging has practically revolutionised the way we diagnose disease. As showcased throughout this thesis, advancements are however not restricted to the development of new imaging modalities, but refined diagnostic abilities and novel biomarkers are more than often a result of refined acquisition and post-processing schemes. This aim of clinical imaging research – to develop effective and refined diagnostic tools, and to identify accurate and specific clinical biomarkers – has also been the specific aim of this thesis.

In Study I – IV vascular SWE has been clinically applied for atherosclerotic plaque characterisation, in Study V – VII a novel method for non-invasive relative pressure assessment has been developed, and in Study VIII a reconstruction method for multigrid tomographic imaging has been implemented in a pre-clinical setting. Together, these separate parts complement each other in the attempt of improved cardiovascular image diagnostics: SWE providing constitutive tissue mapping, νWERP enabling for refined hemodynamic probing, and the multigrid reconstruction approach allowing for efficient pre-clinical imaging, being an important contributor to progress in imaging and clinical research. In the following paragraphs the main outcomes and implications of all studies will be discussed, putting the results into a clinical context as well as commenting on specific study limitations.

6.1. Vascular shear wave elastography

In the first part of this thesis, focus was on evaluating the ability of using SWE for vascular image diagnostics, quantifying tissue stiffness as a biomarker for plaque

risk stratification, or in order to track changes in arterial constitutive behaviour. However, as explored extensively throughout Study I–IV, confined cardiovascular tissue aggravates elastographic assessments by inducing complex acoustic response.

a) Group and phase velocity and confined wave propagation

In Study I, the impact of geometrical confinement on SWE accuracy was highlighted, where conventional group velocity analysis showed a systematic underestimation of shear modulus in confined media. On the contrary, fitting dispersion-induced high-frequency phase velocities to a Lamb-wave based propagation model (taking the confined geometries into account) rendered accurate estimates of shear modulus, with relative errors of below 10% over a range of physiological stress levels.

Even though intuitive from an engineering perspective, the fact that unconfined group velocity estimates are unsuccessful in quantifying the stiffness of geometrically confined specimens is important for the clinical usage of SWE. To date, all commercially available clinical elastography devices are using group velocity-based stiffness reconstructions, and consequently there are no physical restrictions in simply transferring the same equipment into cardiovascular diagnostics. In fact, studies exist employing group velocity-based stiffness reconstruction for arterial [377] or atherosclerotic purposes [255, 278], but as highlighted by the results of Study I the quantification might underestimate true stiffness. If not utilising confined wave propagation models, reporting group velocity alone (i.e. not quantifying shear modulus) could be a preferable option, as e.g. in Study IV. With confined media presenting a non-linear relationship between group velocity and tissue stiffness (as in e.g. Equation 3.35), the clinical value of arterial group velocity however remains to be assessed, even though Studies II-IV indicate a defined potential in atherosclerotic plaque differentiation.

Others have employed phase velocity analysis to estimate arterial stiffness [203, 280, 378], and only in the last few years a growing number of studies have been published utilising refined wave propagation models to accurately recover arterial stiffness [279, 379-382]. With reference to existing literature, it is important to note that the utilised propagation description (Equation 3.35) is based on a plate-based Lamb wave model [203], itself simplifying the assessed arterial phantom geometries. As observed, derived estimates will depend on the utilised frequency spectrum, and it is only if restricting data to higher frequencies (above 500 Hz) that accurate stiffness values can be retrieved. That estimates of the arterial phantoms deviate when incorporating lower frequencies is a direct result of the fundamental difference in wave propagation between a plate (constricting the waves in one dimension - thickness) and a hollow cylinder (constricting the waves in two dimensions – thickness and curvature). At low frequencies, the wavelength of the propagating acoustic shear wave will be in the same length scale as the curvature of the arterial phantom, and apparent differences will be observed between the experimental data and the theoretical plate-based model. However, at high

frequencies, the wavelength will be significantly smaller than the curvature of the arterial phantom, and experimental data will converge towards the plate-based model. This fact has been observed previously where Couade et al. [280] recommended fitting data above 1 kHz to obtain accurate estimates in arterial phantoms. Along the same lines, Maksuti et al. [383] showed from numerical studies how the fundamental flexural F(1,1) mode of a hollow cylinder converges with the plate-based antisymmetric A(0) mode at around 400 Hz in geometries identical to the ones experimentally assessed in Study I. In a recent study, Li et al. even proposed an inverse procedure to determine a critical frequency above which dispersion data can be used to determine arterial stiffness [379], again supporting the findings in Study I. In comparison to these aforementioned studies, the cut-off threshold of 500 Hz in Study I was empirically chosen based on preliminary data observations, attempting to remove significant low-frequency deviations whilst still maintaining sufficiently large bandwidth.

Regarding the observed dispersion behaviour, it should also be noted that the utilised propagation model only takes into account geometrical dispersion, i.e. dispersion caused by the interference between the propagating wave and the confining geometrical boundaries. To this, dispersion may also arise due to intrinsic material properties, where material thermal conductance, chemical composition, or viscoelastic behaviour causes wave energy absorption. In particular, viscous dispersion behaviour has been utilised to derive viscoelastic properties of imaged tissue [384, 385], however for bounded cardiovascular media it has been shown that viscous dispersion plays a comparably inferior role to geometrical dispersion [386, 387]. In fact with PVA exhibiting viscoelastic behaviour [388], the accurate estimates in Study I support the notion that geometrical dispersion may suffice in describing observed phase velocities in confined media.

Advancing from Study I, the subsequent Studies II-IV were all performed with the clinical goal of improved plaque risk stratification using SWE. In comparison to the arterial tissue or the arterial phantoms of Study I, atherosclerotic plaques exhibit even greater geometrical confinement, with *in-vivo* plaques being both irregular in shape and composition. For that reason, Study II was conducted again on simplified phantom specimens, specifically designed to isolate the influence of plaque-like confined media on SWE differentiability and performance. In-line with the results of Study I, Study II shows how group velocity consistently underestimates reference values, whereas accuracy improves with phase velocities at increasing frequencies. However, opposing results are seen with regards to phantom plaque differentiability where group velocity showed superior ability in separating phantom plaques of different stiffness from each other. Only when using phase velocities at around 1 kHz was comparable phantom plaque differentiation observed, but even then group velocity showed superior differentiability. This poses interesting implications when translated into a clinical setting: if striving for improved plaque risk stratification – i.e. attempting to

separate plaques of different constitutive composition – a method with inferior absolute accuracy might be preferred. As supported by the findings from Study IV, group velocity seem to have certain diagnostic abilities, and similar examples exist in literature supporting this notion [255, 278, 389]. The reason for the improved differentiability by group velocity analysis is difficult to isolate, but may spur from the improved robustness in group velocity compared to phase velocity estimates. As reported in Study II, group velocity estimates exhibited an average variation of 11% compared to 20% in corresponding phase velocity, with phase velocity variations potentially spurring from low frequency interactions with geometrical boundaries, as well as high frequency signal deterioration. High-frequency estimates might improve in precision if utilising shorter push duration [198] or modified beam width [390], however the effect on plaque differentiability remains to be investigated.

With this in mind, it is still important to remember that even though superior in differentiating phantom plaques of different stiffness, group velocity does not directly quantify tissue stiffness in such confined media. For a true quantification of plaque stiffness, one would again have to describe the observed wave propagation with an appropriate acoustic model (just like a Lamb-wave based model was utilised for the arterial phantoms in Study I). A defined obstacle however is the heterogeneity of atherosclerotic plaques as a group, with significant variations in size, shape, and composition observed between different plaque specimens. With that, no unique wave propagation model exist to describe their acoustic behaviour, and consequently, a major part of the results of Study II – IV consisted of direct estimates of wave velocity rather than indirect derivations of tissue stiffness. Detailed studies of elasticity imaging coupled to plaque stiffness have been performed using patient-specific numerical simulations [391-394], and such studies might shed further light on the correlation between observed wave velocity and plaque composition. However, a generalisation of such findings into a generic plaque population remains dubious, and the clinical implications of wave velocity versus tissue stiffness remain to be clarified for cardiovascular purposes.

Apart from the main findings on plaque differentiability, results from Study II also highlighted the relation between phantom plaque differentiability and SWE push location and imaging plane, respectively. With SWE output seemingly invariant to push location within a given imaging plane, the difference between imaging planes is noteworthy. In particular, transverse imaging rendered higher particle velocity, lower SNR, and consistently lower shear wave velocities compared to longitudinal imaging. With phantom plaque stiffness independent of observer view plane, the behaviour is rather a consequence of the fundamental wave propagation of the induced shear waves. In longitudinal imaging, the induced shear wave will propagate in the axial vessel direction, following the arterial wall and phantom plaque as an effective wave guide [202, 395, 396]. On the contrary, in transverse imaging, the induced shear wave will propagate seemingly unobstructed through the surrounding tissue before traversing the arterial wall and phantom plaque as an

embedded inclusion rather than as a wave guide. Based on the results of Study II, it seem clear that the transverse inclusion based wave transfers a larger portion of the wave energy into the phantom plaque itself, whereas the longitudinal wave guide causes characteristic dispersion behaviour obstructing optimal energy transfer. That this would render lower observed wave velocities in the transverse view is not obvious, however the behaviour has been validated in numerical studies [397] where an identical phantom plaque setup was evaluated. In literature, plaque elastography has been attempted in both longitudinal [242, 243, 254, 255, 277, 278] and transverse imaging planes [253, 273] but, as indicated by Study IV, the two imaging planes might even perform differently with respect to plaque risk stratification. With that in mind, the observed differences in Study II are important to consider when progressing cardiovascular SWE into a clinical setting.

b) Ex-vivo and in-vivo carotid plaque characterisation

The utilised phantom setups of Study I and II both serve a defined purpose, where such controlled *in-vitro* experiments can successfully isolate effects of e.g. geometrical confinement or push location on SWE performance. However, extrapolating results from such simplified studies into a clinical setting is challenging, in particular when considering the complexity in shape and composition of human atherosclerotic plaques. In an attempt to translate the developed data analysis of Study I and II into more realistic plaque tissue, the experimental setup of Study III was therefore developed. Presented merely as a proof-of-concept setup, results show how SWE data can be retrieved from an *ex-vivo* plaque sample but also how changes in observed wave velocity seemed correlated to intraplaque compositional changes seen by micro-CT imaging. Results also indicate defined dispersion-like behaviour in *ex-vivo* plaque tissue, even though the fitted Lamb-based model may not be a suitable approach outside the presented proof-of-concept setup. To this, the results also highlight the difficulty of plaque SWE, where the irregular shape of the investigated plaque obstructed transverse SWE imaging. Isolated *ex-vivo* investigation of plaque tissue has been used in several studies as a validating complement to performed *in-vivo* imaging [246, 253, 273, 398], and has even been utilised to study detailed constitutive response [399]. With such, the developed setup of Study III has a defined potential to serve as a tool for further detailed plaque investigations, however was not explored to any further extent in this thesis.

Instead, a direct advancement into clinical practice was carried out in Study IV, where an implementation of the developed SWE data analysis was performed on a clinical carotid plaque cohort. The main finding of the study was that AHA type VI plaques showcased significantly higher group velocity compared to any other plaque type, and that similar differentiation was observed for longitudinal phase velocity imaging at the highest frequency band (400-500 Hz). The findings bear particular clinical impact, where AHA type VI plaques are not only identified as the most rupture prone phenotype [140, 151, 152], but also since AHA type VI plaques do not necessarily correlate with stenosis degree [400]. By so, the

differentiation provided by SWE expands on current clinical guidelines for plaque risk stratification, where both group and phase velocity could act as novel biomarkers for plaque differentiation.

It is noteworthy and slightly counterintuitive that the culprit set of AHA type VI plaques showcases increasing wave velocities, especially considering the traditional view of a lipid-rich, soft plaque being the most rupture prone one. The causal reason for this observed wave velocity increase is also difficult to isolate, especially considering the inhomogeneous plaque phenotypes incorporated in the AHA type VI classification (including visible surface defects, active plaque core, intraplaque haemorrhage, thrombus formation, etc.). However, it is worth noting that in the studied cohort of Study IV, the increasing LRNC content seemed balanced by an increasing fibrous cap volume. That is, the studied lipid-rich culprit lesions were also associated with a generally larger fibrous cap, potentially leading to an observed stiffer behaviour. This reasoning is also supported by other findings, where collagenous deposits have been correlated to reduced plaque displacement levels [276]. To disentangle the exact effect of lipid-rich core content and fibrous cap distribution on observed wave propagation, further isolated experimental or numerical studies might be necessary. Regardless, the observed differentiation indicates a promising potential of SWE for cardiovascular plaque characterisation.

In addition to the plaque type differentiation, a set of intraplaque parameters correlated to retrieved group and phase velocity, respectively. In particular, group velocity showed positive correlation with LRNC content, and high-frequency phase velocity correlated with fibrous cap/necrotic core volume – both parameters associated with the identification of vulnerable TFCA. The correlations are in-line with the increasing velocities for AHA type VI plaques, and might again be influenced by the apparent increase in fibrous cap volume. However, with correlations also observed with other important structural plaque characteristics (most importantly decreasing phase velocities with increasing intraplaque haemorrhage volume, supporting previous findings where increasing strain levels were observed in (fibro)atheromatous plaques [253]), the combined group and phase velocity approach of Study I-IV provides a novel set of plaque biomarkers with which larger studies on plaque risk stratification and improved patient outcome could be studied. Again, detailed numerical studies could also be attempted to disentangle specific wave propagation behaviour as a function of varying intraplaque composition.

Discussing Study IV, it is worth contrasting the retrieved results to the ones observed in Study I-III. The plaque cohort did not come with any reference wave velocity or stiffness, however slightly higher phase velocities seemed indicated at 400-500 Hz compared to the corresponding group velocity metric, supporting the observed group velocity underestimation in Study I and II. However, this behaviour did not seem to be present for the important AHA type VI plaques in transverse view, where group velocities exceeded the corresponding phase velocities. The robustness of group velocity compared to phase velocity indicated

in Study II however seemed reflected in Study IV, where consistently larger deviations were observed for the retrieved phase velocities compared to the corresponding group velocity metric. With this, it should be noted that the retrieved phase velocities in Study IV were given at consistently lower frequencies than what was studied in-detail in Study II. The reason for this was restrictions in the clinically used SWE system, where a pre-defined 400 μs push duration was set. With push duration inversely proportional to dispersion bandwidth [198], a shortened push might have rendered higher phase velocities, with potentially improved accuracy (as indicated by Study I-II). However, the exact implication of a shortened push in a clinical setting remains to be evaluated.

c) Reference methods

In Study I, mechanical tensile-testing was performed to validate the retrieved phantom shear modulus. However, using the customised fixation and pressurisation setup, the testing was performed under effective biaxial tension (with the intraluminal pressurisation inducing orthogonal circumferential stress), mimicking the stress state of the SWE imaging. With such, the quasi-static testing rendered reference values of *Young's modulus*, which using assumptions of tissue isotropy, could be converted to *shear modulus*. Alternatively, direct shear modulus estimations could have been achieved by imposing angular twisting and torque loading (as recommended for tubular structures by the American Society for Testing and Materials [364]). However, when assessing hyperelastic soft tissue (such as PVA [351]), low energy torsional buckling may aggravate twist testing and complicate the derivation of elastic properties [401], and consequently the tensile-test substitute was chosen as a validating testing method.

In Study II, SWE group velocity from large homogeneous blocks of PVA was chosen ahead of mechanical testing. This was primarily chosen since validation was here performed against wave velocity rather than tissue stiffness. Importantly, group velocity was consistently used as a reference metric ahead of phase velocity, following the minor viscous dispersion observed in PVA, as well as the comparably large dimensions of the reference phantoms, minimising geometrical dispersion. Following this, the wave propagation through the reference phantoms could be likened to the wave propagation through an infinite, elastic medium, without any apparent dispersion (as shown in the extended results in [402]).

In Study III, pre-clinical micro-CT imaging was utilised as a reference method to the *ex-vivo* SWE imaging. For plaque tissue, CT has excellent calcium specificity, and a small intraplaque calcification was successfully identified in the imaged endarterectomy specimen. Additionally, micro-CT showcases excellent spatial resolution, with the imaged plaque in Study III reconstructed at a resolution of less than 50 μm^3. However, CT somewhat lacks plaque soft-tissue contrast, and pre-clinical MRI would have enabled differentiation of e.g. fibrous cap from plaque loose matrix. However calcifications are poorly observed in traditional MRI, and a multi-contrast protocol similar to the one utilised in Study IV might have been

required for optimal results. With all this in mind, the main determinant of the utilised micro-CT over pre-clinical MRI came from equipment availability, where developments of an in-house micro-CT system (in part through Study VIII) spurred the incorporation of the equipment in Study III.

Lastly, in Study IV, MRI with dedicated carotid surface coils was utilised as a reference modality to the *in-vivo* SWE. As a non-invasive tool MRI represents the validating gold-standard with regards to plaque characterisation, and it has been used as a reference method in previous image-based studies [242, 403, 404]. By so the method served as an excellent benchmark for the retrieved SWE imaging, even though reader bias and lack of intermodality spatial registration could have influenced the retrieved data.

d) Comparative performance and clinical perspective

In all of the above, SWE has been evaluated as a method for refined vascular assessment. However, as reviewed in Section 3.4.1., SWE is only one of several available ultrasound elastography techniques. Clinical interrogation of plaque composition has been attempted by both intravascular [194] and non-invasive strain imaging [242], and ARFI for constitutive carotid plaque characterisation has been explored in conjunction to validating MRI [404] or with reference histology [243, 276, 398]. In comparison, SWE has not been as extensively employed for carotid plaque characterisation, with only a few examples of feasibility and reproducibility existing in literature, in these cases using direct group velocity reconstruction [255, 278]. With this in mind, the summarised results of Study I-IV represent a definite technique advancement, progressing refined SWE into clinical studies of plaque behaviour and phenotype.

To date, no extensive comparison of the different ultrasound elastography techniques exist with regards to carotid plaque characterisation. In particular, with the different techniques employed using different acquisition settings, imaging setups, cohort specifications, and at different clinical stages, a quantified comparison is also difficult. As with all imaging techniques, the different ultrasound elastography variations all come with specific pros and cons. IVUS strain imaging has demonstrated high sensitivity for vulnerable plaques [194, 246, 273] however suffers from its inherent invasiveness. Relatively mature clinical results have been obtained using non-invasive strain imaging [242, 253], but the technique is slightly limited by the connection to physiologically induced displacements. ARFI imaging has also shown exciting results in several recent plaque studies [243, 276, 405], however only provides a relative measure of strain against surrounding tissue. In comparison SWE enables absolute quantification of tissue stiffness, but is at the same time obstructed by complex wave propagation behaviour and the need for tracking shear waves over a series of frames to reconstruct an imaged object. However, rather than competing against each other, the summarised efforts spent on atherosclerotic ultrasound elastography today clearly shows how refined plaque characterisation can be achieved by image-based

constitutive mapping. Isolation of vulnerable culprit lesions has a direct connection to improved patient outcome, and further advancements in the general field of cardiovascular ultrasound elastography bears high promise for improved health care.

To sum up, Study I-IV were all conducted with the aim of progressing cardiovascular SWE closer to clinical practice, refining data output and evaluating performance specifically for atherosclerotic plaque characterisation. The performed studies have all highlighted the importance of taking acoustic wave propagation into account when evaluating SWE output, with method accuracy and performance directly related to the behaviour of the assessed shear wave. In particular, combined group and phase velocity analysis provide a set of novel biomarkers for plaque risk stratification, showcasing exciting potential in detecting vulnerable culprit lesions *in-vivo*. In general, the ability to complement conventional structural imaging with non-invasive constitutive imaging by SWE has exciting clinical implementation, and could serve as an important tool for refined screening or assessment of atherosclerotic plaques as well as in the evaluation of early-stage cardiovascular remodelling.

6.2. Non-invasive cardiovascular relative pressure estimation

In the second part of this thesis, focus was shifted from constitutive assessment of the cardiovascular system, to hemodynamic evaluation of cardiovascular flow.

a) νWERP – Original method performance

In Study V, a novel method for non-invasive relative pressure assessment was introduced: νWERP. In νWERP, a complete fluid mechanical description of cardiovascular flow is utilised, using the concept of a *virtual field* to enable arbitrary probing of relative pressure throughout any imaged vascular structure. As shown in Study V, the method shows excellent accuracy in isolated patient-specific models, with precise relative pressures derived through complex, tortuous vasculatures, and with outputs being robust against high levels of added, spurious image noise. Furthermore, the method was also validated in a clinical *in-vivo* setting, where aortic relative pressures were successfully assessed in five adolescent patients with congenital cardiovascular disease. In fact, the utilised *in-vivo* cohort represented a particularly challenging study case, where the assessed hemodynamic environment was complicated by narrow aortic geometries and abnormal flow profiles [406]. With this in mind, the maintained νWERP accuracy underlines the method's versatility, enabling probing of relative pressure into previously inaccessible flow domains.

In Study V, analysis of νWERP spatiotemporal behaviour was performed using the simulated flow through a patient-specific AAD. As presented in Section 5.2., temporal sampling had slightly higher influence on output accuracy at the noise-free state, whereas a virtually equal influence was observed with introduced image

noise. As such, trade-off between spatial versus temporal resolution could be determined by the assessed flow rather than by the utilised method. If evaluating low flow domains with high anatomical constriction such as more peripheral vasculatures, high spatial resolution would be required to capture the assessed morphology. Conversely, higher temporal resolution might be required if evaluating quick transient events. Regardless, the versatility of νWERP makes it applicable in both scenarios, allowing for robust refined hemodynamic analysis of cardiovascular events.

For all vasculatures evaluated in Study V, relative pressures were also derived using a few alternative method approaches. However, applying these flow based estimates onto the unconventional and complex cases of Study V become problematic, specifically following these previous methods' inherent assumptions. The clinical standard of simplified Bernoulli [58, 313] relies on a single measure of peak velocity, and the extended unsteady Bernoulli also neglects a large portion of the assessed flow [62]. Consequently, significant errors are reported in Study V, in particular for the highly non-laminar AAD. The direct work-energy formulation WERP also deteriorates with vascular branching, and divergence is observed in low-flow diastolic regimes again making the method unfit for the assessed flows of Study V. With more refined full-field approaches such as PPE showing inferior behaviour even in simplified setups [322], this all underlines the novelty of νWERP, improving estimate accuracy and enabling the extension of relative pressure into unexplored flow domains.

b) νWERP-t – extension into turbulent flow domains

As presented in Study V, νWERP uses an explicit description of fluid mechanical behaviour to derive relative pressures over arbitrary flow segments. However, as reviewed in Section 3.1.4., the appearance of stochastic flow variations may induce turbulent energy dissipation, potentially influencing the assessed relative pressure. For severe degrees of stenosis, incoherent post-stenotic turbulence is a typically observed feature [81, 135], and similarly complex congenital disease may induce stochastic flow [407, 408]. With the *in-silico* cases of Study V retrieved as a synthetic measure over a single cardiac cycle only, and with the corresponding *in-vivo* cohort not necessarily inducing high-turbulent flows, such stochastic behaviour did thus not play a significant role for the retrieved results. However, to broaden method applicability, as well as to allow for the incorporation of turbulent cardiovascular flow scenarios, an appropriate method extension was implemented in Study VI.

In Study VI νWERP-t was presented, derived by statistically describing acquired flow as a mean field and a related covariance quantity, and including such behaviour in the evaluation of virtual work-energy. Applied on both stenotic *in-vitro* phantoms as well as appended cycles from the complex AAD of Study V (by so allowing for incoherent intra-cycle variation to occur), the method showed excellent accuracy with relative errors similar to that in Study V. Again comparing favourably against alternative approaches, the method also underlines the

versatility initially showcased in Study V, with the approach now handling not only multibranched, tortuous vasculatures, but also turbulence-inducing high-flow regimes.

In the comparison to other methods, the evaluation again becomes hampered by these alternative methods' inherent assumptions. Specifically real work-energy approaches such as WERP-t or TP will be obstructed by branching vasculatures where $Q|_{\Gamma_i} \neq Q|_{\Gamma_o}$, or in phases of low flow, where $Q \to 0$: both points highlighted in the *in-silico* results where severe method deterioration occurs during the later diastolic phase. However, the difference between νWERP-t and WERP-t in the steady-state stenotic phantoms is less intuitive. Without any low diastolic flows, and with a single-vessel geometry, νWERP-t and WERP-t should theoretically converge. However, WERP-t showcased a systematic underestimation of ΔP compared to νWERP.

One hypothesis explaining this difference could be that the acquired flow field is affected by high-turbulent noise, where the acquired mean quantity is shifted from its expected theoretical value. However, as shown by the extended results on noise-corrupted νWERP-t estimates in the appended paper in Part II, this hypothesis is not sufficient in explaining the observed discrepancy, and would rather cause a random shift around the accurate νWERP-t value.

Instead, a second explanation could be that the acquired flow field appears as non-divergence free (i.e. $\nabla \cdot \boldsymbol{V} \neq 0$), again following stochastic flow fluctuations in the assessed flow. If such would be the case, fundamental physical flow behaviour would be violated, and the derivation of WERP-t would no longer hold. However, νWERP-t would still be valid, as the introduced virtual field is guaranteed to be divergence free ($\nabla \cdot \boldsymbol{w} = 0$).

To test this hypothesis, an alternative divergence-free Stokes equivalent $\boldsymbol{V}^\dagger$ can be introduced, solved as

$$\boldsymbol{V}^\dagger + \nabla^2 \boldsymbol{V}^\dagger + \nabla \lambda = \boldsymbol{V} + \nabla^2 \boldsymbol{V} \tag{6.1}$$

$$\nabla \cdot \boldsymbol{V}^\dagger = 0 \tag{6.2}$$

$$\boldsymbol{V}^\dagger = \begin{cases} \boldsymbol{V}, & \Gamma_i \\ 0, & \Gamma_w \end{cases}. \tag{6.3}$$

With such, $\boldsymbol{V}^\dagger$ preserves the spatial properties of $\boldsymbol{V}$ whilst at the same time having a guaranteed divergence free behaviour.

In fact, if applying WERP-t on the Stokes equivalent $\boldsymbol{V}^\dagger$ of the *in-vitro* dataset, estimation output improves drastically, with only minor deviations observed

against the aforementioned νWERP-t results (comparative performance provided in the appended paper in Part II). Even in the *in-silico* dataset, this renders improved output accuracy where the initial systolic peak is recovered at higher precision using the divergence free WERP-t.

This does not only explain the observed discrepancy between νWERP-t and WERP-t, but does also provide further evidence of the advantages of νWERP-t: using the virtual approach divergence free flow behaviour is guaranteed, and regardless of flow variations robust output measures can be achieved. Along the same lines, the difference in energy weighting between virtual and real approach means that the different methods will rely differently on mean field and covariance data, respectively. With νWERP-t enhancing advective contributions over turbulent energy dissipation, the accuracy of the mean field estimation will be of higher importance compared to the accuracy of the covariance estimation, and vice versa in the real work-energy case. With covariance capture potentially sensitive to velocity encoding or apparent SNR [409-411] this might have clinical implications, however the general applicability of these results remains to be explored.

Continuing on the comparative performance in Study VI, the TP formulation is also worth commenting. The theoretical formulation of WERP-t and TP coincides for relative pressure exclusively governed by turbulent energy dissipation. However, distinct method differences are observed following the covariance filtering introduced in TP by Equation 4.45. As evident, the masking of non-positive covariance entries improves accuracy in the evaluated *in-vitro* set. Importantly however, is that there exists no theoretical reason to why such filtering would be applicable in an arbitrary flow case, and in reality negative off-diagonal covariance entries can very well appear (i.e. for $\mathrm{Cov}[\boldsymbol{v}_i, \boldsymbol{v}_j]$ in which $i \neq j$). As evident in the complex AAD, the masking of TP incorrectly exaggerates turbulent energy dissipation, skewing data output even further away from the true estimates, than WERP-t does. It remains to be clarified why TP performs satisfactory in the *in-vitro* cohort, but the general applicability of the masking seems doubtful.

In its presented form, νWERP and νWERP-t relies on full-field measurements of blood flow to derive accurate estimates of relative pressure. Simplifications into planar 2D flow acquisitions have been evaluated using the direct-work WERP method [64] and similar adjustments could be envisaged for the virtual approach. However, this would again involve reducing the complexity of the assessed fluid mechanical environment, and it remains to be determined how this would affect output accuracy, especially in the evaluated multibranched, tortuous vasculatures of Study V. Based on the rapid development of medical imaging, more complex data analysis is being brought into clinical practice, and 3D-based flow metrics could very well be incorporated into clinical diagnostics following promising clinical results [19, 218, 412, 413]. The progress in 3D ultrasound flow-imaging [185, 186] also indicates how such analysis would not be modality-specific, again showing defined promise for such refined clinical hemodynamic analysis.

c) Clinical applicability and potential of relative pressure analysis

With both νWERP and νWERP-t presented, and with the methods aimed at refined hemodynamic assessment, a final clinical investigation was performed in Study VII. The study not only showcased a clinical implementation of νWERP, but was also conducted using νWERP as a tool for assessing cardiovascular disease behaviour. Specifically, aortic hemodynamics was evaluated in a DCM cohort, investigating aortic relative pressure in cardiac disease. Importantly, as patients had time to respond to treatment between inclusion and imaging, the cohort was split in two: one group containing responding patients with recovered LV function, DCM_{mod}, and one containing non-responding patients with maintained reduced LV function, DCM_{red}. With that, the hemodynamic changes could also be inferred in conjunction to patient treatment response.

In short, the DCM_{red} group showed a significantly reduced maximum aortic relative pressure, whilst maintaining their minimum aortic relative pressure. The same group also indicated significantly increased PWV, aortic stiffness, and systolic blood pressure, whereas TTP was significantly increased in all DCM patients, regardless of LV status or treatment response.

The results are worth coupling to their relation to fundamental cardiovascular physiology. Firstly, maximum aortic relative pressure represents the forward-directed peak acceleration of ejected blood coming from the heart. That the DCM_{red} group showed an impaired peak acceleration is thus not surprising, and is also in-line with previous findings in DCM indicating deteriorating aortic outflow acceleration [414] and reduced LVOT outflow gradient [415] as a function of progressing disease. Together, the findings also illustrate how impaired ventricular function impacts downstream vascular hemodynamics, highlighting how vascular response could be used as a secondary measure of cardiac function.

Secondly, minimum aortic relative pressure is related to the deceleration of blood during late systole, and was seemingly not affected by the progressing disease. In fact, minimum aortic relative pressure has been less coupled to cardiac function, and is rather associated with aortic reservoir function [416]. A maintained minimum aortic relative pressure might thus indicate maintained reservoir behaviour, however, this is opposed by the significant differences inferred in aortic stiffness. Instead, the findings suggest a complex relationship between cardiac function, aortic behaviour, and derived relative pressure. In other conditions, aortic relative pressure has been associated to both cardiac and aortic function [220], further supporting this coupled notion.

Thirdly, TTP is a metric directly associated to the temporal pumping efficiency of the LV, where a shortened TTP indicates a faster ventricular contraction, and vice versa. With this in mind, it is noteworthy that all DCM subjects showed a significantly increased TTP, regardless of LV status. That is: even though patients respond differently to the administered treatment (with some indicating

significantly improved cardiac functionality), an underlying conductive deficiency seems to prevail. Ventricular conduction delay is commonly reported in DCM [417], and has also been shown to be one of the strongest predictors of long-term mortality [418]. Our results seem to indicate a remaining, latent conductive abnormality masked by the pharmaceutically improved cardiac output, and with idiopathic DCM connected to the development of heart failure [419], such underlying pathological remains could have detrimental long-term effects even when short-term cardiac recovery is observed.

Further, aortic stiffness directly relates to reservoir aortic function and the constitutive properties of the systemic vasculature. From the reported results, aortic stiffness was significantly increased in the DCM_{red} group, being in-line with previous findings on similar patients [420]. In general, aortic stiffening is a commonly described vascular response to cardiac deficiencies, where increasing stiffness may help to maintain an effective forward-flow of blood into the peripheral circulation. With such, the results again highlight how vascular adaption follows on cardiac disease, with aortic assessment potentially complementing existing clinical protocols.

Complementing the functional evaluation above, the correlation analysis indicated fairly weak relationships between aortic relative pressure and cardiac structural and functional metrics in DCM. This is worth contrasting to the clear differentiation observed with the derived aortic metrics. That is: the assessment of relative pressure successfully separates DCM patients with different cardiac function, however, is not strongly correlated to any conventional metric used to clinically assess such patients. Others have also indicated an independent association between aortic relative pressure and LV remodelling [421], highlighting relative pressure as a complementary and independent biomarker for refined cardiac diagnosis.

To isolate causal factors influencing aortic relative pressure an additional virtual *in-silico* cohort was also analysed. Results showed how reservoir aortic stiffness and radius were the two dominating factors influencing aortic relative pressure, with cardiac properties having a comparably inferior impact. The two however counteract in their influence on relative pressure: increasing aortic stiffness increases relative pressure, whereas increasing aortic area decreases relative pressure. With both stiffness and area increasing in the DCM_{red} group, the net decrease in maximum aortic relative pressure might thus not be completely clarified by these aortic components. Instead, the reduction could be attributed to cardiac changes such as modified contractility [422] or delayed contraction (as indicated by the increased TTP), however could just as well indicate a nonlinear coupling between individual reservoir factors. Regardless, the combined clinical and virtual results suggest that both reservoir and cardiac function is altered in DCM.

With several aortic hemodynamic factors altered in DCM, and with non-responding DCM_{red} patients showing different behaviour from responding DCM_{mod} patients, Study VII has one interesting clinical indication. Namely, that cardiac treatment efficacy might be coupled to vascular adaption abilities. In general, the antihypertensive treatment administered to the evaluated cohort has been shown to reduce both blood pressure and arterial stiffness [423], being part of a general strategy to reduce ventricular load. However, in the non-responding group, poor vascular adaption might render an ineffective response, keeping the ventricle in a state where excessive work is required to maintain systemic perfusion. Further, with sustained hypertension linked to aortic dilation [424], and with area shown to decrease relative pressure (from the virtual cohort results), the non-responders will experience decreasing acceleration of the ejected blood, despite working harder to maintain cardiac output. If further medication is introduced to force a decrease in aortic stiffness, a continuous depression in relative pressure will occur, pushing the patient down a detrimental pathological remodelling spiral. Thus, through poor adaption of the vasculature, the clinical treatment protocol fails to unload the heart. Coupling drug efficacy to arterial function is not a new concept [425], however our study indicates how a unified look at cardiac, aortic, and system function is required to successfully unload and treat pathological cardiac conditions.

To summarise, in Study V-VII a novel method for accurate probing of relative pressure was formulated, evaluated, validated, and clinically implemented. Results indicate improved estimation accuracy, and the preliminary clinical data in Study VII highlights how such refined assessment can aid in our understanding of cardiovascular disease. The introduction of refined imaging with enhanced diagnostic abilities and associated novel biomarkers is quickly helping clinicians to progress from a population-based to a patient-specific diagnostic approach. νWERP and νWERP-t are examples of such refined methods, opening up for the non-invasive evaluation of relative pressure through previously unexplored and inaccessible vasculatures. Its clinical impact remains to be determined, however incorporating hemodynamic behaviour into the overall assessment of cardiovascular disease is not to be overlooked.

6.3. Tomographic reconstruction for pre-clinical imaging

In Study VIII a multigrid reconstruction approach was presented, with specific application examples given for cardiovascular research (reconstructing both an endarterectomy *ex-vivo* plaque as well as a 3D printed CTA model of the thoracic vasculature). Conceptually, the approach uses domain splitting and connected operator masking to separate regions of different discretisation or regularisation, with cross-talk between regions handled through reduction and broadcast operators. While the method does not enhance the quality of available single-grid reconstructions, it does enable maintained accuracy within a pre-determined ROI even when the surrounding background is reconstructed at considerably lower quality. As shown, neither multigrid discretisation, regularisation, nor a

combination of discretisation and regularisation had any significant effect on ROI recovery in the evaluated numerical phantoms.

In addition to the maintained ROI image quality, a particular advantage of the developed multigrid reconstruction method lies in the resulting computational speed-up. If utilising a multigrid resolution approach with a coarsely discretised background, high-resolution ROI reconstructions can be achieved in less than 10% of the time required for a total complete reconstruction. With coarser background reconstruction resulting in decreased memory usage and less demanding forward and backward projections, the observed speed-up is not surprising, but the obtained results do indicate efficient implementation of the proposed multigrid approach. Furthermore, the method not only enables computational speed-up, but also allows for full-resolution ROI reconstruction in cases where complete full-resolution reconstructions would be obstructed by sheer data size. As exemplified by the utilised micro-CT system, 400 projections acquired at 2400x2400 pixels would result in sinogram data of approximately 8.3 GB. Even though physically permissible, forward and backward projection of such data would put high demands on available computational resources. Instead, the multigrid reconstruction approach allows for ROI-reconstruction at full resolution using conventional desktop computers.

It is important to note that the developed multigrid method only handles cases of ROI reconstruction in a completely acquired dataset, and that the method does not naturally translate into problems of so called local tomography where parts of the imaged objected is truncated during acquisition. For such, single-grid reconstruction methods have been proposed [426-429], and confusingly the term ROI reconstruction has also sometimes been used in this field [426-428]. In theory a combination of local tomography and multigrid reconstruction could very well be attempted, however was deemed beyond the scope of Study VIII.

Along the same lines it should also be noted that the presented approach assumes a-priori knowledge of the chosen multigrid ROI. That is: ROI positioning is provided as an input for the multigrid reconstruction method. Even though limiting potential out-of-view incidental findings, there are experimental settings where a-priori ROI positioning would be known. *Ex-vivo* imaging such as the endarterectomy sample is one example, and a cardiac ROI could very well be pre-determined in a thoracic scan. The presented multigrid method could even be utilised to generate a hierarchically discretised reconstruction following user-guided refinements of ROI positioning, and it should be noted that the presented multigrid approach is not limited to a single ROI, but can be expanded into multiple, or nested ROIs. Larger scan volume could thus be included in the multigrid setting, coarsely reconstructing larger volumes before potential nested refinements are introduced in a secondary step.

In Study VIII, the multigrid approach was presented in isolation and was only benchmarked against corresponding single-grid reconstruction results. Other

multiresolution reconstruction approaches have been proposed using either wavelets [430-432], or by imposing explicit continuity constraints on the boundary between ROI and background [433, 434]. In contrast to the presented multigrid approach, the boundary handling in [433, 434] might be advantageous in handling domain cross-talk, however the effect of imposed boundary conditions on the ROI reconstruction remains to be determined.

To summarise, in Study VIII a multigrid reconstruction approach was developed and verified in both a numerical and experimental setting. The method was specifically developed for the reconstruction of pre-clinical micro-CT data, where multigrid discretisation enables full-resolution ROI reconstructions and where a-priori ROI positioning is feasible when imaging *ex-vivo* structures or pre-determined objects. Work remains to be done in benchmarking against alternative approaches, however its usage for pre-clinical cardiovascular research was highlighted in Study III, as well as in experimental test results in Study VIII.

Chapter 7

Future outlook

Even though seemingly endless at the beginning, there is only so much you can do in five years of PhD studies. Importantly, the studies of this thesis are not providing finalised or completed forms of the presented methods, but are rather forming a foundation on which further developments, refinements, and clinical investigations can be performed. With such, there are several areas were future work can be envisaged and where continued research could lead to a matured clinical usage of the presented techniques.

SWE seems to have potential for improved atherosclerotic plaque characterisation, however, as indicated by the results of Study I-IV cardiovascular structures impose complex wave propagation response. Detailed technical investigations could thus be highly beneficial in understanding observed clinical response. Patient-specific modelling has been utilised to study acoustic response in atherosclerotic plaques [391-394], and experimental inverse modelling has also been attempted to describe mechanical plaque behaviour [399, 435]. Incorporating anisotropic or viscous tissue behaviour into such models could shed further light on the complex response of atherosclerotic SWE, and coupling pre-clinical data as such from Study III with histological validations could also be highly beneficial in deciphering defined tissue response. In particular SWE-based attenuation-mapping [436] could have specific potential for diagnostic plaque imaging, considering the importance of soft-tissue components on predicted plaque vulnerability.

If staying with the derived outputs of Study IV, the diagnostic abilities of SWE group and phase velocity should be studied in larger cohorts in order to clarify their clinical implications. Additionally, alternative image acquisition protocols should be explored to improve the frequency range over which phase velocities can be retrieved, as well as to map the robustness of the evaluated outputs. To this, shear wave tracking along tilted vessels or automated ECG triggered pushing could also be introduced to overcome potential practical issues related to clinical ultrasound elastography.

Looking ahead with regards to cardiovascular SWE, the transition from 2D to 3D imaging poses interesting technical challenges, and even though 3D strain imaging has been attempted by others [186, 196, 437] 3D ultrasound elastography plaque

imaging remains to be explored. Additionally, translation of SWE into myocardial assessment has clear clinical implications, especially considering the constitutive myocardial changes observed in heart failure patients [191], or following myocardial infarction [438]. Myocardial elastography is under exploration [439-441], however developments to handle temporal cardiac movements and aggravated image quality are still required.

For cardiovascular flow assessment, νWERP has exciting potential in advancing clinical assessments into previously unexplored vasculatures. Study VII showcases only one example of where novel hemodynamic assessment improves our understanding of cardiovascular disease, but many other application areas could be explored. Renal failure has been coupled to hemodynamic alterations [442], intraventricular flow and pressure changes seem determining in the long-term development of hypertrophic cardiomyopathy [89, 90], and flow disruptions are intrinsically coupled to the initiation and development of atherosclerosis [141, 443, 444]. Using νWERP on cerebrovascular flows, and mapping plaque phenotype to hemodynamic environment would be a very exciting method translation, coupling the developments in Study V-VII to the clinical question explored in Study I-IV.

With regards to the practical implementation of νWERP, development work is still required to create an automated and clinician-friendly user interface. The necessity of full-field data might also be slightly limiting in a clinical setting, wherefore translation into 2D flow assessments (as attempted with WERP in [64, 90]) could be explored. However, with the added clinical value of 4D flow MRI showcased in a number of studies [19, 22, 81, 218, 220, 413] and with 2D/3D Doppler ultrasound showing promising potential in preliminary studies [184-186] the clinical incorporation of full-field flow measurements could very well be realised in the near future.

The turbulence-driven behaviour in Study VI should also be explored in a clinical setting. Firstly, *in-vivo* validation of the method would be advisable, and secondly, specific method behaviour as a function of covariance or mean field quality could also be mapped in detail. Furthermore, with incoherent flow associated to a range of cardiovascular pathologies, the method could be applied in novel clinical settings exploring turbulence-induced pulmonary hypertension, mapping post-stenotic relative pressure in relation to bicuspid aortic valve disease and thoracic aortic aneurysms, or again assessing turbulent energy dissipation around plaque-prone vasculatures.

Lastly some methodological features of νWERP could also be further evaluated, implementing a temporally changing virtual field (suitable for e.g. intraventricular flows where the geometrical domain varies over time), or evaluating the effect of different virtual fields or boundary conditions on method accuracy and robustness.

For the multigrid reconstruction approach, a majority of the evaluation was performed on simplified numerical phantoms and further detailed validation in a

clinical setting could be beneficial. The introduced concept of domain splitting however opens up for interesting technical advancements, one being multithreaded parallelisation where full-field high-resolution reconstructions could be achieved by distributed multigrid solvers. Incorporating energy-dependent operators would be another possibility, especially if attempting an implementation towards spectral CT.

Chapter 8

Conclusion

The eight studies of this thesis have all been conducted with the same endeavour: to refine current state cardiovascular image diagnostics, and to improve our ability to non-invasively assess cardiovascular disease. The results have shown how non-invasive ultrasound Shear Wave Elastography (SWE) can be used to accurately quantify vascular stiffness as well as to differentiate atherosclerotic plaques of varying stiffness or rupture vulnerability. Furthermore, νWERP - a novel method for non-invasive relative pressure estimation – has been introduced and validated, with abilities spanning beyond state-of-the-art including assessments of turbulent, multi-branched, highly complex vasculatures, with a clinical implementation performed to highlight arterial changes in cardiac disease. Lastly, a study on pre-clinical image reconstruction has shown how high-resolution imaging can be achieved by effective domain splitting, proving valuable as a complementary tool in clinical research.

Specific conclusions from each of the eight included studies are summarised below.

Study I Geometrical confinement has a significant impact on SWE output accuracy. However, using appropriate frequency-based phase velocity analysis, accurate quantification of tissue stiffness can be achieved as demonstrated on tissue-mimicking arterial phantoms. On the contrary, spatiotemporal group velocity analysis with assumptions of infinite medium wave propagation systematically underestimates tissue stiffness when applied on geometrically confined media.

Study II SWE can be used to differentiate phantom plaques of different mechanical stiffness. However this ability seems directly dependent on the used wave speed metrics and image specifications, with longitudinal imaging using either group or high-frequency (≥1 kHz) phase velocity showing superior differentiability. Results also indicate that SWE accuracy and plaque differentiability is independent of push location.

Study III Using combined SWE and micro-CT imaging, changes in *ex-vivo* assessed shear wave group velocity seemed correlated with intraplaque composition. Isolated *ex-vivo* analysis using SWE was however aggravated by the irregular geometry and constricted size of the isolated plaque.

Study IV Non-invasive detection of vulnerable carotid plaque lesions can be achieved by combined group and phase velocity SWE analysis, as indicated by results from a clinical *in-vivo* cohort. Furthermore, the combined approach provides a set of biomarkers correlated to vulnerable plaque features, offering a more comprehensive mapping of plaque morphology in-clinics.

Study V Using the concept of virtual work-energy – isolating vascular regions by the introduction of a virtual field – the νWERP method can be used to accurately estimate cardiovascular relative pressures through arbitrary vasculatures. νWERP shows excellent performance in complex, patient-specific simulations, and also performs satisfactory in a validating *in-vivo* cohort.

Study VI By incorporating incoherent turbulent flow fluctuations in the theoretical derivation, an extended νWERP-t formulation can be utilised to estimate turbulence-driven relative pressures. νWERP-t compares favourably against alternative state-of-the-art methods, showing excellent accuracy in both *in-vitro* and *in-silico* tests.

Study VII Utilising non-invasive phase-contrast imaging, significant changes in aortic hemodynamics were observed in DCM patients. Specifically, decreased maximum positive relative pressure, increased time-to-peak relative pressure, as well as increased PWV and aortic stiffness were all inferred. With a virtual cohort analysis isolating arterial stiffness and area to be the determining factors influence relative pressure this signals a defined role of the arterial side even in cardiac disease, acting as a complement to conventional cardiac biomarkers and potentially linking vascular adaption to cardiac treatment efficacy.

Study VIII Using domain splitting and corresponding operator masking, tomographic multigrid image reconstruction can be achieved with both numerical and experimental tests indicating a significant computational speed-up compared to conventional full-resolution methods. Importantly, the proposed multigrid approach even allows for full-system high-resolution ROI reconstructions in cases where complete high-resolution reconstructions are complicated by sheer data size – as shown in a pre-clinical micro-CT system.

References

[1] M. Herzberger, "Optics from Euclid to Huygens," *Applied Optics,* vol. 5, pp. 1383-1393, 1966.

[2] I. Newton, *Opticks, or, a treatise of the reflections, refractions, inflections & colours of light*: Courier Corporation, 1952.

[3] N. Yao and Z. L. Wang, *Handbook of microscopy for nanotechnology*: Springer, 2005.

[4] N. Weiskopf, K. Mathiak, S. W. Bock, F. Scharnowski, R. Veit, W. Grodd*, et al.*, "Principles of a brain-computer interface (BCI) based on real-time functional magnetic resonance imaging (fMRI)," *IEEE transactions on biomedical engineering,* vol. 51, pp. 966-970, 2004.

[5] S. Mendis, P. Puska, B. Norrving, and W. H. Organization, *Global atlas on cardiovascular disease prevention and control*: Geneva: World Health Organization, 2011.

[6] M. D. Cheitlin, W. F. Armstrong, G. P. Aurigemma, G. A. Beller, F. Z. Bierman, J. L. Davis*, et al.*, "ACC/AHA/ASE 2003 guideline update for the clinical application of echocardiography: summary article: a report of the American College of Cardiology/American Heart Association Task Force on Practice Guidelines (ACC/AHA/ASE Committee to Update the 1997 Guidelines for the Clinical Application of Echocardiography)," *Journal of the American College of Cardiology,* vol. 42, pp. 954-970, 2003.

[7] S. B. King, S. C. Smith, J. W. Hirshfeld, D. A. Morrison, D. O. Williams, A. K. Jacobs*, et al.*, "2007 focused update of the ACC/AHA/SCAI 2005 guideline update for percutaneous coronary intervention," *Journal of the American College of Cardiology,* vol. 51, pp. 172-209, 2008.

[8] P. Greenland, J. S. Alpert, G. A. Beller, E. J. Benjamin, M. J. Budoff, Z. A. Fayad*, et al.*, "2010 ACCF/AHA guideline for assessment of cardiovascular risk in asymptomatic adults: a report of the American College of Cardiology Foundation/American Heart Association task force on practice guidelines developed in collaboration with the ASE, ASNC, SAIP, SCAI, SCCT, and SCMR," *Journal of the American College of Cardiology,* vol. 56, pp. e50-e103, 2010.

[9] R. M. Sigrist, J. Liau, A. El Kaffas, M. C. Chammas, and J. K. Willmann, "Ultrasound elastography: review of techniques and clinical applications," *Theranostics,* vol. 7, p. 1303, 2017.

[10] P. Dyverfeldt, M. Bissell, A. J. Barker, A. F. Bolger, C.-J. Carlhäll, T. Ebbers*, et al.*, "4D flow cardiovascular magnetic resonance consensus statement," *Journal of Cardiovascular Magnetic Resonance,* vol. 17, p. 1, 2015.

[11] D. A. Weber and M. Ivanovic, "Ultra-high-resolution imaging of small animals: implications for preclinical and research studies," *Journal of Nuclear Cardiology,* vol. 6, pp. 332-344, 1999.

[12] M. N. Levy, A. J. Pappano, and R. M. Berne, *Cardiovascular physiology* vol. 146: Mosby Elsevier Philadelphia, 2007.

[13] L. B. Rowell, "Human cardiovascular adjustments to exercise and thermal stress," *Physiological reviews,* vol. 54, pp. 75-159, 1974.

[14] W. Aoi and Y. Marunaka, "Importance of pH homeostasis in metabolic health and diseases: crucial role of membrane proton transport," *BioMed research international,* vol. 2014, 2014.

[15] M. Carlsson, M. Ugander, H. Mosén, T. Buhre, and H. Arheden, "Atrioventricular plane displacement is the major contributor to left ventricular pumping in healthy adults, athletes, and patients with dilated cardiomyopathy," *American Journal of Physiology-Heart and Circulatory Physiology,* vol. 292, pp. H1452-H1459, 2007.

[16] W. F. Boron and E. L. Boulpaep, *Medical Physiology*: Elsevier Health Sciences, 2016.

[17] L. A. Taber, D. A. Voronov, and A. Ramasubramanian, "The role of mechanical forces in the torsional component of cardiac looping," *Annals of the New York Academy of Sciences,* vol. 1188, pp. 103-110, 2010.

[18] P. J. Kilner, G.-Z. Yang, A. J. Wilkes, R. H. Mohiaddin, D. N. Firmin, and M. H. Yacoub, "Asymmetric redirection of flow through the heart," *Nature,* vol. 404, pp. 759-761, 2000.

[19] P. M. Arvidsson, S. J. Kovács, J. Töger, R. Borgquist, E. Heiberg, M. Carlsson*, et al.*, "Vortex ring behavior provides the epigenetic blueprint for the human heart," *Scientific reports,* vol. 6, 2016.

[20] D. D. Streeter Jr, H. M. Spotnitz, D. P. Patel, J. Ross Jr, and E. H. Sonnenblick, "Fiber orientation in the canine left ventricle during diastole and systole," *Circulation research,* vol. 24, pp. 339-347, 1969.

[21] H. L. Falsetti, M. S. Verani, C. J. Chen, and J. A. Cramer, "Regional pressure differences in the left ventricle," *Catheterization and cardiovascular diagnosis,* vol. 6, pp. 123-134, 1980.

[22] P. M. Arvidsson, J. Töger, G. Pedrizzetti, E. Heiberg, R. Borgquist, M. Carlsson*, et al.*, "Hemodynamic forces using 4D flow MRI: an independent biomarker of cardiac function in heart failure with left ventricular dyssynchrony?," *American journal of physiology. Heart and circulatory physiology,* 2018.

[23] A. Pasipoularides, "Clinical assesment of ventricular ejection dynamics with and without outflow obstruction," ed: Journal of the American College of Cardiology, 1990.

[24] P. P. Sengupta, B. K. Khandheria, J. Korinek, J. Wang, and M. Belohlavek, "Biphasic tissue Doppler waveforms during isovolumic phases are associated with asynchronous deformation of subendocardial and subepicardial layers," *Journal of applied physiology,* vol. 99, pp. 1104-1111, 2005.

[25] W. A. Goetz, E. Lansac, H.-S. Lim, P. A. Weber, and C. M. Duran, "Left ventricular endocardial longitudinal and transverse changes during isovolumic contraction and relaxation: a challenge," *American Journal of Physiology-Heart and Circulatory Physiology,* vol. 289, pp. H196-H201, 2005.

[26] M. I. Noble, "The contribution of blood momentum to left ventricular ejection in the dog," *Circulation research,* vol. 23, pp. 663-670, 1968.

[27] L. N. Katz, "The role played by the ventricular relaxation process in filling the ventricle," *American Journal of Physiology-Legacy Content,* vol. 95, pp. 542-553, 1930.

[28] G. A. Brecher and A. T. Kissen, "Ventricular diastolic suction at normal arterial pressures," *Circulation research,* vol. 6, pp. 100-106, 1958.

[29] L. Shmuylovich, C. S. Chung, and S. J. Kovács, "Point: Left ventricular volume during diastasis is the physiological in vivo equilibrium volume and is related to diastolic suction," *Journal of applied physiology,* vol. 109, pp. 606-608, 2010.

[30] L. H. Peterson, R. E. Jensen, and J. Parnell, "Mechanical properties of arteries in vivo," *Circulation Research,* vol. 8, pp. 622-639, 1960.

[31] D. Bergel, "The static elastic properties of the arterial wall," *The Journal of physiology,* vol. 156, pp. 445-457, 1961.
[32] P. B. Dobrin, "Mechanical properties of arteries," *Physiological reviews,* vol. 58, pp. 397-460, 1978.
[33] K. M. Thakali, J. J. Galligan, G. D. Fink, and S. W. Watts, "Arterial and venous function in hypertension," *Comprehensive Hypertension. Edinburgh, United Kingdom: Elsevier,* pp. 205-222, 2007.
[34] J. A. Vita and J. F. Keaney Jr, "Endothelial function: a barometer for cardiovascular risk?," ed: Am Heart Assoc, 2002.
[35] G. A. Holzapfel, T. C. Gasser, and R. W. Ogden, "A new constitutive framework for arterial wall mechanics and a comparative study of material models," *Journal of elasticity and the physical science of solids,* vol. 61, pp. 1-48, 2000.
[36] H. Wolinsky and S. Glagov, "A lamellar unit of aortic medial structure and function in mammals," *Circulation research,* vol. 20, pp. 99-111, 1967.
[37] M. K. O'Connell, S. Murthy, S. Phan, C. Xu, J. Buchanan, R. Spilker*, et al.*, "The three-dimensional micro-and nanostructure of the aortic medial lamellar unit measured using 3D confocal and electron microscopy imaging," *Matrix Biology,* vol. 27, pp. 171-181, 2008.
[38] Z. S. Jackson, A. I. Gotlieb, and B. L. Langille, "Wall tissue remodeling regulates longitudinal tension in arteries," *Circulation research,* vol. 90, pp. 918-925, 2002.
[39] T. C. Gasser, "The Biomechanical Rupture Risk Assessment of Abdominal Aortic Aneurysms—Method and Clinical Relevance," in *Biomedical Technology*, ed: Springer, 2018, pp. 233-253.
[40] A. J. Pappano and W. G. Wier, "Overview of the Circulation and Blood," *Cardiovascular Physiology,* pp. 1-9, 2013.
[41] B. Alberts, A. Johnson, J. Lewis, M. Raff, K. Roberts, and P. Walter, "Blood vessels and endothelial cells," in *Molecular Biology of the Cell. 4th edition*, ed: Garland Science, 2002.
[42] J. A. Chirinos, P. Segers, T. C. Gillebert, A. K. Gupta, M. L. De Buyzere, D. De Bacquer*, et al.*, "Arterial properties as determinants of time-varying myocardial stress in humans," *Hypertension,* vol. 60, pp. 64-70, 2012.
[43] N. Stergiopulos, J.-J. Meister, and N. Westerhof, "Determinants of stroke volume and systolic and diastolic aortic pressure," *American Journal of Physiology-Heart and Circulatory Physiology,* vol. 270, pp. H2050-H2059, 1996.
[44] D. Burkhoff, I. Mirsky, and H. Suga, "Assessment of systolic and diastolic ventricular properties via pressure-volume analysis: a guide for clinical, translational, and basic researchers," *American Journal of Physiology-Heart and Circulatory Physiology,* vol. 289, pp. H501-H512, 2005.
[45] B. D. Levine, L. D. Lane, J. C. Buckey, D. B. Friedman, and C. G. Blomqvist, "Left ventricular pressure-volume and Frank-Starling relations in endurance athletes. Implications for orthostatic tolerance and exercise performance," *Circulation,* vol. 84, pp. 1016-1023, 1991.
[46] W. L. Maughan, K. Sunagawa, D. Burkhoff, and K. Sagawa, "Effect of arterial impedance changes on the end-systolic pressure-volume relation," *Circulation Research,* vol. 54, pp. 595-602, 1984.
[47] D. Burkhoff, G. Sayer, D. Doshi, and N. Uriel, "Hemodynamics of mechanical circulatory support," *Journal of the American College of Cardiology,* vol. 66, pp. 2663-2674, 2015.

[48] G. Pedrizzetti, G. La Canna, O. Alfieri, and G. Tonti, "The vortex - an early predictor of cardiovascular outcome?," *Nature Reviews Cardiology,* vol. 11, pp. 545-553, 2014.

[49] Y. Richter and E. R. Edelman, "Cardiology is flow," *Circulation,* vol. 113, pp. 2679-2682, 2006.

[50] D. L. Fry, "Acute vascular endothelial changes associated with increased blood velocity gradients," *Circulation research,* vol. 22, pp. 165-197, 1968.

[51] S. Glagov, C. Zarins, D. P. Giddens, and D. N. Ku, "Hemodynamics and atherosclerosis. Insights and perspectives gained from studies of human arteries," *Archives of pathology & laboratory medicine,* vol. 112, pp. 1018-1031, 1988.

[52] J. N. Cohn, R. Ferrari, and N. Sharpe, "Cardiac remodeling—concepts and clinical implications: a consensus paper from an international forum on cardiac remodeling," *Journal of the American College of Cardiology,* vol. 35, pp. 569-582, 2000.

[53] B. L. Langille, "Arterial remodeling: relation to hemodynamics," *Canadian journal of physiology and pharmacology,* vol. 74, pp. 834-841, 1996.

[54] D. Bernoulli, *Hydrodynamica: sive de viribus et motibus fluidorum commentarii*: Johannis Reinholdi Dulseckeri, 1738.

[55] P. K. Kundu, I. M. Cohen, and D. Dowling, "Fluid Mechanics 4th," ed: Elsevier, 2008.

[56] D. J. Brown and F. W. Smith Jr, "Stenosis hemodynamics: from physical principles to clinical indices," *Journal of veterinary internal medicine,* vol. 16, pp. 650-657, 2002.

[57] M. S. Firstenberg, E. E. Abel, T. J. Papadimos, and R. S. Tripathi, "Nonconvective forces: a critical and often ignored component in the echocardiographic assessment of transvalvular pressure gradients," *Cardiology research and practice,* vol. 2012, 2012.

[58] J. N. Oshinski, W. J. Parks, C. P. Markou, H. L. Bergman, B. E. Larson, D. N. Ku*, et al.*, "Improved measurement of pressure gradients in aortic coarctation by magnetic resonance imaging," *Journal of the American College of Cardiology,* vol. 28, pp. 1818-1826, 1996.

[59] N. P. Jenkins and C. Ward, "Coarctation of the aorta: natural history and outcome after surgical treatment," *QJM: An International Journal of Medicine,* vol. 92, pp. 365-371, 1999.

[60] A. Vahanian, H. Baumgartner, J. Bax, E. Butchart, R. Dion, G. Filippatos*, et al.*, "Guidelines on the management of valvular heart disease: The Task Force on the Management of Valvular Heart Disease of the European Society of Cardiology," *European heart journal,* vol. 28, pp. 230-268, 2007.

[61] H. Baumgartner, V. Falk, J. J. Bax, M. De Bonis, C. Hamm, P. J. Holm*, et al.*, "2017 ESC/EACTS Guidelines for the management of valvular heart disease," *European Heart Journal,* vol. 38, pp. 2739-2791, 2017.

[62] M. S. Firstenberg, P. M. Vandervoort, N. L. Greenberg, N. G. Smedira, P. M. McCarthy, M. J. Garcia*, et al.*, "Noninvasive estimation of transmitral pressure drop across the normal mitral valve in humans: importance of convective and inertial forces during left ventricular filling," *Journal of the American College of Cardiology,* vol. 36, pp. 1942-1949, 2000.

[63] D. Marlevi, B. Ruijsink, M. Balmus, D. Dillon-Murphy, D. Fovargue, K. Pushparajah*, et al.*, "Estimation of Cardiovascular Relative Pressure Using Virtual Work-Energy," *Scientific reports,* vol. 9, p. 1375, 2019.

[64] F. Donati, S. Myerson, M. M. Bissell, N. P. Smith, S. Neubauer, M. J. Monaghan*, et al.*, "Beyond Bernoulli," *Circulation: Cardiovascular Imaging,* vol. 10, p. e005207, 2017.

[65] E. Riesenkampff, J. F. Fernandes, S. Meier, L. Goubergrits, S. Kropf, S. Schubert*, et al.*, "Pressure Fields by Flow-Sensitive, 4D, Velocity-Encoded CMR in Patients With Aortic Coarctation," *JACC: Cardiovascular Imaging,* vol. 7, pp. 920-926, 2014/09/01/ 2014.

[66] C. Vlachopoulos, M. O'Rourke, and W. W. Nichols, *McDonald's blood flow in arteries: theoretical, experimental and clinical principles*: CRC press, 2011.

[67] S.-W. Lee, D. S. Smith, F. Loth, P. F. Fischer, and H. S. Bassiouny, "Importance of flow division on transition to turbulence within an arteriovenous graft," *Journal of biomechanics,* vol. 40, pp. 981-992, 2007.

[68] K. Hutchison and E. Karpinski, "In vivo demonstration of flow recirculation and turbulence downstream of graded stenoses in canine arteries," *Journal of biomechanics,* vol. 18, pp. 285-296, 1985.

[69] Ø. Evju and K.-A. Mardal, "On the assumption of laminar flow in physiological flows: Cerebral aneurysms as an illustrative example," in *Modeling the Heart and the Circulatory System*, ed: Springer, 2015, pp. 177-195.

[70] J. Hinze, "Turbulence McGraw-Hill Book Company," *Inc., New York, NY,* p. 488, 1959.

[71] D. C. Wilcox, *Turbulence modeling for CFD* vol. 2: DCW industries La Canada, CA, 1998.

[72] S. M. Ross, *Introduction to probability models*: Academic press, 2014.

[73] P. Dyverfeldt, R. Gårdhagen, A. Sigfridsson, M. Karlsson, and T. Ebbers, "On MRI turbulence quantification," *Magnetic resonance imaging,* vol. 27, pp. 913-922, 2009.

[74] N. Wilson, S. Goldberg, D. Dickinson, and O. Scott, "Normal intracardiac and great artery blood velocity measurements by pulsed Doppler echocardiography," *Heart,* vol. 53, pp. 451-458, 1985.

[75] J. Töger, M. Kanski, M. Carlsson, S. J. Kovács, G. Söderlind, H. Arheden*, et al.*, "Vortex ring formation in the left ventricle of the heart: analysis by 4D flow MRI and Lagrangian coherent structures," *Annals of biomedical engineering,* vol. 40, pp. 2652-2662, 2012.

[76] M. Markl, P. J. Kilner, and T. Ebbers, "Comprehensive 4D velocity mapping of the heart and great vessels by cardiovascular magnetic resonance," *Journal of Cardiovascular Magnetic Resonance,* vol. 13, p. 7, 2011.

[77] K. Ivanov, M. Kalinina, and Y. I. Levkovich, "Blood flow velocity in capillaries of brain and muscles and its physiological significance," *Microvascular research,* vol. 22, pp. 143-155, 1981.

[78] R. A. Nishimura, C. M. Otto, R. O. Bonow, B. A. Carabello, J. P. Erwin, L. A. Fleisher*, et al.*, "2017 AHA/ACC focused update of the 2014 AHA/ACC guideline for the management of patients with valvular heart disease: a report of the American College of Cardiology/American Heart Association Task Force on Clinical Practice Guidelines," *Journal of the American College of Cardiology,* vol. 70, pp. 252-289, 2017.

[79] Z. Stankovic, B. D. Allen, J. Garcia, K. B. Jarvis, and M. Markl, "4D flow imaging with MRI," *Cardiovascular diagnosis and therapy,* vol. 4, pp. 173-192, 2014.

[80] J. Wong, R. Chabiniok, N. Dedieu, E. Sammut, T. Schaeffter, and R. Razavi, "Age-related changes in intraventricular kinetic energy: a physiological or

pathological adaptation?," *American Journal of Physiology-Heart and Circulatory Physiology,* vol. 310, pp. H747-H755, 2016.

[81] P. Dyverfeldt, M. D. Hope, E. E. Tseng, and D. Saloner, "Magnetic resonance measurement of turbulent kinetic energy for the estimation of irreversible pressure loss in aortic stenosis," *JACC: Cardiovascular Imaging,* vol. 6, pp. 64-71, 2013.

[82] H. Ha, J. Lantz, M. Ziegler, B. Casas, M. Karlsson, P. Dyverfeldt*, et al.*, "Estimating the irreversible pressure drop across a stenosis by quantifying turbulence production using 4D Flow MRI," *Scientific Reports,* vol. 7, 2017.

[83] R. M. Lang, M. Bierig, R. B. Devereux, F. A. Flachskampf, E. Foster, P. A. Pellikka*, et al.*, "Recommendations for chamber quantification," *European Heart Journal-Cardiovascular Imaging,* vol. 7, pp. 79-108, 2006.

[84] E. Stead, J. Warren, A. Merrill, and E. Brannon, "The cardiac output in male subjects as measured by the technique of right atrial catheterization. Normal values with observations on the effect of anxiety and tilting," *The Journal of clinical investigation,* vol. 24, pp. 326-331, 1945.

[85] S. C. Robinson and M. Brucer, "Range of normal blood pressure: a statistical and clinical study of 11,383 persons," *Archives of Internal Medicine,* vol. 64, pp. 409-444, 1939.

[86] T. G. Pickering, G. A. Harshfield, H. D. Kleinert, S. Blank, and J. H. Laragh, "Blood pressure during normal daily activities, sleep, and exercise: comparison of values in normal and hypertensive subjects," *Jama,* vol. 247, pp. 992-996, 1982.

[87] A. M. Master, L. I. Dublin, and H. H. Marks, "The normal blood pressure range and its clinical implications," *Journal of the American Medical Association,* vol. 143, pp. 1464-1470, 1950.

[88] A. Pappano and W. Wier, "Hemodynamics," *Cardiovascular Physiology,* pp. 119-33, 2013.

[89] M. S. Maron, I. Olivotto, S. Betocchi, S. A. Casey, J. R. Lesser, M. A. Losi*, et al.*, "Effect of left ventricular outflow tract obstruction on clinical outcome in hypertrophic cardiomyopathy," *New England Journal of Medicine,* vol. 348, pp. 295-303, 2003.

[90] P. M. Elliott, A. Anastasakis, M. A. Borger, M. Borggrefe, F. Cecchi, P. Charron*, et al.*, "2014 ESC Guidelines on diagnosis and management of hypertrophic cardiomyopathy: the Task Force for the Diagnosis and Management of Hypertrophic Cardiomyopathy of the European Society of Cardiology (ESC)," *European heart journal,* vol. 35, pp. 2733-2779, 2014.

[91] J. Eriksson, A. F. Bolger, T. Ebbers, and C. J. Carlhäll, "Assessment of left ventricular hemodynamic forces in healthy subjects and patients with dilated cardiomyopathy using 4D flow MRI," *Physiological reports,* vol. 4, p. e12685, 2016.

[92] P. H. Spooner, M. P. Perry, R. O. Brandenburg, and G. D. Pennock, "Increased intraventricular velocities: an unrecognized cause of systolic murmur in adults," *Journal of the American College of Cardiology,* vol. 32, pp. 1589-1595, 1998.

[93] G. A. Roth, C. Johnson, A. Abajobir, F. Abd-Allah, S. F. Abera, G. Abyu*, et al.*, "Global, regional, and national burden of cardiovascular diseases for 10 causes, 1990 to 2015," *Journal of the American College of Cardiology,* vol. 70, pp. 1-25, 2017.

[94] C. J. O'Donnell and E. G. Nabel, "Genomics of cardiovascular disease," *New England Journal of Medicine,* vol. 365, pp. 2098-2109, 2011.

[95] R. Estruch, E. Ros, J. Salas-Salvadó, M.-I. Covas, D. Corella, F. Arós*, et al.*, "Primary prevention of cardiovascular disease with a Mediterranean diet," *New England Journal of Medicine,* vol. 368, pp. 1279-1290, 2013.

[96] J. A. Ambrose and R. S. Barua, "The pathophysiology of cigarette smoking and cardiovascular disease: an update," *Journal of the American college of cardiology,* vol. 43, pp. 1731-1737, 2004.

[97] L. F. Van Gaal, I. L. Mertens, and E. Christophe, "Mechanisms linking obesity with cardiovascular disease," *Nature,* vol. 444, p. 875, 2006.

[98] J. L. Anderson and D. A. Morrow, "Acute myocardial infarction," *New England Journal of Medicine,* vol. 376, pp. 2053-2064, 2017.

[99] P. G. Steg, S. K. James, D. Atar, L. P. Badano, C. B. Lundqvist, M. A. Borger*, et al.*, "ESC Guidelines for the management of acute myocardial infarction in patients presenting with ST-segment elevation: The Task Force on the management of ST-segment elevation acute myocardial infarction of the European Society of Cardiology (ESC)," *European heart journal,* vol. 33, pp. 2569-2619, 2012.

[100] J. L. Anderson, C. D. Adams, E. M. Antman, C. R. Bridges, R. M. Califf, D. E. Casey*, et al.*, "ACC/AHA 2007 guidelines for the management of patients with unstable angina/non–ST-elevation myocardial infarction: a report of the American College of Cardiology/American Heart Association Task Force on Practice Guidelines," *Journal of the American College of Cardiology,* vol. 50, pp. e1-e157, 2007.

[101] T. Ramanathan and H. Skinner, "Coronary blood flow," *Continuing Education in Anaesthesia, Critical Care & Pain,* vol. 5, pp. 61-64, 2005.

[102] J.-W. Son, W.-J. Park, J.-H. Choi, H. Houle, M. A. Vannan, G.-R. Hong*, et al.*, "Abnormal left ventricular vortex flow patterns in association with left ventricular apical thrombus formation in patients with anterior myocardial infarction," *Circulation Journal,* vol. 76, pp. 2640-2646, 2012.

[103] S. D. Roes, S. Hammer, R. J. van der Geest, N. A. Marsan, J. J. Bax, H. J. Lamb*, et al.*, "Flow assessment through four heart valves simultaneously using 3-dimensional 3-directional velocity-encoded magnetic resonance imaging with retrospective valve tracking in healthy volunteers and patients with valvular regurgitation," *Investigative radiology,* vol. 44, pp. 669-675, 2009.

[104] L. Agati, S. Cimino, G. Tonti, F. Cicogna, V. Petronilli, L. De Luca*, et al.*, "Quantitative analysis of intraventricular blood flow dynamics by echocardiographic particle image velocimetry in patients with acute myocardial infarction at different stages of left ventricular dysfunction," *European Heart Journal–Cardiovascular Imaging,* vol. 15, pp. 1203-1212, 2014.

[105] A. Bergstra, T. Svilaas, D. van Veldhuisen, A. van den Heuvel, I. van der Horst, and F. Zijlstra, "Haemodynamic patterns in ST-elevation myocardial infarction: incidence and correlates of elevated filling pressures," *Netherlands Heart Journal,* vol. 15, pp. 95-99, 2007.

[106] J. Biller, W. M. Feinberg, J. E. Castaldo, A. D. Whittemore, R. E. Harbaugh, R. J. Dempsey*, et al.*, "Guidelines for carotid endarterectomy: a statement for healthcare professionals from a special writing group of the Stroke Council, American Heart Association," *Circulation,* vol. 97, pp. 501-509, 1998.

[107] G. L. Raff, A. Abidov, S. Achenbach, D. S. Berman, L. M. Boxt, M. J. Budoff*, et al.*, "SCCT guidelines for the interpretation and reporting of coronary computed tomographic angiography," *Journal of cardiovascular computed tomography,* vol. 3, pp. 122-136, 2009.

[108] P. A. Tonino, B. De Bruyne, N. H. Pijls, U. Siebert, F. Ikeno, M. vant Veer*, et al.*, "Fractional flow reserve versus angiography for guiding percutaneous coronary intervention," *New England Journal of Medicine,* vol. 360, pp. 213-224, 2009.

[109] B. J. Maron, J. A. Towbin, G. Thiene, C. Antzelevitch, D. Corrado, D. Arnett*, et al.*, "Contemporary definitions and classification of the cardiomyopathies: an American Heart Association scientific statement from the council on clinical cardiology, heart failure and transplantation committee; quality of care and outcomes research and functional genomics and translational biology interdisciplinary working groups; and council on epidemiology and prevention," *Circulation,* vol. 113, pp. 1807-1816, 2006.

[110] "Report of the 1995 World Health Organization/International Society and Federation of Cardiology Task Force on the Definition and Classification of Cardiomyopathies," *Circulation,* vol. 93, pp. 841-842, 1996.

[111] P. H. Gibson, H. Becher, and J. B. Choy, "Classification of left ventricular size: diameter or volume with contrast echocardiography?," *Open Heart,* vol. 1, p. e000147, 2014.

[112] A. Gavazzi, R. De Maria, G. Renosto, A. Moro, M. Borgia, A. Caroli*, et al.*, "The spectrum of left ventricular size in dilated cardiomyopathy: clinical correlates and prognostic implications. SPIC (Italian Multicenter Cardiomyopathy Study) Group," *Am Heart J,* vol. 125, pp. 410-22, Feb 1993.

[113] A. G. Japp, A. Gulati, S. A. Cook, M. R. Cowie, and S. K. Prasad, "The diagnosis and evaluation of dilated cardiomyopathy," *Journal of the American College of Cardiology,* vol. 67, pp. 2996-3010, 2016.

[114] C. S. Rihal, R. A. Nishimura, L. K. Hatle, K. R. Bailey, and A. J. Tajik, "Systolic and diastolic dysfunction in patients with clinical diagnosis of dilated cardiomyopathy. Relation to symptoms and prognosis," *Circulation,* vol. 90, pp. 2772-2779, 1994.

[115] R. G. Assomull, S. K. Prasad, J. Lyne, G. Smith, E. D. Burman, M. Khan*, et al.*, "Cardiovascular magnetic resonance, fibrosis, and prognosis in dilated cardiomyopathy," *Journal of the American College of Cardiology,* vol. 48, pp. 1977-1985, 2006.

[116] E. Begic, Z. Begic, and N. Naser, "Clinical Course and Treatment of Dilated Cardiomyopathy During Twenty Years of Follow-up," *Medical Archives,* vol. 72, p. 68, 2018.

[117] C.-M. Yu, W.-H. Fung, H. Lin, Q. Zhang, J. E. Sanderson, and C.-P. Lau, "Predictors of left ventricular reverse remodeling after cardiac resynchronization therapy for heart failure secondary to idiopathic dilated or ischemic cardiomyopathy," *The American journal of cardiology,* vol. 91, pp. 684-688, 2003.

[118] G. Hasenfuss, C. Holubarsch, H.-P. Hermann, K. Astheimer, B. Pleske, and H. Just, "Influence of the force—frequency relationship on haemodynamics and left ventricular function in patients with non-failing hearts and in patients with dilated cardiomyopathy," *European heart journal,* vol. 15, pp. 164-170, 1994.

[119] A. F. Bolger, E. Heiberg, M. Karlsson, L. Wigström, J. Engvall, A. Sigfridsson*, et al.*, "Transit of blood flow through the human left ventricle mapped by cardiovascular magnetic resonance," *Journal of Cardiovascular Magnetic Resonance,* vol. 9, pp. 741-747, 2007.

[120] J. M. Lee, J. J. Park, H. W. Jung, Y.-S. Cho, I.-Y. Oh, C.-H. Yoon*, et al.*, "Left ventricular thrombus and subsequent thromboembolism, comparison of anticoagulation, surgical removal, and antiplatelet agents," *Journal of atherosclerosis and thrombosis,* p. 13540, 2012.

[121] M. N. Hirt, N. A. Sörensen, L. M. Bartholdt, J. Boeddinghaus, S. Schaaf, A. Eder*, et al.*, "Increased afterload induces pathological cardiac hypertrophy: a new in vitro model," *Basic research in cardiology,* vol. 107, p. 307, 2012.

[122] B. J. Gersh, B. J. Maron, R. O. Bonow, J. A. Dearani, M. A. Fifer, M. S. Link*, et al.*, "2011 ACCF/AHA guideline for the diagnosis and treatment of hypertrophic cardiomyopathy: a report of the American College of Cardiology Foundation/American Heart Association Task Force on practice guidelines," *Journal of the American College of Cardiology,* vol. 58, pp. e212-e260, 2011.

[123] P. M. Shah, "Hypertrophic cardiomyopathy and diastolic dysfunction," ed: Journal of the American College of Cardiology, 2003.

[124] J. K. Gwathmey, S. E. Warren, G. M. Briggs, L. Copelas, M. D. Feldman, P. J. Phillips*, et al.*, "Diastolic dysfunction in hypertrophic cardiomyopathy. Effect on active force generation during systole," *The Journal of clinical investigation,* vol. 87, pp. 1023-1031, 1991.

[125] E. D. Wigle, H. Rakowski, B. P. Kimball, and W. G. Williams, "Hypertrophic cardiomyopathy: clinical spectrum and treatment," *Circulation,* vol. 92, pp. 1680-1692, 1995.

[126] A. C. To, A. Dhillon, and M. Y. Desai, "Cardiac magnetic resonance in hypertrophic cardiomyopathy," *JACC: Cardiovascular Imaging,* vol. 4, pp. 1123-1137, 2011.

[127] A. B. Lewis, "Clinical profile and outcome of restrictive cardiomyopathy in children," *American heart journal,* vol. 123, pp. 1589-1593, 1992.

[128] S. S. Kushwaha, J. T. Fallon, and V. Fuster, "Restrictive cardiomyopathy," *New England Journal of Medicine,* vol. 336, pp. 267-276, 1997.

[129] J. R. Benotti, W. Grossman, and P. F. Cohn, "Clinical profile of restrictive cardiomyopathy," *Circulation,* vol. 61, pp. 1206-1212, 1980.

[130] S. A. Hunt, "ACC/AHA 2005 guideline update for the diagnosis and management of chronic heart failure in the adult: a report of the American College of Cardiology/American Heart Association Task Force on Practice Guidelines (Writing Committee to Update the 2001 Guidelines for the Evaluation and Management of Heart Failure)," *Journal of the American College of Cardiology,* vol. 46, pp. e1-e82, 2005.

[131] C. M. Otto, J. Kuusisto, D. D. Reichenbach, A. M. Gown, and K. D. O'Brien, "Characterization of the early lesion of'degenerative'valvular aortic stenosis. Histological and immunohistochemical studies," *Circulation,* vol. 90, pp. 844-853, 1994.

[132] A. Carpentier, B. Branchini, J. Cour, E. Asfaou, M. Villani, A. Deloche*, et al.*, "Congenital malformations of the mitral valve in children. Pathology and surgical treatment," *The Journal of thoracic and cardiovascular surgery,* vol. 72, pp. 854-866, 1976.

[133] K. Maganti, V. H. Rigolin, M. E. Sarano, and R. O. Bonow, "Valvular heart disease: diagnosis and management," in *Mayo Clinic Proceedings*, 2010, pp. 483-500.

[134] R. A. Nishimura, C. M. Otto, R. O. Bonow, B. A. Carabello, J. P. Erwin, R. A. Guyton*, et al.*, "2014 AHA/ACC Guideline for the management of patients with valvular heart disease: executive summary," *Circulation,* p. CIR. 0000000000000029, 2014.

[135] W. Schöbel, W. Voelker, K. Haase, and K.-R. Karsch, "Extent, determinants and clinical importance of pressure recovery in patients with aortic valve stenosis," *European heart journal,* vol. 20, pp. 1355-1363, 1999.

[136] H. Boudoulas, A. J. Kolibash Jr, P. Baker, B. D. King, and C. F. Wooley, "Mitral valve prolapse and the mitral valve prolapse syndrome: a diagnostic classification and pathogenesis of symptoms," *American heart journal,* vol. 118, pp. 796-818, 1989.

[137] L. H. Cohn, G. S. Couper, S. F. Aranki, R. J. Rizzo, N. M. Kinchla, and J. J. Collins, "Long-term results of mitral valve reconstruction for regurgitation of the myxomatous mitral valve," *The Journal of thoracic and cardiovascular surgery,* vol. 107, pp. 143-151, 1994.

[138] B. A. Carabello, "Ventricular Adaptation to Valvular Heart Disease," in *Valvular Heart Disease*, ed: Springer, 2009, pp. 59-72.

[139] P. Libby, P. M. Ridker, and G. K. Hansson, "Progress and challenges in translating the biology of atherosclerosis," *Nature,* vol. 473, p. 317, 2011.

[140] J.-M. Cai, T. S. Hatsukami, M. S. Ferguson, R. Small, N. L. Polissar, and C. Yuan, "Classification of human carotid atherosclerotic lesions with in vivo multicontrast magnetic resonance imaging," *Circulation,* vol. 106, pp. 1368-1373, 2002.

[141] M. Naghavi, P. Libby, E. Falk, S. W. Casscells, S. Litovsky, J. Rumberger*, et al.*, "From vulnerable plaque to vulnerable patient a call for new definitions and risk assessment strategies: part I," *Circulation,* vol. 108, pp. 1664-1672, 2003.

[142] M. Naghavi, P. Libby, E. Falk, S. W. Casscells, S. Litovsky, J. Rumberger*, et al.*, "From vulnerable plaque to vulnerable patient a call for new definitions and risk assessment strategies: Part II," *Circulation,* vol. 108, pp. 1772-1778, 2003.

[143] I. Tabas, K. J. Williams, and J. Borén, "Subendothelial lipoprotein retention as the initiating process in atherosclerosis: update and therapeutic implications," *Circulation,* vol. 116, pp. 1832-1844, 2007.

[144] N. J. Stone, J. G. Robinson, A. H. Lichtenstein, C. N. B. Merz, C. B. Blum, R. H. Eckel*, et al.*, "2013 ACC/AHA guideline on the treatment of blood cholesterol to reduce atherosclerotic cardiovascular risk in adults: a report of the American College of Cardiology/American Heart Association Task Force on Practice Guidelines," *Journal of the American College of Cardiology,* vol. 63, pp. 2889-2934, 2014.

[145] W. Hollander, "Role of hypertension in atherosclerosis and cardiovascular disease," *The American journal of cardiology,* vol. 38, pp. 786-800, 1976.

[146] J. A. Beckman, M. A. Creager, and P. Libby, "Diabetes and atherosclerosis: epidemiology, pathophysiology, and management," *Jama,* vol. 287, pp. 2570-2581, 2002.

[147] J. L. Goldstein, Y. Ho, S. K. Basu, and M. S. Brown, "Binding site on macrophages that mediates uptake and degradation of acetylated low density lipoprotein, producing massive cholesterol deposition," *Proceedings of the National Academy of Sciences,* vol. 76, pp. 333-337, 1979.

[148] I. Tabas, G. García-Cardeña, and G. K. Owens, "Recent insights into the cellular biology of atherosclerosis," *J cell Biol,* vol. 209, pp. 13-22, 2015.

[149] J. Nelson, O. Wani, H. May, and M. Budoff, "Potential benefits of eicosapentaenoic acid on atherosclerotic plaques," *Vascular pharmacology,* vol. 91, pp. 1-9, 2017.

[150] F. Otsuka, K. Sakakura, K. Yahagi, M. Joner, and R. Virmani, "Has our understanding of calcification in human coronary atherosclerosis progressed?," *Arteriosclerosis, thrombosis, and vascular biology,* vol. 34, pp. 724-736, 2014.

[151] H. C. Stary, "Natural history and histological classification of atherosclerotic lesions: an update," *Arteriosclerosis, thrombosis, and vascular biology,* vol. 20, pp. 1177-1178, 2000.

[152] P. K. Shah, "Mechanisms of plaque vulnerability and rupture," *Journal of the American college of cardiology,* vol. 41, pp. S15-S22, 2003.

[153] P. T. Kovanen, M. Kaartinen, and T. Paavonen, "Infiltrates of activated mast cells at the site of coronary atheromatous erosion or rupture in myocardial infarction," *Circulation,* vol. 92, pp. 1084-1088, 1995.

[154] K. A. Eagle, R. A. Guyton, R. Davidoff, F. H. Edwards, G. A. Ewy, T. J. Gardner*, et al.*, "ACC/AHA 2004 guideline update for coronary artery bypass graft surgery: a report of the American College of Cardiology/American Heart Association Task Force on Practice Guidelines (Committee to Update the 1999 Guidelines for Coronary Artery Bypass Graft Surgery)," *Circulation,* vol. 110, p. e340, 2004.

[155] W. C. Little, M. Constantinescu, R. J. Applegate, M. A. Kutcher, M. T. Burrows, F. R. Kahl*, et al.*, "Can coronary angiography predict the site of a subsequent myocardial infarction in patients with mild-to-moderate coronary artery disease?," *Circulation,* vol. 78, pp. 1157-1166, 1988.

[156] D. Giroud, J. M. Li, P. Urban, B. Meier, and W. Rutishauser, "Relation of the site of acute myocardial infarction to the most severe coronary arterial stenosis at prior angiography," *The American journal of cardiology,* vol. 69, pp. 729-732, 1992.

[157] D. Kardoulas, A. Katsamouris, P. T. Gallis, T. P. Philippides, N. Anagnostakos, D. Gorgoyannis*, et al.*, "Ultrasonographic and histologic characteristics of symptom-free and symptomatic carotid plaque," *Cardiovascular surgery,* vol. 4, pp. 580-590, 1996.

[158] P. Libby, P. M. Ridker, and A. Maseri, "Inflammation and atherosclerosis," *Circulation,* vol. 105, pp. 1135-1143, 2002.

[159] Z. Li, V. Taviani, T. Tang, U. Sadat, V. Young, A. Patterson*, et al.*, "The mechanical triggers of plaque rupture: shear stress vs pressure gradient," *The British journal of radiology,* vol. 82, pp. S39-S45, 2009.

[160] Z.-Y. Li and J. H. Gillard, "Plaque rupture: plaque stress, shear stress, and pressure drop," *Journal of the American College of Cardiology,* vol. 52, pp. 499-500, 2008.

[161] G. Mancia, R. Fagard, K. Narkiewicz, J. Redán, A. Zanchetti, M. Böhm*, et al.*, "2013 Practice guidelines for the management of arterial hypertension of the European Society of Hypertension (ESH) and the European Society of Cardiology (ESC): ESH/ESC Task Force for the Management of Arterial Hypertension," *Journal of hypertension,* vol. 31, pp. 1925-1938, 2013.

[162] S. Lewington, R. Clarke, N. Qizilbash, R. Peto, R. Collins, and P. S. Collaboration, "Age-specific relevance of usual blood pressure to vascular mortality: a meta-analysis of individual data for one million adults in 61 prospective studies," *The Lancet,* vol. 360, pp. 1903-1913, 2002.

[163] P. M. Kearney, M. Whelton, K. Reynolds, P. Muntner, P. K. Whelton, and J. He, "Global burden of hypertension: analysis of worldwide data," *The lancet,* vol. 365, pp. 217-223, 2005.

[164] A. M. Sinclair, C. G. Isles, I. Brown, H. Cameron, G. D. Murray, and J. W. Robertson, "Secondary hypertension in a blood pressure clinic," *Archives of Internal Medicine,* vol. 147, pp. 1289-1293, 1987.

[165] T. T. Kek, D. Erdogan, S. S. T. Kek, V. Akkaya, and M. ö. Zcan, "Changes in left ventricular outflow and intraventricular flow patterns in hypertension and controls: A Doppler echocardiographic study," *Acta cardiologica,* vol. 60, pp. 333-336, 2005.

[166] T. Wakatsuki, J. Schlessinger, and E. L. Elson, "The biochemical response of the heart to hypertension and exercise," *Trends in biochemical sciences,* vol. 29, pp. 609-617, 2004.

[167] C. S. Lam, V. L. Roger, R. J. Rodeheffer, B. A. Borlaug, F. T. Enders, and M. M. Redfield, "Pulmonary hypertension in heart failure with preserved ejection fraction: a community-based study," *Journal of the American College of Cardiology,* vol. 53, pp. 1119-1126, 2009.

[168] D. Chemla, V. Castelain, P. Herve, Y. Lecarpentier, and S. Brimioulle, "Haemodynamic evaluation of pulmonary hypertension," *European Respiratory Journal,* vol. 20, pp. 1314-1331, 2002.

[169] M. F. O'Rourke, "Arterial aging: pathophysiological principles," *Vascular medicine,* vol. 12, pp. 329-341, 2007.

[170] S. Huveneers, M. J. Daemen, and P. L. Hordijk, "Between Rho (k) and a hard place: the relation between vessel wall stiffness, endothelial contractility, and cardiovascular disease," *Circulation research,* vol. 116, pp. 895-908, 2015.

[171] R. M. Weisbrod, T. Shiang, L. Al Sayah, J. L. Fry, S. Bajpai, C. A. Reinhart-King, *et al.*, "Arterial stiffening precedes systolic hypertension in diet-induced obesity," *Hypertension,* vol. 62, pp. 1105-1110, 2013.

[172] M. D. Reller, M. J. Strickland, T. Riehle-Colarusso, W. T. Mahle, and A. Correa, "Prevalence of congenital heart defects in metropolitan Atlanta, 1998-2005," *The Journal of pediatrics,* vol. 153, pp. 807-813, 2008.

[173] J. F. Parker, B. Farrell, D. Streeten, M. Blackman, H. Sondheimer, and J. G. Anderson, "Hypertensive mechanisms in coarctation of the aorta. Further studies of the renin-angiotensin system," *The Journal of thoracic and cardiovascular surgery,* vol. 80, pp. 568-573, 1980.

[174] A. E. Hirst, V. J. Johns, and S. W. Kime, "Dissecting aneurysm of the aorta: a review of 505 cases," *Medicine,* vol. 37, p. 217, 1958.

[175] W. D. Edwards, D. S. Leaf, and J. E. Edwards, "Dissecting aortic aneurysm associated with congenital bicuspid aortic valve," *Circulation,* vol. 57, pp. 1022-1025, 1978.

[176] E. W. Larson and W. D. Edwards, "Risk factors for aortic dissection: a necropsy study of 161 cases," *The American journal of cardiology,* vol. 53, pp. 849-855, 1984.

[177] D. Dillon-Murphy, A. Noorani, D. Nordsletten, and C. A. Figueroa, "Multi-modality image-based computational analysis of haemodynamics in aortic dissection," *Biomechanics and modeling in mechanobiology,* vol. 15, pp. 857-876, 2016.

[178] K. T. Dussik, "Über die Möglichkeit, hochfrequente mechanische Schwingungen als diagnostisches Hilfsmittel zu verwerten," *Zeitschrift für die gesamte Neurologie und Psychiatrie,* vol. 174, pp. 153-168, 1942.

[179] I. Edler and C. H. Hertz, "The use of ultrasonic reflectoscope for the continuous recording of the movements of heart walls," *Clinical physiology and functional imaging,* vol. 24, pp. 118-136, 2004.

[180] J. P. Bingham, *Ultrasonic guided wave interpretation for structural health inspections*: The College of William and Mary, 2008.

[181] A. Burtin, N. Hovius, and J. M. Turowski, "Seismic monitoring of torrential and fluvial processes," *Earth Surface Dynamics,* vol. 4, 2016.

[182] A. P. Sarvazyan, O. V. Rudenko, S. D. Swanson, J. B. Fowlkes, and S. Y. Emelianov, "Shear wave elasticity imaging: a new ultrasonic technology of medical diagnostics," *Ultrasound in medicine & biology,* vol. 24, pp. 1419-1435, 1998.

[183] P. Hoskins, "A review of the measurement of blood velocity and related quantities using Doppler ultrasound," *Proceedings of the Institution of Mechanical Engineers, Part H: Journal of Engineering in Medicine,* vol. 213, pp. 391-400, 1999.

[184] J. A. Jensen and P. Munk, "A new method for estimation of velocity vectors," *IEEE transactions on ultrasonics, ferroelectrics, and frequency control,* vol. 45, pp. 837-851, 1998.
[185] M. Correia, J. Provost, M. Tanter, and M. Pernot, "4D ultrafast ultrasound flow imaging: in vivo quantification of arterial volumetric flow rate in a single heartbeat," *Physics in Medicine & Biology,* vol. 61, p. L48, 2016.
[186] J. Provost, C. Papadacci, J. E. Arango, M. Imbault, M. Fink, J.-L. Gennisson*, et al.*, "3D ultrafast ultrasound imaging in vivo," *Physics in medicine and biology,* vol. 59, p. L1, 2014.
[187] J. Ophir, I. Cespedes, H. Ponnekanti, Y. Yazdi, and X. Li, "Elastography: a quantitative method for imaging the elasticity of biological tissues," *Ultrasonic imaging,* vol. 13, pp. 111-134, 1991.
[188] V. W. S. Wong, J. Vergniol, G. L. H. Wong, J. Foucher, H. L. Y. Chan, B. Le Bail*, et al.*, "Diagnosis of fibrosis and cirrhosis using liver stiffness measurement in nonalcoholic fatty liver disease," *Hepatology,* vol. 51, pp. 454-462, 2010.
[189] S. E. Cross, Y.-S. Jin, J. Rao, and J. K. Gimzewski, "Nanomechanical analysis of cells from cancer patients," *Nature nanotechnology,* vol. 2, p. 780, 2007.
[190] S. Suresh, "Biomechanics and biophysics of cancer cells," *Acta Materialia,* vol. 55, pp. 3989-4014, 2007.
[191] B. A. Borlaug, C. S. Lam, V. L. Roger, R. J. Rodeheffer, and M. M. Redfield, "Contractility and ventricular systolic stiffening in hypertensive heart disease: insights into the pathogenesis of heart failure with preserved ejection fraction," *Journal of the American College of Cardiology,* vol. 54, pp. 410-418, 2009.
[192] C. Naim, G. Cloutier, E. Mercure, F. Destrempes, Z. Qin, W. El-Abyad*, et al.*, "Characterisation of carotid plaques with ultrasound elastography: feasibility and correlation with high-resolution magnetic resonance imaging," *European radiology,* vol. 23, pp. 2030-2041, 2013.
[193] J. R. Doherty, G. E. Trahey, K. R. Nightingale, and M. L. Palmeri, "Acoustic radiation force elasticity imaging in diagnostic ultrasound," *IEEE transactions on ultrasonics, ferroelectrics, and frequency control,* vol. 60, pp. 685-701, 2013.
[194] C. L. De Korte and A. F. Van Der Steen, "Intravascular ultrasound elastography: an overview," *Ultrasonics,* vol. 40, pp. 859-865, 2002.
[195] I. Z. Nenadic, M. W. Urban, J. F. Greenleaf, J.-L. Gennisson, M. Bernal, and M. Tanter, *Ultrasound Elastography for Biomedical Applications and Medicine*: Wiley, 2019.
[196] K. Nightingale, "Acoustic radiation force impulse (ARFI) imaging: a review," *Current medical imaging reviews,* vol. 7, pp. 328-339, 2011.
[197] P. Song, X. Bi, D. C. Mellema, A. Manduca, M. W. Urban, J. F. Greenleaf*, et al.*, "Quantitative assessment of left ventricular diastolic stiffness using cardiac shear wave elastography: a pilot study," *Journal of Ultrasound in Medicine,* vol. 35, pp. 1419-1427, 2016.
[198] E. Widman, E. Maksuti, C. Amador, M. W. Urban, K. Caidahl, and M. Larsson, "Shear wave elastography quantifies stiffness in ex vivo porcine artery with stiffened arterial region," *Ultrasound in Medicine and Biology,* vol. 42, pp. 2423-2435, 2016.
[199] M. Tanter and M. Fink, "Ultrafast imaging in biomedical ultrasound," *IEEE transactions on ultrasonics, ferroelectrics, and frequency control,* vol. 61, pp. 102-119, 2014.
[200] T. Loupas, J. Powers, and R. W. Gill, "An axial velocity estimator for ultrasound blood flow imaging, based on a full evaluation of the Doppler equation by means of a two-dimensional autocorrelation approach," *IEEE transactions on ultrasonics, ferroelectrics, and frequency control,* vol. 42, pp. 672-688, 1995.

[201] H. Lamb, "On waves in an elastic plate," *Proceedings of the Royal Society of London. Series A, Containing papers of a mathematical and physical character,* vol. 93, pp. 114-128, 1917.

[202] D. C. Gazis, "Three-Dimensional Investigation of the Propagation of Waves in Hollow Circular Cylinders. I. Analytical Foundation," *The Journal of the Acoustical Society of America,* vol. 31, pp. 568-573, 1959.

[203] M. Bernal, I. Nenadic, M. W. Urban, and J. F. Greenleaf, "Material property estimation for tubes and arteries using ultrasound radiation force and analysis of propagating modes," *The Journal of the Acoustical Society of America,* vol. 129, pp. 1344-1354, 2011.

[204] I. I. Rabi, J. R. Zacharias, S. Millman, and P. Kusch, "A new method of measuring nuclear magnetic moment," *Physical Review,* vol. 53, p. 318, 1938.

[205] P. C. Lauterbur, "Image formation by induced local interactions: examples employing nuclear magnetic resonance," 1973.

[206] F. Bloch, "Nuclear induction," *Physical review,* vol. 70, p. 460, 1946.

[207] E. M. Purcell, H. C. Torrey, and R. V. Pound, "Resonance absorption by nuclear magnetic moments in a solid," *Physical review,* vol. 69, p. 37, 1946.

[208] B. F. Byrd III, N. B. Schiller, E. H. Botvinick, and C. B. Higgins, "Normal cardiac dimensions by magnetic resonance imaging," *The American journal of cardiology,* vol. 55, pp. 1440-1442, 1985.

[209] P. Hunold, T. Schlosser, F. M. Vogt, H. Eggebrecht, A. Schmermund, O. Bruder*, et al.*, "Myocardial late enhancement in contrast-enhanced cardiac MRI: distinction between infarction scar and non–infarction-related disease," *American Journal of Roentgenology,* vol. 184, pp. 1420-1426, 2005.

[210] T. G. Reese, R. M. Weisskoff, R. N. Smith, B. R. Rosen, R. E. Dinsmore, and V. J. Wedeen, "Imaging myocardial fiber architecture in vivo with magnetic resonance," *Magnetic Resonance in Medicine,* vol. 34, pp. 786-791, 1995.

[211] M. Sundaram, M. H. McGuire, D. R. Herbold, S. E. Beshany, and J. W. Fletcher, "High signal intensity soft tissue masses on T1 weighted pulsing sequences," *Skeletal radiology,* vol. 16, pp. 30-36, 1987.

[212] D. P. O'Regan, B. Ariff, C. Neuwirth, Y. Tan, G. Durighel, and S. A. Cook, "Assessment of severe reperfusion injury with T2* cardiac MRI in patients with acute myocardial infarction," *Heart,* vol. 96, pp. 1885-1891, 2010.

[213] A. A. Di Tucci, G. Matta, S. Deplano, A. Gabbas, C. Depau, D. Derudas*, et al.*, "Myocardial iron overload assessment by T2* magnetic resonance imaging in adult transfusion dependent patients with acquired anemias," *haematologica,* vol. 93, pp. 1385-1388, 2008.

[214] C. Neil, T. H. Nguyen, A. Kucia, B. Crouch, A. Sverdlov, Y. Chirkov*, et al.*, "Slowly resolving global myocardial inflammation/oedema in Tako-Tsubo cardiomyopathy: evidence from T2-weighted cardiac MRI," *Heart,* vol. 98, pp. 1278-1284, 2012.

[215] B. Knutson, A. Westdorp, E. Kaiser, and D. Hommer, "fMRI visualization of brain activity during a monetary incentive delay task," *Neuroimage,* vol. 12, pp. 20-27, 2000.

[216] R. J. Sevick, J. S. Tsuruda, and P. Schmalbrock, "Three-dimensional time-of-flight MR angiography in the evaluation of cerebral aneurysms," *Journal of computer assisted tomography,* vol. 14, pp. 874-881, 1990.

[217] P. D. Gatehouse, J. Keegan, L. A. Crowe, S. Masood, R. H. Mohiaddin, K.-F. Kreitner*, et al.*, "Applications of phase-contrast flow and velocity imaging in cardiovascular MRI," *European radiology,* vol. 15, pp. 2172-2184, 2005.

[218] J. Eriksson, A. F. Bolger, T. Ebbers, and C.-J. Carlhäll, "Four-dimensional blood flow-specific markers of LV dysfunction in dilated cardiomyopathy," *European Heart Journal-Cardiovascular Imaging,* vol. 14, pp. 417-424, 2013.
[219] A. Harloff, F. Albrecht, J. Spreer, A. Stalder, J. Bock, A. Frydrychowicz*, et al.*, "3D blood flow characteristics in the carotid artery bifurcation assessed by flow-sensitive 4D MRI at 3T," *Magnetic resonance in medicine,* vol. 61, pp. 65-74, 2009.
[220] P. Lamata, A. Pitcher, S. Krittian, D. Nordsletten, M. M. Bissell, T. Cassar*, et al.*, "Aortic relative pressure components derived from four-dimensional flow cardiovascular magnetic resonance," *Magnetic resonance in medicine,* vol. 72, pp. 1162-1169, 2014.
[221] M. Markl, F. Wegent, T. Zech, S. Bauer, C. Strecker, M. Schumacher*, et al.*, "In vivo wall shear stress distribution in the carotid artery: effect of bifurcation geometry, internal carotid artery stenosis, and recanalization therapy," *Circulation: Cardiovascular Imaging,* vol. 3, pp. 647-655, 2010.
[222] C. Baltes, S. Kozerke, M. S. Hansen, K. P. Pruessmann, J. Tsao, and P. Boesiger, "Accelerating cine phase-contrast flow measurements using k-t BLAST and k-t SENSE," *Magnetic resonance in medicine,* vol. 54, pp. 1430-1438, 2005.
[223] C. Santelli, M. Loecher, J. Busch, O. Wieben, T. Schaeffter, and S. Kozerke, "Accelerating 4D flow MRI by exploiting vector field divergence regularization," *Magnetic resonance in medicine,* vol. 75, pp. 115-125, 2016.
[224] W. C. Röntgen, "On a new kind of rays," *Science,* vol. 3, pp. 227-231, 1896.
[225] G. N. Hounsfield, "Computerized transverse axial scanning (tomography): Part 1. Description of system," *The British journal of radiology,* vol. 46, pp. 1016-1022, 1973.
[226] A. M. Cormack, "Representation of a function by its line integrals, with some radiological applications," *Journal of applied physics,* vol. 34, pp. 2722-2727, 1963.
[227] W. H. Oldendorf, "Isolated flying spot detection of radiodensity dis-continuities-displaying the internal structural pattern of a complex object," *IRE transactions on bio-medical electronics,* vol. 8, pp. 68-72, 1961.
[228] G. Montalescot, U. Sechtem, S. Achenbach, F. Andreotti, C. Arden, A. Budaj*, et al.*, "2013 ESC guidelines on the management of stable coronary artery disease: the Task Force on the management of stable coronary artery disease of the European Society of Cardiology," *European heart journal,* vol. 34, pp. 2949-3003, 2013.
[229] T. Steiner, S. Juvela, A. Unterberg, C. Jung, M. Forsting, and G. Rinkel, "European Stroke Organization guidelines for the management of intracranial aneurysms and subarachnoid haemorrhage," *Cerebrovascular diseases,* vol. 35, pp. 93-112, 2013.
[230] C. T. January, L. S. Wann, J. S. Alpert, H. Calkins, J. E. Cigarroa, J. C. Cleveland*, et al.*, "2014 AHA/ACC/HRS guideline for the management of patients with atrial fibrillation: a report of the American College of Cardiology/American Heart Association Task Force on Practice Guidelines and the Heart Rhythm Society," *Journal of the American College of Cardiology,* vol. 64, pp. e1-e76, 2014.
[231] G. T. Herman, "Correction for beam hardening in computed tomography," *Physics in Medicine & Biology,* vol. 24, p. 81, 1979.
[232] N. Ducros, J. F. P. J. Abascal, B. Sixou, S. Rit, and F. Peyrin, "Regularization of nonlinear decomposition of spectral x-ray projection images," *Medical physics,* vol. 44, pp. e174-e187, 2017.

[233] A. Katsevich, "An improved exact filtered backprojection algorithm for spiral computed tomography," *Advances in Applied Mathematics,* vol. 32, pp. 681-697, 2004.

[234] L. A. Feldkamp, L. Davis, and J. W. Kress, "Practical cone-beam algorithm," *Josa a,* vol. 1, pp. 612-619, 1984.

[235] F. Natterer, *The mathematics of computerized tomography*: SIAM, 2001.

[236] C. Byrne, "A unified treatment of some iterative algorithms in signal processing and image reconstruction," *Inverse problems,* vol. 20, p. 103, 2003.

[237] A. H. Andersen and A. C. Kak, "Simultaneous algebraic reconstruction technique (SART): a superior implementation of the ART algorithm," *Ultrasonic imaging,* vol. 6, pp. 81-94, 1984.

[238] O. Scherzer, M. Grasmair, H. Grossauer, M. Haltmeier, and F. Lenzen, *Variational methods in imaging*: Springer, 2009.

[239] E. Hansis, D. Schafer, O. Dossel, and M. Grass, "Evaluation of iterative sparse object reconstruction from few projections for 3-D rotational coronary angiography," *IEEE Transactions on Medical Imaging,* vol. 27, pp. 1548-1555, 2008.

[240] M. Renker, A. Ramachandra, U. J. Schoepf, R. Raupach, P. Apfaltrer, G. W. Rowe*, et al.*, "Iterative image reconstruction techniques: applications for cardiac CT," *Journal of cardiovascular computed tomography,* vol. 5, pp. 225-230, 2011.

[241] T. G. Flohr, S. Schaller, K. Stierstorfer, H. Bruder, B. M. Ohnesorge, and U. J. Schoepf, "Multi–detector row CT systems and image-reconstruction techniques," *Radiology,* vol. 235, pp. 756-773, 2005.

[242] M.-H. Roy Cardinal, M. H. Heusinkveld, Z. Qin, R. G. Lopata, C. Naim, G. Soulez*, et al.*, "Carotid artery plaque vulnerability assessment using noninvasive ultrasound elastography: Validation with MRI," *American Journal of Roentgenology,* vol. 209, pp. 142-151, 2017.

[243] T. J. Czernuszewicz, J. W. Homeister, M. C. Caughey, M. A. Farber, J. J. Fulton, P. F. Ford*, et al.*, "In vivo carotid plaque stiffness measurements with ARFI ultrasound in endarterectomy patients," in *Ultrasonics Symposium (IUS), 2015 IEEE International*, 2015, pp. 1-4.

[244] A. Nair, B. D. Kuban, E. M. Tuzcu, P. Schoenhagen, S. E. Nissen, and D. G. Vince, "Coronary plaque classification with intravascular ultrasound radiofrequency data analysis," *Circulation,* vol. 106, pp. 2200-2206, 2002.

[245] T. Saam, M. Ferguson, V. Yarnykh, N. Takaya, D. Xu, N. Polissar*, et al.*, "Quantitative evaluation of carotid plaque composition by in vivo MRI," *Arteriosclerosis, thrombosis, and vascular biology,* vol. 25, pp. 234-239, 2005.

[246] C. L. de Korte, A. F. van der Steen, E. I. Céspedes, G. Pasterkamp, S. G. Carlier, F. Mastik*, et al.*, "Characterization of plaque components and vulnerability with intravascular ultrasound elastography," *Physics in Medicine & Biology,* vol. 45, p. 1465, 2000.

[247] M. Wintermark, S. S. Jawadi, J. H. Rapp, T. Tihan, E. Tong, D. Glidden*, et al.*, "High-resolution CT imaging of carotid artery atherosclerotic plaques," *American Journal of Neuroradiology,* vol. 29, pp. 875-882, 2008.

[248] T. G. Brott, J. L. Halperin, S. Abbara, J. M. Bacharach, J. D. Barr, R. L. Bush*, et al.*, "2011 ASA/ACCF/AHA/AANN/AANS/ACR/ASNR/CNS/SAIP/SCAI/SIR/SNIS/SVM/SVS guideline on the management of patients with extracranial carotid and vertebral artery disease," *Journal of the American College of Cardiology,* vol. 57, pp. e16-e94, 2011.

[249] A. P. Burke, F. D. Kolodgie, A. Farb, D. Weber, and R. Virmani, "Morphological predictors of arterial remodeling in coronary atherosclerosis," *Circulation,* vol. 105, pp. 297-303, 2002.
[250] S. Glagov, E. Weisenberg, C. K. Zarins, R. Stankunavicius, and G. J. Kolettis, "Compensatory enlargement of human atherosclerotic coronary arteries," *New England Journal of Medicine,* vol. 316, pp. 1371-1375, 1987.
[251] G. Pasterkamp, A. H. Schoneveld, A. C. van der Wal, C. C. Haudenschild, R. J. Clarijs, A. E. Becker*, et al.*, "Relation of arterial geometry to luminal narrowing and histologic markers for plaque vulnerability: the remodeling paradox," *Journal of the American College of Cardiology,* vol. 32, pp. 655-662, 1998.
[252] P. Libby, "Current concepts of the pathogenesis of the acute coronary syndromes," *Circulation,* vol. 104, pp. 365-372, 2001.
[253] H. H. Hansen, G. J. de Borst, M. L. Bots, F. L. Moll, G. Pasterkamp, and C. L. de Korte, "Validation of noninvasive in vivo compound ultrasound strain imaging using histologic plaque vulnerability features," *Stroke,* p. STROKEAHA. 116.014139, 2016.
[254] X. Wang, D. C. Jackson, C. C. Mitchell, T. Varghese, S. M. Wilbrand, B. G. Rocque*, et al.*, "Classification of symptomatic and asymptomatic patients with and without cognitive decline using non-invasive carotid plaque strain indices as biomarkers," *Ultrasound in medicine & biology,* vol. 42, pp. 909-918, 2016.
[255] K. V. Ramnarine, J. W. Garrard, B. Kanber, S. Nduwayo, T. C. Hartshorne, and T. G. Robinson, "Shear wave elastography imaging of carotid plaques: feasible, reproducible and of clinical potential," *Cardiovascular ultrasound,* vol. 12, p. 1, 2014.
[256] A. Gray-Weale, J. Graham, J. Burnett, K. Byrne, and R. Lusby, "Carotid artery atheroma: comparison of preoperative B-mode ultrasound appearance with carotid endarterectomy specimen pathology," *The Journal of cardiovascular surgery,* vol. 29, pp. 676-681, 1988.
[257] M.-L. M. Grønholdt, B. M. Wiebe, H. Laursen, T. G. Nielsen, T. Schroeder, and H. Sillesen, "Lipid-rich carotid artery plaques appear echolucent on ultrasound B-mode images and may be associated with intraplaque haemorrhage," *European journal of vascular and endovascular surgery,* vol. 14, pp. 439-445, 1997.
[258] L. Gerrit, E. J. Sijbrands, D. Staub, B. Coll, J. Folkert, S. B. Feinstein*, et al.*, "Noninvasive imaging of the vulnerable atherosclerotic plaque," *Current problems in cardiology,* vol. 35, pp. 556-591, 2010.
[259] D. E. Goertz, M. E. Frijlink, D. Tempel, L. C. van Damme, R. Krams, J. A. Schaar*, et al.*, "Contrast harmonic intravascular ultrasound: a feasibility study for vasa vasorum imaging," *Investigative radiology,* vol. 41, pp. 631-638, 2006.
[260] D. E. Goertz, M. E. Frijlink, D. Tempel, V. Bhagwandas, A. Gisolf, R. Krams*, et al.*, "Subharmonic contrast intravascular ultrasound for vasa vasorum imaging," *Ultrasound in medicine & biology,* vol. 33, pp. 1859-1872, 2007.
[261] E. Vicenzini, M. F. Giannoni, G. Sirimarco, M. C. Ricciardi, M. Toscano, G. L. Lenzi*, et al.*, "Imaging of plaque perfusion using contrast-enhanced ultrasound–Clinical significance," *Perspectives in Medicine,* vol. 1, pp. 44-50, 2012.
[262] L. H. Eraso, M. P. Reilly, C. Sehgal, and E. R. Mohler, "Emerging diagnostic and therapeutic molecular imaging applications in vascular disease," *Vascular medicine,* vol. 16, pp. 145-156, 2011.
[263] A. König and V. Klauss, "Virtual histology," *Heart,* vol. 93, pp. 977-982, 2007.
[264] M. Gaarder and T. Seierstad, "Measurements of carotid intima media thickness in non-invasive high-frequency ultrasound images: the effect of dynamic range setting," *Cardiovascular ultrasound,* vol. 13, p. 5, 2015.

[265] L. Dong, W. S. Kerwin, M. S. Ferguson, R. Li, J. Wang, H. Chen*, et al.*, "Cardiovascular magnetic resonance in carotid atherosclerotic disease," *Journal of cardiovascular magnetic resonance,* vol. 11, p. 53, 2009.

[266] J. H. Rudd, E. Warburton, T. D. Fryer, H. Jones, J. Clark, N. Antoun*, et al.*, "Imaging atherosclerotic plaque inflammation with [18F]-fluorodeoxyglucose positron emission tomography," *Circulation,* vol. 105, pp. 2708-2711, 2002.

[267] C. V. Bourantas, H. M. Garcia-Garcia, V. Farooq, A. Maehara, K. Xu, P. Généreux*, et al.*, "Clinical and angiographic characteristics of patients likely to have vulnerable plaques: analysis from the PROSPECT study," *JACC: Cardiovascular Imaging,* vol. 6, pp. 1263-1272, 2013.

[268] S. Inaba, G. S. Mintz, N. Z. Farhat, J. Fajadet, D. Dudek, A. Marzocchi*, et al.*, "Impact of positive and negative lesion site remodeling on clinical outcomes: insights from PROSPECT," *JACC: Cardiovascular Imaging,* vol. 7, pp. 70-78, 2014.

[269] X. Wu, A. Maehara, G. S. Mintz, T. Kubo, K. Xu, S.-Y. Choi*, et al.*, "Virtual histology intravascular ultrasound analysis of non-culprit attenuated plaques detected by grayscale intravascular ultrasound in patients with acute coronary syndromes," *The American journal of cardiology,* vol. 105, pp. 48-53, 2010.

[270] H. Shi, C. C. Mitchell, M. McCormick, M. A. Kliewer, R. J. Dempsey, and T. Varghese, "Preliminary in vivo atherosclerotic carotid plaque characterization using the accumulated axial strain and relative lateral shift strain indices," *Physics in Medicine & Biology,* vol. 53, p. 6377, 2008.

[271] H. Kanai, H. Hasegawa, M. Ichiki, F. Tezuka, and Y. Koiwa, "Elasticity imaging of atheroma with transcutaneous ultrasound: preliminary study," *Circulation,* vol. 107, pp. 3018-3021, 2003.

[272] C. L. De Korte, G. Pasterkamp, A. F. Van Der Steen, H. A. Woutman, and N. Bom, "Characterization of plaque components with intravascular ultrasound elastography in human femoral and coronary arteries in vitro," *Circulation,* vol. 102, pp. 617-623, 2000.

[273] J. A. Schaar, C. L. De Korte, F. Mastik, C. Strijder, G. Pasterkamp, E. Boersma*, et al.*, "Characterizing vulnerable plaque features with intravascular elastography," *Circulation,* vol. 108, pp. 2636-2641, 2003.

[274] D. Dumont, R. H. Behler, T. C. Nichols, E. P. Merricks, and C. M. Gallippi, "ARFI imaging for noninvasive material characterization of atherosclerosis," *Ultrasound in Medicine and Biology,* vol. 32, pp. 1703-1711, 2006.

[275] J. J. Dahl, D. M. Dumont, J. D. Allen, E. M. Miller, and G. E. Trahey, "Acoustic radiation force impulse imaging for noninvasive characterization of carotid artery atherosclerotic plaques: a feasibility study," *Ultrasound in medicine & biology,* vol. 35, pp. 707-716, 2009.

[276] T. J. Czernuszewicz, J. W. Homeister, M. C. Caughey, M. A. Farber, J. J. Fulton, P. F. Ford*, et al.*, "Non-invasive in vivo characterization of human carotid plaques with acoustic radiation force impulse ultrasound: Comparison with histology after endarterectomy," *Ultrasound in medicine & biology,* vol. 41, pp. 685-697, 2015.

[277] T. J. Czernuszewicz, J. W. Homeister, M. C. Caughey, Y. Wang, H. Zhu, B. Y. Huang*, et al.*, "Performance of acoustic radiation force impulse ultrasound imaging for carotid plaque characterization with histologic validation," *Journal of vascular surgery,* vol. 66, pp. 1749-1757. e3, 2017.

[278] J. Garrard, P. Ummur, S. Nduwayo, B. Kanber, T. Hartshorne, K. West*, et al.*, "Shear Wave Elastography May Be Superior to Greyscale Median for the Identification of Carotid Plaque Vulnerability: A Comparison with Histology," *Ultraschall in der Medizin (Stuttgart, Germany: 1980),* vol. 36, pp. 386-390, 2015.

[279] E. Maksuti, E. Widman, D. Larsson, M. W. Urban, M. Larsson, and A. Bjallmark, "Arterial Stiffness Estimation by Shear Wave Elastography: Validation in Phantoms with Mechanical Testing," *Ultrasound Med Biol,* vol. 42, pp. 308-21, Jan 2016.

[280] M. Couade, M. Pernot, C. Prada, E. Messas, J. Emmerich, P. Bruneval*, et al.*, "Quantitative assessment of arterial wall biomechanical properties using shear wave imaging," *Ultrasound in medicine & biology,* vol. 36, pp. 1662-1676, 2010.

[281] A. M. Mahmoud, D. Dutta, L. Lavery, D. N. Stephens, F. S. Villanueva, and K. Kim, "Noninvasive detection of lipids in atherosclerotic plaque using ultrasound thermal strain imaging: in vivo animal study," *Journal of the American College of Cardiology,* vol. 62, pp. 1804-1809, 2013.

[282] J. Roquer, T. Segura, J. Serena, E. Cuadrado-Godia, M. Blanco, J. García-García*, et al.*, "Value of carotid intima-media thickness and significant carotid stenosis as markers of stroke recurrence," *Stroke,* vol. 42, pp. 3099-3104, 2011.

[283] O. T. Raitakari, M. Juonala, M. Kähönen, L. Taittonen, T. Laitinen, N. Mäki-Torkko*, et al.*, "Cardiovascular risk factors in childhood and carotid artery intima-media thickness in adulthood: the Cardiovascular Risk in Young Finns Study," *Jama,* vol. 290, pp. 2277-2283, 2003.

[284] M. Helfand, D. I. Buckley, M. Freeman, R. Fu, K. Rogers, C. Fleming*, et al.*, "Emerging risk factors for coronary heart disease: a summary of systematic reviews conducted for the US Preventive Services Task Force," *Annals of internal medicine,* vol. 151, pp. 496-507, 2009.

[285] L. Hansen and W. R. Taylor, "Is increased arterial stiffness a cause or consequence of atherosclerosis?," *Atherosclerosis,* vol. 249, pp. 226-227, 2016.

[286] C. Palombo and M. Kozakova, "Arterial stiffness, atherosclerosis and cardiovascular risk: pathophysiologic mechanisms and emerging clinical indications," *Vascular pharmacology,* vol. 77, pp. 1-7, 2016.

[287] S. Oberoi, U. J. Schoepf, M. Meyer, T. Henzler, G. W. Rowe, P. Costello*, et al.*, "Progression of arterial stiffness and coronary atherosclerosis: longitudinal evaluation by cardiac CT," *American journal of roentgenology,* vol. 200, pp. 798-804, 2013.

[288] L. M. Van Bortel, S. Laurent, P. Boutouyrie, P. Chowienczyk, J. Cruickshank, T. De Backer*, et al.*, "Expert consensus document on the measurement of aortic stiffness in daily practice using carotid-femoral pulse wave velocity," *Journal of hypertension,* vol. 30, pp. 445-448, 2012.

[289] D. Newman and S. Greenwald, "Validity of the Moens-Korteweg equation," in *The Arterial System*, ed: Springer, 1978, pp. 109-115.

[290] J. Vappou, J. Luo, and E. E. Konofagou, "Pulse wave imaging for noninvasive and quantitative measurement of arterial stiffness in vivo," *American journal of hypertension,* vol. 23, pp. 393-398, 2010.

[291] J. Luo, K. Fujikura, L. S. Tyrie, M. D. Tilson, and E. E. Konofagou, "Pulse wave imaging of normal and aneurysmal abdominal aortas in vivo," *IEEE transactions on medical imaging,* vol. 28, pp. 477-486, 2008.

[292] I. Z. Apostolakis, S. D. Nandlall, and E. E. Konofagou, "Piecewise pulse wave imaging (pPWI) for detection and monitoring of focal vascular disease in murine aortas and carotids in vivo," *IEEE transactions on medical imaging,* vol. 35, pp. 13-28, 2015.

[293] J. Alvarez-Linera, J. Benito-León, J. Escribano, J. Campollo, and R. Gesto, "Prospective evaluation of carotid artery stenosis: elliptic centric contrast-enhanced MR angiography and spiral CT angiography compared with digital

subtraction angiography," *American journal of neuroradiology,* vol. 24, pp. 1012-1019, 2003.

[294] A. S. Agatston, W. R. Janowitz, F. J. Hildner, N. R. Zusmer, M. Viamonte, and R. Detrano, "Quantification of coronary artery calcium using ultrafast computed tomography," *Journal of the American College of Cardiology,* vol. 15, pp. 827-832, 1990.

[295] N. Sunkara, N. D. Wong, and S. Malik, "Role of coronary artery calcium in cardiovascular risk assessment," *Expert review of cardiovascular therapy,* vol. 12, pp. 87-94, 2014.

[296] R. S. Elkeles, I. F. Godsland, M. D. Feher, M. B. Rubens, M. Roughton, F. Nugara*, et al.*, "Coronary calcium measurement improves prediction of cardiovascular events in asymptomatic patients with type 2 diabetes: the PREDICT study," *European heart journal,* vol. 29, pp. 2244-2251, 2008.

[297] L. J. Shaw, J. Narula, and Y. Chandrashekhar, "The never-ending story on coronary calcium: is it predictive, punitive, or protective?," ed: Journal of the American College of Cardiology, 2015.

[298] R. Zainon, J. Ronaldson, T. Janmale, N. Scott, T. Buckenham, A. Butler*, et al.*, "Spectral CT of carotid atherosclerotic plaque: comparison with histology," *European radiology,* vol. 22, pp. 2581-2588, 2012.

[299] D. P. Cormode, E. Roessl, A. Thran, T. Skajaa, R. E. Gordon, J.-P. Schlomka*, et al.*, "Atherosclerotic plaque composition: analysis with multicolor CT and targeted gold nanoparticles," *Radiology,* vol. 256, pp. 774-782, 2010.

[300] T. S. Hatsukami, R. Ross, N. L. Polissar, and C. Yuan, "Visualization of fibrous cap thickness and rupture in human atherosclerotic carotid plaque in vivo with high-resolution magnetic resonance imaging," *Circulation,* vol. 102, pp. 959-964, 2000.

[301] W. Kerwin, D. Xu, F. Liu, T. Saam, H. Underhill, N. Takaya*, et al.*, "Magnetic resonance imaging of carotid atherosclerosis: plaque analysis," *Topics in Magnetic Resonance Imaging,* vol. 18, pp. 371-378, 2007.

[302] Y. Watanabe, M. Nagayama, T. Suga, K. Yoshida, S. Yamagata, A. Okumura*, et al.*, "Characterization of atherosclerotic plaque of carotid arteries with histopathological correlation: vascular wall MR imaging vs. color Doppler ultrasonography (US)," *Journal of Magnetic Resonance Imaging: An Official Journal of the International Society for Magnetic Resonance in Medicine,* vol. 28, pp. 478-485, 2008.

[303] A. I. MacIsaac and E. J. Topol, "Toward the quiescent coronary plaque," *Journal of the American College of Cardiology,* vol. 22, pp. 1228-1241, 1993.

[304] A. M. Shaaban and A. J. Duerinckx, "Wall shear stress and early atherosclerosis: a review," *American Journal of Roentgenology,* vol. 174, pp. 1657-1665, 2000.

[305] J. J. Wentzel, R. Corti, Z. A. Fayad, P. Wisdom, F. Macaluso, M. O. Winkelman*, et al.*, "Does shear stress modulate both plaque progression and regression in the thoracic aorta?: Human study using serial magnetic resonance imaging," *Journal of the American College of Cardiology,* vol. 45, pp. 846-854, 2005.

[306] T. Roleder, J. Jąkała, G. L. Kałuża, Ł. Partyka, K. Proniewska, E. Pociask*, et al.*, "The basics of intravascular optical coherence tomography," *Postępy w Kardiologii Interwencyjnej= Advances in Interventional Cardiology,* vol. 11, p. 74, 2015.

[307] I.-K. Jang, B. E. Bouma, D.-H. Kang, S.-J. Park, S.-W. Park, K.-B. Seung*, et al.*, "Visualization of coronary atherosclerotic plaques in patients using optical coherence tomography: comparison with intravascular ultrasound," *Journal of the American College of Cardiology,* vol. 39, pp. 604-609, 2002.

[308] H. Yabushita, B. E. Bouma, S. L. Houser, H. T. Aretz, I.-K. Jang, K. H. Schlendorf*, et al.*, "Characterization of human atherosclerosis by optical coherence tomography," *Circulation,* vol. 106, pp. 1640-1645, 2002.

[309] H. Jia, F. Abtahian, A. D. Aguirre, S. Lee, S. Chia, H. Lowe*, et al.*, "In vivo diagnosis of plaque erosion and calcified nodule in patients with acute coronary syndrome by intravascular optical coherence tomography," *Journal of the American College of Cardiology,* vol. 62, pp. 1748-1758, 2013.

[310] A. V. Finn, M. Nakano, J. Narula, F. D. Kolodgie, and R. Virmani, "Concept of vulnerable/unstable plaque," *Arteriosclerosis, thrombosis, and vascular biology,* vol. 30, pp. 1282-1292, 2010.

[311] R. M. Wyman, R. D. Safian, V. Portway, J. J. Skillman, R. G. McKAY, and D. S. Baim, "Current complications of diagnostic and therapeutic cardiac catheterization," *Journal of the American College of Cardiology,* vol. 12, pp. 1400-1406, 1988.

[312] H. Omran, H. Schmidt, M. Hackenbroch, S. Illien, P. Bernhardt, G. von der Recke*, et al.*, "Silent and apparent cerebral embolism after retrograde catheterisation of the aortic valve in valvular stenosis: a prospective, randomised study," *The Lancet,* vol. 361, pp. 1241-1246, 2003.

[313] L. Hatle, A. Brubakk, A. Tromsdal, and B. Angelsen, "Noninvasive assessment of pressure drop in mitral stenosis by Doppler ultrasound," *Heart,* vol. 40, pp. 131-140, 1978.

[314] H. Baumgartner, S. Khan, M. Derobertis, L. Czer, and G. Maurer, "Discrepancies between Doppler and catheter gradients in aortic prosthetic valves in vitro. A manifestation of localized gradients and pressure recovery," *Circulation,* vol. 82, pp. 1467-1475, 1990.

[315] H. Baumgartner, T. Stefenelli, J. Niederberger, H. Schima, and G. Maurer, ""Overestimation" of catheter gradients by Doppler ultrasound in patients with aortic stenosis: a predictable manifestation of pressure recovery," *Journal of the American College of Cardiology,* vol. 33, pp. 1655-1661, 1999.

[316] D. Garcia, J. G. Dumesnil, L.-G. Durand, L. Kadem, and P. Pibarot, "Discrepancies between catheter and Doppler estimates of valve effective orifice area can be predicted from the pressure recovery phenomenon: practical implications with regard to quantification of aortic stenosis severity," *Journal of the American College of Cardiology,* vol. 41, pp. 435-442, 2003.

[317] H. Ha, J. P. Kvitting, P. Dyverfeldt, and T. Ebbers, "Validation of pressure drop assessment using 4D flow MRI-based turbulence production in various shapes of aortic stenoses," *Magnetic resonance in medicine,* vol. 81, pp. 893-906, 2019.

[318] D. Garcia, P. Pibarot, J. G. Dumesnil, F. d. r. Sakr, and L.-G. Durand, "Assessment of aortic valve stenosis severity: a new index based on the energy loss concept," *Circulation,* vol. 101, pp. 765-771, 2000.

[319] T. Ebbers, L. Wigström, A. F. Bolger, J. Engvall, and M. Karlsson, "Estimation of relative cardiovascular pressures using time-resolved three-dimensional phase contrast MRI," *Magnetic Resonance in Medicine: An Official Journal of the International Society for Magnetic Resonance in Medicine,* vol. 45, pp. 872-879, 2001.

[320] S. B. S. Krittian, P. Lamata, C. Michler, D. A. Nordsletten, J. Bock, C. P. Bradley*, et al.*, "A finite-element approach to the direct computation of relative cardiovascular pressure from time-resolved MR velocity data," *Medical Image Analysis,* vol. 16, pp. 1029-1037, 2012/07/01/ 2012.

[321] F. Donati, D. A. Nordsletten, N. P. Smith, and P. Lamata, "Pressure mapping from flow imaging: enhancing computation of the viscous term through velocity reconstruction in near-wall regions," in *2014 36th Annual International Conference of the IEEE Engineering in Medicine and Biology Society*, 2014, pp. 5097-5100.

[322] C. Bertoglio, R. Núņez, F. Galarce, D. Nordsletten, and A. Osses, "Relative pressure estimation from velocity measurements in blood flows: state-of-the-art and new approaches," 2016.

[323] H. Švihlová, J. Hron, J. Málek, K. Rajagopal, and K. Rajagopal, "Determination of pressure data from velocity data with a view toward its application in cardiovascular mechanics. Part 1. Theoretical considerations," *International Journal of Engineering Science,* vol. 105, pp. 108-127, 2016.

[324] F. Donati, C. A. Figueroa, N. P. Smith, P. Lamata, and D. A. Nordsletten, "Non-invasive pressure difference estimation from PC-MRI using the work-energy equation," *Medical image analysis,* vol. 26, pp. 159-172, 2015.

[325] H. Ha, G. B. Kim, J. Kweon, H. K. Huh, S. J. Lee, H. J. Koo*, et al.*, "Turbulent kinetic energy measurement using phase contrast MRI for estimating the post-stenotic pressure drop: in vitro validation and clinical application," *PloS one,* vol. 11, p. e0151540, 2016.

[326] U. Gülan, C. Binter, S. Kozerke, and M. Holzner, "Shear-scaling-based approach for irreversible energy loss estimation in stenotic aortic flow–an in vitro study," *Journal of biomechanics,* vol. 56, pp. 89-96, 2017.

[327] L. M. Friedman, C. Furberg, D. L. DeMets, D. M. Reboussin, and C. B. Granger, *Fundamentals of clinical trials* vol. 4: Springer, 2010.

[328] A. S. Plump, J. D. Smith, T. Hayek, K. Aalto-Setälä, A. Walsh, J. G. Verstuyft*, et al.*, "Severe hypercholesterolemia and atherosclerosis in apolipoprotein E-deficient mice created by homologous recombination in ES cells," *Cell,* vol. 71, pp. 343-353, 1992.

[329] C. T. Pappas, R. M. Mayfield, C. Henderson, N. Jamilpour, C. Cover, Z. Hernandez*, et al.*, "Knockout of Lmod2 results in shorter thin filaments followed by dilated cardiomyopathy and juvenile lethality," *Proceedings of the National Academy of Sciences,* vol. 112, pp. 13573-13578, 2015.

[330] Y. Suzuki, J. K. Lyons, A. C. Yeung, and F. Ikeno, "In vivo porcine model of reperfused myocardial infarction: in situ double staining to measure precise infarct area/area at risk," *Catheterization and Cardiovascular Interventions,* vol. 71, pp. 100-107, 2008.

[331] D. Eble, J. Walker, A. Samarel, and F. Spinale, "Myosin heavy chain synthesis during the progression of chronic tachycardia induced heart failure in rabbits," *Basic research in cardiology,* vol. 93, pp. 50-55, 1998.

[332] E. Lancelot, V. Amirbekian, I. Brigger, J.-S. Raynaud, S. Ballet, C. David*, et al.*, "Evaluation of matrix metalloproteinases in atherosclerosis using a novel noninvasive imaging approach," *Arteriosclerosis, thrombosis, and vascular biology,* vol. 28, pp. 425-432, 2008.

[333] Z. Liu, G. A. Kastis, G. D. Stevenson, H. H. Barrett, L. R. Furenlid, M. A. Kupinski*, et al.*, "Quantitative analysis of acute myocardial infarct in rat hearts with ischemia-reperfusion using a high-resolution stationary SPECT system," *Journal of Nuclear Medicine,* vol. 43, pp. 933-939, 2002.

[334] R. Lecomte, E. Croteau, M.-E. Gauthier, M. Archambault, A. Aliaga, J. Rousseau*, et al.*, "Cardiac PET imaging of blood flow, metabolism, and function in normal and infarcted rats," *IEEE Transactions on Nuclear Science,* vol. 51, pp. 696-704, 2004.

[335] M. Nahrendorf, C. Badea, L. W. Hedlund, J.-L. Figueiredo, D. E. Sosnovik, G. A. Johnson*, et al.*, "High-resolution imaging of murine myocardial infarction with delayed-enhancement cine micro-CT," *American Journal of Physiology-Heart and Circulatory Physiology,* vol. 292, pp. H3172-H3178, 2007.
[336] C. Errico, J. Pierre, S. Pezet, Y. Desailly, Z. Lenkei, O. Couture*, et al.*, "Ultrafast ultrasound localization microscopy for deep super-resolution vascular imaging," *Nature,* vol. 527, p. 499, 2015.
[337] F. Beekman and F. van der Have, "The pinhole: gateway to ultra-high-resolution three-dimensional radionuclide imaging," ed: Springer, 2007.
[338] G. Wang, H. Yu, and B. De Man, "An outlook on x-ray CT research and development," *Medical physics,* vol. 35, pp. 1051-1064, 2008.
[339] S. Gundacker, E. Auffray, K. Pauwels, and P. Lecoq, "Measurement of intrinsic rise times for various L (Y) SO and LuAG scintillators with a general study of prompt photons to achieve 10 ps in TOF-PET," *Physics in Medicine & Biology,* vol. 61, p. 2802, 2016.
[340] M. Gössl, D. Versari, H. A. Hildebrandt, T. Bajanowski, G. Sangiorgi, R. Erbel*, et al.*, "Segmental heterogeneity of vasa vasorum neovascularization in human coronary atherosclerosis," *JACC: Cardiovascular imaging,* vol. 3, pp. 32-40, 2010.
[341] A. C. Langheinrich, R. M. Bohle, S. Greschus, N. Hackstein, G. Walker, S. von Gerlach*, et al.*, "Atherosclerotic lesions at micro CT: feasibility for analysis of coronary artery wall in autopsy specimens," *Radiology,* vol. 231, pp. 675-681, 2004.
[342] P. A. Helm, H. J. Tseng, L. Younes, E. R. McVeigh, and R. L. Winslow, "Ex vivo 3D diffusion tensor imaging and quantification of cardiac laminar structure," *Magnetic Resonance in Medicine: An Official Journal of the International Society for Magnetic Resonance in Medicine,* vol. 54, pp. 850-859, 2005.
[343] G. E. Trahey, M. L. Palmeri, R. C. Bentley, and K. R. Nightingale, "Acoustic radiation force impulse imaging of the mechanical properties of arteries: in vivo and ex vivo results," *Ultrasound in medicine & biology,* vol. 30, pp. 1163-1171, 2004.
[344] V. D. Schepkin, W. W. Brey, P. L. Gor'kov, and S. C. Grant, "Initial in vivo rodent sodium and proton MR imaging at 21.1 T," *Magnetic resonance imaging,* vol. 28, pp. 400-407, 2010.
[345] F. D. Doty, G. Entzminger, J. Kulkarni, K. Pamarthy, and J. P. Staab, "Radio frequency coil technology for small-animal MRI," *NMR in Biomedicine: An International Journal Devoted to the Development and Application of Magnetic Resonance In vivo,* vol. 20, pp. 304-325, 2007.
[346] P. Marzola, F. Osculati, and A. Sbarbati, "High field MRI in preclinical research," *European journal of radiology,* vol. 48, pp. 165-170, 2003.
[347] M. Lakshman and A. Needles, "Screening and quantification of the tumor microenvironment with micro-ultrasound and photoacoustic imaging," *Nature Methods,* vol. 12, 2015.
[348] W. W. Moses, "Fundamental limits of spatial resolution in PET," *Nuclear Instruments and Methods in Physics Research Section A: Accelerators, Spectrometers, Detectors and Associated Equipment,* vol. 648, pp. S236-S240, 2011.
[349] P. Zanzonico, "Noninvasive imaging for supporting basic research," in *Small animal imaging*, ed: Springer, 2017, pp. 3-32.
[350] I. Mano, H. Goshima, M. Nambu, and M. Iio, "New polyvinyl alcohol gel material for MRI phantoms," *Magnetic resonance in medicine,* vol. 3, pp. 921-926, 1986.
[351] J. Fromageau, E. Brusseau, D. Vray, G. Gimenez, and P. Delachartre, "Characterization of PVA cryogel for intravascular ultrasound elasticity imaging,"

IEEE transactions on ultrasonics, ferroelectrics, and frequency control, vol. 50, pp. 1318-1324, 2003.

[352] K. Surry, H. Austin, A. Fenster, and T. Peters, "Poly (vinyl alcohol) cryogel phantoms for use in ultrasound and MR imaging," *Physics in Medicine & Biology,* vol. 49, p. 5529, 2004.

[353] S. R. Deans, *The Radon transform and some of its applications*: Courier Corporation, 2007.

[354] J. McLaughlin and D. Renzi, "Shear wave speed recovery in transient elastography and supersonic imaging using propagating fronts," *Inverse Problems,* vol. 22, p. 681, 2006.

[355] M. H. Wang, M. L. Palmeri, V. M. Rotemberg, N. C. Rouze, and K. R. Nightingale, "Improving the robustness of time-of-flight based shear wave speed reconstruction methods using RANSAC in human liver in vivo," *Ultrasound in medicine and biology,* vol. 36, pp. 802-813, 2010.

[356] C. Amador, P. Song, D. D. Meixner, S. Chen, and M. W. Urban, "Improvement of shear wave motion detection using harmonic imaging in healthy human liver," *Ultrasound in medicine & biology,* vol. 42, pp. 1031-1041, 2016.

[357] P. Song, H. Zhao, M. W. Urban, A. Manduca, S. V. Pislaru, R. R. Kinnick*, et al.*, "Improved shear wave motion detection using pulse-inversion harmonic imaging with a phased array transducer," *IEEE transactions on medical imaging,* vol. 32, pp. 2299-2310, 2013.

[358] J. Bercoff, S. Chaffai, M. Tanter, L. Sandrin, S. Catheline, M. Fink*, et al.*, "In vivo breast tumor detection using transient elastography," *Ultrasound in medicine & biology,* vol. 29, pp. 1387-1396, 2003.

[359] L. Sandrin, B. Fourquet, J.-M. Hasquenoph, S. Yon, C. Fournier, F. Mal*, et al.*, "Transient elastography: a new noninvasive method for assessment of hepatic fibrosis," *Ultrasound in medicine & biology,* vol. 29, pp. 1705-1713, 2003.

[360] G. Ferraioli, C. Filice, L. Castera, B. I. Choi, I. Sporea, S. R. Wilson*, et al.*, "WFUMB guidelines and recommendations for clinical use of ultrasound elastography: Part 3: liver," *Ultrasound in medicine & biology,* vol. 41, pp. 1161-1179, 2015.

[361] R. G. Barr, K. Nakashima, D. Amy, D. Cosgrove, A. Farrokh, F. Schafer*, et al.*, "WFUMB guidelines and recommendations for clinical use of ultrasound elastography: Part 2: breast," *Ultrasound in medicine & biology,* vol. 41, pp. 1148-1160, 2015.

[362] A. Itoh, E. Ueno, E. Tohno, H. Kamma, H. Takahashi, T. Shiina*, et al.*, "Breast disease: clinical application of US elastography for diagnosis," *Radiology,* vol. 239, pp. 341-350, 2006.

[363] R. Brown, *Physical testing of rubber*: Springer Science & Business Media, 2006.

[364] ASTM, "ASTM Standard E143-02: Standard test method for shear modulus at room temperature," 2008.

[365] J. Sun, X.-Q. Zhao, N. Balu, M. B. Neradilek, D. A. Isquith, K. Yamada*, et al.*, "Carotid plaque lipid content and fibrous cap status predict systemic CV outcomes: the MRI substudy in AIM-HIGH," *JACC: Cardiovascular Imaging,* vol. 10, pp. 241-249, 2017.

[366] H. Ota, M. J. Reeves, D. C. Zhu, A. Majid, A. Collar, C. Yuan*, et al.*, "Sex differences in patients with asymptomatic carotid atherosclerotic plaque: in vivo 3.0-T magnetic resonance study," *Stroke,* vol. 41, pp. 1630-1635, 2010.

[367] C. Randall, "Absorbing boundary condition for the elastic wave equation: Velocity-stress formulation," *Geophysics,* vol. 54, pp. 1141-1152, 1989.

[368] H. Elman, V. E. Howle, J. Shadid, R. Shuttleworth, and R. Tuminaro, "Block preconditioners based on approximate commutators," *SIAM Journal on Scientific Computing,* vol. 27, pp. 1651-1668, 2006.

[369] J. A. Sotelo, I. Valverde, P. B. Beerbaum, G. F. Greil, T. Schaeffter, R. Razavi*, et al.*, "Pressure gradient prediction in aortic coarctation using a computational-fluid-dynamics model: validation against invasive pressure catheterization at rest and pharmacological stress," *Journal of Cardiovascular Magnetic Resonance,* vol. 17, p. Q78, 2015.

[370] N. Gaddum, J. Alastruey, P. Beerbaum, P. Chowienczyk, and T. Schaeffter, "A technical assessment of pulse wave velocity algorithms applied to non-invasive arterial waveforms," *Annals of biomedical engineering,* vol. 41, pp. 2617-2629, 2013.

[371] S. E. Brett, A. Guilcher, B. Clapp, and P. Chowienczyk, "Estimating central systolic blood pressure during oscillometric determination of blood pressure: proof of concept and validation by comparison with intra-aortic pressure recording and arterial tonometry," *Blood pressure monitoring,* vol. 17, pp. 132-136, 2012.

[372] M. Willemet, P. Chowienczyk, and J. Alastruey, "A database of virtual healthy subjects to assess the accuracy of foot-to-foot pulse wave velocities for estimation of aortic stiffness," *American Journal of Physiology-Heart and Circulatory Physiology,* vol. 309, pp. H663-H675, 2015.

[373] J. Alastruey, K. H. Parker, and S. J. Sherwin, "Arterial pulse wave haemodynamics," in *11th International Conference on Pressure Surges*, 2012, pp. 401-442.

[374] N. C. Schwertman and R. de Silva, "Identifying outliers with sequential fences," *Computational statistics & data analysis,* vol. 51, pp. 3800-3810, 2007.

[375] Z. Wang, A. C. Bovik, H. R. Sheikh, and E. P. Simoncelli, "Image quality assessment: from error visibility to structural similarity," *IEEE transactions on image processing,* vol. 13, pp. 600-612, 2004.

[376] B. Chen, X. Duan, Z. Yu, S. Leng, L. Yu, and C. McCollough, "Development and validation of an open data format for CT projection data," *Medical physics,* vol. 42, pp. 6964-6972, 2015.

[377] Z. Li, L. Du, F. Wang, and X. Luo, "Assessment of the arterial stiffness in patients with acute ischemic stroke using longitudinal elasticity modulus measurements obtained with Shear Wave Elastography," *Medical ultrasonography,* vol. 18, pp. 182-189, 2016.

[378] G.-Y. Li, Q. He, G. Xu, L. Jia, J. Luo, and Y. Cao, "An ultrasound elastography method to determine the local stiffness of arteries with guided circumferential waves," *Journal of biomechanics,* vol. 51, pp. 97-104, 2017.

[379] G.-Y. Li, Q. He, L. Jia, P. He, J. Luo, and Y. Cao, "An inverse method to determine arterial stiffness with guided axial waves," *Ultrasound in Medicine and Biology,* vol. 43, pp. 505-516, 2017.

[380] A. V. Astaneh, M. W. Urban, W. Aquino, J. F. Greenleaf, and M. N. Guddati, "Arterial waveguide model for shear wave elastography: implementation and in vitro validation," *Physics in Medicine & Biology,* vol. 62, p. 5473, 2017.

[381] Y. Guo, Y. Wang, E. J.-H. Chang, and W.-N. Lee, "Multidirectional estimation of arterial stiffness using vascular guided wave imaging with geometry correction," *Ultrasound in medicine & biology,* vol. 44, pp. 884-896, 2018.

[382] C.-C. Shih, X. Qian, T. Ma, Z. Han, C.-C. Huang, Q. Zhou*, et al.*, "Quantitative assessment of thin-layer tissue viscoelastic properties using ultrasonic micro-

elastography with lamb wave model," *IEEE transactions on medical imaging,* vol. 37, pp. 1887-1898, 2018.

[383] E. Maksuti, F. Bini, S. Fiorentini, G. Blasi, M. W. Urban, F. Marinozzi*, et al.*, "Influence of wall thickness and diameter on arterial shear wave elastography: a phantom and finite element study," *Physics in Medicine & Biology,* vol. 62, p. 2694, 2017.

[384] C. Amador, M. W. Urban, S. Chen, Q. Chen, K.-N. An, and J. F. Greenleaf, "Shear elastic modulus estimation from indentation and SDUV on gelatin phantoms," *IEEE Transactions on Biomedical Engineering,* vol. 58, pp. 1706-1714, 2011.

[385] A. García, M. Martínez, and E. Pena, "Viscoelastic properties of the passive mechanical behavior of the porcine carotid artery: influence of proximal and distal positions," *Biorheology,* vol. 49, pp. 271-288, 2012.

[386] T.-M. Nguyen, M. Couade, J. Bercoff, and M. Tanter, "Assessment of viscous and elastic properties of sub-wavelength layered soft tissues using shear wave spectroscopy: theoretical framework and in vitro experimental validation," *IEEE transactions on ultrasonics, ferroelectrics, and frequency control,* vol. 58, pp. 2305-2315, 2011.

[387] A. Caenen, D. Shcherbakova, B. Verhegghe, C. Papadacci, M. Pernot, P. Segers*, et al.*, "A versatile and experimentally validated finite element model to assess the accuracy of shear wave elastography in a bounded viscoelastic medium," *IEEE transactions on ultrasonics, ferroelectrics, and frequency control,* vol. 62, pp. 439-450, 2015.

[388] N. Yang, "Viscoelastic properties of poly (vinyl alcohol) nanofibres and hydrogels measured by atomic force microscopy," *Phys Canada,* vol. 64, pp. 141-143, 2008.

[389] Z. Lou, J. Yang, L. Tang, Y. Jin, J. Zhang, C. Liu*, et al.*, "Shear Wave Elastography Imaging for the Features of Symptomatic Carotid Plaques: A Feasibility Study," *Journal of Ultrasound in Medicine,* vol. 36, pp. 1213-1223, 2017.

[390] M. L. Palmeri, Y. Deng, N. C. Rouze, and K. R. Nightingale, "Dependence of shear wave spectral content on acoustic radiation force excitation duration and spatial beamwidth," in *2014 IEEE International Ultrasonics Symposium*, 2014, pp. 1105-1108.

[391] J. R. Doherty, D. M. Dumont, G. E. Trahey, and M. L. Palmeri, "Acoustic radiation force impulse imaging of vulnerable plaques: a finite element method parametric analysis," *Journal of biomechanics,* vol. 46, pp. 83-90, 2013.

[392] L. Thomas-Seale, L. Hollis, D. Klatt, I. Sack, N. Roberts, P. Pankaj*, et al.*, "The simulation of magnetic resonance elastography through atherosclerosis," *Journal of biomechanics,* vol. 49, pp. 1781-1788, 2016.

[393] R. A. Baldewsing, C. L. de Korte, J. A. Schaar, F. Mastik, and A. F. van Der Steen, "A finite element model for performing intravascular ultrasound elastography of human atherosclerotic coronary arteries," *Ultrasound in medicine & biology,* vol. 30, pp. 803-813, 2004.

[394] J. Porée, B. Chayer, G. Soulez, J. Ohayon, and G. Cloutier, "Noninvasive Vascular Modulography Method for Imaging the Local Elasticity of Atherosclerotic Plaques: Simulation and In Vitro Vessel Phantom Study," *IEEE transactions on ultrasonics, ferroelectrics, and frequency control,* vol. 64, pp. 1805-1817, 2017.

[395] D. Chimenti and A. H. Nayfeh, "Leaky Lamb waves in fibrous composite laminates," *Journal of applied physics,* vol. 58, pp. 4531-4538, 1985.

[396] A. Mal, P.-C. Xu, and Y. Bar-Cohen, "Analysis of leaky Lamb waves in bonded plates," *International journal of engineering science,* vol. 27, pp. 779-791, 1989.

[397] M. Urban, K. Carlson, and D. D. Daescu, "Finite element models of wave propagation in embedded vessels with simulated plaques," in *Ultrasonics Symposium (IUS), 2017 IEEE International*, 2017, pp. 1-1.

[398] R. H. Behler, T. J. Czernuszewicz, T. C. Nichols, H. Zhu, J. W. Homeister, E. P. Merricks*, et al.*, "Acoustic radiation force beam sequence performance for detection and material characterization of atherosclerotic plaques: preclinical, ex vivo results," *IEEE transactions on ultrasonics, ferroelectrics, and frequency control,* vol. 60, pp. 2471-2487, 2013.

[399] V. M. Heiland, C. Forsell, J. Roy, U. Hedin, and T. C. Gasser, "Identification of carotid plaque tissue properties using an experimental–numerical approach," *Journal of the mechanical behavior of biomedical materials,* vol. 27, pp. 226-238, 2013.

[400] T. Saam, H. R. Underhill, B. Chu, N. Takaya, J. Cai, N. L. Polissar*, et al.*, "Prevalence of American Heart Association type VI carotid atherosclerotic lesions identified by magnetic resonance imaging for different levels of stenosis as measured by duplex ultrasound," *Journal of the American College of Cardiology,* vol. 51, pp. 1014-1021, 2008.

[401] A. Ertepinar and A. Wang, "Torsional buckling of an elastic thick-walled tube made of rubber-like material," *International Journal of Solids and Structures,* vol. 11, pp. 329-337, 1975.

[402] D. Marlevi, E. Maksuti, M. W. Urban, R. Winter, and M. Larsson, "Plaque characterization using shear wave elastography—evaluation of differentiability and accuracy using a combined ex vivo and in vitro setup," *Physics in Medicine & Biology,* vol. 63, p. 235008, 2018.

[403] C. Huang, X. Pan, Q. He, M. Huang, L. Huang, X. Zhao*, et al.*, "Ultrasound-based carotid elastography for detection of vulnerable atherosclerotic plaques validated by magnetic resonance imaging," *Ultrasound in Medicine and Biology,* vol. 42, pp. 365-377, 2016.

[404] J. R. Doherty, J. J. Dahl, P. G. Kranz, N. El Husseini, H.-C. Chang, N.-k. Chen*, et al.*, "Comparison of acoustic radiation force impulse imaging derived carotid plaque stiffness with spatially registered MRI determined composition," *IEEE transactions on medical imaging,* vol. 34, pp. 2354-2365, 2015.

[405] G. Torres, T. J. Czernuszewicz, J. W. Homeister, M. A. Farber, and C. M. Gallippi, "ARFI variance of acceleration (VoA) for noninvasive characterization of human carotid plaques in vivo," in *Engineering in Medicine and Biology Society (EMBC), 2017 39th Annual International Conference of the IEEE*, 2017, pp. 2984-2987.

[406] K. Itatani, K. Miyaji, Y. Qian, J. L. Liu, T. Miyakoshi, A. Murakami*, et al.*, "Influence of surgical arch reconstruction methods on single ventricle workload in the Norwood procedure," *The Journal of thoracic and cardiovascular surgery,* vol. 144, pp. 130-138, 2012.

[407] Y. Qian, J. Liu, K. Itatani, K. Miyaji, and M. Umezu, "Computational hemodynamic analysis in congenital heart disease: simulation of the Norwood procedure," *Annals of biomedical engineering,* vol. 38, pp. 2302-2313, 2010.

[408] S. Rees, D. Firmin, R. Mohiaddin, R. Underwood, and D. Longmore, "Application of flow measurements by magnetic resonance velocity mapping to congenital heart disease," *The American journal of cardiology,* vol. 64, pp. 953-956, 1989.

[409] C. Binter, U. Gülan, M. Holzner, and S. Kozerke, "On the accuracy of viscous and turbulent loss quantification in stenotic aortic flow using phase-contrast MRI," *Magnetic resonance in medicine,* vol. 76, pp. 191-196, 2016.

[410] C. Binter, V. Knobloch, R. Manka, A. Sigfridsson, and S. Kozerke, "Bayesian multipoint velocity encoding for concurrent flow and turbulence mapping," *Magnetic resonance in medicine,* vol. 69, pp. 1337-1345, 2013.

[411] H. Ha and H. Park, "Comparison of turbulent flow measurement schemes for 4D flow MRI," *Journal of Visualization,* vol. 22, pp. 541-553, 2019.

[412] C. Binter, A. Gotschy, S. H. Sündermann, M. Frank, F. C. Tanner, T. F. Lüscher*, et al.*, "Turbulent kinetic energy assessed by multipoint 4-dimensional flow magnetic resonance imaging provides additional information relative to echocardiography for the determination of aortic stenosis severity," *Circulation: Cardiovascular Imaging,* vol. 10, p. e005486, 2017.

[413] J. Zajac, J. Eriksson, P. Dyverfeldt, A. F. Bolger, T. Ebbers, and C. J. Carlhäll, "Turbulent kinetic energy in normal and myopathic left ventricles," *Journal of Magnetic Resonance Imaging,* vol. 41, pp. 1021-1029, 2015.

[414] K. Isaaz and A. Pasipoularides, "Noninvasive assessment of intrinsic ventricular load dynamics in dilated cardiomyopathy," *Journal of the American College of Cardiology,* vol. 17, pp. 112-121, 1991.

[415] D. Avramides, A. Perakis, V. Voudris, and P. Gezerlis, "Noninvasive assessment of left ventricular systolic function by stress-shortening relation, rate of change of power, preload-adjusted maximal power, and ejection force in idiopathic dilated cardiomyopathy: prognostic implications," *Journal of the American Society of Echocardiography,* vol. 13, pp. 87-95, 2000.

[416] P. Reymond, N. Westerhof, and N. Stergiopulos, "Systolic hypertension mechanisms: effect of global and local proximal aorta stiffening on pulse pressure," *Annals of biomedical engineering,* vol. 40, pp. 742-749, 2012.

[417] W. F. Kerwin, E. H. Botvinick, J. W. O'Connell, S. H. Merrick, T. DeMarco, K. Chatterjee*, et al.*, "Ventricular contraction abnormalities in dilated cardiomyopathy: effect of biventricular pacing to correct interventricular dyssynchrony," *Journal of the American College of Cardiology,* vol. 35, pp. 1221-1227, 2000.

[418] D. V. Unverferth, R. D. Magorien, M. L. Moeschberger, P. B. Baker, J. K. Fetters, and C. V. Leier, "Factors influencing the one-year mortality of dilated cardiomyopathy," *The American journal of cardiology,* vol. 54, pp. 147-152, 1984.

[419] G. M. Felker, R. E. Thompson, J. M. Hare, R. H. Hruban, D. E. Clemetson, D. L. Howard*, et al.*, "Underlying causes and long-term survival in patients with initially unexplained cardiomyopathy," *New England Journal of Medicine,* vol. 342, pp. 1077-1084, 2000.

[420] S. Bonapace, A. Rossi, M. Cicoira, G. Golia, L. Zanolla, L. Franceschini*, et al.*, "Aortic stiffness correlates with an increased extracellular matrix turnover in patients with dilated cardiomyopathy," *American heart journal,* vol. 152, pp. 93. e1-93. e6, 2006.

[421] K. Bouaou, I. Bargiotas, T. Dietenbeck, E. Bollache, G. Soulat, D. Craiem*, et al.*, "Analysis of aortic pressure fields from 4D flow MRI in healthy volunteers: Associations with age and left ventricular remodeling," *Journal of Magnetic Resonance Imaging,* 2019.

[422] G. Hasenfuss, L. Mulieri, B. Leavitt, P. Allen, J. Haeberle, and N. Alpert, "Alteration of contractile function and excitation-contraction coupling in dilated cardiomyopathy," *Circulation research,* vol. 70, pp. 1225-1232, 1992.

[423] T. Dudenbostel and S. P. Glasser, "Effects of antihypertensive drugs on arterial stiffness," *Cardiology in review,* vol. 20, 2012.

[424] M. F. O'Rourke and W. W. Nichols, "Aortic diameter, aortic stiffness, and wave reflection increase with age and isolated systolic hypertension," *Hypertension,* vol. 45, pp. 652-658, 2005.
[425] J. N. Cohn, D. A. Duprez, and G. A. Grandits, "Arterial elasticity as part of a comprehensive assessment of cardiovascular risk and drug treatment," *Hypertension,* vol. 46, pp. 217-220, 2005.
[426] A. Ziegler, T. Nielsen, and M. Grass, "Iterative reconstruction of a region of interest for transmission tomography," *Medical physics,* vol. 35, pp. 1317-1327, 2008.
[427] F. K. Kopp, R. A. Nasirudin, K. Mei, A. Fehringer, F. Pfeiffer, E. J. Rummeny*, et al.*, "Region of interest processing for iterative reconstruction in x-ray computed tomography," in *Medical Imaging 2015: Physics of Medical Imaging*, 2015, p. 94122E.
[428] R. Clackdoyle, F. Noo, F. Momey, L. Desbat, and S. Rit, "Accurate transaxial region-of-interest reconstruction in helical CT?," *IEEE Transactions on Radiation and Plasma Medical Sciences,* vol. 1, pp. 334-345, 2017.
[429] G. Wang and H. Yu, "The meaning of interior tomography," *Physics in Medicine & Biology,* vol. 58, p. R161, 2013.
[430] S. Bonnet, F. Peyrin, F. Turjman, and R. Prost, "Multiresolution reconstruction in fan-beam tomography," *IEEE Transactions on Image Processing,* vol. 11, pp. 169-176, 2002.
[431] M. Costin, D. Lazaro-Ponthus, S. Legoupil, P. Duvauchelle, and V. Kaftandjian, "A multiresolution image reconstruction method in X-ray microCT," in *2009 IEEE Nuclear Science Symposium Conference Record (NSS/MIC)*, 2009, pp. 3871-3876.
[432] K. Niinimäki, S. Siltanen, and V. Kolehmainen, "Bayesian multiresolution method for local tomography in dental x-ray imaging," *Physics in Medicine & Biology,* vol. 52, p. 6663, 2007.
[433] H. Dang, J. W. Stayman, A. Sisniega, W. Zbijewski, J. Xu, X. Wang*, et al.*, "Multi-resolution statistical image reconstruction for mitigation of truncation effects: application to cone-beam CT of the head," *Phys Med Biol,* vol. 62, pp. 539-559, Jan 21 2017.
[434] Q. Cao, W. Zbijewski, A. Sisniega, J. Yorkston, J. H. Siewerdsen, and J. W. Stayman, "Multiresolution iterative reconstruction in high-resolution extremity cone-beam CT," *Physics in Medicine & Biology,* vol. 61, p. 7263, 2016.
[435] C.-K. Chai, A. C. Akyildiz, L. Speelman, F. J. Gijsen, C. W. Oomens, M. R. van Sambeek*, et al.*, "Local axial compressive mechanical properties of human carotid atherosclerotic plaques—characterisation by indentation test and inverse finite element analysis," *Journal of biomechanics,* vol. 46, pp. 1759-1766, 2013.
[436] I. Z. Nenadic, B. Qiang, M. W. Urban, H. Zhao, W. Sanchez, J. F. Greenleaf*, et al.*, "Attenuation measuring ultrasound shearwave elastography and in vivo application in post-transplant liver patients," *Physics in Medicine & Biology,* vol. 62, p. 484, 2016.
[437] J. E. Lindop, G. M. Treece, A. H. Gee, and R. W. Prager, "3D elastography using freehand ultrasound," *Ultrasound in medicine & biology,* vol. 32, pp. 529-545, 2006.
[438] F. A. Pirzada, J. M. Weiner, and W. B. Hood Jr, "Experimental myocardial infarction: 14. Accelerated myocardial stiffening related to coronary reperfusion following ischemia," *Chest,* vol. 74, pp. 190-195, 1978.
[439] E. E. Konofagou, J. D'hooge, and J. Ophir, "Myocardial elastography—A feasibility study in vivo," *Ultrasound in medicine & biology,* vol. 28, pp. 475-482, 2002.
[440] B. J. Fahey, K. R. Nightingale, S. A. McAleavey, M. L. Palmeri, P. D. Wolf, and G. E. Trahey, "Acoustic radiation force impulse imaging of myocardial

radiofrequency ablation: Initial in vivo results," *IEEE transactions on ultrasonics, ferroelectrics, and frequency control,* vol. 52, pp. 631-641, 2005.

[441] E. Konofagou, "Myocardial Elastography," *Cardiac Mapping,* pp. 1073-1082, 2019.

[442] B. De Bruyne, G. Manoharan, N. H. Pijls, K. Verhamme, J. Madaric, J. Bartunek*, et al.*, "Assessment of renal artery stenosis severity by pressure gradient measurements," *Journal of the American College of Cardiology,* vol. 48, pp. 1851-1855, 2006.

[443] K. S. Cunningham and A. I. Gotlieb, "The role of shear stress in the pathogenesis of atherosclerosis," *Laboratory investigation,* vol. 85, p. 9, 2005.

[444] P. R. Moreno, "Vulnerable plaque: definition, diagnosis, and treatment," *Cardiology clinics,* vol. 28, pp. 1-30, 2010.

Part II

Research papers

Author contributions

Oh, I get by with a little help from my friends.

With a Little Help from My Friends (John Lennon & Paul McCartney), 1967

Study I D.L.*, E.M., E.W., M.L., and A.B. conceived of the study. D.L.* conducted all experiments, with D.L.*, E.M. and E.W. contributing to the data post-processing. D.L.* and E.W. performed the statistical analysis. E.M. drafted the manuscript, with input from all authors.

Study II D.M., E.M., M.W.U., and M.L. conceived of the study. D.M. conducted all experiments, data post-processing, and statistical analysis. D.M. drafted the manuscript, with input from all authors.

Study III D.L.*, M.C.-T. and M.L. conceived of the study. Specimen retrieval and clinical input was given by J.R. Imaging experiments were conducted by D.L.*, with data analysis supervised by M.L. and T.C.G. D.L.* wrote the final manuscript with input from all authors.

Study IV S.M. initiated the project, with clinical data acquisition performed by R.H. J.K.D. and H.O. performed the MRI-data analysis. D.M., M.L. and M.W.U. decided on the methodological structure, with all data analysis and interpretation performed by D.M. D.M. wrote the final manuscript with input from all authors.

Study V D.M. and D.N. conceived of the study. D.N. conceived of the method with input from P.L., C.B., and D.M. D.M. and D.N. completed the implementation, with all numerical tests and data analysis performed by D.M. M.B. provided the iterative linear solver, and D.F. implemented the spatial data noise filtering. D.D.-M. and A.F. developed the patient-specific simulations. B.R., K.P., and R.R. collected the *in-vivo* data. D.M. and D.N. wrote the final manuscript with input from all authors.

*D.L. are the pre-marital initials of D.M. (David Marlevi, previously David Larsson)

Study VI D.M. and D.N. conceived of the study. D.N. conceived of the method with input from D.M. and P.L. Experimental data was acquired by H.H. and T.E., and simulation data was generated by D.D.-M. and C.A.F, and processed by D.F and D.M. Data analysis was performed by D.M. with supervision from D.N. D.M. wrote the manuscript with input from all authors.

Study VII D.N. conceived of the study. D.M. performed all *in-vivo* data analysis. B.R., M.H., L.A., E.S. and R.C. collected the *in-vivo* data, along with the structural cardiac assessment. J.S. and S.U. provided the semi-automated segmentation software. J.M.-H. and J.A. were responsible for the virtual cohort analysis. D.M. wrote the manuscript, with input from all authors.

Study VIII H.K., J.W.-B., and D.M. conceived of the method, and D.M., H.K., J.-W.B., K.J.B. and M.C.-T. decided on study design. Data analysis was performed by D.M., M.C.-T. and B.G. The experimental sessions were carried out by D.M. The manuscript writing was coordinated by D.M., with all authors contributing to specific paper sections.